THÈSE

En vue de l'obtention du

DOCTORAT DE L'UNIVERSITÉ DE TOULOUSE

Délivré par : *l'Institut National Polytechnique de Toulouse (INP Toulouse)*

Présentée et soutenue le *20/06/2016* **par :**

Sandrine BERGER

Implementation of a coupled computational chain to the combustion chamber's heat transfer

---

JURY

O. Gicquel	CentraleSupélec, EM2C	Rapporteur
D. Escudié	INSA Lyon, CETHIL	Rapporteur
M. El Hafi	Mines d'Albi, RAPSODEE	Examinateur
M.P. Errera	ONERA	Examinateur
L.Y.M. Gicquel	CERFACS	Directeur de thèse
F. Duchaine	CERFACS	Co-Directeur de thèse
S. Richard	Turbomeca	Invité

École doctorale et spécialité :
MEGEP : Énergétique et transferts
Unité de Recherche :
CERFACS - CIFRE SAFRAN TURBOMECA
Directeurs de Thèse :
Laurent Gicquel et *Florent Duchaine*

Résumé

La conception des moteurs aéronautiques est soumise à de nombreuses contraintes telles que les gains de performance ou les normes environnementales de plus en plus exigeantes. Face à ces objectifs souvent contradictoires, les nouvelles technologies de moteur tendent vers une augmentation de la température locale et globale dans les étages chauds. En conséquence, les parties solides comme les parois du brûleur sont soumises à des niveaux de température élevés ainsi que d'importants gradients de température, tous deux critiques pour la durée de vie du moteur. Il est donc essentiel pour les concepteurs de caractériser précisément la thermique locale de ces systèmes. Aujourd'hui, la température de paroi est évaluée par des essais de coloration. Pour limiter ces essais relativement chers et complexes, des outils numériques haute fidélité capables de prédire la température de paroi des chambres de combustion sont actuellement développés. Cet exercice nécessite de considérer tous les modes de transfert de chaleur (convection, conduction et rayonnement) ainsi que la combustion au sein du brûleur. Ce problème multi-physique peut être résolu numériquement à l'aide de différentes approches numériques. La méthode utilisée dans ce travail repose sur une approche partitionnée qui inclut la résolution de l'écoulement turbulent réactif par un code de simulation aux grandes échelles (LES), un solveur radiatif basé sur la méthode aux ordonnées discrètes ainsi qu'un code de conduction solide. Les diverses questions et difficultés liées à la répartition des ressources informatiques ainsi qu'à la méthodologie de couplage employée pour traiter les disparités d'échelles de temps et d'espace présentes dans chacun des modes de transfert de chaleur sont discutées. La performance informatique des applications couplées est étudiée à travers un modèle très simplifié ainsi que sur une application industrielle. Les paramètres importants sont identifiés et des pistes potentielles d'amélioration sont proposées. La méthodologie de couplage thermique est ensuite étudiée du point de vue physique sur deux configurations distinctes. Pour commencer, l'équilibre thermique entre un fluide réactif et un solide est étudié pour une configuration académique d'accroche flamme. L'influence de la température de paroi de l'accroche flamme sur la stabilisation de flamme est mise en évidence sur des simulations fluide-seul. Ces résultats indiquent trois états d'équilibre théorique différents. La pertinence physique de ces trois états est ensuite évaluée à l'aide de diverses simulations de transfert de chaleur conjugué réalisées pour différentes solutions initiales et conductivités solides. Les résultats indiquent que seulement deux états d'équilibre ont un sens physique et que la bifurcation entre les deux états possibles dépend à la fois de la condition initiale et de la conductivité solide. De plus, pour la gamme de

paramètres testés, la méthodologie de couplage n'a pas d'effet sur les solutions obtenues. Une méthodologie similaire est ensuite appliquée à une chambre de combustion d'hélicoptère pour laquelle le rayonnement est de plus pris en compte. Diverses simulations sont présentées afin d'évaluer l'impact de chacun des processus de transfert de chaleur sur le champ de température : une simulation fluide-seul adiabatique de référence, de transfert de chaleur conjugué, d'interaction thermique fluide-rayonnement ainsi qu'une simulation incluant toutes les physiques. Ces calculs montrent la faisabilité d'un couplage LES/conduction solide dans un contexte industriel et fournissent de bonnes tendances de distribution de température. Pour finir, pour cette géométrie de brûleur et la condition d'opération simulée, les divers résultats montrent que le rayonnement joue un rôle important dans la distribution des températures de paroi. De ce fait, les comparaisons aux essais de coloration sont globalement en meilleur accord quand les trois modes de transfert sont pris en compte.

Abstract

The design of aeronautical engines is subject to many constraints that cover performance gain as well as increasingly sensitive environmental issues. These often contradicting objectives are currently being answered through an increase in the local and global temperature in the hot stages of the engine. As a result, the solid parts encounter very high temperature levels and gradients that are critical for the engine lifespan. Combustion chamber walls in particular are subject to large thermal constraints. It is thus essential for designers to characterize accurately the local thermal state of such devices. Today, wall temperature evaluation is obtained experimentally by complex thermocolor tests. To limit such expensive experiments, efforts are currently performed to provide high fidelity numerical tools able to predict the combustion chamber wall temperature. This specific thermal field however requires the consideration of all the modes of heat transfer (convection, conduction and radiation) and the heat production (through the chemical reaction) within the burner. The resolution of such a multi-physic problem can be done numerically through the use of several dedicated numerical and algorithmic approaches. In this manuscript, the methodology relies on a partitioned coupling approach, based on a Large Eddy Simulation (LES) solver to resolve the flow motion and the chemical reactions, a Discrete Ordinate Method (DOM) radiation solver and an unsteady solid conduction code. The various issues related to computer resources distribution as well as the coupling methodology employed to deal with disparity of time and space scales present in each mode of heat transfer are addressed in this manuscript. Coupled application high performance studies, carried out both on a toy model and an industrial burner configuration evidence parameters of importance as well as potential path of improvements. The thermal coupling approach is then considered from a physical point of view on two distinct configurations. First, one addresses the impact of the methodology and the thermal equilibrium state between a reacting fluid and a solid for a simple flame holder academic case. The effect of the flame holder wall temperature on the flame stabilization pattern is addressed through fluid-only predictions. These simulations highlight interestingly three different theoretical equilibrium states. The physical relevance of these three states is then assessed through the computation of several CHT simulations for different initial solutions and solid conductivities. It is shown that only two equilibrium states are physical and that bifurcation between the two possible physical states depends both on solid conductivity and initial condition. Furthermore, the coupling methodology is shown to have no impact on the solutions within the range of parameters tested.

A similar methodology is then applied to a helicopter combustor for which radiative heat transfer is additionally considered. Different computations are presented to assess the role of each heat transfer process on the temperature field: a reference adiabatic fluid-only simulation, Conjugate Heat Transfer, Radiation-Fluid Thermal Interaction and fully coupled simulations are performed. It is shown that coupling LES with conduction in walls is feasible in an industrial context with acceptable CPU costs and gives good trends of temperature repartition. Then, for the combustor geometry and operating point studied, computations illustrate that radiation plays an important role in the wall temperature distribution. Comparisons with thermocolor tests are globally in a better agreement when the three solvers are coupled.

Un voyage de mille lieues commence toujours par un premier pas.
Lao-Tseu

A tous ceux qui de près ou de loin m'ont amenée ici aujourd'hui,
A mes amis, à ma famille, à Nicolas...

Acknowledgements

Ca y est j'y suis ! C'est la fin d'un beau projet et le début d'un tout autre autour du monde. Ces années de thèse ont été très riches et m'ont beaucoup appris, tant en termes scientifiques et techniques que sur un plan humain. Dans cette si belle aventure, beaucoup de personnes m'ont apporté leur expertise, leur aide et leur soutien et je souhaite aujourd'hui leur dire un sincère et grand merci.

Je remercie tout d'abord les membres du jury, Dany Escudié et Olivier Gicquel, rapporteurs, ainsi que Mouna El Hafi et Marc-Paul Errera, examinateurs, qui ont accepté d'évaluer ce travail et m'ont fourni matière à de nouvelles réflexions.

Je pense ensuite à mes encadrants de laboratoire a qui je transmet mon immense gratitude, Laurent Gicquel et Florent Duchaine qui sont partie intégrante de ce travail et qui ont su chacun à leur manière m'apprendre énormément, m'orienter, me soutenir et me transmettre leur passion pour ce domaine de recherche (et pour les palettes allant du bleu au rouge en passant par le vert). Je remercie à cette occasion Florent d'avoir su rester patient face aux heures que j'ai passé dans son bureau à m'intérroger sur le sens profond de la thermique et de la CFD. Un grand merci ensuite à mes encadrants industriels à TURBOMECA, Thomas Lederlin, encadrant des premières heures et Stéphane Richard qui a pris la relève et m'a tant expliqué sur les moteurs d'hélicoptère et les divers enjeux de leur développement et qui a su défendre mon petit carré. J'en profite pour remercier Jean Lamouroux, qui m'a aussi apporté son support dans la difficile tâche de comprendre et de dompter le moteur dont on ne doit pas prononcer le nom.

J'aimerais aussi remercier l'ensemble des séniors combustion qui détiennent cette fabuleuse expérience et cette capacité de recul si précieux pour nous petits thésards avides de conseils et de solutions. Mes remerciements tout particuliers vont à Bénédicte Cuenot qui m'a ouvert la porte de la communauté combustion et m'a conseillé pour les questions de rayonnement, Antoine Dauptain, dont la créativité et l'ingéniosité m'ont toujours fascinée dans son développement de nouveaux outils et représentations des moteurs et qui a su répondre présent à tous mes "au secours, je représente ça comment avec un schéma???", ainsi qu' à Gabriel Staffelbach, mon magicien HPC, développement

et dépannage en tout genre, devenu un ami précieux. Puisqu'on parle de dépannage en tout genre, je tiens à adresser un grand merci à toute l'équipe de l'administration, et en particulier à Marie, Michelle et Chantal (je crois que je n'ai jamais rencontré quelqu'un qui souriait autant) sans qui tout serait tellement plus compliqué. Mes remerciements aussi à toute l'équipe CSG qui rend tout ça possible et garde le sourire quand on arrive avec toujours plus de questions, de demandes complexes et de problèmes.

Mes remerciements vont aussi aux stagiaires, thésards et post-docs de l'équipe qui ont contribué à faire de cette expérience une richesse. J'ai une pensée particulière pour mes co-bureaux successifs, Damien, qui m'a si gentiment accueillie au labo et dans son monde et avec qui j'ai partagé tellement de conversations passionnantes et passionnées et de tranches de vie, Nikos, co-bureau des derniers instants qui a eu cette façon si particulière et si touchante de prendre soin de moi (et de mon régime alimentaire) et de me faire rire pendant le sprint final de cette thèse. Un sincère merci aussi à Manqi pour les petites attentions tout droit venues de Chine, à l'équipe de Coincheurs d'avoir résisté à l'envie de me zigouiller malgré mes maladresses évidentes, à Clément pour les pauses clopes/fou rires, à Geoff mon co-captain qui m'a appris à prononcer Nukiyama-Tanasawa, à Anne pour le café filles et affiliés et d'avoir tenté d'éveiller mon esprit à quelques notions de chimie, à Corentin d'être resté calme en voyant mes scripts python et de m'avoir fourni autant de conseils judicieux (et de me faire rire avec l'amour qu'il porte à son tapis volant), à César d'avoir réussi à me convaincre que rentrer du boulot à roller c'était cool (contre toutes attentes c'était effectivement cool), à Laure qui ayant les mêmes deadlines que moi m'a permis de dédramatiser, à Chouchou, plasmicien infiltré, qui a entre autres supporté mes états d'âmes de fin de thèse et qui a su me faire croire que j'étais super drôle, et à Dorian, en quelques sortes mon co-thésard, pour son expertise sur les multiperf et pour sa gentillesse.

Je tiens ensuite à dire un immense merci à mes amis, qui sans toujours s'en rendre compte m'ont tellement soutenue dans cette aventure. Dans le désordre, merci aux Bordelais d'être si parfaitement inimitables et drôles, à Hannah qui a toujours une pêche incroyable et ce rire si communicatif, à Amandine qui a rempli ces vacances en Sicile de fou rires, à Manon (ma super cousine) qui a le coeur sur la main et fait des gâteaux au chocolat à tomber par terre, à Célia (notre Chuck Norris féminine à nous) de m'avoir appris à sauter en roller et à faire de l'accroche-branche, de prendre tellement soin de nos papilles (j'associe Corentin à ces remerciements), et d'être si bienveillante et pleine de vie, à mademoiselle lélodie pour nos conversations hétéroclites et fascinantes et d'avoir si souvent fait s'aligner les planètes pour me dire exactement ce qu'il fallait quand il fallait (C'est le talent!), à Fred (docteur du genre qui répond quand on demande s'il y a un docteur dans l'avion) et GG (ma rock star, mon acolyte des plus et des moins, ma coach en "te FZ pas") d'être tous les deux là depuis toutes ces années et de me faire toujours autant rire avec des jeux de mots à la con, enfin merci à Yo, coloc parmis les colocs, qui a su m'amadouer à coup de Bretzels, de mousse au chocolat et de pâte à crèpes préparée à 5h du matin avant de prendre la route pour Bordes, merci pour ces moments magiques et pour les soirée guet-apens.

Toute ma gratitude aussi à ma mère, mon père, Jean, Sylvie, Paul, Leïla et toute ma famille (les Aixois je pense aussi à vous) qui ont chacun contribué à leur façon et sont là depuis les premiers instants.

Enfin, je tiens à dire ma profonde reconnaissance à Nicolas (mon ange gardien, ma bouée canard jaune de fin de thèse) pour son soutien sans faille, sa patience et ses conseils durant l'exercice difficile de bouclage de cette thèse. Merci du fond du coeur d'avoir su me faire rire et rêver et de rendre la vie si jolie ...

'Cause I'm on top of the world, 'ay
I'm on top of the world, 'ay
Waiting on this for a while now
Paying my dues to the dirt
I've been waiting to smile, 'ay
Been holding it in for a while, 'ay
Take you with me if I can
Been dreaming of this since a child
I'm on top of the world.

Imagine Dragons, On Top Of The World

Contents

Chapter 1

Scientific context

Contents

Because of progressive oil shortage, increasingly challenging environmental issues as well as a raising constraint of cost reduction, energy conversion through combustion has become a key current international concern. Since several years now, alternative solutions of renewable energy production more environmental friendly have born and developed in many industrial fields such as terrestrial transport or domestic energy supply. For air transport, such alternatives are today only at a very early development step. Indeed, the high power-to-weight ratio and autonomy required for aeronautical propulsion are today only achievable through hydrocarbon combustion. Addressing both environmental and cost constraints goes therefore through a better mastery of the combustion process. Tremendous efforts are thus deployed to better understand and control all the phenomena at play and produce cleaner and more efficient engines.

The work presented in this manuscript is the result of this specific context. It was funded by Turbomeca-SAFRAN to investigate and produce new methods to support the development of new generations of helicopter gas turbines.

1.1 Working principle of a helicopter engine

After some decades of very different concept trials, all gas turbines basic features as they are known today were clearly established by the beginning of the 1950s (Lefebvre, 2010). These devices are composed of an air intake, one or more compressor stages, a burner, one or more turbine stages and an exit nozzle (Fig. 1.1). Despite this similar global composition of all gas turbines, the specific

characteristics of every components vary with the applications (electrical power production, jet engine, turboshaft). For helicopter engines, restraining constraints of weight and compactness as well as an ability to operate on a very large range of conditions, lead more specifically to the common use of the following components (Fig. 1.1):

- ▷ an air intake designed to ensure the proper conditions at the compressor inlet,
- ▷ few stages of compressors (usually centrifugal) operated by a shaft running through the engine and driven by the high pressure turbine,
- ▷ an annular reverse-flow combustion chamber allowing both engine compactness and a close coupling between the compressor and the turbine (avoiding hence shaft whirling problems),
- ▷ several turbine stages converting gas kinetic energy into power, including a high pressure turbine and several stages of low pressure turbines driving respectively the compressors and the rotor,
- ▷ an exit nozzle.

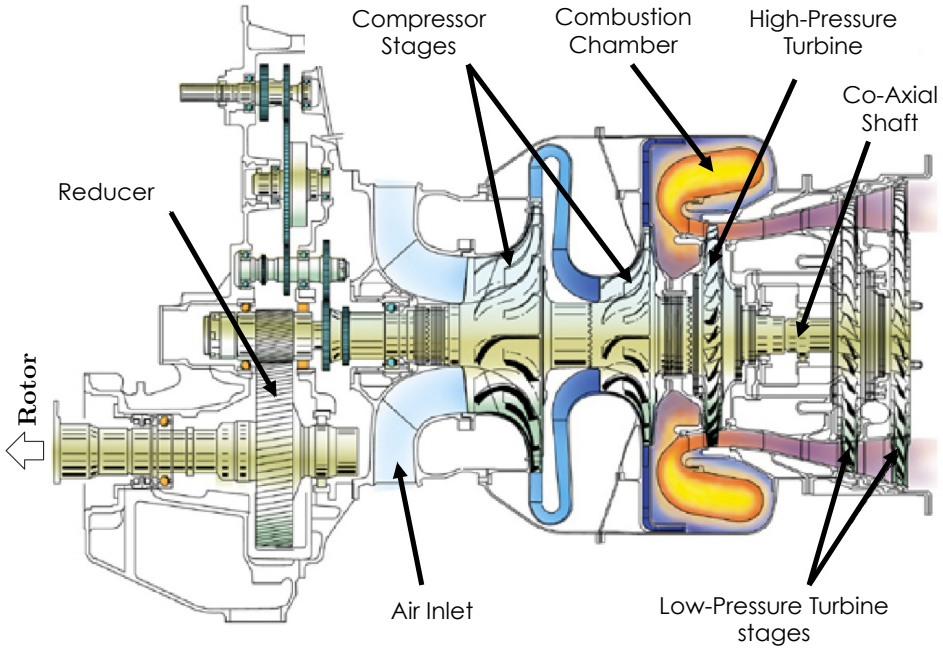

Figure 1.1: Cut view of Turbomeca's Ardiden engine.

While flowing in these various components, the flow undergoes successive thermodynamic changes illustrated by the Brayton cycle (Fig. 1.2). In this ideal case, the air flow entering the engine undergoes an isentropic compression in the compressor stages (1-2), then the isobaric combustion

process adds heat into the system (2-3), burnt gases go through an isentropic expansion in turbine stages (3-4) and finally exhaust in an isobaric process to the atmosphere (4-1). In this ideal cycle, the net output power supplied by the engine for a given mass flow rate corresponds to the difference between the work required to drive the compressor and the work gained in the turbine stages and is proportional to the area limited by the 1-2-3-4 curve in Fig. 1.2. Besides, the Brayton cycle efficiency η is defined as the ratio between the net output power and the input heat (due to combustion). In the absence of pressure and heat losses, this quantity reads:

$$\eta = 1 - \left(\frac{P_2}{P_1}\right)^{\frac{\gamma-1}{\gamma}} \tag{1.1}$$

where P_i is the pressure at the point i of the cycle and γ the gas polytropic exponent. At constant

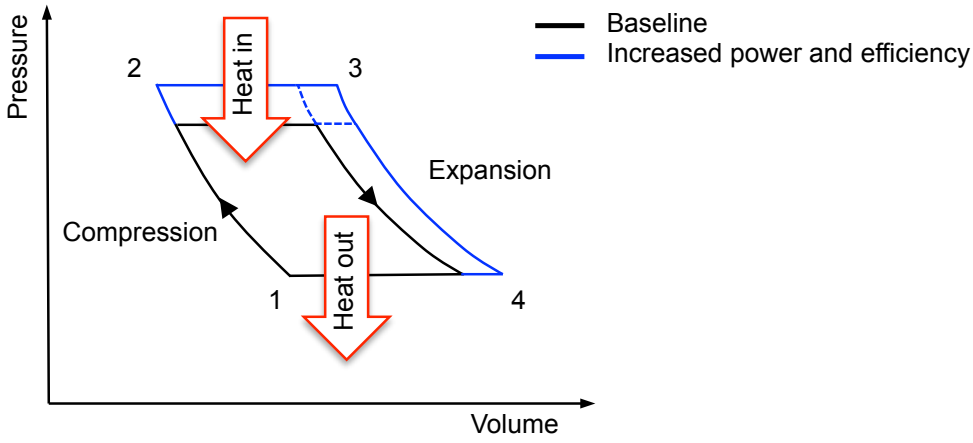

Figure 1.2: Ideal Brayton cycle.

output power, increasing the cycle efficiency thus goes through an increase of the pressure ratio $\frac{P_2}{P_1}$ in the compressor stages. Such a feature however, leads to increased temperatures in the combustion chamber and in the turbine stages. Over the years, gas turbine pressures have risen from 5 to 50 atm with resulting inlet and outlet temperatures respectively going from 450 to 900 K and from 1100 to 1850 K. At the same time expectations for life duration of flame tube liners have increased from a few hundred hours to several tens of thousands of hours, imposing drastic design constraints to these components (Lefebvre, 2010).

The mechanical stresses experienced by the burner liner are small compared to those undergone for instance by rotating components. However, combustion chamber solid parts encounter very high levels of temperature and large thermal gradients that threaten material durability. In modern gas turbines, hot gases in the combustion chamber can reach temperatures of the order of 2500 K. Such temperatures are far above the melting temperature of the materials forming the combustion chamber liner and injection system. Additionally, for the nickel-based or cobalt-based

alloys commonly used, a sharp decrease of the mechanical strength is observed for temperatures above 1100 K (Lefebvre, 2010). Therefore, the natural cooling of the liner through radiation and convection on the casing side is not sufficient to evacuate the heat transferred to the walls on the flame tube side of the liner and to decrease the temperature to an acceptable level. Specific cooling devices are required to cool down the metallic materials and prevent hot gases direct impingement onto the walls.

The required efficiency of such systems has raised over the years. Indeed, the increase of pressure ratios motivated by efficiency gains lead to larger burner inlet temperatures that reduce the casing air ability to cool down the walls by convection. In parallel, the pressure raise in the combustion chamber leads to larger heat transfers by radiation between the hot gas and the wall, further increasing the liner temperature. Finally, decreasing the levels of NO_x emission has mainly been answered through leaner combustion, leading to more air being allocated to combustion. The amount of wall cooling air must hence be minimized to maximize the air available for emission control. All these constraints call for an optimization of wall cooling to find the optimal trade-off between performance of the engine and resistance of the components. However, this requires a detailed knowledge of the metal temperatures and thermal stresses experienced by the combustion chamber solid parts.

Today, complex thermocolor tests allow engine designers to access temperature fields on the internal and external walls of the flame tube. However, this experimental approach imposes some limitations such as the number of prototypes that can be tested and more importantly the few diagnostics made available. To limit such expensive experiments and integrate the knowledge of the thermal environment earlier in the design process, efforts are currently performed to provide high fidelity numerical tools able to predict the combustion chamber wall temperature. Such simulations would provide a path to get out from the trial and error process by allowing an easier determination of the mechanisms responsible for specific and undesired aerothermal response of the combustor. For the numerical resolution of such a thermal problem, one needs to consider the three heat transfer modes existing in nature, namely convection, radiation and conduction.

1.2 Heat transfer processes in a combustion chamber

In a combustion chamber, energy exchange within the fluid and the solid as well as between the two domains is achieved simultaneously through the three existing modes of heat transfer. A schematic representation of these thermal exchanges is provided in Fig. 1.3. Broadly, convection and radiation redistribute energy within the fluid and heat or cool the liner respectively on the flame tube and casing sides. Note that the relative magnitude of these two modes of heat transfer between the fluid and the solid depends on the burner configuration and operating conditions (Lefebvre, 2010). Finally, in reaction to the thermal stresses applied by the fluid, heat is trans-

ported in the solid domain through conduction within the liner. To resolve the thermal problem in a combustion chamber one needs to consider all these heat transfer processes as well as the energy production through the chemical reactions. All these four processes are tightly coupled and each phenomena bounds the evolution of the others.

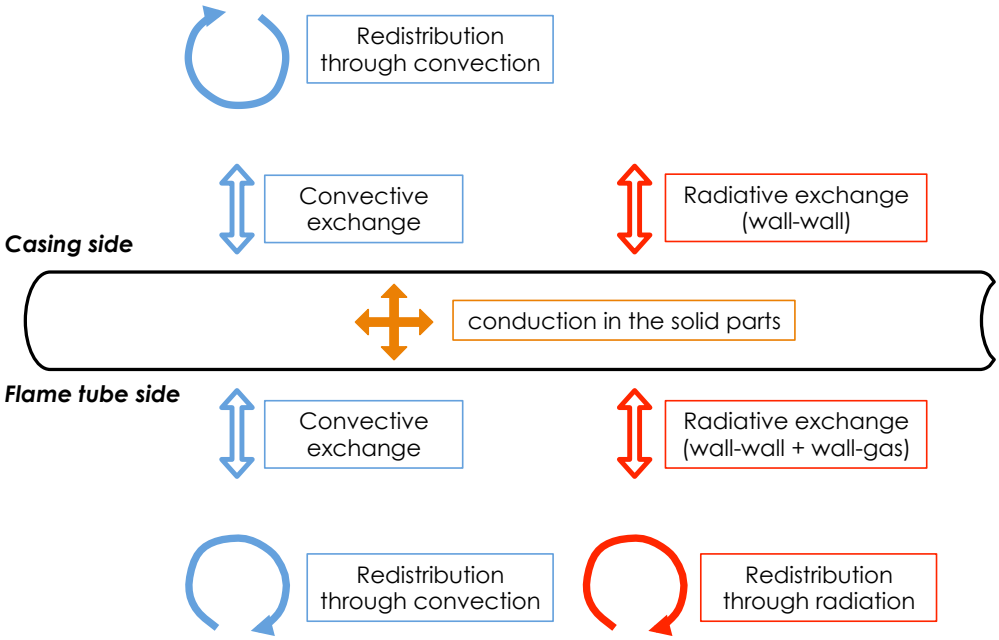

Figure 1.3: Thermal exchanges within the fluid and the solid domains as well as between the two domains.

Numerical tools allowing the numerical resolution of these processes independently in a burner exist since several years now. In particular, to compute the turbulent combustion phenomena (including both convection and energy production due to combustion), three main approaches are available which differ mainly by the respective amount of direct resolution and modeling that is to be provided. By decreasing amount of modeling and increasing associated computational cost, these are: Reynolds Averaged Navier-Stokes (RANS) simulation, Large Eddy Simulation (LES) and Direct Numerical Simulation (DNS) (Pope, 2000; Poinsot & Veynante, 2005). Depending on the flow properties, the geometry, the level of details required, as well as the nature of the target application, the various approaches may/may not be affordable and may/may not provide accurate solutions and sufficient information. While RANS flow simulation is the less expensive method and has thus been used for years, its accuracy is limited by the quality of its models. In the context of reactive flows that are strongly affected by turbulence and the inherent mixing, the use of RANS approaches in configurations as complex as current industrial burners showed some precision limitations and designers turn today more and more towards high fidelity techniques such

as LES. Indeed, the latter is less limited by associated models and can take great advantage of the increasing available computing power. LES is now widely accepted as the reference approach for burner flow simulations (Mahesh *et al.*, 2001; Tucker & Lardeau, 2009) and will be used for the current study. In the same manner, various numerical methods exist to solve the radiative heat transfer and the solid conduction problems in combustion chambers.

However, most numerical studies reported in the literature are limited to the investigation of a single physical sub-system, neglecting the interactions with contiguous domains and with other physics within the same domain. At best these standalone simulations integrate some interactions with the environment through constant physical quantities determined with raw physical phenomena approximations or extracted from experiments as well as from other standalone simulations. None of these approaches, however, allow an effective resolution of the various interactions between the different physical sub-systems. These independent simulations, though sufficient for the study of several phenomena may suffer from serious limitations. In some cases, improving the numerical resolution accuracy of a single sub-component seems to be of limited interest as long as the interactions between the sub-system and its environment is approximately defined. Therefore, a challenging path of improvement explored since several years now lies in the realization of multi-physics simulations in which the interactions between different physical sub-systems are actually solved.

1.3 Multi-physic simulations

Research on multi-physics thermal problems for combustion applications is relatively new and has greatly developed in the last decades. However, most existing studies include the coupling of combustion and either solid conduction or the radiative phenomena but not both. Such three physics simulations have however been reported by Mercier *et al.* (2006) in a RANS context for the simulation of an industrial burner and three physics simulations including a LES solver were performed by Amaya (2010). In this last study, the solid domain was limited to the injection device, precluding any investigation of the three physics effect on the combustion chamber liner temperature.

The resolution of such multi-physics problems jointly in the fluid and the solid domains can be done numerically through the use of two main approaches: monolithic and partitioned coupling. Monolithic techniques consist in producing a new solver handling the resolution of all the considered phenomena within the same computational structure. In other words, this is a all-in-one solver. Such approaches though appealing especially when strong interconnections exist between the sub-system physics, may induce performance and scalability loss for specific sub-systems such as the LES resolution of the flow whose performance relies on specific data structures and solvers. On the contrary, the partitioned approach relies on the development of a coupled framework in which pre-existing codes are used to solve each physical sub-system. This allows the use of ef-

ficient code structure and numerical methods specifically adapted to each set of equations. The solvers are then coupled through information exchange at the sub-system interfaces. In terms of performance, and to actually benefit from such a partitioned context, coupled applications require the use of a highly scalable code coupler to handle the coupled framework created around the various independent solvers. Besides, the computational cost mismatch between the sub-systems needs to be correctly handled to avoid any loss of performance. In such a context, the use of unsteady LES solvers, generally very scalable but highly computer ressource consuming increases performance constraints.

1.4 Objectives and outline of the manuscript

The work is motivated by the will to provide a high-fidelity solution of the thermal problem in a combustion chamber by considering all the means by which energy is exchanged and produced within the system. For this purpose, three codes solving the three heat transfer modes are coupled to investigate the interactions between the various physics in a combustion chamber: a high fidelity Large Eddy Simulation (LES) reacting flow solver, an unsteady solid conduction code and a Discrete Ordinate Method (DOM) radiation solver. Both scientific and engineering issues are investigated. More precisely, the various objectives targeted in this study are successively addressed through the following organization:

- **PART I**: In this introductory part, the three physics at play when investigating the thermal state of a combustion chamber, namely combustion in the fluid domain, conduction within the chamber solid parts as well as radiative heat transfer in the fluid and at walls are successively discussed. The intrinsic different nature of these three processes and the resulting various resolution approaches (modeling approaches, specific assumptions and models) are detailed. Modeling of the interactions between the three physics is then addressed. In this context and acknowledging findings from the literature, several issues are discussed. First, in this manuscript, only mean quantities representative of the permanent regime are sought for. Starting from an initial condition, the simulation consists hence in computing all the sub-system interactions during a transient until the permanent regime is reached. However and since the various phenomena considered are characterized by very different time scales, such a computation of the full transient is not affordable in terms of computational cost and specific techniques are thus deployed. Second, the choice of the interface variables is critical both in terms of solution accuracy and computation stability and has to be done carefully. Coupling strategies chosen to handle both issues are thus discussed. Finally, a specific issue lies in the computational cost mismatch handling between the sub-systems. The impact of computing parameters on coupled simulations scalability is investigated in terms of coupling performance as well as computing resource distribution between the codes. The informatic and numerical implementation of coupled simulations having been addressed in this part, the two remaining parts of the manuscript focus on physical investigations of the interactions

in two different burner devices.

- ▷ **PART II**: In numerical simulations of reactive flows, thermal boundary conditions are rarely well known and are thus treated mostly either as being adiabatic or at approximately fixed isothermal conditions. Such approximations on thermal boundary conditions can lead to several errors and inaccurate predictions of the combustion chamber flow field. In many cases, the wall thermal fields have a significant impact on the reactive flows, especially through the flame stabilization process. To validate the added value of a Conjugate Heat Transfer (CHT) approach in this context and evaluate the coupled aerothermal solution proposed, a simplified academic case is first studied. A detailed investigation of the thermal behavior of a laminar premixed flame stabilized thanks to a square cylinder in a channel flow (Kedia & Ghoniem, 2014*a*,*b*, 2015) is proposed. For this purpose, various standalone fluid DNS as well as coupled CHT simulations are performed. Such an academic configuration although more representative of some canonical laboratory burner than industrial aeronautical combustors allows deeper understanding and identification of the phenomena involved and their interactions without raising issues on potential modeling effects.

- ▷ **PART III**: To properly evaluate the thermal environment of combustors, combustion, conduction and radiation should be taken into account as well as a realistic thermal modeling of the multiperforated walls. Besides, and in light of the literature results, the use of a LES flow solver is required to perform accurate burner coupled simulations. In this context, an objective of this work is to provide an evaluation of the solid steady state temperature field in a helicopter engine combustor while assessing the contribution of the different heat transfer mechanisms. For this purpose, various standalone and coupled simulations are performed. These include a reference adiabatic fluid-only simulation, and three multi-physics coupled simulations: Conjugate Heat Transfer (CHT), Radiation-Fluid Thermal Interaction (RFTI) and Combined Combustion, Conduction and Radiation (3CR) simulations. The various coupled simulations allow an evaluation of the interactions between all the physical sub-components. Note finally that for these exercise, the prediction capabilities of the methods is assessed through comparisons between experimental results and coupled simulations.

Specific elements of the work performed during this PhD thesis were published in the following articles:

Berger, S., Richard, S., Staffelbach, G., Duchaine, F. & Gicquel, L.Y.M. 2015 Aerothermal prediction of an aeronautical combustion chamber based on the coupling of Large Eddy Simulation, solid conduction and radiation solvers. *ASME Turbo Expo 2015: Turbine Technical Conference and Exposition, Montréal, Quebec, Canada.*

Berger, S., Richard, S., Staffelbach, G., Duchaine, F. & Gicquel, L.Y.M. 2016 On the sensitivity of a helicopter combustor wall temperature to convective and radiative thermal loads. *Applied Thermal Engineering* In press.

Berger, S., Duchaine, F. & Gicquel, L.Y.M. 2016 Influence des conditions aux limites thermiques sur la stabilisation d'une flamme laminaire prémélangée. *Congrés Français de Thermique*.

Berger, S., Richard, S., Duchaine, F. & Gicquel, L.Y.M. 2016 Variations of anchoring pattern of a bluff-body stabilised laminar premixed flame as a function of the wall temperature. *ASME Turbo Expo 2016: Turbine Technical Conference and Exposition, Seoul, South Korea*.

Part I

Multi-physic coupled simulations

Introduction

To answer the current objective of investigating the thermal state of a burner and perform highly performant multi-physics coupled simulations, several topics are to be addressed and are successively discussed in this part. First, the physical specificities of combustion, solid conduction and radiation as well as the resulting numerical methods and models employed for their numerical resolution needs to be recalled. Having determined the approaches used for the independent resolution of the three phenomena, the resolution of the thermal problem required then the inclusion of the interactions between the sub-systems. In the partitioned coupling approach retained for the present computations, this is achieved via a regular exchange of specific physical quantities between the solvers. In such a context and to perform accurate and stable coupled simulations at an affordable computational cost, the treatment of the time and length scales disparities between the sub-systems as well as the choice of the interface variables is critical. Coupling strategies developed to handle these issues are thus discussed in this part. Finally, an additional disparity between the sub-systems arise from the very different computational cost associated to the resolution of the various physical phenomena. Such a feature has to be correctly addressed by the coupling methodology to avoid computational resource waste and achieve highly performant coupled simulations.

All the issues highlighted here are discussed in this first part. The physics and the numerical methods employed to solve combustion, solid conduction and radiation are briefly recalled in Chapter 2. The coupling strategy between the sub-systems is then discussed in Chapter 3, acknowledging various studies from the literature. Finally, questions relative to coupled simulation performance are addressed in Chapter 4.

Chapter 2

Physical problem and numerical resolution of the combustion, solid conduction and radiation phenomena

Contents

When investigating the thermal state of a burner, three physics are to be considered, namely combustion in the fluid, conduction within the chamber solid parts as well as radiative heat transfer in the fluid and at walls. As already mentioned in the introduction (Chapter 1), the current multi-physics partitioned approach relies on the resolution of these three phenomena with different dedicated codes namely AVBP, AVTP and PRISSMA to solve respectively combustion, solid conduction and radiation. These three phenomena are intrinsically different. Their resolution relies on different approaches, assumptions and models, specific to each physics.

In this chapter, the physics of the three independent problems is described as well as the associated numerical resolution methods. All these physics and various existing resolution strategies in terms of numerics and modeling are the subject of very well written reference books and previous PhD thesis manuscripts. The description of the resolution method of each physics is restricted here to the approaches developed in the codes selected for the present study and emphasis is made

on specific issues linked to the present multi-physics approach. Reactive flows are the focus of Section 2.1 followed by the heat transfer through solid conduction and radiation respectively in Sections 2.2 and 2.3.

2.1 Reactive flows

The reactive flow within a burner is in itself a multi-physics problem and the combustion process results from complex two-way couplings between the fluid motion, species and heat diffusion as well as chemical reactions. As a result, the consideration of such a phenomenon requires the inclusion of both fluid mechanics and chemistry. The resolution of a fluid mechanics problem, even in a non-reactive context is already a complex task in itself and is first discussed in the present section. The consideration of a multi-species flow and the inclusion of chemical reactions is addressed in a second time. Note that when solving a reactive flow problem, the strong relation between the flow and the chemical reactions motivates the usual joint consideration of both phenomena within the same solver. Only a brief description of the physical phenomena and their numerical resolution is presented here. All these developments and further details can be recovered in text books such as Pope (2000) (non-reactive flows) or Williams (1985) and Poinsot & Veynante (2005) (reactive flows).

2.1.1 Flow physics and numerical resolution

Viscous flows can be phenomenologically separated in two categories: laminar and turbulent flows[1]. Such a property characterizes the flow regime and is determining for its resolution.

Flow regime: laminar versus turbulent

The drastic difference between laminar and turbulent flows was in particular highlighted by Reynolds in 1883 with a simple experiment (Reynolds, 1883) illustrated in Fig. 2.1. He injected a thin stream of dye into a water pipe flow and observed the effect of increasing the flow rate. At low flow rates, the dye stream trajectory was well-defined and parallel to the pipe axis. Its diameter very slightly increased when flowing downstream. As the flow rate was increased over a threshold value, the dye path spreads towards the pipe walls, following three dimensional irregular motions. Reynolds observed that the transition from one behavior to another occurred within a fixed range ($[2000 - 3000]$) of what is called today the Reynolds number and denoted Re (Reynolds, 1894). This non-dimensional number evaluates the ratio between inertia and viscous

[1] Valuable observation of both flow regimes is proposed through numerous photographs of different simple configurations in Van Dyke (1982).

forces and is nowadays widely used to characterize flow regimes:

$$Re = \frac{UL}{\nu} \tag{2.1}$$

where U and L are characteristic velocity and length scale of the flow and ν the fluid kinematic viscosity. A low Reynolds number indicates a flow dominated by viscous forces and is thus char-

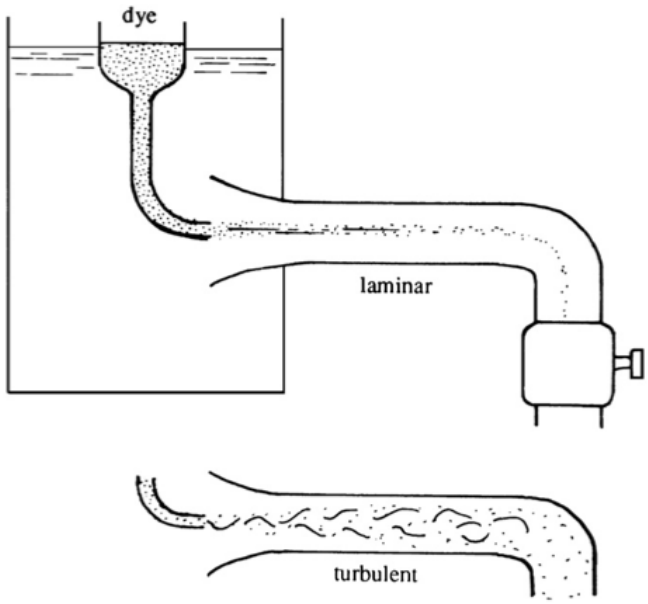

Figure 2.1: Reynolds's experiment. From (Kundu et al., 2011).

acteristic of laminar flows while a high Reynolds number corresponds to a turbulent flow where inertial forces are predominant. The range of Re for which the flow switches from one regime to the other is usually referred to as the transitional regime and is very dependent on the configuration.

While laminar flows are characterized by regular paths with fluid particles moving in parallel layers, turbulent flows have an apparent random three dimensional behavior. They are composed of eddies of multiple length-scales (and time-scales) ranging from the integral length scale comparable to the flow scale to the Kolmogorov length-scale characteristic of the smallest eddies. Turbulent kinetic energy is produced in the largest structures and then transferred gradually to smaller and smaller scales through unsteady eddies stretching and break up. At the Kolmogorov scale, inertia and viscous forces balance, the kinetic energy contained in the smaller eddies eventually dissipates into heat. This fluctuation energy cascade principle was first formalized by Richardson in 1922 (Richardson, 1922) then by Kolmogorov (Kolmogorov *et al.*, 1937) and is the key of the current understanding of turbulence. A graphical representation of this concept is provided in Fig. 2.2

where a schematic turbulent flow energy spectrum is shown as a function of the wavenumber κ.

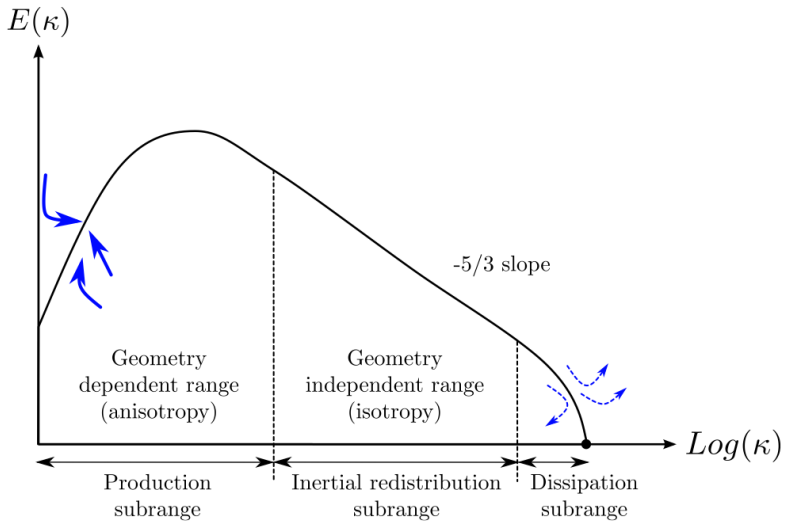

Figure 2.2: Turbulent energy spectrum as a function of the wave number κ. From (Fransen, 2013)

At a high Reynolds number, a separation of scales can be assumed (Pope, 2000). While the large scale motions control the flow transport and mixing and are strongly geometry dependent, the small scales behavior is mostly controlled by the fluid viscosity and the energy received from the large scales. Therefore, the latter are known to have universal and only diffusive properties. Due to the effective transport and mixing ensured by large turbulent scales, turbulent flows are much more sought after in industrial applications than laminar flows. Besides, turbulence also enhances heat exchange rates at fluid-solid interfaces and are thus favored for numerous internal cooling applications.

Despite the strong phenomenological differences between laminar and turbulent flows, both regimes can be mathematically described with the same set of equations. These equations and their resolution are discussed in the next paragraph.

Flow resolution

The flow dynamics was first described mathematically by Euler in 1757 (Euler, 1757) for inviscid fluids. Sixty five years later, Navier introduced a viscosity coefficient in the equations (Navier, 1822). Finally, after contributions from various scientists through the years, Stokes published in 1845 the conservative equations for viscous fluids in their current form (Stokes, 1845) known as the Navier-Stokes equations.

Due to its highly non-linear nature, this set of equations rarely gives right to analytic solutions. Instead, flow problems are spatially discretized on computational grids and solved numerically. For such purposes, an additional complexity arises in the context of turbulent flows: all the flow time and length scales are described in the balance equations leading thus to a huge amount of information to be resolved on the computational mesh. As a result, solving the full equations over the whole turbulence spectrum is not achievable (in terms of computing capabilities) in general. To overcome this issue and solve the flow field at an affordable CPU cost, various resolution approaches have been developed during multiple years of research. These differ mainly by the respective amount of direct resolution and modeling that is to be provided. In general, the complexity and the associated CPU cost increase with the level of details provided by each method. In addition, depending on the flow properties (Reynolds number), the geometry, the level of details required, as well as the nature of the target application, the various approaches may/may not provide accurate solutions and sufficient information. Three of the leading computational formalism for turbulent flows are discussed here: Direct Numerical Simulation (DNS), Large Eddy Simulation (LES) and Reynolds Averaged Navier-Stokes (RANS) simulation. For each method, the respective parts of the turbulence spectrum which are resolved or modeled are summarized in Fig. 2.3.

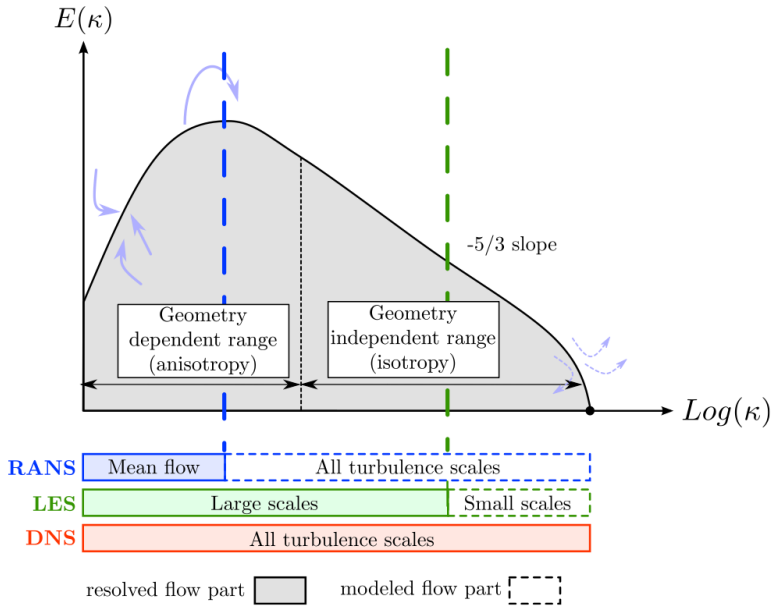

Figure 2.3: Turbulent energy spectrum as a function of the wave number and various approaches modelisation domain. From (Fransen, 2013)

Direct Numerical Simulation

The full balance equations are numerically resolved: turbulent motions are explicitly computed

over the entire spectrum or equivalently for the full range of spatial and time scales (Fig. 2.3). When considering non-reactive flows[2], DNS are thus model free and often assimilated to numerical experiments. This approach has provided very valuable insight into the understanding of the complex non-reactive and reactive turbulent flows and allowed for instance to produce efficient combustion models (Poinsot, 1996; Chen *et al.*, 2006; Chen, 2011). However, such a full resolution of the turbulent flow requires a specifically defined grid with extremely small cell sizes (to resolve the smallest scales). In industry like applications, at least three orders of magnitude separate the flow system size from the mesh size needed to resolve the smallest eddies (Bockhorn *et al.*, 2009), therefore precluding the use of DNS in such flows. This approach is for now limited to simplified geometries and laminar or low Reynolds number turbulent flows (because the computational cost increases as Re^3 (Pope, 2000)). In other words, only academic applications can be pursued with this method. In this manuscript, a DNS approach is employed to compute an academic laminar bluff-body flame which is then used to go deeper in the understanding of thermal multi-physics simulations.

In most practical turbulent applications, it is not feasible to resolve all relevant scales explicitly and models are introduced to reduce the dynamic range of scales to solve and to account for influences of unresolved features on the resolved quantities. Two main classes of modeling are today present and described hereafter: RANS and LES.

Reynolds Averaged Navier-Stokes

This approach developed in the sixties aims at solving the mean flow values while modeling all the turbulent fluctuations. The RANS set of equations is obtained by time or ensemble averaging the Navier-Stokes balance equations. Therefore, variables are subdivided into an explicitly resolved part (mean quantity) and an unresolved modeled part covering the entire turbulence spectrum Fig. 2.3. The production of both turbulent and turbulent combustion models (for reactive flows) is thus needed to properly account for the impact of the fluctuation fields on the mean. This modeling process has received extensive attention from the scientific community both in non-reactive (Pope, 2000) and reactive contexts (Poinsot & Veynante, 2005; Bockhorn *et al.*, 2009).

RANS simulations provide a global knowledge of the flow mean repartition at a reduced CPU cost. Over the past decades, such numerical tools have been increasingly integrated into the design process of industrial devices such as aeronautical engines. Moreover, the reduced restitution times encountered with such techniques allowed their extensive use in optimization processes (Duchaine *et al.*, 2009*b*), hence reducing drastically the number of experimental tests required during the development of industrial devices. Despite such clear advantages and because of the indubitable dependency of the large turbulent structures on the flow geometry, RANS simulations are somewhat limited by the required adaptation of turbulence and turbulent combustion models to the

[2] reactive flows require in addition the use of a chemical model

specificities of the flow considered. In addition, in reactive flows that are inherently affected by mixing, the use of RANS approaches in configurations as complex as current industrial burners showed some precision limitations and designers turn today more and more towards high fidelity techniques such as LES.

Large Eddy Simulation

Just like in RANS approaches, LES provides a solution to the Navier-Stokes equations at a reduced CPU cost compared to DNS by resolving some features of the turbulent flow while modeling others. However, the resolved part is much consequent in LES: the large scales which contain most of the energy and are application dependent are resolved (Fig. 2.3) and modeling is reduced to the smaller dissipative scales known to have a more universal behavior and costly to resolve. Since this approach relies on the universality of the small scale behavior, models are much less dependent on the considered application. As a main consequence, LES offers more predictivity capabilities than RANS.

The LES set of equations results from a spatial filtering of the Navier-Stokes equations: the large structures are resolved while all the scales of the turbulent flow below the filter length scale are filtered out. Due to the filtering of non-linear terms in the balance equations, sub-grid scale closures are needed which raises additional unknown terms which need to be modeled. In practice the scale separation between resolved and modeled features is often achieved directly via the computational mesh. Therefore, the more refined the mesh is the smaller are the resolved turbulent scales. As a result, for a given configuration, an increase of the computing capacity allows theoretically to include more and more resolution (with smaller and smaller cells) and less and less levels of modelisation. This specific point is a prerequisite for the development of SGS models which should hence tend towards zero as the grid resolution increases towards that required for DNS.

Originating from the meteorologic scientific field in the sixties (Lilly, 1966; Deardorff, 1970), this approach developed significantly in the last decades with the increase of computing power. Indeed, the computational overhead induced by LES compared to RANS computations is substantial. First, performing accurate LES imposes more demanding grid refinement constraints, leading to meshes with larger number of points and cells. Second, the resolution of the Navier-Stokes equations through such a high fidelity method requires the use of specifically designed highly precise numerical schemes providing both low numerical dissipation and low dispersion errors. This can be achieved with high order schemes that however induce additional computational costs. Note that the numerical resolution of the equations in the code AVBP is briefly discussed in the following. Finally, for statistically stationary flows, several flow through times are to be computed to obtain the flow mean fields (time averaged) further enlarging the overall cost of the simulation. As an example, the LES computation of a single sector of a helicopter annular combustion chamber requires around 50000 CPU hours, while a corresponding RANS computation would be dozen

times less CPU consuming.

Despite its increased cost, the valuability of LES for burner development has very recently led to the increased integration of such methods into the design phase. For the development of Turbomeca combustion chambers for instance, the number of LES computations in 2012 represented only 10% of the number of RANS computations performed. In 2015, the trend completely reversed and RANS simulations represented only 5% of the total number of numerical simulations carried out at Turbomeca. Besides, the unsteady nature of LES provides possibilities to study transient phases such as ignition and extinction. Several attempts have been made to confront LES solutions of increasingly complex configuration against experimental results and provided very satisfying results (Gicquel *et al.*, 2012). Still, this approach is relatively new and numerous developments from various research teams are still ongoing.

This approach is used in this manuscript to solve for the fluid flow in a multi-physics context and evaluate the thermal environment of an industrial burner for which DNS is clearly out of reach. However in such a complex and highly turbulent configuration, the resolution of the large energy containing turbulent scales in the viscous wall region is computationally unaffordable. Instead, the near-wall motions are modeled. In the present study, a classic wall-law approach is employed and described in the next paragraph.

Near-wall flow modeling

Wall treatment plays a crucial role in the prediction of wall-bounded flows. In LES of high Reynolds industrial applications, fully resolved turbulent boundary layers are not affordable due to the grid resolution required to accurately compute the shear stress and heat fluxes at walls. Wall laws based on boundary layer theory and inherited from RANS approaches (Schlichting, 1955; Cebeci & Cousteix, 2005) are therefore commonly used to account for the near-wall flow behavior and accordingly compute these quantities. Note that different approaches exist in the literature such as zonal approaches for which the near-wall flow is solved with a separate set of equations or hybrid RANS/LES methods (Piomelli, 2008). Various wall-laws exist with more or less complex formulations. The specific wall-law employed in this manuscript for the LES of an industrial burner is detailed below. Further details regarding the implementation in the solver AVBP can be found in (Schmitt, 2005).

Wall flows are generally described with normalized wall variables. Introducing the wall shear stress:

$$\tau_w = \left(\mu \partial u / \partial y\right)_w \tag{2.2}$$

where μ is the fluid dynamic viscosity, u and y respectively stand for the tangential velocity and the direction normal to the wall and the subscripts w refers to wall quantities, one defines the

friction velocity:

$$u_\tau = \sqrt{\tau_w/\rho} \tag{2.3}$$

with ρ the fluid density. The normalized distance to the wall y^+ as well as the normalized velocity u^+ then read respectively:

$$y^+ = \frac{y u_\tau}{\nu} \tag{2.4}$$

$$u^+ = \frac{u}{u_\tau} \tag{2.5}$$

where ν is the kinematic viscosity. If a wall modeled approach is to be retained, these normalized quantities are then linked through the so-called wall laws.

The turbulent boundary layer is characterized by its thickness δ_v, depending on the Reynolds number of the flow and is decomposed into an external layer ($y/\delta_v \geq 0.2$) controlled by turbulence, and an internal thin viscous layer ($y/\delta_v \leq 0.2$), itself made of 3 sub-layers:

- ▷ The first layer, for $y^+ \leq 5$, is the viscous sub-layer, where u^+ follows a linear function of y^+.
- ▷ The layer $40 \leq y^+ \leq 300$ according to (Cebeci & Cousteix, 2005) corresponds to the inertial layer, characterized by the well-known log law given by:

$$u^+ = 1/\kappa \quad ln(y^+) + C_1 \tag{2.6}$$

  where $\kappa = 0.41$ is the Karman constant determined experimentally (von Kármán, 1930) and $C_1 = 5.4$ for internal flows.

- ▷ Between these two layers is an intermediate zone commonly called buffer zone, where transition between the linear and the log law occurs. In this zone neither the linear nor the log law is accurate. In AVBP, a threshold value $y^+ = 11$ is fixed under which the linear law is used while for superior values the log law is used.

The thermal aspect of near-wall modelisation can be treated in a similar way. In this case, a friction temperature, similar to the friction velocity is introduced:

$$T_\tau = \frac{Q_w}{\rho \; C_p \; u_\tau} \tag{2.7}$$

where Q_w is the wall heat flux and C_p the fluid heat capacity. Then, a non-dimensional temperature reads:

$$T^+ = \frac{T_w - \overline{T}}{T_\tau} \tag{2.8}$$

where $\overline{T}$ is the mean local temperature.

The normalized temperature follows the same two zone principle than the normalized velocity, with a linear region and a log region:

- ▷ in the viscous sub-layer ($y^+ \leq 5$),

$$T^+ = Pr\ y^+ \tag{2.9}$$

- ▷ for $40 \leq y^+ \leq 300$, the Kader law is imposed (Kader, 1981):

$$T^+ = \frac{Pr_t}{\kappa} ln(y^+) + C_2 \tag{2.10}$$

with Pr and Pr_t respectively the molecular and turbulent Prandtl numbers. $\frac{Pr_t}{\kappa}$ is fixed here to 2.12 and C_2 depends on the molecular Prandtl number: $C_2 = (3.85\ Pr^{1/3} - 1.3)^2 + 2.12\ ln(Pr)$.

In addition to the specific treatment of the near-wall flows, and as previously mentioned, a key issue for the realization of high-fidelity simulations lies in the numerical formalism employed for the resolution of the balance equations. The numerical choices made in the AVBP solver are briefly described in the next paragraph.

2.1.2 Numerics in the AVBP solver

The LES/DNS code AVBP solves the compressible reacting Navier-Stokes equations for momentum, mass and energy conservation on unstructured hybrid grids. The solver is based on a finite volume cell-vertex formulation and relies on an explicit time integration approach. A second order Galerkin scheme is used in all the present simulations for the resolution of the diffusion terms (Donéa *et al.*, 2000). The convective terms are resolved thanks to two different classes of numerical schemes:

- ▷ A Lax-Wendroff (LW) (Lax & Wendroff, 1960) scheme, second-order accurate in time and space which provides a fairly good accuracy at a low computational cost. This scheme tends however to provide less accurate dispersion and dissipation properties for medium-to-high wave numbers.
- ▷ Two different Taylor-Galerkin schemes: TTGC (Colin & Rudgyard, 2000) and TTG4A (Quartapelle & Selmin, 1993) third-order accurate in space and third-order (TTGC) or fourth-order (TTG4A) accurate in time. Both schemes ensure better dissipation and dispersion properties than the LW scheme. Note however that this improved accuracy has a significant cost: Simulations performed with TTGC or TTG4A are around 2.5 more CPU consuming than LW computations.

Further details concerning the numerical methods implemented in AVBP can be found in (Lamarque, 2007).

The time explicit integration implies a control of the time-step by the limiting acoustic Courant-Friedrichs-Lewy (CFL) condition. For a given value of the CFL, the time step is given by

$$\Delta t_f = \frac{CFL\ \Delta x}{u + c_s} \tag{2.11}$$

where u is the local convective velocity and c_s the local speed of sound. In a perfect gas, the speed of sound depends on the fluid properties and reads,

$$c_s = \sqrt{\frac{\gamma RT}{\mathcal{M}}} \tag{2.12}$$

with γ the ratio of specific heat, R the ideal gas constant, T the temperature and $\mathcal{M}$ the gas molar mass.

2.1.3 Multi-species reactive flows

The description of multi-species reactive flows requires in addition to the resolution of the non-reactive Navier-Stokes equations, the calculation of chemical source terms as well as the resolution of a transport equation for each mixture species. The full Navier-Stokes equations governing reactive flows are briefly recalled in Appendix A. In AVBP, reduced kinetic schemes are developed to account for chemical reactions. Classic Arrhenius laws are used to compute reaction rates which are then used to determine the energy and species source terms.

When dealing with reactive turbulent flows, additional complexities come from the strong relations that lie between chemical reactions and turbulent mixing (Peters & Rogg, 1993). On one hand, turbulence is modified by the combustion process through changes of flow properties (density and viscosity) with local temperature as well as acceleration of the flow through the flame front due to heat release. On the other hand, turbulence stretches and wrinkles the flame front, thus affecting the consumption rate and the flame local propagation speed. These interactions are highly non-linear and can cause antagonist effects. As an example, flame stretching and wrinkling due to turbulence can lead to an incredibly higher consumption rate whereas a too high stretch and wrinkling can lead to local quenching and eventually blow-off of the entire flame. These interactions are the topic of a huge amount of studies (Poinsot & Veynante, 2005) and accurate numerical resolution of turbulence/combustion interactions is still an open topic. Indeed, while in a DNS framework, the flame as well as its interactions with turbulent mixing is explicitly resolved, the use of RANS or LES approaches introduces the need for turbulent combustion models. Some usual models are reviewed in Poinsot & Veynante (2005) or Pitsch (2006) and the specific method of flame thickening employed for the present study is briefly described in Appendix A.

Note that due to the high mixing inherent to turbulent flows, these are widely used in aeronautical

combustion chambers (Poinsot & Veynante, 2005). Indeed, an efficient and fast mixing of fresh reactants enhance the combustion process while improved mixing between burnt and fresh gases helps the burnt gases cooling process and hence prevents critical hot spot impingement onto the turbine blades. Note also that turbulence increases the heat transfer between the flow and the walls which is of particular interest for the present study.

2.2 Solid conduction

Energy transfers by conduction happen without transfer of mass. This process spontaneously appears when a temperature gradient occurs within a material system. Heat conduction in solids is a diffusion-type problem and can be described mathematically through the so-called heat equation. Most of the notions detailed here can be found in reference books such as Bédat & Giovannini (2012) or Taine & Petit (1995).

2.2.1 The heat equation

Heat diffusion in solid materials is governed by the heat equation. Fourier established this equation in 1822 (Fourier, 1822) by decomposing the problem into three different components: heat storage within a small solid element, heat transport in space and exchanges between the interior and the exterior through boundary conditions (Narasimhan, 1999). A fascinating review of this work, the scientific context in which Fourier established this equation as well as the derived benefits in numerous diffusion-type problems applied to various scientific fields (electricity, chemical diffusion ...) can be found in Narasimhan (1999).

In the absence of internal heat source, the unsteady heat equation reads:

$$\frac{\partial \rho C T}{\partial t} = [\nabla \cdot (\lambda \nabla T)] \tag{2.13}$$

with

- T the temperature,
- ρ the density,
- C the specific heat capacity (material ability to store energy),
- λ the thermal conductivity (material ability to transport heat) considered homogeneous (isotropic conduction).

These material properties are linked through the thermal diffusivity which characterizes the material ability to respond to external perturbations (here imposed by the fluid through convection

and radiation),

$$a = \frac{\lambda}{\rho\ C}. \tag{2.14}$$

In AVTP, the temperature dependency of the specific heat capacity C and the thermal conductivity λ is approximated with polynomial laws whose parameters depend on the material.

When physical properties are constant the heat equation becomes linear and simplifies to:

$$\frac{\partial T}{\partial t} = a\nabla^2 T \tag{2.15}$$

Finally, for a stationary problem, the heat equation reduces to the Laplace equation:

$$\nabla^2 T = 0 \tag{2.16}$$

This equation is independent from the material thermal conductivity. In this specific case, solution uniqueness is ensured as long as appropriate boundary conditions are provided. Considering an unsteady problem, an additional initial condition is required to solve the system.

Boundary conditions can be defined through three different mathematical formulations. Note that hereafter subscript w refers to the problem unknown at the boundary condition while subscript ref corresponds to a quantity that is prescribed at the boundaries.

Dirichlet boundary condition
Temperature is imposed at the wall surface:

$$T_w = T_{ref} \tag{2.17}$$

Neumann boundary condition
The heat flux is imposed at the wall surface:

$$q_w = -\lambda \left(\frac{\partial T}{\partial n}\right)_w = q_{ref} \tag{2.18}$$

Note that a stationary problem including only Neumann boundary conditions is not well posed (Bédat & Giovannini, 2012): i.e. infinite set of solutions.

Robin boundary condition
The heat flux is imposed with a relaxation term:

$$q_w = q_{ref} + k_{ref}(T_{ref} - T_w) \tag{2.19}$$

where k_{ref} is a stiffness coefficient.

2.2.2 Numerics in the AVTP solver

The code AVTP solves the unsteady heat equation. It is derived from the previously described fluid code AVBP and shares its parallel treatment of unstructured hybrid grids. Therefore, the second order Galerkin diffusion scheme (Donea & Huerta, 2003) for spatial discretization comes from the AVBP solver. Time integration can be performed either with an explicit or an implicit approach. The implicit approach is used in the present work with a first order forward Euler scheme. Finally, the resolution of the implicit system is done with a parallel matrix free conjugate gradient method (Frayssé *et al.*, 2005). The time step Δt determination is based on the diffusion velocity of the temperature from one cell to the next, and ensues from the Fourier condition:

$$F = \frac{a\Delta t}{\Delta x^2} \tag{2.20}$$

with Δx the grid smallest cell size.

2.3 Radiative heat transfer

Thermal radiation refers to the transport of energy via electromagnetic waves. This phenomenon can be conceptualized as a stream of photons which carry energy. From this corpuscular nature of light, the equation governing heat transfers through radiation, the Radiative Transfer Equation (RTE) belongs to the transport equations: it describes the transport of photons and their interactions with the surrounding medium. The solution to this equation called the radiative intensity depends on position, direction and frequency. Integration of this quantity over all directions of the solid angle and for all frequencies is thus necessary to obtain macroscopic quantities only function of position such as the radiative source term used in the fluid energy equation.

Radiation does not follow the usual principles of the other two modes of heat exchange, namely convection and conduction. First, unlike convection and conduction processes, heat transfer by radiation is a non-local phenomenon: the determination of the energy content at a specific location requires to apply the energy conservation over the entire domain under consideration (rather than on an infinitesimal volume like for convection and conduction). Second, treating the directional and frequential dependency of the radiative phenomena requires the use of specific methods. Finally, thermal radiation propagates at the speed of light. Therefore, in most but astronomical applications, this heat transfer process reaches its thermodynamic equilibrium much faster than the other energy transport processes. As a result, the temporal dependency of radiative quantities is neglected and the equations are resolved in their stationary form.

Note that all the notions and assumptions presented in this chapter can be found with more details in books dedicated to heat transfer by radiation such as Siegel & Howell (2002) or Modest (2003).

2.3.1 The Radiative Transfer Equation (RTE)

As already mentioned, radiative heat transfer has a spectral dependency. Therefore, within this section, a distinction is made between monochromatic (at a given frequency) and total (over the entire spectrum) quantities. Note that monochromatic quantities may be expressed as a function of frequency ν, wavelength λ or wavenumber η. For the present discussion, expressions are given as a function of the frequency and monochromatic quantities are indicated with the subscript ν.

Radiative intensity

The radiative field is characterized by the radiative intensity I which depends on the position x, the direction of propagation u and the frequency ν. The monochromatic radiative intensity $I_\nu(x,u)$ at a location $P(x)$ in the direction β and at a frequency ν is defined as the monochromatic energy flux $d\Phi_\nu(x,\beta)$ crossing an elementary surface dS (centered at x and with a normal n) in an elementary solid angle $d\Omega$ (around the direction β):

$$I_\nu(x,\beta) = \frac{d\Phi(x,\beta)}{\beta.n\ d\Omega\ dS} \tag{2.21}$$

Based on such an expression, the total radiative intensity at a given point x and for a given direction β can be obtained by integration over the entire spectrum:

$$I(x,\beta) = \int_0^\infty I_\nu(x,\beta)d\nu. \tag{2.22}$$

The resolution of the radiative heat transfer phenomenon is achieved through the determination of the radiative intensity field. The latter can be modified through interactions between the photons and the propagation medium. Such processes are detailed in the following.

Participative medium

In combustion applications, interactions occur between gas molecules or particles (droplet, soot) and photons by absorption, emission and diffusion. Therefore, the fluid local composition and energetic state modifies the radiative energy propagation so that such a medium is called participative. The refractive index of the medium is considered constant and equal to unity. As a consequence, the direction and velocity of propagation of the photons are not modified. Additionally, the medium is non-polarizing and in local thermodynamic equilibrium.

Energy attenuation by absorption

When penetrating a gas layer of radiatively active species, radiative energy is gradually attenuated by absorption. This energy decrease may be evaluated via the monochromatic absorption coefficient $\kappa_{\nu,a}$ which is defined as the inverse of the absorption mean free path. As a result, the

energy variation due to absorption $dI_{\nu,a}(x,\beta)$ on an optical path ds equals:

$$dI_{\nu,a}(x,\beta) = -\kappa_{\nu,a} I_\nu(x,\beta) ds \tag{2.23}$$

Energy gain by emission

In the same way, introducing the monochromatic emission coefficient $\kappa_{\nu,e}$ and considering that every infinitesimal volume is in local thermodynamic equilibrium, the energy variation due to emission is proportional to the black-body emission $I^0_\nu(x)$:

$$dI_{\nu,e}(x,\beta) = \kappa_{\nu,e} I^0_\nu(x) ds \tag{2.24}$$

where, under Lambert's law, (diffuse radiation), the black body radiative intensity is given as a function of the temperature and the frequency by Planck's Law (Planck, 1901):

$$I^0_\nu(x) = I^0_\nu(T) = \frac{2h\nu^3}{C_0^2(e^{\frac{h\nu}{kT}} - 1)} \tag{2.25}$$

where h and k are respectively the Planck's and the Boltzmann's constants and C_0 the speed of light in vacuum. Another consequence of the local thermal equilibrium is that no frequential redistribution occurs between absorption and emission. As a result:

$$\kappa_{\nu,e} = \kappa_{\nu,a} = \kappa_\nu \tag{2.26}$$

This is known as the Kirchoff's law (Kirchhoff, 1860) and κ_ν is commonly called the monochromatic absorption coefficient. Its determination for the resolution of the radiative problem is achieved via spectral models which are detailed in Section 2.3.2.

Energy gain or attenuation by scattering

The third way gas molecules can interact with photons is scattering. It consists in a deviation of the optical path by scattering centers and hence induces a redistribution of the incident radiation over directions. Scattering has two distinct contributions: an energy gain from other directions by in-scattering as well as an energy loss to other directions by out-scattering. Scattering is often neglected in combustion applications involving small scale components such as aeronautical engines. Therefore, the interaction between combustion gases and radiation is limited to absorption and emission phenomena.

Transfer equation

Under the current hypotheses on radiative heat exchanges and participative medium, the Radiative Transfer Equation (RTE) reads;

$$\frac{dI_\nu(x,\beta)}{ds} = \kappa_\nu \left[I^0_\nu(x) - I_\nu(x,\beta)\right] \tag{2.27}$$

The author of the first derivation of this equation in the history is not clear. According to Stamnes & Stamnes (2015), it should be attributed to Lommel in 1889 (Lommel, 1889). Note that the RTE is a linear form of the general Boltzmann equations (Boltzmann, 1872) (transport equations).

To resolve the RTE, additional knowledge about the radiative intensity entering/leaving the domain through boundaries is mandatory. For this purpose, both inlets/outlets boundaries and walls are to be considered. For the current study, inlets and outlets are considered as totally absorbent. Walls in industrial combustion chambers are composed of metals. Their absorptivity is high and liners are thick enough to assume that no electromagnetic waves can penetrate through them so that no transmission of light through the solid is possible. As a result, incident photons can either be absorbed or reflected by the solid surface and the solid is considered opaque. Besides, reflection at the wall is considered diffuse and isotropic (Lambertian). In addition, the solid surface emits radiation. Like emission by a participative medium (Section 2.3.1), the energy released by the surface is related to the black-body emission. A quantity called emissivity ϵ is hence introduced, which refers to the ratio of the radiative intensity emitted by the surface to the black-body emission at the same temperature. This coefficient is non-dimensional and varies between 0 and 1. In practice, the emissivity may vary with direction and frequency. However, such dependencies are often neglected and the wall emissivity will thus be a constant in the current study. Note that surfaces with constant emissivity over the spectrum are called grey. When $\varepsilon = 1$, the surface behaves like a black-body: all the incident radiation is absorbed. On the contrary if $\varepsilon = 0$, the surface is perfectly reflective.

Considering an opaque (i.e. non transmissive) grey surface and diffuse Lambertian reflection at the wall, the radiative intensity entering the domain through the wall is given by

$$I_\nu(x_w, \underset{\beta.n>0}{\beta}) = \underbrace{\varepsilon I^0_\nu(T_w)}_{emission} + \underbrace{\frac{1-\varepsilon}{\pi}\int_{\beta'.n<0} I_\nu(x_w,u') \mid \beta'.n \mid d\beta'}_{reflection} \tag{2.28}$$

where n and T_w are local values at x_w (wall position) and are respectively the wall normal oriented towards the domain and the surface temperature.

As already mentioned the determination of the radiative intensity field over the entire domain is

not sufficient to include the radiative process into the fluid energy equation. To do so, macroscopic quantities are required.

Macroscopic source term and wall flux

Integral quantities are defined by integration over all the directions of the solid angle. The monochromatic incident radiation G_ν at r includes the contribution of the radiative intensity from the whole solid angle:

$$G_\nu(x) = \int_{4\pi} I_\nu(x,\beta) d\Omega \tag{2.29}$$

In the same manner, the monochromatic radiative flux vector characterizes the net energy flux in r:

$$q_\nu(x) = \int_{4\pi} I_\nu(x,\beta)\ u\ d\Omega \tag{2.30}$$

The radiative source term contributing to fluid energy conservation equation is hence obtained by double integration over the direction and the frequencies: From theses integral quantities, the radiative source term entering the fluid energy conservation equation is obtained by spectral integration:

$$Sr(x) = \int_0^\infty \int_{4\pi} \kappa_\nu \left[I_\nu^0(x) - I_\nu(x,\beta) \right] d\Omega d\nu \tag{2.31}$$

This quantity may also be re-expressed as a function of the integral quantities defined above:

$$Sr(x) = \int_0^\infty \kappa_\nu \left[4\pi I_\nu^0(x) - G_\nu(x) \right] d\nu \tag{2.32}$$

Likewise the radiative flux vector at the wall is given by:

$$q(x_w) = \int_0^\infty q_\nu(x_w).n(x_w) d\nu \tag{2.33}$$

Both of these quantities only depend on the space coordinate for which to the combustion equations are solved. The main difficulties of the resolution of the radiative problem therefore lies in the angular and frequential integrations imposed by this physics and are required to obtain corresponding macroscopic quantities.

Resolution approaches

Over the years, numerous approaches have been developed to solve the radiative problem. Aside from the very few problems that admit analytic solutions, the numerical methods of resolution of radiation may be separated into two main categories: deterministic and statistical approaches.

Statistical approaches are specific variations of the more general Monte Carlo methods (MC) (Zhang, 2011; Dunn & Shultis, 2011) which can be used to solve various physical problems relying on their statistical characteristics. When applied to the radiative heat transfer problem, the MC method uses statistical analysis to simulate the directional and frequential dependency of the radiative phenomena: a large number of random optical rays is generated with random directions, frequency and point of emission. This method is very accurate and can simulate complex physical phenomena without simplifying assumptions. Although its computational cost was for long restrictive for combustion coupled applications, promising developments have been made (Zhang, 2011; Refahi, 2013).

Deterministic methods rely on the discretization of the variables of the phase space. Among them are the ray tracing method, very accurate but CPU consuming and generally used to compute benchmark cases for the development of simplified approaches (Coelho *et al.*, 2003*a*). The P_N approaches, first introduced by Jeans (Jeans, 1917) and still widely used (Modest & Yang, 2008; Gerardin *et al.*, 2012), as well as the Discrete Ordinates Method (DOM). The latter approach was initially proposed by Chandrasekhar (1960) to solve mono-dimensional problems within the astrophysics field. This method is intensively used to solve radiative problems including combustion applications and is known to provide a good trade-off between solution accuracy and CPU cost (Krishnamoorthy *et al.*, 2005; Jones & Paul, 2005; Coelho, 2007). Recent advances on DOM can be found in the review by Coelho (Coelho, 2014).

The radiative solver PRISSMA used for the present study relies on the DOM formalism. The next section briefly describes the principle of the resolution of the radiative problem in PRISSMA. Note that the specific parallelism implementation and computing performance of PRISSMA are not addressed in this manuscript. Extensive investigations of such matters have been performed in Poitou *et al.* (2012*a*).

2.3.2 Resolution in PRISSMA

DOM consists in a directional discretization of the solid angle through a numerical quadrature. Each direction is then spatially discretized over the domain. Finally, the frequential dependency is accounted for via a spectral model that may introduce a spectral discretization. These three levels of discretization are detailed below.

Angular discretization

Space is first discretized over a finite number of directions N_{dir}, specifically distributed over the 4π solid angle through a numerical quadrature. For some quadratures, a weight is associated to each direction. The RTE is hence resolved in the entire domain for each direction, providing at each

point of space several values of the radiative intensity corresponding to each discrete direction. The weighted sum of the different contributions then gives access to the incident radiation and the radiative flux fields in the domain.

Various quadratures have been developed over the years (Carlson, 1971; Fiveland, 1987; Truelove, 1987; Thurgood *et al.*, 1995; Mishra *et al.*, 2006). Among them, the present calculations rely either on the LC_{11} ($N_{dir} = 96$) or on the S_4 ($N_{dir} = 24$) quadratures. The latter belongs to the category of the S_N quadratures defined by Carlson (Carlson, 1971), Fiveland (Fiveland, 1987) and Truelove (Truelove, 1987) and for which the number of directions is given by $N_{dir} = N(N + 2)$ in the denomination S_N. The accuracy and CPU cost associated to a DOM computation are strongly influenced by the chosen quadrature.

The reduced error provided by the LC_{11} quadrature with respect to other quadratures was demonstrated in Koch & Becker (2004). In addition, Joseph *et al.* (2009) showed very good agreement of the solutions provided with this quadrature and a Monte Carlo approach on a laboratory combustion chamber. Note that in this work, authors also indicate a pretty good restitution of the radiative field with a S_4 quadrature at a reduced cost compared to the LC_{11} quadrature. The same conclusion was brought by Poitou (2009) for a different laboratory combustion chamber configuration. Poitou further highlighted the excellent trade-off between accuracy and CPU cost provided by this numerical quadrature. Finally, the use of a S_N quadrature with a higher order seems unjustified according to the comparisons on radiative wall heat fluxes performed by Kayakol *et al.* (2000) between experiments and numerical solutions obtained with a S_4 and a S_6 quadratures.

Acknowledging these studies, two quadratures are used in the present manuscript, the LC_{11} and the S_4 quadratures. Each discrete direction defined by the numerical quadrature is then spatially discretized by the computational grid. Such a discretization is discussed in the next section.

Spatial discretization

The RTE is integrated using the finite volume approach described in the work of Joseph (Joseph, 2004). Different spatial differencing schemes may be used (Coelho, 2014) to perform the spatial integration. In the solver PRISSMA, the exponential scheme (Sakami & Charette, 1998), the step scheme (Liu *et al.*, 2000) and the Diamond Mean Flux Scheme (DMFS) (Ströhle *et al.*, 2001) are available. It was demonstrated that this last method is well suited and efficient on unstructured grids (Joseph *et al.*, 2005) and accurate results are provided as long as the mesh cells optical thickness is low.

Finally, the last discretization of the radiative problem concerns the spectral dependency. The

whole spectrum discretization through a spectral model is the topic of the next section.

Spectral properties and models

In combustion, two sources of radiation may be considered: non-luminous radiation induced by gaseous species and luminous radiation corresponding to the contribution of soot particles. Inclusion of luminous radiation require the determination of the soot volume fraction fields within the combustion chamber. Such an exercise is not straightforward. While the processes of soot formation from precursors (mostly in locally rich regions of the flame), development and oxidation (mostly in locally lean regions) are now globally understood, the production of reliable models is still a wide topic of study. Among others, Kennedy (1997) and Wang (2011) proposed interesting reviews on soot physics and modeling. In the current study, discussion is confined to non-luminous radiation. Principal gaseous radiant species in combustion reduce to the combustion products H_2O, CO_2 and CO, other gases being considered transparent (radiatively inactive). Since the medium is considered non-scattering, the interaction of the mixture with radiation expresses only through the mixture absorption coefficient κ_ν.

Considering a pure gas, the absorption spectrum distribution results from the combination of all the energy transitions allowed in the gas (electronic, vibrational and rotational transitions). Therefore, the spectrum is generally constituted by hundreds of thousands of spectral lines and vary from one gas to another. Additionally, the spectrum are influenced by local temperature and pressure. As a result, in a combustion chamber, the absorption spectrum distribution and the spectrum lines intensity depend on the local thermodynamic state: mixture composition, temperature and pressure.

In radiative numerical computations of practical applications, it is not feasible to account for each individual line of the absorption spectra. Accordingly, spectral properties are described via a spectral model. Numerous models can be found in the literature, more or less adapted to the characteristics of specific applications and with different levels of details. These models may be separated into three different categories: line-by-line, band and global models. Line-by-line models reproduce each line of the spectrum providing the more accurate spectrum description. These spectra are experimentally measured and are accessible in databases such as the HITEMP database (Rothman *et al.*, 2010). For infrared radiation over the temperature range encountered in a combustion chamber, the spectrum includes around one million lines. The use of such detailed models is clearly unaffordable for coupled simulations of complex geometries. This technique is restricted to very simple test cases and limited to the development of simpler models.

The development of such models consist in a representation of the absorption frequency dependency on bands of given width. For this purpose, assumptions are made on the spectrum that

may reduced the scope of application of the models. Spectral models are therefore often developed for specific target applications. Such models fall into two categories depending whether or not they conserve a frequency dependency. Band models describe the spectrum in frequency bands, providing thus a simplified description of the property frequency dependencies. They represent a high advance from line-by-line models and allow the resolution of the radiative phenomena in industrial configurations with complex geometry. However, in a multi-physics context, radiative computations employing such models are still too CPU consuming. To overcome such issues, global models for which the band width covers the entire spectrum (leading hence to even reduced CPU costs) are constructed. The absorption coefficient depends no longer on frequency. Note that with such models, only grey conditions are admitted at walls.

In the current study, the spectral dependency of the absorption properties of H_2O, CO and CO_2 are taken into account with a global model: the Full Spectrum based on the SNBcK (FS-SNBcK) initially proposed by Liu *et al.* (Liu *et al.*, 2004). The ability of the FS-SNBcK model to provide good results in the field of combustion at a reduced CPU cost has been demonstrated on academic configurations and real combustion chambers in Poitou *et al.* (2009) and Amaya (2010). Note that as as demonstrated in Poitou *et al.* (2011), the spectral model is the first parameter of influence both for accuracy and CPU cost.

2.4 Conclusion

The three physics at play when investigating the thermal state of a combustion chamber, namely combustion in the fluid, conduction within the chamber solid parts as well as radiative heat transfer in the fluid and at walls have been successively discussed in this chapter. The different nature of these three processes have been recalled and the resulting various resolution approaches (modeling approaches, specific assumptions and models) detailed. The resolution methods retained for the present study are:

- ▷ The reactive flow is solved with the DNS/LES solver AVBP. While the DNS approach consists in solving all the flow scales, in LES, only the large geometry dependent scales are resolved while the small scales known to have a universal behavior are modeled. Such an approach induces an important cost overhead compared to RANS approaches and its use in a multi-physics context may raise specific issues in terms of performance. In addition, for the real industrial burner computations proposed in Part III, the resolution of the large energy containing turbulent scales in the viscous wall region is computationally unaffordable and a classic wall-law approach is introduced to model the near-wall motions. Finally, the choice of a high fidelity method requires the use of precise numerical schemes providing both low numerical dissipation and low dispersion errors. In AVBP two different classes of numerical schemes providing various orders of accuracy are available. For each configuration discussed in this manuscript, both will systematically be tested.

- ▷ The unsteady heat equation is solved with AVTP whose structure is derived from that of the flow solver. Boundary conditions can be enforced through various mathematical formulations which will be discussed in the next chapter in light of the multi-physics context.
- ▷ Radiative heat transfer is solved through a DOM formalism in PRISSMA. Such an approach introduces three levels of discretization. The solid angle is first discretized through a numerical quadrature. Acknowledging previous studies form the literature, two quadratures are selected for the present study: the LC_{11} and the S_4 quadratures. Each discrete direction is then spatially discretized by the computational grid and the RTE is integrated using the finite volume approach. For this purpose, the DMFS differencing scheme is employed. Besides, it is worth noting that only non-luminous radiation is considered here. The spectral dependency of radiant species (H_2O, CO_2 and CO) is taken into account via the global spectral model FS-SNBcK. The ability of the FS-SNBcK model to provide good results in the field of combustion at a reduced CPU cost has already been demonstrated on academic configurations and real combustion chambers in the literature.

The resolution of all these three physics having been discussed in a standalone context, the next issues to address concerns the modelisation of the various interactions between the independent components. Such a topic is discussed in the next chapter.

Chapter 3

Multi-physic approaches to predict a combustion chamber thermal state

Contents

As already mentioned in the introduction, the resolution of a thermal problem requires the consideration of the three modes of heat transfer, convection, conduction and radiation as well as the means by which energy is produced or consumed, the latter being reduced for the present problem to the chemical reactions. The corresponding phenomena of combustion[1], solid conduction and radiative heat transfer have been defined along with existing numerical tools allowing their independent resolution in the previous chapter. The remaining issue to yield a fully multi-physics resolution of the thermal problem lies now in the modelisation of the interactions between these different physical processes.

In numerical simulations, interactions between these sub-systems are classically either neglected or treated with a decoupled approach. Hence, given a sub-system of interest, the effects of its environment (i.e. the rest of the universe) is accounted for through various approximations. These

[1]Note that combustion is in itself a multi-physics coupled problem: it results from complex interactions between the fluid motion (at various length scales due to turbulence), species and heat diffusion as well as chemical reactions. Such interactions are already handled in the AVBP code and details are provided in Section 2.1 and Appendix A. The present discussion consider the reactive flow as a single physical sub-system.

may come out of simple analytic considerations or derived from standalone simulations as well as from correlations established on the basis of experimental measurements. Considering for instance the liner of a combustion chamber, Lefebvre (2010) proposed some relations to estimate the internal (flame tube side) and the external (casing side) temperature of the liner by considering the radiative and convective exchanges between the flow field and the walls. Likewise classical expression which can be found in the literature, Lefebvre (2010) for example expressed convective fluxes thanks to the assumption that a linear relation exists between the convective heat flux Q_{conv} and the driving temperature difference following Newton's heat flux law[2]:

$$Q_{conv} = h_{ref}(T_{ref} - T_w) \tag{3.1}$$

where h_{ref} is a reference convective heat transfer coefficient, T_w the surface temperature and T_{ref} a reference temperature. In the same manner, Lefebvre (2010) wrote the radiative heat flux as commonly found in the literature:

$$Q_{rad} = \sigma(\epsilon_{ref} T_{ref}^4 - \alpha_{ref} T_w^4) \tag{3.2}$$

where σ is the Stefan–Boltzmann constant, ϵ is the gas emissivity at temperature T_{ref}, and α the gas absorptivity at temperature T_w. These fluxes may then be used as boundary conditions for conduction computations in the material. The accuracy and reliability of the results rely on the determination of the reference quantities. The development of specific correlations has received extensive attention for various target applications (Woschni, 1967; Gauntner & Sucec, 1978; Morel & Keribar, 1985; Sundberg, 2006; Lefebvre, 2010). On complex industrial geometries, these quantities may also be obtained by fluid-only simulations. Such approaches allow to consider the thermal problem without the additional complexities inherent to coupled simulations. Depending on the application and on the required level of accuracy, these may not be sufficient to treat a problem. Indeed, two main drawbacks arise from these methods. First, the reliability of the results depends greatly on the source of the determination of the reference quantities. Additionally, these do not allow to effectively solve the physical sub-system interactions. Therefore such methods can lead to too approximate solutions in highly physically coupled problems. The resolution of all the sub-systems as well as their various interactions is thus mandatory for an accurate resolution of many thermal problems.

For this purpose, one needs to consider all the interactions between combustion, solid conduction and fluid as well as solid surface radiation. The global thermal problem is thus decomposed into three smaller multi-physics problems including two sub-systems and their interaction (Fig. 3.1).

1. The aerothermal field near the solid walls results in an energy transfer between the fluid and the solid by convection[3] while the solid surface temperature thermally bounds the flow.

[2]This law assumes that the heat transfer coefficient is independent from the temperature difference between the solid and its surrounding fluid

[3]Heat transfer by convection is the addition of two processes namely advection (heat transfer by bulk fluid flow)

Finding the equilibrium temperature corresponds to a joint problem known as Conjugate Heat Transfer (CHT).

2. Local fluid property (species, temperature and pressure) fields determine the gas absorption and emission which impact the radiative source term (note that to compute the latter quantity an additional definition of boundary conditions is required) while the radiative source term introduces a modification of the fluid energetic content and thermal state. This coupled problem is often referred to as Radiation Fluid Thermal Interaction (RFTI).

3. Solid surface temperature and emissivity (which, in practice, depends itself on temperature) impacts the radiative energy absorbed, emitted or reflected at walls while the global radiative field induces an energy transfer from/to the solid. In an analogy to the RFTI denomination, this problem is called Radiation Solid Thermal Interaction (RSTI) in this manuscript.

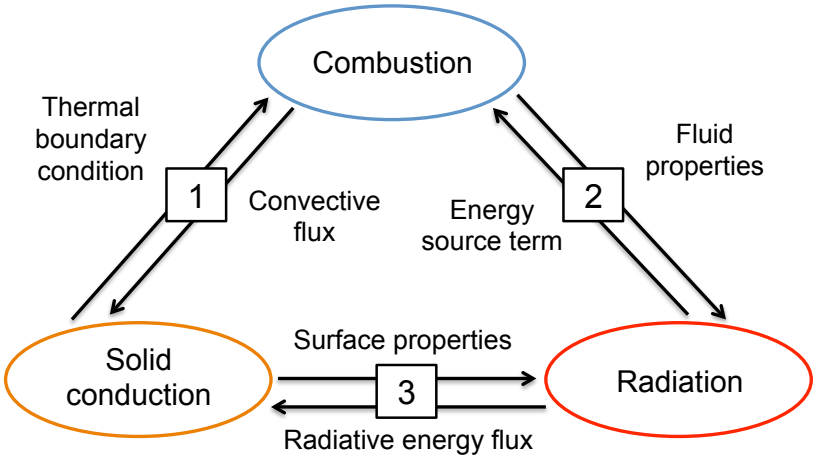

Figure 3.1: Physical interactions between combustion, solid conduction and radiation.

Combustion, solid conduction and radiation interact simultaneously and form a closed loop where one sub-system bounds the evolution of the others. Consider the thermal problem of a burner initially off and at the thermal equilibrium. A change of conditions like for instance the engine ignition, leads to an adaptation of the various sub-systems and the simultaneous evolution of their interactions. Such a transient phase lasts until a new global equilibrium is found, corresponding to the permanent regime. In this manuscript, only mean quantities representative of the permanent regime are sought for. Starting from an initial condition, the simulation consists hence in computing all the sub-system interactions during a transient until the permanent regime is reached. However, during the transient phase, the three phenomena adapt on very different time scales. While radiation is an instantaneous process (in most applications but astronomy), flow convection is characterized by time scales of the order of ms (chemistry time scales range them

and heat diffusion.

from around $10^{-9}s$ for intermediate reactions to approximately $1s$ for some reactions such as NOx production) and heat conduction in the solid parts require some seconds or more to adapt. The various physical phenomena are thus characterized by very different time scales that need to be dealt with for the resolution of the thermal problem.

When seeking to solve numerically a multi-physics coupled problem, two main approaches can be envisaged: monolithic and partitioned coupling. Monolithic techniques (Patankar, 1980; Sundén, 1980; Divo & Kassab, 2007; Li & Kong, 2011; Donde *et al.*, 2012; Nordström & Berg, 2013) consist in the simultaneous resolution of all the sub-systems in a single solver. Interactions between the sub-systems are then directly taken into account. Note that a single grid is usually used for all the sub-systems. Therefore, when different domains are to be distinguished (fluid cells and solid cells for instance in CHT applications), specific methods are applied to flag the cells associated to each domain (Patankar, 1980; Nordström & Berg, 2013; Kedia *et al.*, 2014). Monolithic techniques are naturally conservative. When strong interconnections exist between the physical models such approaches can produce a very efficient code (Heil *et al.*, 2008). However, and as can be observed from the previous chapter, the equations governing reactive flows, heat diffusion in solids and radiative heat transfer have very distinct mathematical properties and the numerical methods used for their resolution differ a lot. Therefore, the resolution of the various sub-systems within the same code structure may be highly complex and could result in performance losses. On the contrary, the partitioned approach (Jones & Paul, 2005; Radenac *et al.*, 2005, 2008; Duchaine *et al.*, 2009*a*; Maheu *et al.*, 2012; Amaya, 2010; Hallez *et al.*, 2011; He & Oldfield, 2011; Poitou *et al.*, 2011; Jauré *et al.*, 2013; He, 2013; Errera & Baqué, 2013; Errera & Chemin, 2013) relies on the development of a coupled framework in which independent legacy codes are used to solve each physics. Each solver structure and numerics acknowledge the specificities of each physical component. The solvers are then coupled through information exchange at the sub-system interfaces. In such cases energy conservation at all times is not necessarily achieved and specific coupling sub-iteration (Lindström & Nordström, 2010) or correction techniques (Radenac, 2006) are sometimes employed. In this manuscript, all the numerical studies are carried out with partitioned approaches. Note that with the approach adopted (detailed hereafter) conservation is not guaranteed at each iteration but is usually obtained for the steady converged solution.

The choice of a partitioned approach raises, specific numerical and computing performance issues. The CPU cost associated to the resolution of the various physics differs a lot. To give some orders of magnitude and for the methods as well as solvers presented in Chapter 2, the solid conduction code is the cheapest in terms of CPU. The cost associated to the flow solver is approximately 10 times larger and the radiative solver cost represents around 10 000 times that of the conduction code. Questions concerning partitioned techniques computing performance and how the CPU cost mismatch between the sub-systems is handled are addressed later on in Chapter 4. Only numerical issues are discussed for now. First, as already mentioned, each sub-system is characterized by very different time and length scales. As a consequence, a large mismatch may exist between the

various component temporal and spatial discretizations. Such discontinuities need to be carefully managed and require the development of specific tools and methodologies. These depend both on the specificities of the solvers used and on the characteristics of the target application (steady state versus transient processes for instance). Second, coupled physical components interact through an interface which may be linear, surfacic or volumetric and cover a part or the entire domain of each sub-system. When seeking to numerically resolve a coupled problem, the choice of the interface variables is critical both in terms of solution accuracy and computation stability (Giles, 1997; Duchaine *et al.*, 2009*a*; Jauré, 2012; Errera & Chemin, 2013). In the present manuscript, the treatment of the physical time and the interface variables is referred to as the coupling strategy. Note that an additional complexity arises from the spatial scale mismatch between each sub-systems. Indeed, each physics may be discretized on different meshes which are usually not coincident. Interpolation methods are thus required to transfer the physical fields between each solver grids. This specific topic is out of the scope of the present manuscript. Further details concerning interpolation algorithms can be found in Alonso *et al.* (2006), Jauré (2012) and Jauré *et al.* (2013).

In the present chapter, the three couple of sub-systems interactions CHT, RFTI and RSTI involved in the determination of the thermal state of a combustion chamber are discussed. A brief literature review is proposed for each of the interaction problems and the numerical resolution is detailed considering the treatment of the numerical issues highlighted above.

3.1 Conjugate Heat Transfer (CHT)

Perelman (1961) first formulated the concept of CHT, solving the conduction equation simultaneously for a heated body and a liquid flowing past it. Numerous studies followed this work, considering various academic configurations. A review of analytic studies of CHT problems for academic and industrial applications has been published by Dorfman & Renner (2009).

Numerous applications exist in which the fluid and the solid are strongly thermally coupled. These problems may only be understood and analytically or numerically accurately resolved by considering the joint problem. For instance, Fan *et al.* (2013) conducted thermal investigations in a bluff-body micro-combustor, highlighting a strong relation between the flow field, heat transport processes and flame stabilization. CHT steady simulations were performed with additional computation of surface to surface radiation between the inner surfaces of the combustor (Section 3.3). The results revealed a strong variation of the combustor stability limits as a function of the solid material. Indeed, for large solid thermal conductivity, conduction within the solid walls induced an efficient preheating of the fresh mixture. This resulted in an expansion of the gaseous volume, leading to an important flame stretch and thus to lower blow-off limits than with low conductive materials. Similarly, material emissivity was shown to have an important impact on stability

limits. Such two-way physical coupling would have been missed with a decoupled resolution of the fluid and solid domains. The necessity of a coupled approach was also evidenced by Darıcı *et al.* (2015). The transient heat transfer in thick walled mini pipes was analyzed for simultaneously developing laminar flows. A parametric study was conducted for various values of fluid to solid properties and characteristic non-dimensional numbers (Peclet, Biot, Prandtl). The influence of conjugation was shown to be highly correlated to most of the parameters studied.

Among all the parameters studied in Darıcı *et al.* (2015), one non-dimensional number is of particular interest for the present study: the Biot number. Indeed, the temperature field in a combustion chamber liner results from an equilibrium between heat diffusion inside the solid domain and fluxes imposed by the fluid domain on both sides of the liner. Such an equilibrium can be characterized through the Biot number which is the ratio of the convective heat transfer between the solid and the flow h and the conductive heat transfer within the solid. This number reads:

$$Bi = \frac{hL_c}{\lambda_s} \tag{3.3}$$

where h is the convective heat transfer coefficient (Eq. (3.1)), L_c a characteristic length and λ_s the solid conductivity. If $Bi > 1$, the transport of heat within the solid domain is less efficient than its exchange at the surface and strong thermal heterogeneities appear in the material. On the contrary, the solid body is considered as thermally thin when $Bi < 0.1$ and the temperature can be assumed as almost homogeneous. The Biot number provides hence some a priori indications on the thermal response of the system.

With the continuous increase in computing resources, coupled simulations for CHT have extensively developed within different application domains. In the field of aeronautical propulsion, this type of simulation is daily used in the design process of gas turbine components. Indeed, the metal temperature of the hot stages is critical for the reliability of the engine. More specifically, most CHT works in this field address the impingement of combustion hot products exiting the chamber on the turbine blades and the efficiency of various cooling systems specific to the geometry of the blades (Han *et al.*, 2001; Heidmann *et al.*, 2003; York & Leylek, 2003; Facchini *et al.*, 2004; Luo & Razinsky, 2007; Duchaine *et al.*, 2009*a*; Wlassow *et al.*, 2010; He & Oldfield, 2011; Andreini *et al.*, 2012; Duchaine *et al.*, 2013). The temperature in the blade metal is controlled by the material properties and the interaction between the blade and the fluids circulating in the engine (the hot gases exiting the combustion chamber and the cold gases from the cooling systems). Among others, using Reynolds Average Navier-Stokes (RANS) approaches, York & Leylek (2003) and more recently Andreini *et al.* (2012) came to the conclusion that the prediction accuracy of blades temperature with CHT is limited by turbulence models accuracy. In combustion chambers, mixing and turbulence not only control thermal aspects but also the combustion process. Taking into account turbulence in an accurate way is thus mandatory for burner applications. Since in Large Eddy Simulation (LES), turbulence modeling is restricted to small dissipative scales, this

approach seems to be preferable and has already demonstrated a good ability to reproduce experimental results in the CHT context for turbine blade applications (Duchaine *et al.*, 2009*a*, 2013). CHT computations based on LES for combustors have been produced by Jauré (2012) and clearly proved the potential of such approaches. However, some features of the combustor liner were not included in the simulations, precluding any comparison with experiments and predictive results of the real phenomena.

In the literature, the coupling strategy employed to solve CHT problems vary a lot from one study to another. The choice of the coupling strategy is strongly influenced by the nature of both the target application and the numerical solvers. Whether an investigation of the transient or of the permanent regime is sought for and whether quantities of interest are mean or fluctuating variables, lead to completely different requirements for the coupled simulations. Besides, the use of steady or unsteady solvers raises different issues and special procedures need to be applied to overcome associated difficulties.

The resolution of a transient problem may be achieved following a simple concept: both solvers are advanced in time following the natural physical proceeding of the simulated application. Such a simulation may be performed employed a LES (Duchaine *et al.*, 2008) or a RANS solver (Radenac, 2006) to compute the flow equations. However, computing all the transient phase in a time accurate manner may be too expensive depending on the configuration and the physical duration of the transient. To circumvent this problem, (Errera & Baqué, 2013; Gimenez *et al.*, 2016) proposed a specific approach combining the use of a steady fluid solver combined with a dynamic solid solver: A quasi-dynamic procedure is developed in which a sequence of steady fluid computations is coupled with the transient resolution of solid conduction. Such a method allows to compute the temporal evolution of the solid domain during long transient phases.

If only mean quantities characterizing the permanent regime are to be determined, different strategies are deployed. With steady solvers, the resolution of the steady thermal problem is relatively straightforward in terms of physical requirements. The choice of a coupling strategy for such coupled simulations is mainly built on numerical considerations such as simulation stability and convergence rate (Errera & Chemin, 2013; Chemin, 2007). Note that, such simulations are usually chained rather than coupled, meaning that each solver is launched successively for a fixed number of iterations or until convergence, update of the interface fields appears only at the beginning of each simulation. A few dozens or hundreds of loops are generally sufficient to obtain a converged joint thermal state (Chemin, 2007). Finally, when solving the permanent regime problem with unsteady solvers, the task is substantially different. All the studies carried out in this manuscript fall into this category, further explanations are thus provided hereafter.

3.1.1 Coupling strategy

In the following, subscripts s and f respectively stand for variables referring to the solid and the fluid flow sub-systems.

Physical time

If employing unsteady solvers to obtain the mean quantities representative of the thermal permanent regime, a straightforward solution would be to compute a full numerical solution from the initial condition, through the transient regime, until the equilibrium is reached for the whole system. Statistics collection on a sufficiently long time interval of the permanent regime would then allow to access the mean quantities. However, on one hand, the physical time which needs to be computed to converge the solid thermal state is at least of the order of the second while on the other hand, the accuracy and stability in the fluid flow imposes a very low time step ($\Delta t_f \sim O(10^{-8}s)$ for the flow solver AVBP described in Chapter 2 and the applications described in this manuscript). Matching both requirements in a coherent time accurate simulation would thus lead to the computation of incredibly high number of iterations or time steps and is clearly too expensive in terms of CPU for most configurations.

A specific technique is therefore used to accelerate the solid domain compared to the flow. Indeed, since only mean quantities of the converged state are sought for, no consistency is theoretically required between the fluid and the solid physical times. In such cases, the solvers can be desynchronized to accelerate convergence in the solid and save computational time (Duchaine *et al.*, 2008, 2009*a*; Jauré, 2012). Such a technique avoids useless expensive calculations, by allowing a fast evolution of the solid to a converged state where interactions between sub-systems are balanced. Between two coupling exchanges, the solid is advanced in time by a temporal increment of $t_s = \alpha_s \tau_s$ while the fluid part advances for a duration $t_f = \alpha_f \tau_f$ where τ_f and τ_s respectively stand for the fluid and solid characteristic time scales while the constants α_f and α_s set the desynchronization between the fluid and solid domains. Note that various definitions may exist for fluid and solid time scales, the determination of relevant values considering a given problem is not straight forward. In the present manuscript, only steady states are targeted. Solvers are thus desynchronized such as for every simulation $t_s = \alpha_s \tau_s >> t_f = \alpha_f \tau_f$. A time line example of such a desynchronized case is schematized in Fig. 3.2. This method is however limited to the simulation of a thermal steady state, intermediate solutions having no physical meaning.

In terms of mathematical formalism and time response of the solid, the temporal desynchronization between the fluid and the solid domains is equivalent to a decrease of the solid quantity ρC. This observation is further explained on a simplified case. Considering a 1D problem where solid

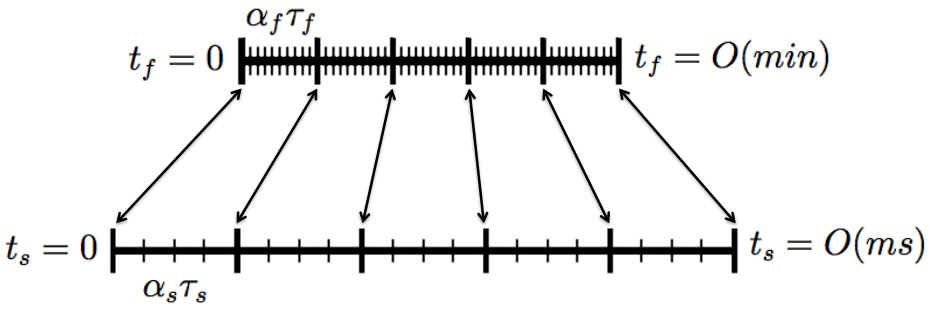

Figure 3.2: Example of a desynchronized CHT coupling time line. Both codes are launched at $t = 0$ but the computed physical times are differ.

properties do not vary with temperature, Eq. (2.15) becomes:

$$\frac{\partial T}{\partial t} = a \frac{\partial^2 T}{\partial x^2} \tag{3.4}$$

Introducing the normalized variables:

$$\begin{cases} x^* = \dfrac{x}{L_c} & (3.5) \\ t^* = \dfrac{t}{\tau_s} \quad \text{with} \quad \tau_s = \dfrac{L_c^2}{a} & (3.6) \end{cases}$$

where τ_s is the solid diffusive time scale (L_C being a characteristic length), leads to the expression:

$$\frac{\partial T}{\partial t^*} = \frac{\partial^2 T}{\partial x^{*2}} \tag{3.7}$$

From this equation, and the expression of t^*, it is clear that an increase of t is equivalent to an increase of $a = \frac{\lambda}{\rho C}$, which can be enforced by a decrease of the quantity ρC. In terms of solid response time, these two modifications lead therefore to the exact same solutions.

Duchaine *et al.* (2009*a*) studied a limit case of fluid and solid solvers desynchronization for which $\alpha = \alpha_s = \alpha_f$. This means that both domains converge to steady state at the same rate. The number of iterations nit between two coupling updates is thus linked to the time step by:

$$\begin{cases} nit_f = \alpha \tau_f / \Delta t_f & (3.8) \\ nit_s = \alpha \tau_s / \Delta t_s & (3.9) \end{cases}$$

Considering a turbine blade application, the authors assessed the impact of the parameter α on the convergence rate of the simulation. Figure 3.3 presents the evolution of the mean temperature within the blade for different values of this coupling parameter. Note that all the values

tested here led to stable simulations that converged towards the same steady state mean solutions. Figure 3.3 evidences that a diminution of α greatly increases the convergence rate. The lower the

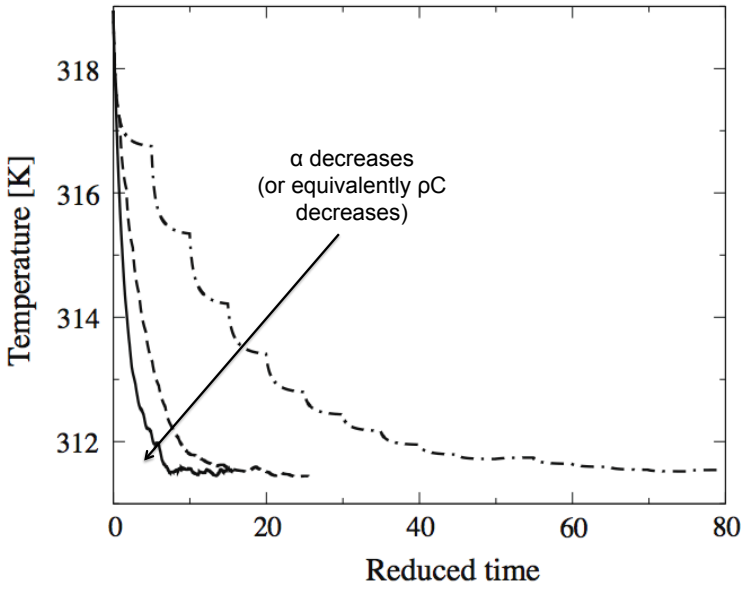

Figure 3.3: Evolution of the mean temperature in the blade as a function of reduced time in the solid $\frac{t_s}{\tau_s}$, for various values of α. Extracted from (Duchaine *et al.*, 2009*a*).

inter-coupling time, the faster the convergence of the coupled simulation. These results emphasize the need for tightly coupled simulations (i.e. high frequency coupling exchanges) between the fluid and the solid domains.

Besides, this temporal desynchronization technique between the fluid and the solid solvers can raise specific problems and require some special care (Jauré, 2012; Jauré *et al.*, 2013). The desynchronization process between the fluid and the solid solvers leads to distortions between the signal sent by the fluid and the signal actually seen by the solid. The relation between the frequency of a signal coming from the fluid f_f and the frequency actually seen by the solid f_s is given by:

$$f_s = f_f \frac{t_f}{t_s} = f_f \frac{\alpha_f \tau_f}{\alpha_s \tau_s} = f_f S_{sf} \tag{3.10}$$

Where S_{sf} is called the frequency temporal scaling factor between the fluid and the solid. Such a modification of the signal frequency may lead to non-physical effects that can be highlighted on a simple 1D model.

Consider the system depicted in Fig. 3.4 comprising:

- ▷ A fluid with a pulsating temperature of the form $T_f(t) = T_{f0} + T_{fluc}\ cos(\omega_0\ t)$ where T_{f0} is the mean temperature while T_{fluc} and ω_0 are respectively the amplitude and the pulsation of the signal.
- ▷ An initially isolated solid in contact with the fluid domain.

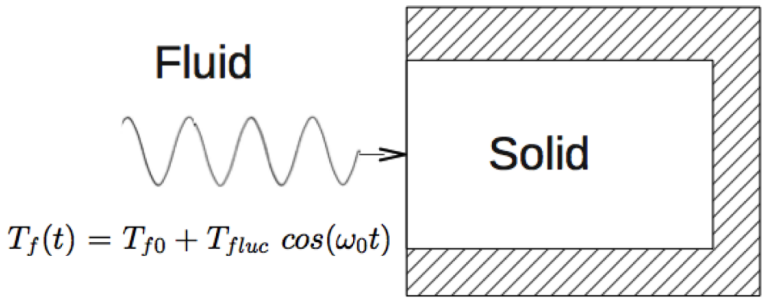

Figure 3.4: 0D configuration of a CHT problem. From (Jauré, 2012)

Taking an initial solid temperature of 373 K and a fluid temperature signal equal to $T_f(t) = 303 + 10\ cos(2\pi\ 380\ t)$, the evolution of the solid temperature can be plotted for different scale factors S_{sf} (Fig. 3.5). When the solvers are synchronized ($S_{sf} = 1$, black curve), the solid temper-

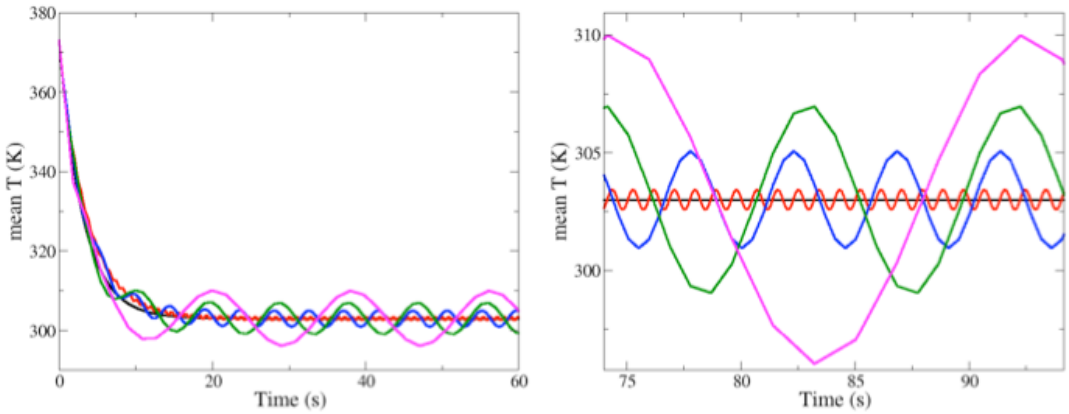

Figure 3.5: Evolution of the solid temperature of the 0D model. The black curve corresponds to $S_{sf} = 1$ and the oscillations period is inversely proportional to the scaling factor. From STRASS project.

ature converges with so small oscillations that they are not visible. Decreasing the scaling factor (i.e. accelerating the solid solver) leads to visible oscillations of the mean temperature. The amplitude and frequency of the oscillations are respectively inversely proportional and proportional

to the temporal scaling factor. However, after a transition period, the solid temperature oscillates around the same value independently of the scaling factor. This value is the steady state of the system. For this reason, in the following, steady solutions are obtained by averaging over a large time period.

In addition, consider the previous 0D model with this time a semi-infinite 1D solid. The perturbation length at 1% can be analytically determined as performed by Jauré (2012) and reads $x_{1\%} = ln(100)\sqrt{\frac{2a}{\omega_0}}$. This result shows that signals with low frequencies can penetrate deep into the solid domain and thus have an impact on the temperature field within the solid. Due to the frequency temporal scaling factor between the fluid and the solid domains, the later acts like a low-pass filter. As a result, the desynchronization of the two solvers leads to temperature signals with lowered frequency and hence an over prediction of the penetration into the solid. When very thin solid materials surrounded by a flow on both sides are considered, the penetration over prediction may lead to an artificial thermal interaction between the fluids on the two sides of the solid. Such a feature may lead to inaccurate solutions of the coupled problem and care is required.

Aside from the specific treatment of the physical time, the choice of the boundary conditions set at the domains interface is critical. This point is the focus of the next section.

Interface variables

Denoting with the subscript w all quantities at the fluid-solid interface, energy conservation of the joint system and temperature continuity imposes:

$$\begin{cases} q_w^f = q_w^s & (3.11) \\ T_w^f = T_w^s & (3.12) \end{cases}$$

Thermal coupling is thus achieved through the exchange of these physical fields between the fluid and the solid domains. In practice, various mathematical constructions of the interface equations exist. Standard formulations are detailed below:

- ▷ Dirichlet conditions: the temperature continuity is imposed at the interface:

$$\begin{cases} T_w^f = T_w^s & (3.13) \\ T_w^s = T_w^f & (3.14) \end{cases}$$

- ▷ Dirichlet-Neumann conditions: the fluid domain imposes a heat flux to the solid domain while the latter sets the skin temperature of the fluid computation:

$$\begin{cases} T_w^f = T_w^s & (3.15) \\ q_w^s = q_w^f & (3.16) \end{cases}$$

This boundary condition is regularly used in CHT simulations. However, in some cases it raises stability issues of the coupled problem (see next section). For this reason, some authors replace the Neumann condition applied to the solid by a combination of the temperature and heat flux fields, leading to the next interface equations.

▷ Dirichlet-Fourier conditions:

$$\begin{cases} T_w^f = T_w^s & (3.17) \\ q_w^s + \gamma T_w^s = q_w^f + \gamma T_w^f & (3.18) \end{cases}$$

where γ is a Coupling Relaxation Parameter (CRP) that is determined to achieve stability and high convergence rate. It is worth noting that the parameter γ is very different from the convective heat transfer coefficient h_{ref} in Eq. (3.1). γ is a numerical relaxing parameter and has no physical meaning. This relaxed boundary condition is referred to as a Fourier condition in the present manuscript. In the literature, various denominations can be found such as Robin or mixed condition. To make appear the variables prescribed to each domain, the previous equations may be rewritten as:

$$\begin{cases} T_w^f = T_w^s & (3.19) \\ q_w^s = q_w^f + \gamma(T_w^f - T_w^s) & (3.20) \end{cases}$$

▷ Fourier-Fourier conditions: the boundary conditions of both domains are set with a combination of the temperature and the heat flux from the other domain:

$$\begin{cases} q_w^f = q_w^s + \gamma_s(T_w^s - T_w^f) & (3.21) \\ q_w^s = q_w^f + \gamma_f(T_w^f - T_w^s) & (3.22) \end{cases}$$

In most cases, the temperature and heat flux fields as well as the coupling relaxation parameter send by one solver are directly treated as classical non-coupled boundary conditions by the other solver. For example, using a Dirichlet condition at the coupled interface for the fluid will lead to the following procedure in the fluid domain:

▷ reception of T_w^s by the fluid,

▷ replacement of the current skin temperature by T_w^s on the boundary conditions,

▷ classical computation.

Note that, some authors propose more sophisticated coupled boundary conditions derived from the four aforementioned standard ones. Among them, He & Oldfield (2011), developed a semi-analytic interfacing method to treat periodic signals at an interface. This approach is based on

the decomposition of interface variables into a time mean and harmonic components. Another set of boundary conditions proposed by Roe *et al.* (2008) is built to broaden the stability limits of the Dirichlet-Neumann conditions. In this detailed formulation called Combined Interface Boundary Condition (CIBC), interface equations are explicitly influenced by the fluid and solid domains. The classical Dirichlet condition is thus replaced by a partial differential equation. Similarly, Koren (2016) proposes an expression of the interface temperature through a differential equation which is numerically solved with an automatic adaptation of the coupling time step.

The numerical implementation of CHT computations in terms of temporal synchronization of the solvers, choice of the interface variables as well as inter-solver exchange frequency has a great impact on stability, accuracy and computational cost of the coupled simulation. In particular, stability is critical for the resolution of CHT problems but enhancing stability often lead to a deterioration of the convergence rate. Hence the challenge in solving CHT problems is to determine the most suitable strategy for given solvers and applications. Several studies on these topics are presented and discussed in the next subsection.

3.1.2 Influence of the coupling strategy on simulations stability and convergence

Stability is a key issue in numerical simulations. In CHT problems, it is controlled by both the boundary conditions and the exchange frequency of the computation (Giles, 1997; Duchaine *et al.*, 2009*a*; Jauré, 2012; Errera & Chemin, 2013). Various stability analyses of CHT problems numerical resolution can be found in the literature. Four of them are presented in Tab. 3.1.2. In these publications, two different stability analyses are used: the amplification factor approach (Godunov & Ryabenki, 1964) or the amplification matrix method (Hirsh, 1988). All these studies are based on the same basic assumptions:

- ▷ The two domains have constant properties and uniform grids.
- ▷ The only modes that may be unstable are those which are normal to the interface between the fluid and the solid domains. Thus, stability analysis consider a 1D problem.
- ▷ On the fluid side, the velocity at the interface is zero. It follows that the Navier-Stokes equations are reduced to a thermal diffusion equation.

Publication	Domains	Boundary conditions	Coupling conditions	Influencing parameters	Method used
(Giles, 1997)	semi-infinite	Dirichlet / Neumann	coupling at each $\Delta t_s = \Delta t_f$		amplification factor (Godunov & Ryabenki, 1964)
(Duchaine *et al.*, 2009*a*)	finite with imposed temperatures on the borders	Dirichlet / Fourier and Dirichlet / Neumann (as a limit case)	$\Delta t_s \neq \Delta t_f$ $nit_s \neq nit_f$ $\alpha = \alpha_s = \alpha_f$ (same convergence rate)	γ_f, α	amplification matrix (Hirsh, 1988)
(Jauré, 2012)	finite with imposed temperatures on the borders	Dirichlet / Neumann	$\Delta t_s \neq \Delta t_f$ $nit_s \neq nit_f$	nit_s, nit_f	amplification matrix (Hirsh, 1988)
(Errera & Chemin, 2013)	infinite fluid and finite solid with an imposed relation between prescribed heat flux and temperature	Dirichlet / Fourier and Fourier / Fourier	coupling at each $\Delta t_s = \Delta t_f$	γ_f	amplification factor (Godunov & Ryabenki, 1964)

Table 3.1: Some coupling strategies stability studies.

Note that to the author knowledge, simplifying hypotheses are always employed in boundary conditions studies. Indeed solving the problem directly in 3D complex geometries is hardly achievable. However, it was recently observed that stability of the 1D purely diffusive model for a given set of boundary conditions was more restrictive than the actual stability range of a 2D realistic configuration (Errera & Duchaine, 2016). Nevertheless, 1D analysis gives an insight on stability issues and allows identifying key influencing parameters. For this reason, some stability analysis from the literature, of particular interest for the present work are discussed below.

An early study carried out by Giles (1997) on the simplified configuration of semi-infinite domains (see Tab. 3.1.2) demonstrated that stability can be reached by imposing at the interface a Neumann condition to the solid domain and a Dirichlet condition to the fluid. This result was however limited to the case for which coupling exchanges were performed at each time step and where domains were synchronized in physical time. More recently various studies investigated stability issues in the context of unsteady desynchronized CHT simulations and steady CHT simulations. Further detailed are given just below.

Stability analysis and convergence rate of unsteady desynchronized CHT simulations

Duchaine *et al.* (2009*a*) and Jauré (2012) extended Giles's result to the case of finite domains desynchronized in time and exchanging data each nit_f fluid iterations and nit_s solid iterations. More specifically, Duchaine *et al.* (2009*a*) analyzed the stability of the Dirichlet-Fourier conditions for the computation of steady state problems with unsteady solvers. This stability analysis focused on the case where $\Delta t_s \neq \Delta t_f$ and $nit_s \neq nit_f$ in the limit case where $\alpha = \alpha_s = \alpha_f$ (solvers converge at the same rate). Introducing a new variable $D = \frac{\gamma_f \Delta x_s}{\lambda_s}$ and using properties (Δt, ρ...) characteristic of a turbine blade, Duchaine *et al.* (2009*a*) built the stability map of Fig. 3.6. Note that the value $D = 0$ implies that $\gamma_f = 0$ and hence corresponds to the classic Neumann condition. The stability domain admits an upper bound D_M almost independent from α and linked to the solid discretization. Under this upper limit, the Fourier boundary condition is always stable for low values of α (i.e. for tight coupling). As α increases to a threshold, the lower limit of the stable domain D_m greatly increases. Then, for even larger values of α, D_m remains practically constant. Besides, for sufficiently large values of the coupling relaxation parameter γ_f, (leading hence to large D), the scheme is stable whatever the exchange frequency (controlled by α). On the contrary, the Neumann condition ($D = 0$) is stable only if tight coupling is achieved. Similarly, Jauré (2012) showed that Dirichlet-Neumann conditions remained stable for tightly coupled systems.

Duchaine *et al.* (2009*a*) also studied the impact of the CRP on the convergence rate of the coupled simulation of the T120D turbine blade, Fig. 3.7. The results revealed that a decrease of the CRP diminishes the time needed to obtain a steady solution. Since the Neumann condition corresponds to the limit case where $\gamma_f = 0$, this condition is that which leads theoretically to the fastest convergence. Nevertheless, stability studies showed that too small values of γ_f may cause

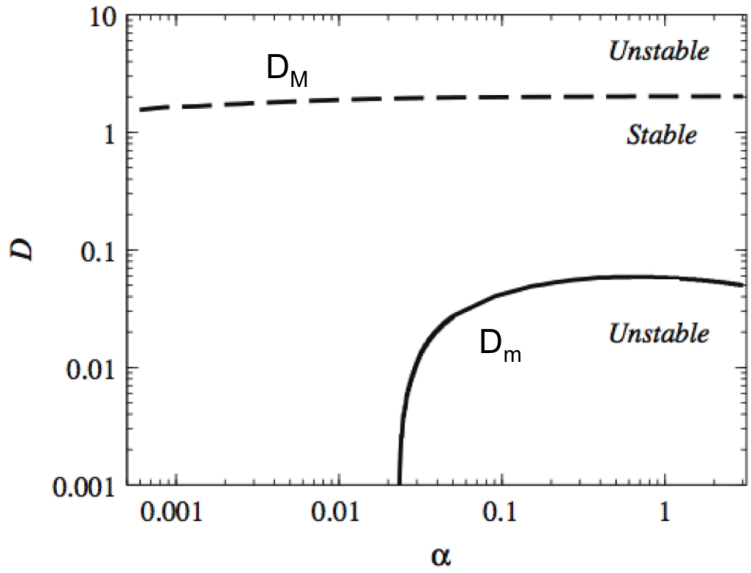

Figure 3.6: Stability map in the (α, D) space of the simplified conjugate heat transfer problem: lower stability limit D_m (solid) and upper stability limit D_M (dashed). From (Duchaine *et al.*, 2009*a*)

stability problems (as highlighted just above by the stability map of Fig. 3.6). Hence, choosing the optimal value of this coefficient has to be done carefully to limit computational resource consumption while maintaining stability.

In the present applications, the fluid and solid solvers are tightly coupled. Therefore and following previous conclusions, the Dirichlet-Neumann set of boundary conditions is used to obtain a high convergence rate of the simulations. For all the simulations reported in this manuscript, no numerical instability was observed. Besides, in Part II, an academic application is investigated whose solutions are steady. Such a feature enables the computation of this specific case within the currently proposed coupled framework but following the methodology proposed in Errera & Chemin (2013) in a steady context. A comparison is thus proposed between the results obtained for the current coupled methodology and that obtained with Errera & Chemin (2013)'s methodology. The stability analyses proposed in Errera & Chemin (2013) in the context of steady CHT simulations is thus detailed in the next paragraph.

Stability analysis and convergence rate of steady CHT simulations

The methodology proposed by Errera & Chemin (2013) relies on a chaining approach. The steady state solution of the joint fluid-solid problem is obtained by converging a pseudo-steady fluid solver through a time-marching scheme while solid conduction is solved with a steady solver. Just like

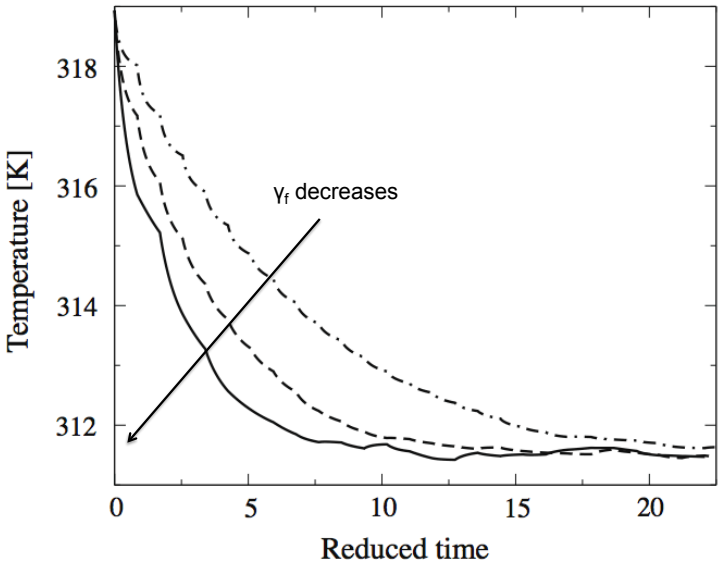

Figure 3.7: Evolution of the mean temperature in the blade as a function of reduced time in the solid $\frac{t_s}{\tau_s}$, for various values of γ_f. Extracted from (Duchaine *et al.*, 2009*a*).

for the desynchronized coupled technique, only the steady-state is pursued, intermediate solutions having no physical meaning. In Errera & Chemin (2013) a stability analysis of the Dirichlet-Fourier conditions in such a framework is proposed. The authors show the existence of an optimal value of γ_f evidenced in Fig. 3.8 which reads:

$$\gamma_f^{opt} = \frac{\lambda_f}{\Delta x_f} \sqrt{\left(1 + \frac{1}{F_f}\right)^2 - 1} - \frac{1}{F_f} \tag{3.23}$$

where $F_f = \frac{\lambda_f \; nit_f \; \Delta t_f}{\rho_f \; c_{pf} \; \Delta x_f^2}$ stands for the Fourier number in the fluid domain with λ the thermal conductivity, nit the number of iterations between two coupling events, Δt the time step, ρ the density, c_p the specific heat capacity and Δx the cell size. This local numerical coefficient defines a transition between two kinds of Fourier boundary conditions on the solid side:

- ▷ $\gamma < \gamma_f^{opt}$ (left part of the curve on Fig. 3.8), the boundary is controlled by a Neumann condition which is prone to instability but allows fast convergence,
- ▷ $\gamma > \gamma_f^{opt}$ (right part of the curve on Fig. 3.8), the boundary is controlled by a Dirichlet condition, a stable but low process.

The intersection between the two curves that occurs for the so called optimal value of γ_f is always stable and leads to the theoretical fastest convergence. The study also showed that in such configurations, the optimal boundary condition of the fluid border is the Dirichlet one. Note that in

Errera & Chemin (2013), a stability analysis was also performed for the couple of Fourier-Fourier conditions. Just like for the study of Dirichlet-Fourier conditions, optimal values of the two coupling parameters (one for each Fourier condition) were determined analytically.

To sum up, a desynchronization technique is used to bridge the temporal discrepancies between the fluid and the solid solvers and obtain mean quantities representative of the permanent thermal regime at a reduced CPU cost. Besides, for stability and high convergence rate reasons, solvers are tightly coupled and interface variables are set with Dirichlet-Neumann boundary conditions. The modelisation of the interactions between the combustion and radiation phenomena raises very different issues. The resolution of such interactions is the topic of the next section.

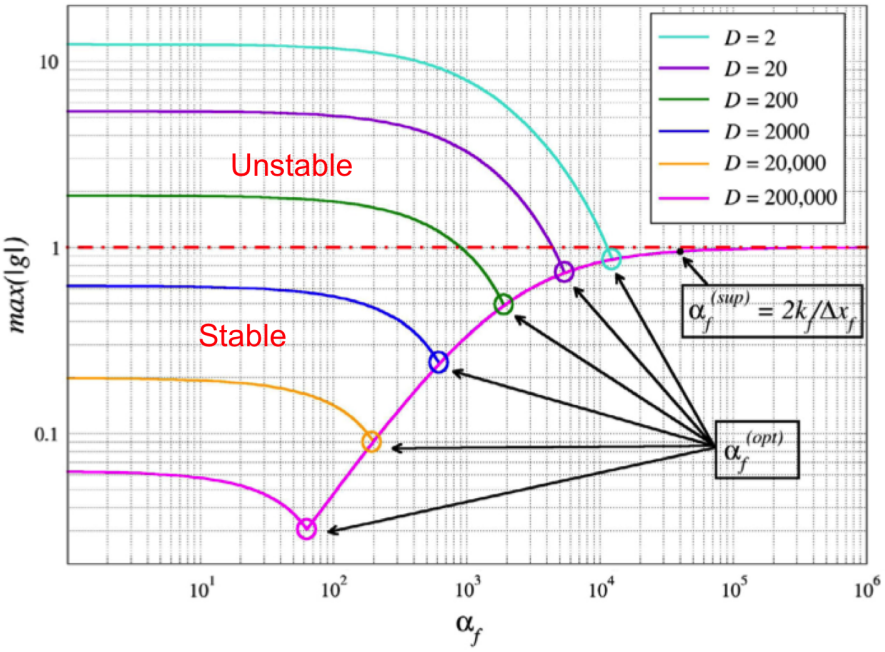

Figure 3.8: Maximum value of the temporal amplification factor of the studied system max($|g|$) as a function of γ_f for six different fluid Fourier numbers. Note that the parameter denoted α_f on this figure corresponds to γ_f in the present discussion. From (Errera & Chemin, 2013).

3.2 Radiation Fluid Thermal Interaction (RFTI)

Despite the potential key role played by radiative heat transfer in combustion systems, this physical phenomenon is conventionally neglected in combustion studies. Indeed, the complexity associated with an accurate resolution of radiation has long been prohibitive. However, a growing number of

studies demonstrate the importance of radiative heat transfer in canonical as well as in practical combustion devices (Modest & Haworth, 2016). Radiation is dictated by the local flow properties in terms of temperature, chemical composition of radiant species and pressure. This phenomenon is thus intrinsically linked to the fluid flow features. In return, heat transfer by radiation alters the energy distribution within the system, modifying hence the local temperature of the flow, and eventually density dependent properties as well as chemistry. Through this process, radiative heat transfer has an influence on the local and global behavior of flames.

Various authors have demonstrated numerically the significant impact of radiative heat transfer on laminar flames. For instance, Ju *et al.* (1998) showed a radiation induced modification of the flame propagation speed and extinction characteristics as well as a reduction of the peak temperatures of a one-dimensional planar laminar premixed flame. Another work by Zhu & Gore (2005) conducted on a one-dimensional laminar diffusion flame evidenced a decrease of the predicted levels of soot and NO pollutants with the inclusion of radiation in the simulation. Various other studies investigating the effects of radiative heat transfer on premixed or diffusion laminar flames have been very recently reviewed in Modest & Haworth (2016). In turbulent flows, the RFTI problem is even more complex. Fluctuations of temperature and species concentrations induced by turbulence are highly non-linearly coupled to fluctuations of the radiation intensity. Therefore, just like convection is enhanced by turbulent motions due to non linear interactions of velocity and temperature fluctuations, radiative heat transfer is also affected by turbulence. This phenomenon is referred to as Turbulence-Radiation Interaction (TRI) in the literature. In practical combustion devices, TRI can induce changes in the mean temperature, heat transfer rates as well as pollutant emissions with an order of magnitude comparable to or even larger than modifications resulting from turbulence-chemistry interactions (Song & Viskanta, 1987). A brief literature review on RFTI studies in the context of reactive flows is proposed in the following. Note that a comprehensive review on this topic (mostly focused on RANS studies) is proposed by Coelho (2007).

Interactions between combustion and radiative heat transfer have traditionally been studied thanks to RANS solvers to account for the flow physics. In such a steady framework and as already discussed in Section 2.1, physical quantities are decomposed in a mean (statistically or temporally) resolved part ($\overline{T}$,$\overline{X}_i$) and a fluctuating modeled part (T',X_i'). A straightforward solution to account for radiation would thus be to compute the mean radiative source term field from the available mean fluid quantities. However, nothing guarantees that the mean radiative source term is equivalent to the radiative source term computed from mean quantities:

$$\overline{S_r(T, X_i)} \neq S_r(\overline{T}, \overline{X}_i) \tag{3.24}$$

In fact, such an assumption would correspond to neglecting TRI effects. This hypothesis may be acceptable when radiant non-reactive slow hot flows are considered such as combustors exhaust

gases, because scalar fluctuations are comparatively small (Soufiani *et al.*, 1990; Mazumder & Modest, 1999). However, in reactive flows, TRI may contribute significantly to the radiative phenomenon and has to be modeled when RANS flow solvers are employed. Such interactions between turbulence and radiation can be formalized mathematically as described just below. Directional and frequential integration of the mean RTE gives an expression of the mean radiative source term. Introducing a decomposition of the variables into mean and fluctuating contributions, leads to four correlation coefficients for TRI, three for emission and one for absorption. The respective influence of these correlations and the resulting impact for their modelisation in RANS simulations has been extensively studied in the literature (Coelho, 2007).

In this context, early studies on TRI relied on decoupled approaches in which radiation was evaluated a posteriori from flow properties (precluding hence a direct evaluation of the impact of radiation on the flow). For this purpose, reference computations were generally obtained via stochastic methods[4] (Jeng *et al.*, 1984). These works which considered mostly academic diffusion flames, demonstrated that TRI greatly increases the mean radiative intensity (Jeng *et al.*, 1984; Grosshandler & Joulain, 1986; Fischer *et al.*, 1987; Faeth *et al.*, 1987). Detailed studies of the impact of TRI on radiation physics and modelisation through each of the four correlations were conducted (Grosshandler & Joulain, 1986; Fischer *et al.*, 1987; Krebs *et al.*, 1994; Coelho, 2004; Eiberger *et al.*, 2015), thus validating or not some assumptions to include or neglect contributions from each correlations in numerical simulations.

To go one step further and acknowledge the impact of radiative heat transfer on reactive flow fields, several authors coupled RANS flow solvers with radiation numerical resolution. Such computations were first reported by Song & Viskanta (1987) who simulated a 2D premixed methane/air flame using the P_1 approach (Jeans, 1917) to solve the RTE and a statistical combustion model. Numerous studies from various authors followed this first achievement. In particular the methane/air diffusion Sandia D flame (Barlow & Frank, 1998) and derivations from this configuration has extensively been studied through coupled simulations (Modest, 2003; Coelho *et al.*, 2003*b*; Coelho, 2004; Wang & Modest, 2007; Eiberger *et al.*, 2015). In particular, Coelho *et al.* (2003*b*) and Coelho (2004) evaluated the influence of neglecting radiation or accounting for this phenomenon through various assumptions using a DOM resolution along with a SLW global spectral model. They obtained acceptable results compared to experiments, with few impact of the different approaches. Modest (2003) simulated the Sandia D flame as well as two additional flames with a doubled and quadrupled diameter (hence increasing the flame optical thickness) and using the P_1 approximation to solve the RTE. The authors reported a decrease of the flame peak temperature when radiation was included in the simulations. TRI was responsible for one third of this decrease and the impact of TRI on peak temperature enlarged with the flame optical thickness. Similar conclusions were drawn in Wang & Modest (2007) for a close derivation from the Sandia D flame

[4]These methods generate temperature and species fluctuations not provided by RANS CFD simulations. The accuracy of such methods has been proven by Zheng *et al.* (2002).

and radiation resolved thanks to a Monte-Carlo approach. Total radiative heat loss was found to be underestimated by 16% when TRI was neglected. Radiation effects on turbulence levels has been the focus of much less studies. Works in this field concluded that radiation decreases the turbulent fluctuations of more or less significant amounts depending on the application (Townsend, 1958; Wang *et al.*, 2008).

Similar coupled simulations to study the interaction between radiation and turbulent combustion have more recently been conducted using LES flow solvers (Jones & Paul, 2005; Coelho, 2009; Poitou, 2009; Amaya, 2010; Zhang, 2011; Poitou *et al.*, 2011, 2012*b*; Gupta *et al.*, 2013; Refahi, 2013; Gonçalves dos Santos *et al.*, 2015). In this context, TRI is effectively resolved for the large scales and potential modeling issues of this process are reduced to sub-grid scale (SGS) TRI (note that this point is further detailed in the following). Poitou (2009), Poitou *et al.* (2012*b*) and Gonçalves dos Santos *et al.* (2015) performed RFTI coupled simulations of a turbulent propane/air flow into a rectangular burner mounted with a triangular flame holder. In these publications, the RTE was solved through a similar DOM approach and the flow was solved with the LES solver AVBP (described in Section 2.1). The authors reported a reduced impact of radiation at a global scale, the total radiative heat loss representing only 2% of the total heat released by combustion. Likewise, the mean flow dynamics fields were practically unaltered by radiative heat exchanges. However, important local variations of the time-averaged temperature up to 150 K were observed in both studies. These modifications of the thermal field impacted both the reaction products (notably a decrease of the temporally and spatially averaged CO mass fraction around 20%) and the flame dynamics. The latter was in particular highlighted by significant variations of the RMS temperature field in both studies. The authors associated these modifications to the lowered burnt gas temperature induced by radiation. As a result, flame stabilization was weaker and hence more sensitive to turbulent motions. A detailed investigation of (resolved) TRI for this configuration was carried out in Poitou *et al.* (2012*b*). The results evidenced that TRI induced a small increase of the total radiative heat loss as well as local variation of more or less 20% of the radiative source term. Finally, Poitou *et al.* (2012*b*) reported a modification of the flow characteristic frequencies with the inclusion of radiation, further emphasizing the impact of TRI.

Similar investigations considering a real industrial burner were proposed by Amaya (2010) (DOM solver for the RTE) and Refahi (2013) (Monte-Carlo solver for the RTE). Both authors drawn the same conclusions than those demonstrated on the laboratory burner mentioned just above. Indicating an impact of radiative heat transfer negligible at a global scale and on the flow dynamics but significantly modifying the thermal and species fields. In addition, these studies reported non-negligible differences between the radiative source term and wall heat fluxes computed from a mean fluid solution and time averaged radiative fields highlighting once again the impact of TRI.

Finally, some attempts to study TRI with the use of DNS simulations have recently been made

with decoupled (Poitou *et al.*, 2007; Poitou, 2009; Roger *et al.*, 2010) or coupled approaches (Wu *et al.*, 2004; Deshmukh *et al.*, 2007). Due to CPU cost restrictions, such approaches considered very idealized configurations but nevertheless allowed to assess the TRI effects with no a priori simplifications of the correlations. In particular, these studies allowed a fine understanding of the root phenomena at play and an investigation of two important issues in the context of multiphysics RFTI simulations employing LES flow solvers. First, the flame thickening influence on radiation (TFLES model described in Appendix A.2.1) has been shown to be negligible in Poitou (2009). Second, Poitou *et al.* (2007), Coelho (2009), Roger *et al.* (2009) and Roger *et al.* (2010) evidenced a low effect of the subgrid scale fluctuations of temperature, and species composition on absorption and emission for very simplified configurations. Note however that although of low amplitude an impact was still observed. Besides, said from some authors, extrapolation of the conclusions to realistic turbulent reactive flows is not straightforward. For these reasons, some authors recently proposed a subgrid scale model for radiative heat transfer (Soucasse *et al.*, 2014). These are however at an early development step and most studies neglect the impact of subgrid scale fluctuations on the resolved scales (Jones & Paul, 2005; Amaya, 2010; Poitou *et al.*, 2011, 2012*b*; Refahi, 2013; Gonçalves dos Santos *et al.*, 2015).

Unlike in the CHT literature, partitioned coupled RFTI simulations (i.e. using separated solvers to resolve the combustion and radiation phenomena) follow very similar coupling strategies. These are further detailed in the next section.

3.2.1 Coupling strategy

In the following, subscripts f and r respectively stand for variables referring to the fluid flow and the radiative sub-systems.

Physical time

Light propagates infinitely fast compared to other phenomena in a combustion chamber. Therefore, in combustion applications, radiative fields adapt instantaneously to the flow conditions. An evolution of radiative fluxes results only from variations in the flow distribution and is thus conditioned by the convective time scale. Since, for the present study, the numerically imposed fluid time step is controlled by acoustics which is 10 to 100 times faster than convective transport, there is no need to update the radiative fields at each fluid iteration as long as the flow remains low Mach. The fluid characteristic convective time τ_{conv}, is hence introduced as:

$$\tau_{conv} = \frac{L_c}{u} \tag{3.25}$$

where L_c is a characteristic length and u the flow bulk velocity. Since an evolution of the numerical flow fields may be assimilated to the transport of one fluid molecule from one cell to another, Wang

(2005) and Leacanu (2005) proposed a criterion based on the smallest mesh cell size Δx_{min}:

$$\tau_{conv} = \frac{\Delta x_{min}}{u} \tag{3.26}$$

At the same time, considering the CFL limited flow time step given in Eq. (2.11) and assuming that the convective velocity u is negligible compared to the speed of sound, one obtains the following relation:

$$\Delta t_f = CFL\ \frac{\Delta x_{min}}{c_s} = CFL\ \frac{u}{c_s}\frac{\Delta x_{min}}{u} = M\ CFL\ \tau_{conv} \tag{3.27}$$

with Δt_f denoting the flow solver time step and M the Mach number. As a result, the number of fluid iterations nit_f between two coupling exchanges between the fluid and the radiative solver is given by:

$$nit_f = \frac{\tau_{conv}}{\Delta t_f} = \frac{1}{M\ CFL} \tag{3.28}$$

which leads to $nit_f \sim 7$. In practice, 7 fluid iterations are not sufficient to obtain significant modifications of the fluid and impact the radiative fields. Indeed the evaluation of the fluid characteristic convective time through the smallest mesh cell size Eq. (3.26) is not well suited for the present case. For this reason and since the radiation solver has a CPU cost largely above the fluid solver, tests are performed to ensure that the chosen value of nit_f is the optimal trade-off between accuracy and computing time.

Interface variables

In RFTI coupled simulations, interface variables are volumetric. Fluid temperature T, pressure P and species mole fractions X_k fields are used by the radiative solver to compute the gas absorption κ_ν and resulting black body radiative intensity I^0_ν and radiative source term Sr while the latter acts as a source (or sink) term for the fluid energy equation ($\dot{Q}$ in Eq. (A.12)). Interface conditions of the RFTI problem read:

$$\begin{cases} \kappa_\nu = f(T^f, P^f, X^f_k) & (3.29) \\ I^0_\nu = g(T^f, \kappa_\nu) & (3.30) \\ \dot{Q} = Sr^r & (3.31) \end{cases}$$

Interface variables from the fluid are imposed in the radiative solver through the functions f and g while the radiative source term is directly imposed in the energy equation.

3.3 Radiation Solid Thermal Interaction (RSTI)

Finally, the interaction between the solid and the radiative process is considered. First, it seems important to remind that metals commonly used in combustion chambers can be considered as

opaque (incident radiation can only be absorbed or reflected). As a result, radiation is only considered at the solid surface (Modest, 2003). From this, the resolution approach of this problem depends on whether or not the media contained in the domain delimited by the solid surfaces participates or not in the radiative process.

In the case of a transparent media, the radiative flux received by the solid surfaces is computed from the surface temperatures and geometrical properties. Considering the simplified case of two radiating surfaces S_1 and S_2 at temperatures respectively equal to T_1 and T_2, the radiative heat flux $q^r_{1\to2}$ emitted by S_1 and received by S_2 reads:

$$q^r_{1\to2} = h_r F_{12}(T_1 - T_2) \tag{3.32}$$

where

- h_r is the radiative exchange coefficient given by $h_r = 4\epsilon\sigma\left[(T_1 + T_2)/2\right]^3$.
- F_{12} is the view factor which indicates the fraction of energy emitted by S_1 and received by S_2. This quantity depends only on geometrical considerations and can be obtained via a double surface integral. Numerous databases exist in which the view factor expression is given for relatively simple academic configurations (Siegel & Howell, 2002; Modest, 2003).

The radiative flux expression given in Eq. (3.32) is easily extended to configurations including more than two surfaces by summation over the contribution of all the surfaces. Applications considering radiative exchanges from a solid-to-solid point of view are numerous. Among them are for example spacecraft thermal modeling (Chin *et al.*, 1992), micro-combustors (Kuo & Ronney, 2007) or atmospheric reentry (Joshi & Leyland, 2012).

When considering an enclosure filled with a participative media, the resolution approach is noticeably different. The resolution of the radiative problem in such cases follows the concepts, equations and models described in Section 2.3. Note that in the present manuscript, the RSTI has not been studied independently like for the CHT and RFTI problems. The RSTI is one of the interactions composing the coupled simulation including all the three sub-components combustion, radiation and solid conduction. In such a case, the heat flux imposed to the solid is thus the addition of both convective and radiative contributions. In terms of physical quantities exchanged, the RSTI coupled system follows the same principles than the CHT system.

3.3.1 Coupling strategy

In the following, subscripts s and r respectively stand for variables referring to the solid and the radiative sub-systems.

Physical time

Since the RSTI is only studied in a coupled framework where all the sub-systems and their interactions are included, the treatment of the physical time follows on from that set between the fluid and radiative solvers. For each coupling exchange performed between those solvers, an exchange is additionally achieved between the solid and radiative solvers.

Interface variables

Solid surface temperature and emissivity (which itself depends on temperature) impact the radiative energy absorbed, emitted or reflected at walls while the global radiative field induces an energy transfer from/to the solid. For the present computations, the wall emissivity is assumed independent of the local temperature.

Just like for the CHT simulation, Dirichlet-Neumann conditions are used at the interface, the radiative solver imposes a heat flux to the solid domain while the latter sets the skin temperature for the radiative heat transfer computation:

$$\begin{cases} T_w^r = T_w^s & (3.33) \\ q_w^s = q_w^r & (3.34) \end{cases}$$

3.4 Conclusion

In this chapter, the modelisation of the interactions between the reactive flow, conduction within the solid parts and radiative heat transfer was addressed. In this context, several issues were discussed. First, in this manuscript, only mean quantities representative of the permanent regime are sought for. Starting from an initial condition, the simulation consists hence in computing all the sub-system interactions during a transient until the permanent regime is reached. However and since the various phenomena considered are characterized by very different time scales such a computation of the full transient is not affordable in terms of CPU cost and specific techniques are thus deployed. Second, the choice of the interface variables is critical both in terms of solution accuracy and computation stability and has to be done carefully.

Specific coupling strategies chosen to handle both issues have then been discussed in this chapter for the three couple of sub-system interactions CHT, RFTI and RSTI:

- ▷ CHT: When employing unsteady solvers to obtain the mean quantities representative of the thermal permanent regime, the solvers can be desynchronized to accelerate convergence in the solid and save computational time. Note that such a temporal desynchronization

between the fluid and the solid domains is equivalent to a decrease of the solid quantity ρC. Besides, acknowledging the results of existing stability analyses from the literature, the Dirichlet-Neumann interface conditions are retained to perform these coupled simulations since these ensure the theoretical highest convergence rate as long as stability can be achieved (i.e. if solvers are tightly coupled).

- ▷ RFTI: in combustion applications, radiative fields adapt instantaneously to the flow conditions. The radiative fields update is therefore set in accordance with the flow fields evolution in terms of temperature and species distribution. In practice and since the radiation solver has a CPU cost largely above the fluid solver one, tests are performed to find an optimal trade-off between accuracy and computing time. Interface variables from the fluid are imposed in the radiative solver through the dependency of radiative properties on fluid species, temperature and pressure while the radiative source term is directly imposed in the fluid energy equation.
- ▷ Since the RSTI is only studied in a coupled framework where all the sub-systems and their interactions are included, the treatment of the physical time follows on from that set between the fluid and radiative solvers. Besides, in terms of physical quantities exchanged at the interface, the RSTI coupled system follows the same principles as the CHT system (Dirichlet-Neumann interface conditions).

Having discussed the numerical treatment of these three multi-physics problems including only two sub-systems and their interaction, the resolution of the global thermal problem in a combustion chamber requires the simultaneous resolution of all the sub-systems and their interactions at the same time, following the principles detailed for the smaller multi-physics problems.

Finally, a specific issue was mentioned in the chapter and has not been addressed yet: the CPU cost mismatch between the sub-systems needs to be handled to ensure a good performance of the coupled applications. This topic is discussed in detail in the next chapter.

Chapter 4

Coupled application computing performance: issues inherent to the partitioned approach

Contents

Over the years, the constant improvement of processor technologies as well as the development of parallel architectures using more and more computing entities has led to an explosion of the computing power supplied by supercomputers. This, combined with the growing will to produce highly performant software, allowed the resolution of increasingly more complex physical phenomena encompassing additional levels of details. In the aeronautics, for instance, the numerical resolution of the flow field in complex geometries was long limited to the use of RANS approaches. In the past decades, the concomitant development of parallel architectures offering many computing cores and of very scalable codes made available LES for industrial applications. When seeking to numerically resolve complex physical problems, computing performance is essential. Indeed, the availability of a high computing power is meaningless if developed software are not accordingly thought to take advantage of the specific features of supercomputers. As a result, for a given

available computing power, computing performance determines what can be simulated or not. In the climate field, for example, a model performance will determine the total number of years that a simulation will cover or the number of different scenarii that will be computed in a few weeks or months (Worley *et al.*, 2011; Domke & Wang, 2012). During the design phase of a helicopter combustion chamber, given an available computing power, the numerical application performance sets the CPU cost and restitution time of the simulations and hence limits the number of different configurations that will be possible to treat during a numerical simulation campaign.

In 2005, the traditional approaches used to raise CPU performance reached a threshold (Sutter, 2005). To overtake this limitation, the High Performance Computing (HPC) community turned to hyperthreading and multicore architectures, further emphasizing the need for applications that scale efficiently for very high numbers of cores [1].

Within the highly demanding current context for parallel efficiency, code coupling adds additional complexities. In particular, the resolution of multi-physics problems through partitioned approaches requires the use of specific and highly scalable methods. First, the resolution of the interactions between the various components require the exchange of a huge amount of data between solvers, usually distributed over a large number of cores. Efficient communication and interpolation algorithms are thus required. In addition, the resources available for the coupled simulation should be carefully distributed between the solvers to avoid CPU wasting and maintain coupled applications scalability. A first guess would be to consider the load inherent to each code involved in the coupled framework and accordingly allocate the resources to the different solvers. However, experience has shown that such simple considerations lead in some cases to poor performance and unexpected scaling behavior of the coupled applications. This evidenced the need to consider in addition other parameters such as communications between solvers. Both classical load balancing and impact of the code to code communication overload are discussed in the present chapter.

The parallelism management, strong scaling and performance bottlenecks associated to each separated code used in the present study are not addressed here. The influence of the numerical modeling parameters intrinsic to each code is not detailed. The study investigates the impact of the computing parameters on coupled simulation scalability and focus is on the coupling performance as well as resource distribution between legacy codes.

Unless explicitly mentioned, all the coupled applications are run with the OpenPALM code coupler. The software capabilities exploited for the current study are detailed in the first section (4.1). Then, the working principle of a coupled application is described (Section 4.2), highlighting the need to consider two different components when seeking for the optimization of the restitu-

[1] Note that disruptive technologies already exist and are still developed but will ask for intensive rewriting of the current applications framework.

tion time of a coupled simulation: the internal computational time of the various solvers (load balancing) and the communication time between solvers. These two components are discussed in terms of implications for resource distribution and influencing parameters in Sections 4.3 and 4.4 respectively. In particular, the equations governing optimal core distribution based only on the internal computational time are discussed in Section 4.3. Then the impact of various parameters on communication times is investigated on a toy model in Section 4.4 and an analytic modeling of such times is proposed to understand the phenomena at play and exploit the results for real computations. Finally, the last section concludes on the advances provided by the work done in this document, as well as on remaining paths and options to explore in a will to improve computational performance of coupled simulations.

4.1 Code coupling with OpenPALM

The OpenPALM code coupler (Piacentini *et al.*, 2011; Refloch *et al.*, 2011; Duchaine *et al.*, 2015) provides a library of functionalities allowing the creation of a framework of independent code components or algorithms interacting with each other. The software is highly modular and flexible, hence capable of handling very different applications (Rochoux *et al.*, 2014; Amaya, 2010). Once an appropriate framework has been produced to address a specific physical problem, the software manages the execution scheduling of the various entities as well as the communications between them. The components may be executed in a sequential or concurrent way. For the present couplings, all the codes run concurrently: each of the components are launched at the beginning of the simulation and compute at the same time. During the execution, the exchange of physical fields is handled by the CWIPI library (Refloch *et al.*, 2011) linked with OpenPALM. The various code interfaces are generally discretized on different and non-coincident grids and distributed on several computing cores. Therefore, a complex communication scheme is built between the cores allocated to the different solvers and physical fields are interpolated between grids (Jauré *et al.*, 2013). As a result, the communication algorithm is split into two phases:

- ▷ an initialization consisting in the determination of the inter-code communication routes and the interpolation coefficients,
- ▷ a communication phase during which physical fields are interpolated and exchanged.

For applications that do not involve moving meshes (hence for which the inter-code communication scheme and interpolation coefficients do not vary in time), the initialization phase is only performed once at the beginning of the computation. Then, during the communication phases, the cores allocated to the different codes exchange data directly via point-to-point MPI communications. This fully distributed method was shown to ensure a good scalability of the coupled application (Jauré *et al.*, 2011) compared to a method where all the information to exchange is gathered on one computing core.

4.2 Coupling working principle

The working principle of the coupling process considered here is illustrated in Fig. 4.1 for a coupled simulation including three different codes. The coupled computation splits into two different

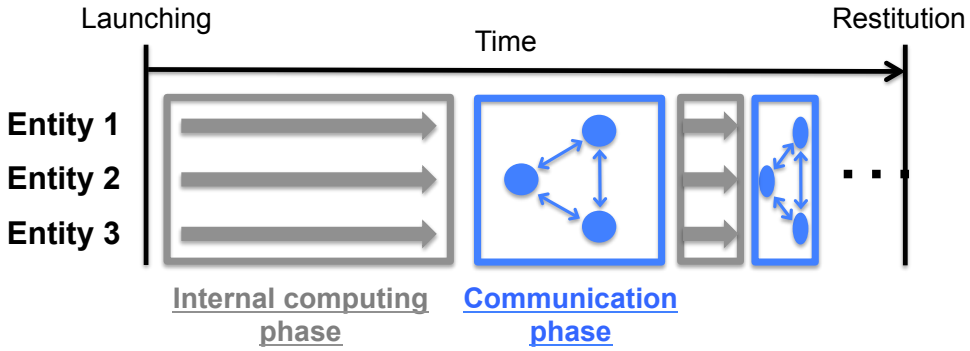

Figure 4.1: Working principle of a coupled simulation including three different computation codes.

phases. First, during the computing phase, each code independently performs a fixed number of iterations (which may be different for each solver). As previously mentioned this is achieved concurrently, meaning that the CPU resources are distributed between the components. Once the computation of the prescribed number of iterations is completed, the communication phase starts: the codes exchange data, two-by-two, at their interfaces. This phase begins when the two codes involved in the communications are available (i.e. when the computation part is completed). In other words, if the coupling framework includes more than two components, two solvers can exchange data as soon as both computing phases are over, even if the other codes are still computing. For clarity reasons, following developments are made on the basis of a coupled simulation including only two entities. Further generalization of the results to more components is relatively straight forward.

The time line corresponding to a coupled simulation including two entities is detailed in Fig. 4.2. Code 1 and code 2 are launched at the same time and compute each a prescribed number of iterations. This is called the internal computing time (in grey). In this example, and right after the launch phase, the internal computing phase is longer for code 1 than for code 2. All the cores allocated to the second code wait (in green) until code 1 is finished. Then the exchange phase starts (in blue) before a new cycle starts.

From Fig. 4.2, it is clear that the reduction of the restitution time of such a coupled simulation, may be achieved through the suppression of the wait time as well as the reduction of the communication time. These two paths of improvement are thus explored in detail in this study. The objective is double. First, the present work aims at providing guidelines to perform efficient

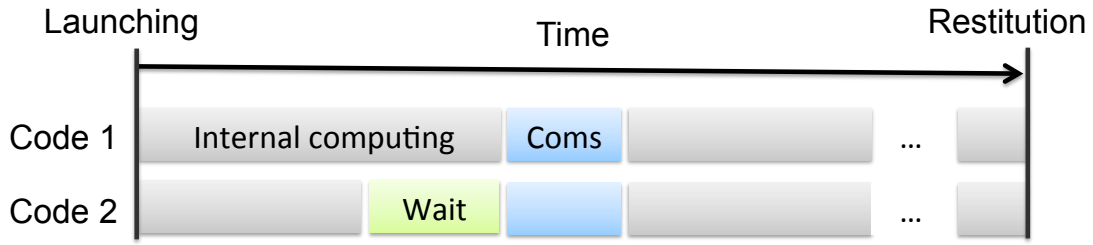

Figure 4.2: Time line corresponding to a coupled simulation including two codes.

coupled computations by an intelligent distribution of the available computing resources. Second, the communication phase is investigated in detail to understand the influencing parameters and demonstrate the need for further developments of current coupling methods to achieve more performant couplings.

Throughout the present study, various notions of time are used. For an easier understanding of the denominations, these are detailed hereafter:

- ▷ the physical time simulated, may vary from one component to another and is equal to the time step multiplied by the number of iterations computed.
- ▷ the restitution time, refers to the time passed from the launch to the end of the simulation (when the totality of the requested physical time, or number of iterations is computed).
- ▷ the local restitution time is used to characterize the time needed between the start and the end of a single action such as the computation of one code iteration, or the exchange of a unique data field.
- ▷ the internal computational time is associated to each code and independent of the coupling process. It refers to the local restitution time required to compute the prescribed number of iterations between two coupling events.
- ▷ the external communication time between codes refers to one exchange of data between the code entities.
- ▷ the CPU time corresponds to the computational power consumed on a machine. That is to say, the time during which the cores are dedicated to simulation summed over the number of cores (with no differentiation between the instants when the cores are computing, waiting or involved in a communication).

To address the current problem, the optimum core distribution is first determined considering only the internal computational time of each code, leaving aside considerations about external communications. The latter are investigated in the following section.

4.3 Intuitive load balancing based on the internal computational time of each component

The restitution time optimization of a coupled simulation is primarily achieved by the suppression of the wait time (Fig. 4.2). This is achieved through the synchronization of each code internal computational time. This time corresponds to everything that happens in a code between two coupling events. It includes the time required to solve the equations, the internal communications between the cores attributed to the same code as well as the time needed to read/write input/output files. The internal computational time differs from one code to an other. It depends on a large number of parameters such as the complexity of the physics which are solved, the code structure, the partitioning or the outputs requested by the user. The influence of such internal parameters on the performance of the codes is a topic of study in itself and is not discussed here. Only the variation of the internal computational time with the number of allocated cores is considered. For each code entity included in the coupled simulation, the optimal cores repartition equations developed here, take as inputs the internal computational time and its evolution with the number of cores. The latter is embedded assuming a known form of the code Speed-Up (SU). Two specific cases are considered. First, a perfect scalability is assumed, that is to say that if the number of cores dedicated to a monocode simulation is increased by a factor b (> 1), the restitution time of the simulation is divided by b. Secondly, a less restrictive hypothesis is made: the restitution time is divided by a coefficient a (< 1) times b, this will be called non-ideal affine speed-up.

4.3.1 General problem equation under the perfect scalability hypothesis

First, each code is supposed to scale perfectly with the number of cores. Let n be the number of codes included in a given coupled simulation and N the total number of cores allocated to the simulation. The objective is to distribute adequately the N cores between the n codes. For each code entity i, assuming the perfect scalability hypothesis, the local restitution time t_i between two coupling events (i.e. the internal computational time) is equal to the CPU time required to perform one iteration s_i, multiplied by the number of iterations between two coupling events nit_i, divided by the number of cores allocated to the solver N_i:

$$t_i = \frac{s_i \; nit_i}{N_i} \qquad i = 1, n. \tag{4.1}$$

To synchronize each code internal computational time, all the t_i must be equal for $i = 1, n$. Therefore, synchronization of two computing codes implies $t_1 = t_2$ and leads to the relation:

$$\frac{s_1 \; nit_1}{N_1} = \frac{s_2 \; nit_2}{N_2}, \tag{4.2}$$

equivalent to:

$$N_2 = \alpha_1^2 N_1 \qquad \text{where} \quad \alpha_1^2 = \frac{s_2 \; nit_2}{s_1 \; nit_1} \tag{4.3}$$

As $N = N_1 + N_2 = (1+\alpha_1^2)\; N_1$, the optimal number of cores for each code is given by the following system:

$$\begin{cases} N_1 = \dfrac{N}{1+\alpha_1^2} & (4.4) \\ N_2 = \alpha_1^2 \; \dfrac{N}{1+\alpha_1^2} & (4.5) \end{cases}$$

When extending this relation to a coupled simulation including n computational codes, the ideal cores repartition equations become:

$$\begin{cases} N_1 = \dfrac{N}{1+\sum\limits_{j=1}^{n} \alpha_1^j} \qquad \text{where} \quad \alpha_l^k = \dfrac{s_k nit_k}{s_l nit_l} & (4.6) \\ N_i = \alpha_1^i \; \dfrac{N}{1+\sum\limits_{j=1}^{n} \alpha_1^j} & (4.7) \end{cases}$$

4.3.2 Integration of a non-ideal affine speed-up for each code

Common solvers rarely present a perfect scalability. Most of them are optimized to provide good performance on a core number range corresponding to what is ordinarily used for its target applications. Several models exist to predict, from specific input data, the theoretical parallel efficiency of a standalone simulation. Many of them are built from the Amdahl's law (Amdahl, 1967). This law is based on the separation of the computation into two different parts. A distinction is made between what it parallelisable and what is always sequential and strongly restrict the considered code scalability. This decomposition is widely used in the HPC field. For instance, Gourdain's analytic speed-up model (Gourdain *et al.*, 2009) can be mentioned, for its proposition of a more detailed version of the Amdahl's law. Another work by Woo & Lee (2008), aims at integrating to this law a scalability notion in terms of energy consumption.

The performance of computational codes is evaluated through various tests among which are scalability tests. An example of the SU curves obtained for different applications and on different supercomputers with the AVBP solver is given in Fig. 4.3. It can be observed that the various cases lead to significantly different SU curves. Therefore, scaling tests should be performed for any component involved in a coupled application previous to the use of the equations developed below.

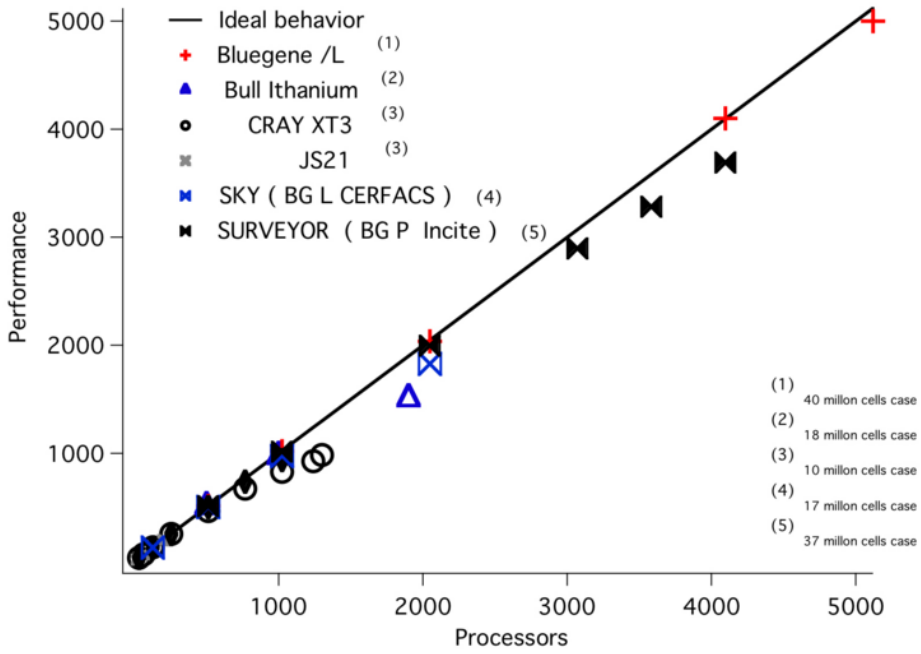

Figure 4.3: Speed-up curve obtained with the solver AVBP for different configurations on various machines.

For the present work, each code SU is assumed to be known and to have an non-ideal affine form within the range of computing cores number considered. Under that hypothesis, each component SU curve as a function of the number of cores can be approximated through a linear regression; leading to an equation in the form:

$$SU_i = a_i N_i \tag{4.8}$$

From this expression, the internal computational time t_i^{eff} associated to code i reads:

$$t_i^{eff} = \frac{s_i nit_i}{a_i \; N_i} \tag{4.9}$$

Under the hypothesis of non-ideal affine SU for each code, the equations governing the optimal cores repartition (Eq. (4.7) for ideal SU) becomes:

$$\begin{cases} N_1 = \dfrac{N}{1 + \sum\limits_{j=1}^{n} \alpha_1^j \; a_j^1} \quad \text{where} \quad \alpha_l^k = \dfrac{s_k nit_k}{s_l nit_l} \text{ and } a_k^l = \dfrac{a_l}{a_k} & (4.10) \\ N_i = \alpha_1^i \; a_i^1 \; \dfrac{N}{1 + \sum\limits_{j=1}^{n} \alpha_1^j \; a_j^1} & (4.11) \end{cases}$$

The use of such equations for a practical application is detailed in the next paragraph.

4.3.3 Practical example on an AVBP-AVTP coupled simulation

Consider now a given coupled application between the fluid solver AVBP and the solid solver AVTP on an industrial combustion chamber. Figure 4.4 shows each component SU for the considered application as well as the corresponding linear regressions. The non-ideal affine SU coefficients a_i (Eq. (4.8)) are given for each curve, and the theoretical ideal SU is indicated for comparison. Note that both codes SU curves are not representative of the actual current capabilities of the solvers and are only used here for illustration purposes. Figure 4.4, indicates a better scaling for AVBP than for AVTP. Indeed, the AVTP curve starts bending at approximately 600 cores. However, within the range of cores considered, both code SU are relatively well approximated through the linear regression. Accurate load balancing can thus be obtained with the proposed method. For the current example, the codes are coupled each $nit_f = 20$ fluid iterations and $nit_s = 1$ solid iterations. In addition, the CPU time associated to each code is respectively $s_f = 169\ s$ and $s_s = 67.4\ s$. The corresponding variation of the internal computational time as a function of the number of cores under perfect and non-ideal affine scalability can be computed from Eqs. (4.1) and (4.9) respectively. The results are shown in Fig. 4.5.

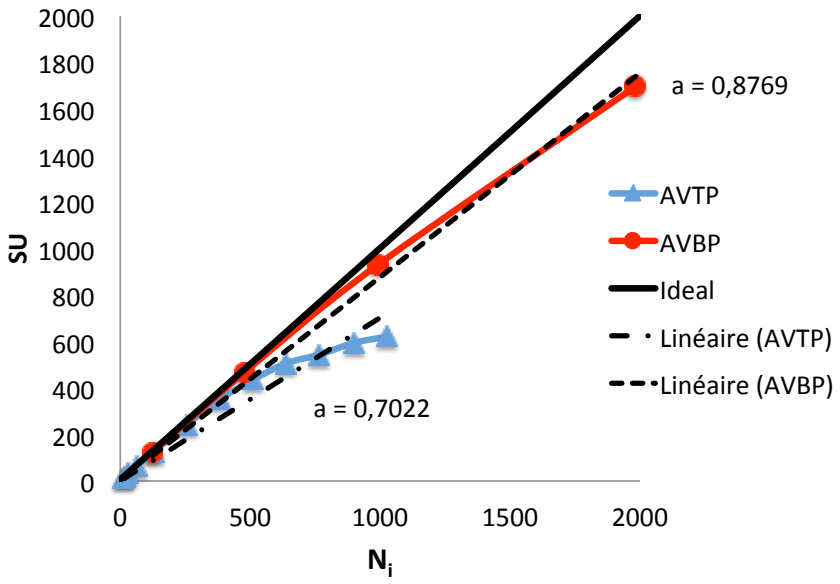

Figure 4.4: SU curves and corresponding linear regression obtained for the LES flow (AVBP) and solid conduction (AVTP) numerical resolutions of a given combustion chamber for a large number of cores.

The code synchronization corresponds to an equality between the solid local restitution time

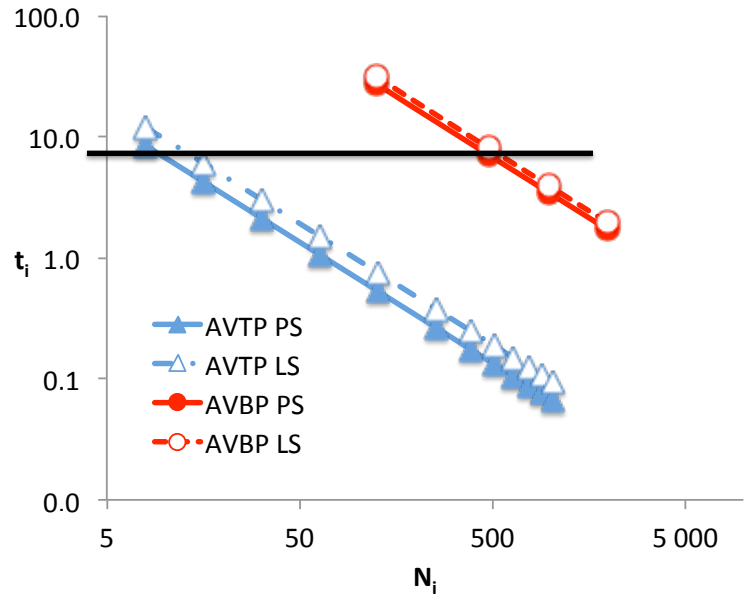

Figure 4.5: Local restitution time associated to the computation of each code iterations between two coupling exchanges between AVBP and AVTP as a function of the number of cores attributed to each code. PS = perfect scaling, LS = non-ideal affine scaling.

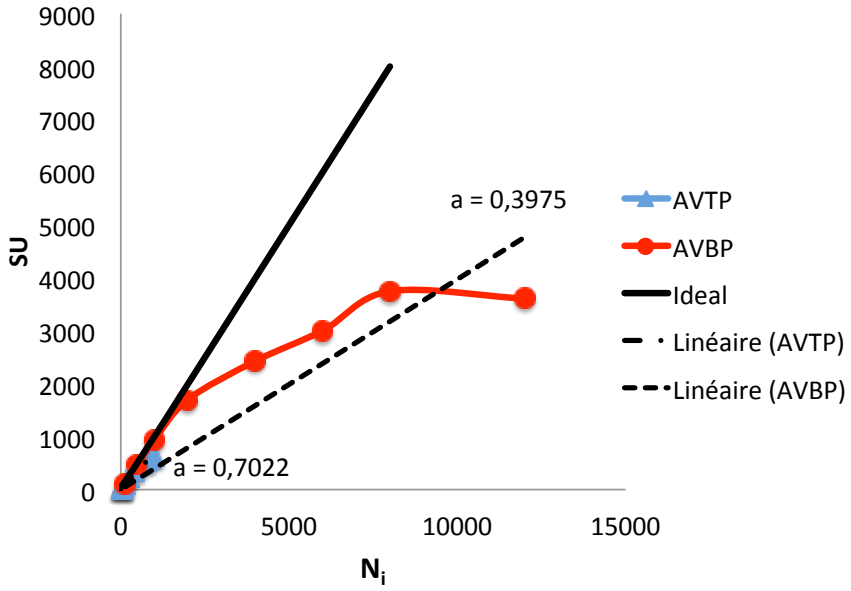

Figure 4.6: SU curves and corresponding linear regression obtained for the LES flow (AVBP) and solid conduction (AVTP) numerical resolutions of a given combustion chamber for a large number of cores.

and the fluid local restitution time between two coupling events. Therefore, all the optimal core distributions possible are given by the couple of points intersected by the black line as it goes from the top to the bottom. The number of cores which should be allocated to each code depends then on the total number of cores available for the simulation. As an example, if N=520 cores are available for the simulation, the optimal repartition given by Eq. (4.11) is $N_f = 507$ and $N_s = 13$. This specific case corresponds to the black line location in Fig. 4.5. This methodology, though clearly useful and relatively simple to implement suffers from two main issues. First, if the SU curve is far from linear Fig. 4.6, the proposed equations will lead to poorly efficient core repartitions. This problem may however be overcome by performing several linear regressions for each interval where the curve is quasi-linear. Second, as mentioned in the introduction, consideration of only the computing phase can in some cases, be insufficient. The core repartition may impact significantly communication times between solvers. This issue is addressed in the next section.

4.4 Communication time between codes

The second component of the restitution time of a coupled simulation corresponds to the time required to exchange the physical fields between each code involved in the coupling framework. This time is affected by machine performance and characteristics as well as by the way external communications between solvers are handled (communication algorithm, interface partitioning).

To provide some orders of magnitude, Fig. 4.7 extracted from Duchaine *et al.* (2015) presents the time required to perform one fluid iteration and one coupling exchange as a function of the total number of computing cores for the CHT simulation presented in the previous section.
The induced overhead due to coupling exchanges increases with the number of cores. Therefore, for a total number of cores around 8000, a coupling exchange costs as much as one single fluid iteration. In this example, coupling exchanges are performed each 20 fluid iterations, leading thus to a reduced impact of the communication time on the whole simulation restitution time. However, in the current context, where the amount of cores used to perform such simulations constantly increases, the communication time may become a major component of the whole computation cost and has to be seriously taken into account. Besides, for accuracy and convergence speed, the exchange frequency should be large (Chapter 3). This further increases the significance of the exchange times in the restitution time of coupled simulations.

Many existing studies on communication schemes focused on parameters that can affect the exchange time between two cores and proposed new algorithms to optimize the communications distribution when a large number of cores is involved (Culler *et al.*, 1993; Bar-Noy & Kipnis, 1994; Alexandrov *et al.*, 1995). Such studies provide insight into the mechanisms of parallel communications and have been used as a basis for the present work. However, in these publications, the focus is on communications in a monocode context rather than for coupled applications. Issues

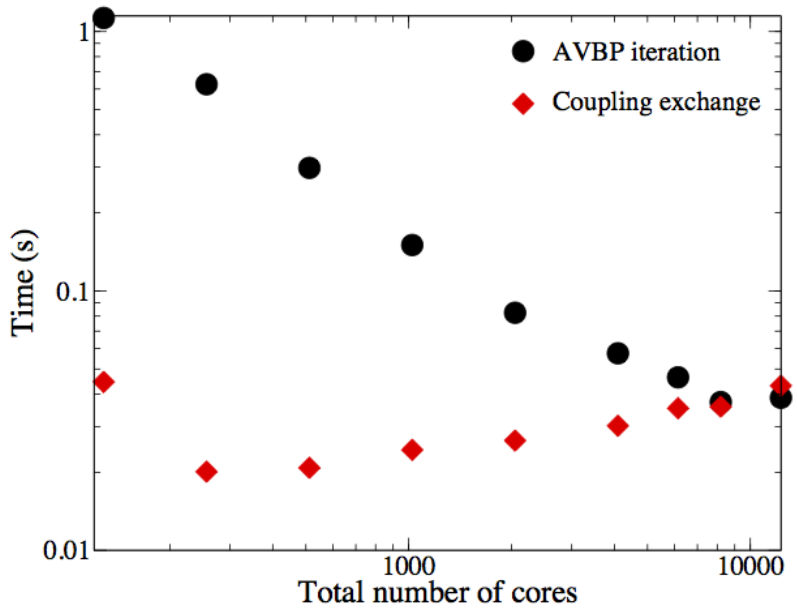

Figure 4.7: Comparison between the time required to achieve a fluid iteration (AVBP) and a coupling exchange (AVBP/AVTP) as a function of the total number of cores allocated to the simulation. From (Duchaine *et al.*, 2015).

of concern are thus relatively different and the results are clearly not directly applicable to the present framework although related in the long term.

In CFD, commonly used super-computers rely mostly on distributed architectures. Therefore, data are exchanged through parallel communications between the individual cores which are performed using the Message Passing Interface (MPI) environment. As a consequence, the present study only considers MPI type communications. The overhead cost induced by such communications between solvers involved in a coupling framework depends on many parameters. To identify them, the code to code communication is first analyzed on a very simplified toy model described below.

4.4.1 Toy description

The toy is composed of two identical codes. Each of these entities build a square including $npts_i$ points distributed on N_i cores where N_i is such that $N_i = m^2$, $m \in \mathbb{N}$. As detailed on Fig. 4.8, the partitioning is homogeneous, i.e. each square edge is cut in the same way (which justifies the need for a number of cores such that $N_i = m^2$). The codes are coupled using the OpenPALM software. At each iteration, each code sends data from every grid point. These data are then interpolated and received on the points of the other executable grid just like for a classic coupling exchange.

Before each communication phase, all the cores are synchronized using a MPI barrier. Exchange times are then measured with the *MPI_wtime* primitive. Both the initialization phase and the communication phase described in Section 4.1 are recorded separately. Since the present study only considers applications including non-moving meshes, a deep analysis of the initialization phase has little interest. The investigation focus is on communication times.

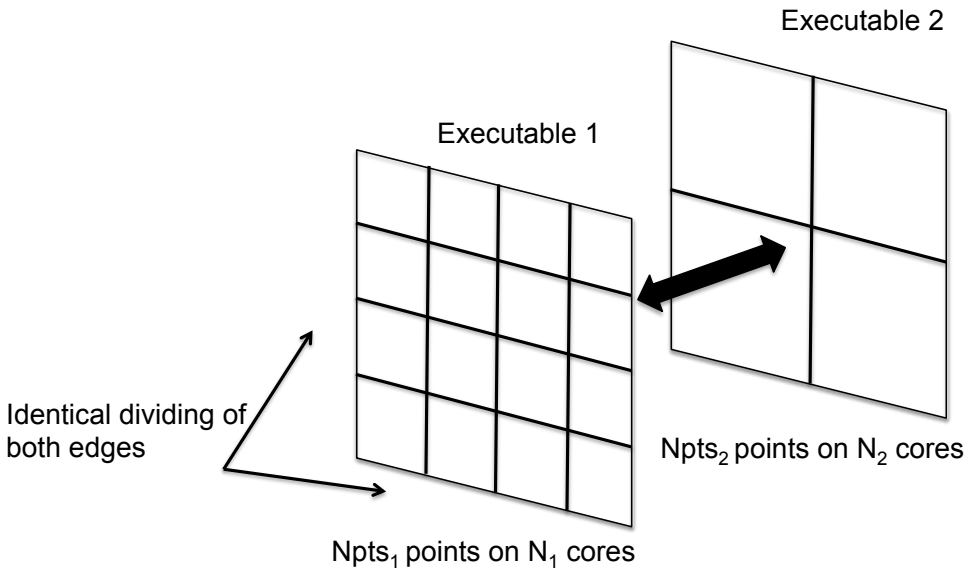

Figure 4.8: Schematic of the inter-code communication toy.

The influence of various parameters is considered:

- ▷ Data can be exchanged in a synchronous or asynchronous mode.
- ▷ The number of cores differs for each executable: $N_i = 1; 4; 9; 16; 25; 36; 49$.
- ▷ The total amount of data exchanged varies by power of ten for ranges that depend on the studied case. This parameter is controlled by the number of points on the grid $npts_i$.
- ▷ The data quantity per core is accounted for thanks to the simultaneous variation of the number of cores and the total amount of data. When the two codes are run on the same number of computing cores, the amount of data per core determines the size of the largest messages. A certain amount of smaller messages are sent at the interface points between cores. This is illustrated on an example in Fig. 4.9. The considered core from executable 1 has to send data to four different cores associated to executable 2: a large message including all the points (in red), and three smaller messages including only information on the points at the interface of the partitioning (in blue and green).

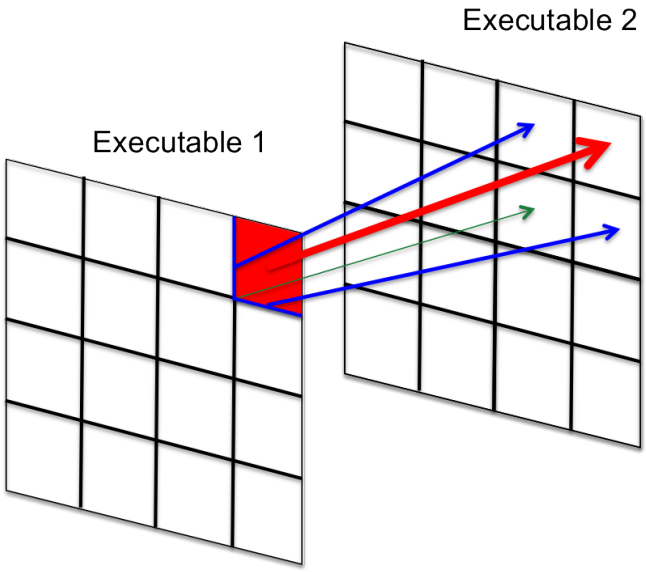

Figure 4.9: Schematic representation of the different messages sent by one core allocated to executable 1 to the cores of executable 2. The arrow thickness increases with the size of the message.

All the communication times presented below are averages performed over 100 ping-pongs (i.e. the two-way trip of a message between two cores). The results come from computations performed on Neptune, a CERFACS based BULL B510 supercomputer. Each computational node includes two processors, itself composed of eight cores. The Infiniband interconnection network offers a theoretical $5GB.s^{-1}$ bandwidth between nodes. The MPI latency is lower than 1 micro-second. For the present tests, MPI communications are performed thanks to the IntelMPI library.

Quantities referring to the first and second executables are respectively indexed with the subscripts 1 and 2. The number of cores is denoted N_i, and the total amount of data sent by a code (in bytes, B) is denoted $datatot_i$ and the quantity of data per core is given by $dataproc_i$.

4.4.2 Case $N_1 = N_2$

The influence of previously mentioned parameters on exchange times is first investigated on the simple case where the number of cores and the number of total grid points are identical for the two codes.

Influence of the communication mode

Two inter-code communication modes are available in OpenPALM: the synchronous and the asynchronous modes. Synchronous communications are based on a blocking primitive: the *MPI_Sendrecv* instruction. With this mode, each exchange is achieved per couple of cores. A "channel" is created between two cores which are thus fully involved in the communication (i.e. the cores can not communicate with other cores or perform different operations). The cores proceed then to the sendings/receipts before changing partner once the communication is completed. These communications are ordered, meaning that each core associates to the cores allocated to the other code following the natural order of process numbering. On the contrary, the asynchronous mode, allows to achieve the exchanges without order and more importantly without any need for synchronization or simultaneous availability of the cores involved in the exchange. As a result, sending and receipts can be achieved in any order and communications can overlap with other operations as long as these operations are independent of the exchanged variables. This mode of data transfer between cores relies on the *MPI_Isend* (sending) and *MPI_Irecv* (reception) primitives. Since these communications are fully non-blocking, the *MPI_wait* primitive is used to ensure communications completion before computing phases are performed. As suggested by Bar-Noy & Kipnis (1994), the difference between these two modes of data exchange may be compared to the difference between phone and mails. A phone conversation requires simultaneous awareness of both participants, none of them can call another one or do anything else before hanging up. On the contrary, one person can send several letters to several other persons without any concern about the reception of these mails.

The effect of the communication mode on the exchange time is investigated in Fig. 4.10 which indicates the evolution of the exchange time as a function of the total amount of data on each grid, for the $N_1 = N_2 = 49$ case, with synchronous and asynchronous communications.

In a logarithmic scale, both curves follow the same global evolution as a function of the global size of the data exchanged. However, whatever the case, synchronous communications are slower than asynchronous ones and this difference tends to increase with the total amount of data on the grid. This observation is directly linked to the working principle of the communication modes.

To explain this point, Fig. 4.11, extracted from Duchaine *et al.* (2015), shows the communication details between two codes on a similar toy than the one used for this study. Yellow traces indicate the communication paths, blue zones correspond to computations, red to the duration for which cores are involved in the communication loop and gray to core waiting. In synchronous mode, while some cores are exchanging data, a certain number of cores are idle and wait for their turn to communicate. As a result, the communication phase is very long. On the contrary, with asynchronous communications, waiting times are short since much more exchanges are performed at the same time. As the communication time increases with the size of data to exchange, the difference between the two modes of communication increases too. For brevity reasons, the toy

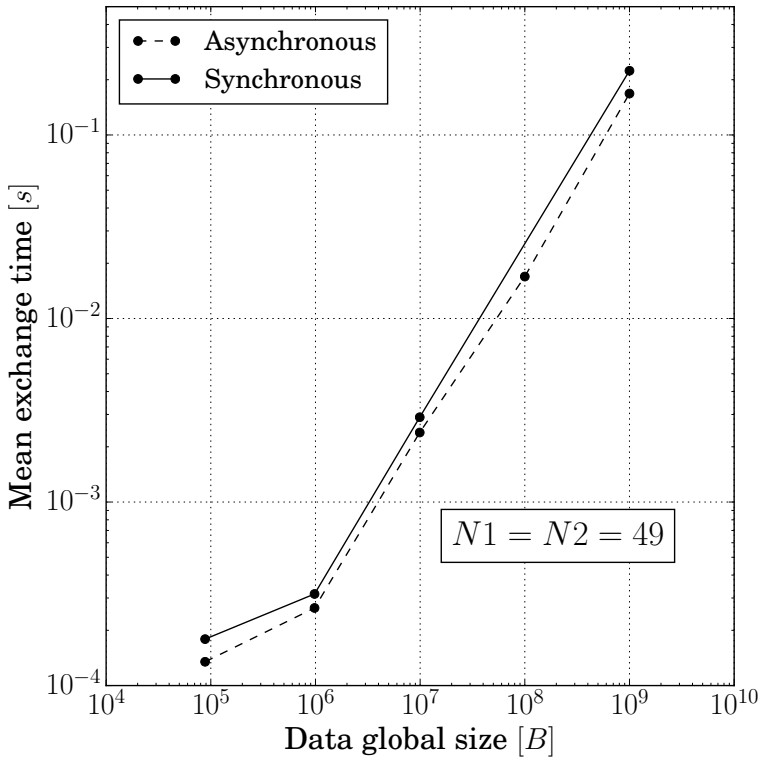

Figure 4.10: Evolution of the exchange time as a function of the global size of the problem for the case $N_1 = N_2 = 49$.

results are shown for the specific case $N_1 = N_2 = 49$. However, it is worth noting that the present conclusions are valid for $N_1 = N_2 = 9; 16; 25; 36; 49$. Below $N_1 = N_2 = 9$, the number of cores is so small that synchronous and asynchronous modes lead to very similar exchange times.

The communication scheme between the cores of each entity is easier to analytically determine for synchronous exchanges. Following investigations are thus based on this communication mode. Note that the global observations would remain the same with asynchronous communications.

Influence of the global size of the problem

The influence of the total amount of data on the grid is now investigated. Figure 4.12 shows the evolution of the exchange time as a function of the total amount of data on the grid, for different values of $N_1 = N_2$. The curves display the same behavior in logarithmic scale, and all present (except for $N_1 = N_2 = 49$) a discontinuous slope for an amount of data around 10^5 (around 10^6 for $N_1 = N_2 = 49$). Moreover, as expected, the exchange time greatly increases with the number of

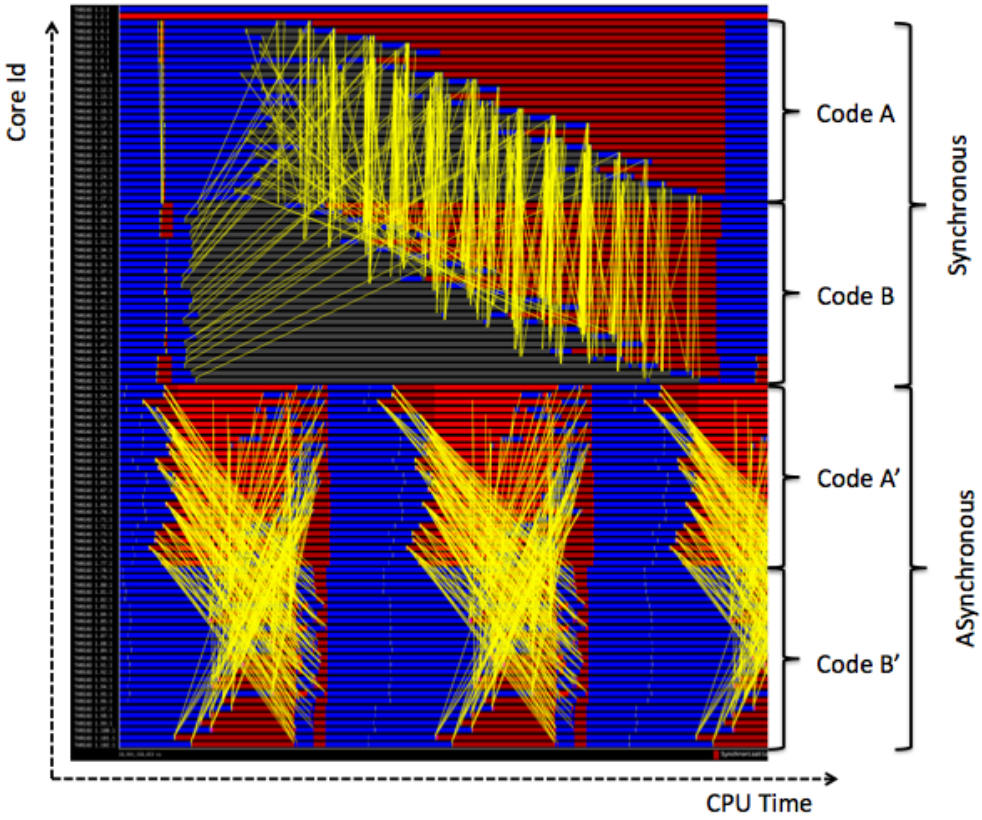

Figure 4.11: Visualization of synchronous and asynchronous routes and communication times. Yellow traces indicate the communication paths, blue zones corresponds to computations, red to communications and gray to core waiting. From (Duchaine *et al.*, 2015).

grid points. On the contrary, for a given number of grid points, the increase of the number of cores on which data are distributed tends to decrease the communication time. For the specific case where only one core is allocated to each executable, the exchange times are particularly higher than what is obtained for the other cases.

Influence of the data quantity per core

To explore the effect of the quantity of data per core on communications, Fig. 4.13 shows the communication times arranged here as a function of the data quantity per core. In the particular case where $N_1 = N_2$ (present case), this parameter corresponds to the size of the largest message that is sent (Fig. 4.9). This different representation of the same data highlights three groups of curves:

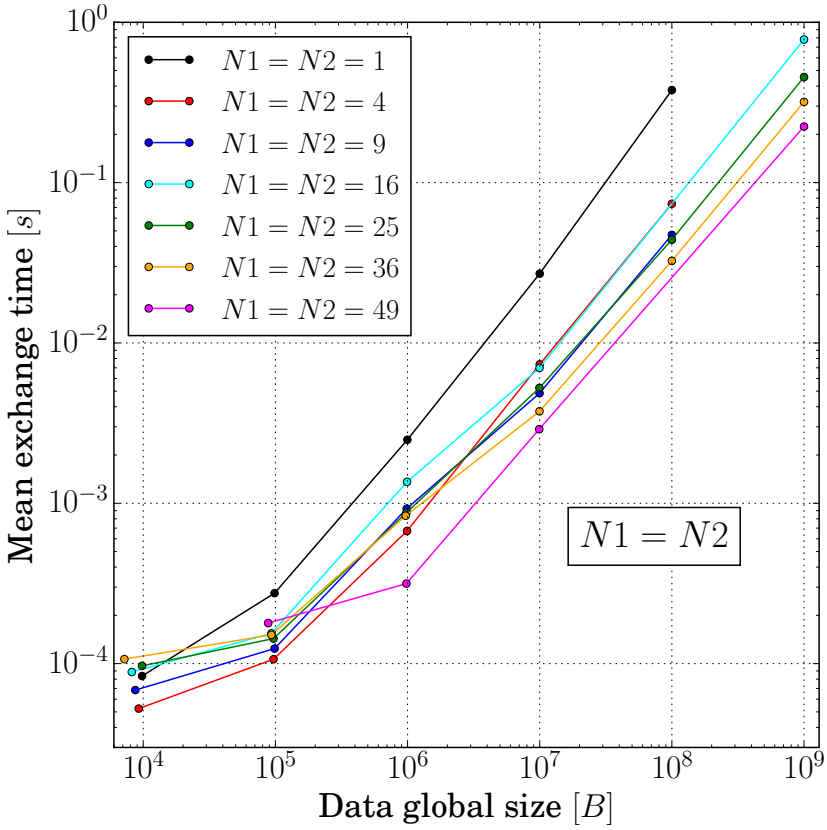

Figure 4.12: Evolution of the exchange time as a function of the total amount of data on the grid, for several values of the number of cores.

- $N_1 = N_2 = 1$ and 4
- $N_1 = N_2 = 9$
- $N_1 = N_2 = 16, 25, 36$ and 49.

These gatherings may be explained by the bandwidth variation between the various levels of the supercomputer network.

The bandwidth between two computing cores of a given machine depends on their relative positioning on the network as well as on the size of the exchanged message. The bandwidth can be measured thanks to a simple tool performing communications between various cores for a gradually increasing amount of data. These cores are placed either on the same processor or on the same node or on different nodes Fig. 4.14. Results obtained for the supercomputer Neptune with a

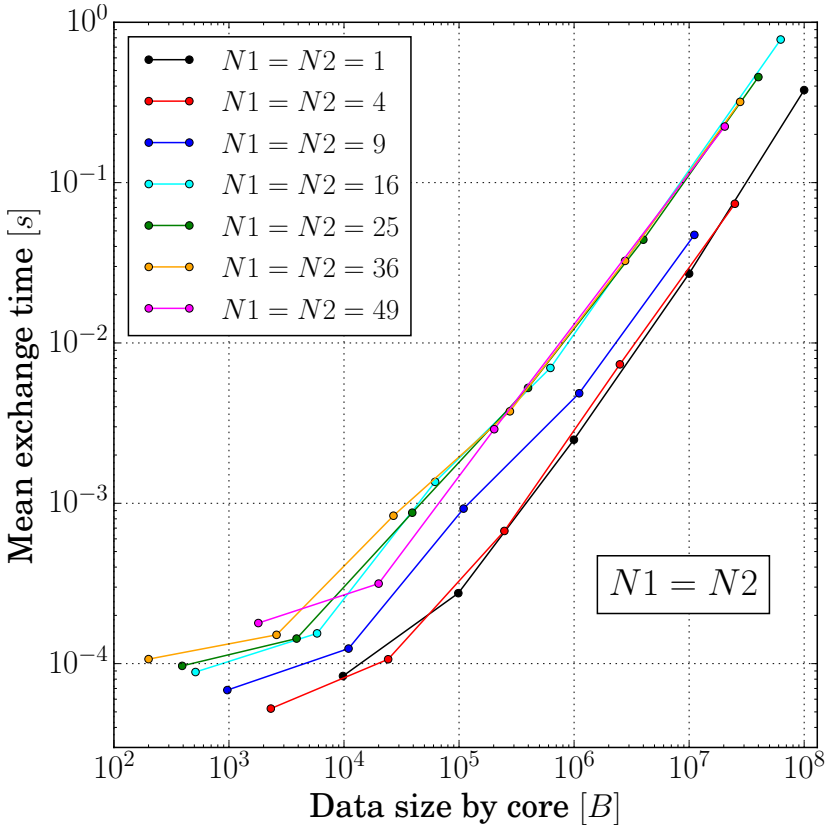

Figure 4.13: Evolution of the exchange time as a function of the data size per core, for several values of the number of cores.

specific tool provided by INRIA are presented on Fig. 4.15. As intuitively expected, whatever the message size, the smaller the distance between cores on the network, the higher the bandwidth. Besides, intra-processor and intra-nodes exchange speeds increase with the amount of data until a maximum is reached. Then the exchange speeds decrease to a plateau slightly above 10^7 bytes. On the opposite, the inter-node speed increases gradually towards a constant value. Bandwidth values provided by supercomputer manufacturers refer to the plateau observed in the curves of Fig. 4.15[2].

Going back to the curves observed in Fig. 4.13, three cases can be distinguished:

- $N_1 = N_2 = 1$ and 4: the cores are distributed on the two processors of a same node. Indeed, core repartition is distributed between processors, meaning for example that if only two

[2]In the Neptune case, the difference between the theoretical inter-nodes bandwidth (5 GB/s) and the value highlighted by these tests ($\simeq 3$ GB/s) is about 2 GB/s

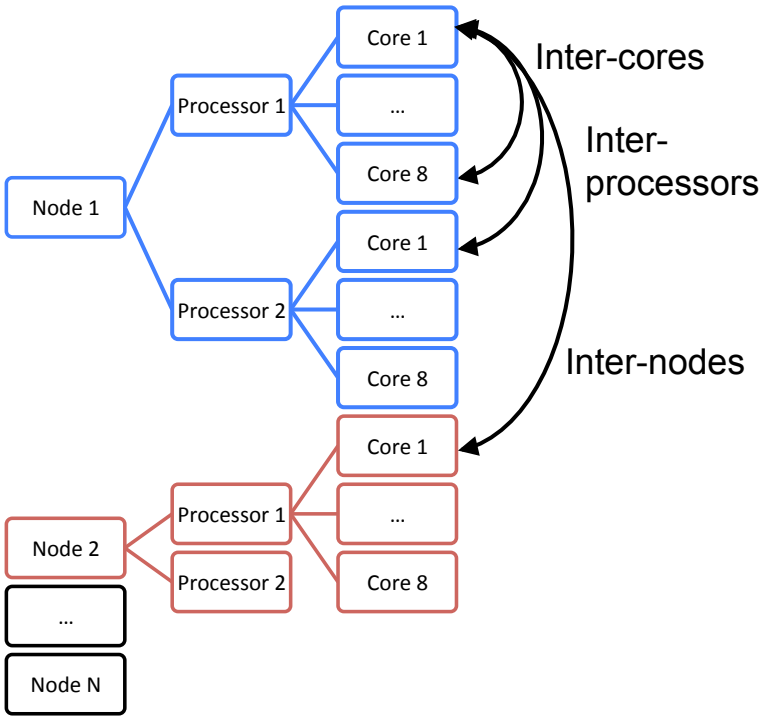

Figure 4.14: Partial schematic of the different network levels of Neptune.

cores are requested, the machine places each of them on a different processor of the same node. Communications are thus achieved within the same node but on potentially different processors. They are thus relatively fast but very dependent on the exchanged message size.

▷ $N_1 = N_2 = 9$: the cores are mainly placed on the same node, only three cores are on a different node. Even though most of the communications are intra-processor or intra-node, some exchanges are made between cores from different nodes.

▷ $N_1 = N_2 = 16, 25, 36$ and 49, the cores are distributed on several nodes (3 to 7 nodes depending on the case). A large part of the communications (if not all) is happening between nodes. Most of the communications are thus made between cores that are quite far from each other on the network resulting in slower exchanges.

These different repartitions of the cores on the computer communication network can explain the three different types of behavior observed on Fig. 4.13.

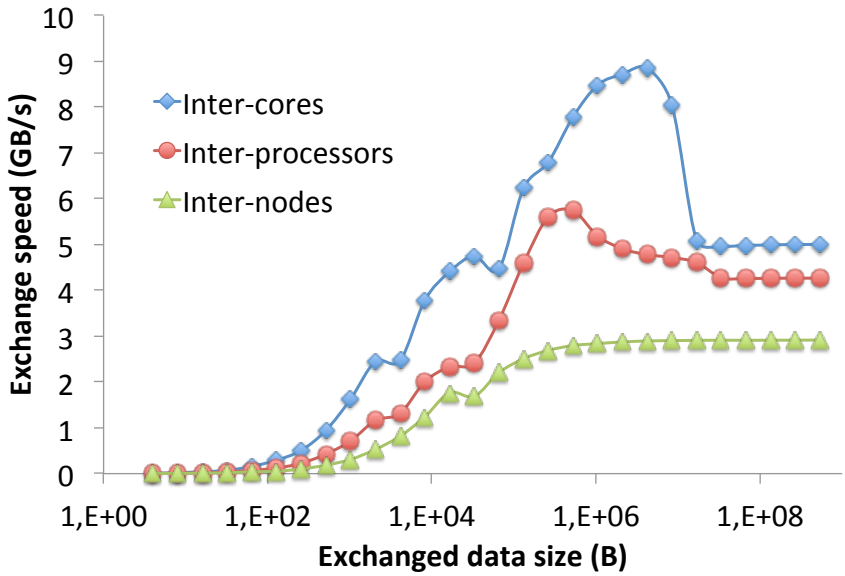

Figure 4.15: Data exchange speeds on Neptune as a function of their size, for three different levels of communication.

Problem equation

A model is now produced to predict the exchange times obtained with the toy from supercomputer characteristic inputs. This model is not an end in itself, however, its allows to better highlight the components underlying coupled communications. The proposed model takes into account six parameters:

- ▷ the total amount of data exchanged $datatot$,
- ▷ the number of cores N,
- ▷ the supercomputer latency (assumed to be constant), denoted L and equal to $1\mu s$ for Neptune,
- ▷ the longest distance present in the communication network hierarchy (intra-processor, intra-nodes or inter-nodes) E_{max},
- ▷ the unitary time associated to a sending/receipt t_{sr}^{unit} whose determination is detailed below,
- ▷ the number of communication stages denoted $f(N)$ and whose meaning is explained below.

Determination of the number of communication stages $f(N)$

Consider the case for which $N_1 = N_2 = 16$. The cores allocated to code 1 and 2 are noted

respectively with the letters A and B and numbered from 0 to 15. The grid distribution over these cores is shown in Fig. 4.16. Since $N_1 = N_2$, the grid partitionings are similar for both codes. As previously explained on Fig. 4.9, a given core of executable 1 has to communicate data with all the cores allocated to executable 2 sharing one or more points on the grid. For instance, core A0 must exchange data with cores B0, B1, B4 and B5, core A1 needs to communicate with B0, B1, B2, B4, B5 and B6 and so on (Fig. 4.16). As a reminder, the synchronous blocking mode of communication is used here. Therefore, knowing that the communication loop follows the natural order of process numbering, and assuming that for given values of $N_1 = N_2$ and *datatot*, all the communications take the same time[3], a detailed scheme of the communications can be produced. This scheme is shown in Fig. 4.17 for the example $N_1 = N_2 = 16$. Each column corresponds to one of the 16 cores allocated to executable 1 and is filled with the core of code 2 involved in a communication with this core. For instance, in column A0 the cores B0, B1, B4 and B5 are listed since only these cores share points with A0. Then, on the same line are placed the communications that can overlap while a new line is used whenever a communication can not be performed until one of the communications on the current line is completed. From this, it is then possible to deduce the total number of communications that cannot be achieved at the same time ($f(N) = 25$ for the example of Fig. 4.17). That number will be referred to in this document as the number of communication stages and is a key parameter of the proposed model. For $N_1 = N_2 = 1$ and $N_1 = N_2 = 4$, this quantity is respectively equal to $f(1) = 1$ and $f(4) = 7$. When $N_1 = N_2 > 4$, the number of communication stages is governed by the following law (determined empirically):

$$f(N) = 8\sqrt{N} - 7 \tag{4.12}$$

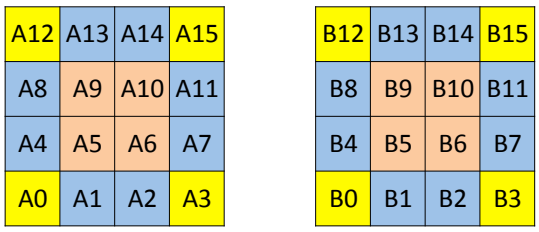

Figure 4.16: Schematic representation of the grids partitioning for code 1 (left) and code 2 (right).

Determination of the unitary time associated to a sending/receipt $t_{sr}^{unit}(datatot, N)$

The detailed communication scheme has been built under the assumption that for given values of $N_1 = N_2$ and *datatot*, all the communications take the same time. This specific time has thus to be determined to serve as an input for the model. Knowing the bandwidth evolution G (Fig. 4.15)

[3]This assumption is strong since it has already been demonstrated that the exchange time greatly depends on the message size and this size vary depending on whether or not the data are send for the entire grid points considered or at the interfaces only (Fig. 4.9).

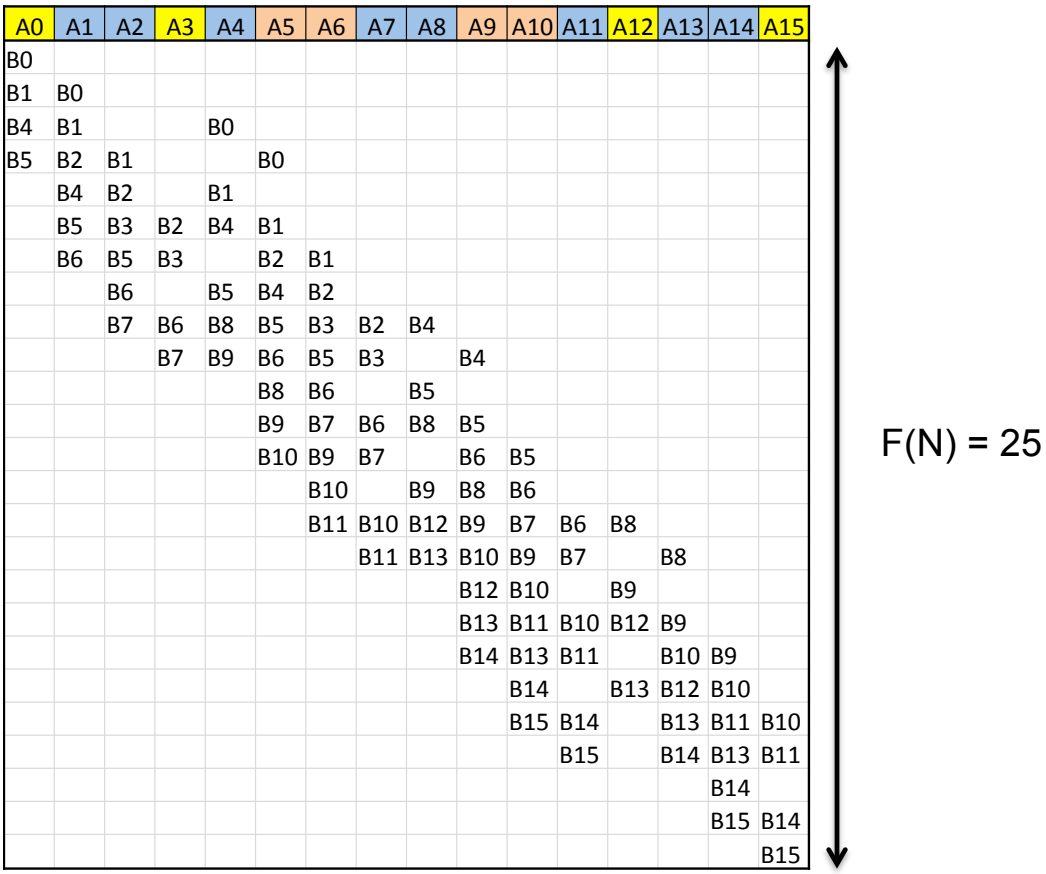

Figure 4.17: Detailed scheme of the communications between cores allocated to code 1 and 2 for $N_1 = N_2 = 16$.

with message size, the variation of the time required to perform one exchange as a function of the message size is easily obtained and is shown in Fig. 4.18. For the present model, the unitary time of sending/receipt, is deduced from Fig. 4.18, by considering the maximal amount of data to be transmitted in one message $(\frac{datatot}{N})$. In other words, all the messages are assumed to have the size of the biggest message to be sent. The choice of the curve used, as a function of the value $N_1 = N_2$ is made so as the used curve refers to the largest distance between the computing cores of the two codes. As a result, to model communication times for $N_1 = N_2 = 1$ or 4, the inter-processor exchanging speed curve is considered while the inter-node curve is used for the other cases. In practice, the time required to perform one exchange as a function of the message size is approximated by two different polynomial laws (one below 10^6 B denoted small and an other one above 10^6 B denoted large). These are shown in Fig. 4.18.

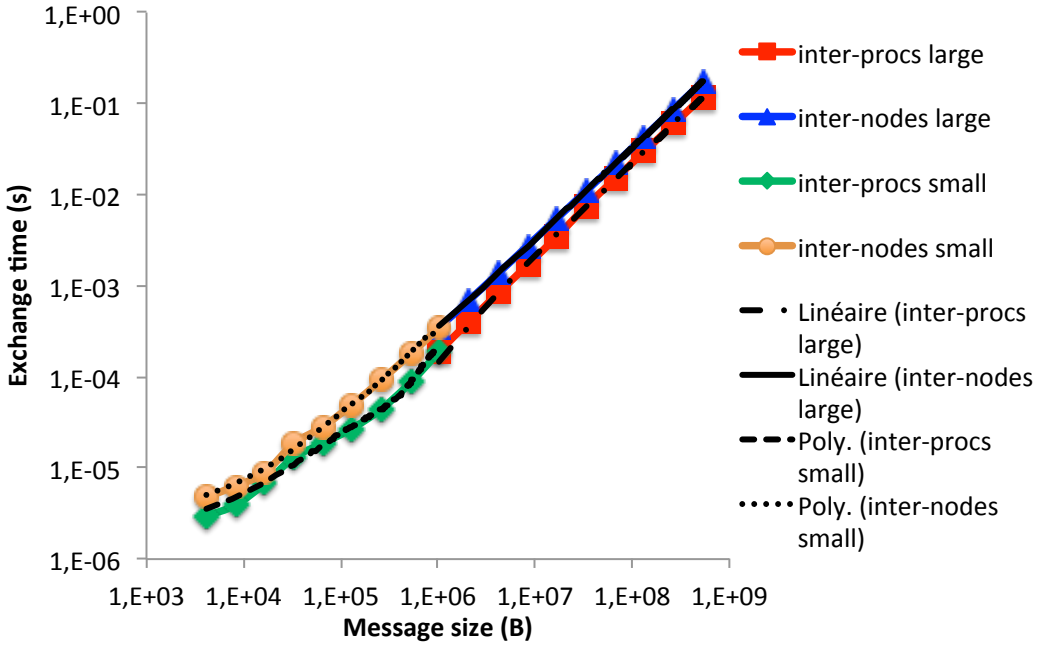

Figure 4.18: Data exchange times on Neptune as a function of their size, for two different levels of communication. Curves are denoted small for message sizes below 10^6 *B and large above* 10^6 *B.*

Proposed model

The communication time T between the cores allocated to the two codes is equal to the sum of the latency times T_L plus the sum of the data sending/receipt times noted hereafter T_{sr}.

Knowing the number of communication stages, the total time linked to the latency T_L is given by:

$$T_L = f(N) \times L. \tag{4.13}$$

In the same way, the total sending/receipt time T_{sr} equals:

$$T_{sr} = f(N) \times t_{sr}^{unit}(datatot, N) \tag{4.14}$$

Finally, the toy communication time predicted by the model reads:

$$T = T_L + T_{sr} = f(N) \times L + t_{sr}^{unit}(datatot, N) \times f(N) \tag{4.15}$$

Comparison between the toy and the model results

Figures 4.19 and 4.20 present the evolution of the exchange time as a function of the total amount of data on the grid for various numbers of cores. Results provided by the toy (solid lines) and the model (dashed lines) are compared. The model provides globally a fairly good approximation

of the exchange times. The less accurate results are obtained for the limit cases of a very low number of cores $N_1 = N_2 = 1$ or 4. In these cases, the model systematically underestimates the communications time. For low numbers of computing cores, few communications are performed, enabling the preponderance of other effects than nominal latency and actual communication times which can slow down the exchanges. Leaving aside these limit cases, the model predictivity is very good for a global amount of data above 10^7 B which interestingly corresponds to the bandwidth plateaus observed in Fig. 4.15. The influence of the number of cores (i.e. the sorting of the curves) is correctly predicted (see zoomed view in Fig. 4.20). Nonetheless, the exchange times scattering when varying the number of cores, is slightly underestimated by the model. Finally, the noticeable change of slope observed for the toy results for a global amount of data equal to 10^5 B is also predicted by the model. Though, for some cases, an additional modification of the slope is observed in the model results for 10^6 B. This specific feature may be attributed to the use of two different polynomial laws to determine the unitary time associated to a sending/receipt for a global amount of data below or above 10^6 B.

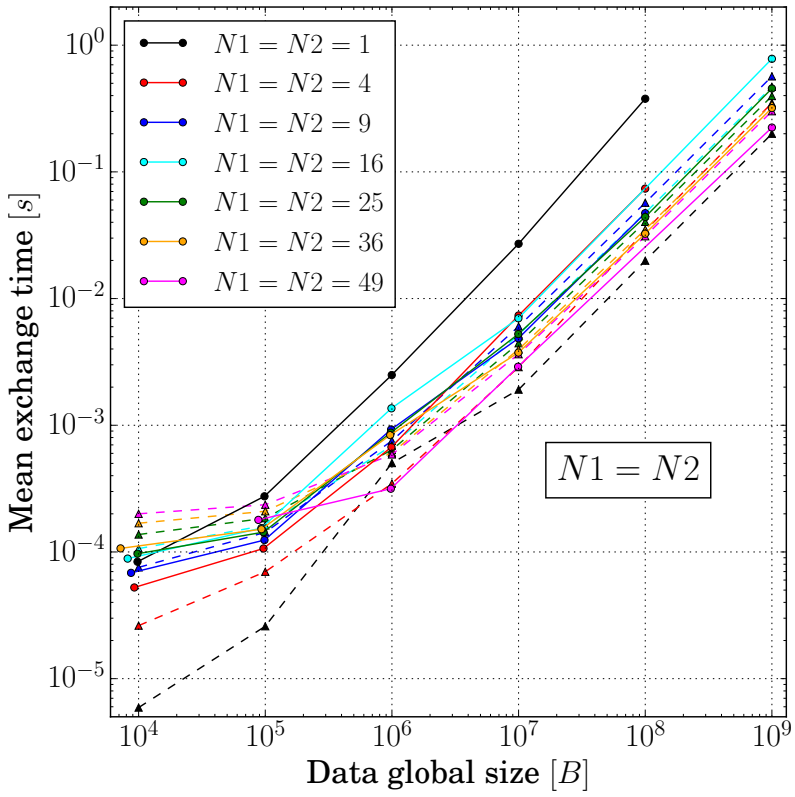

Figure 4.19: Evolution of the exchange time as a function of the total amount of data on the grid, for various numbers of cores. In solid lines, are the results from the toy and in dashed lines the results obtained with the model.

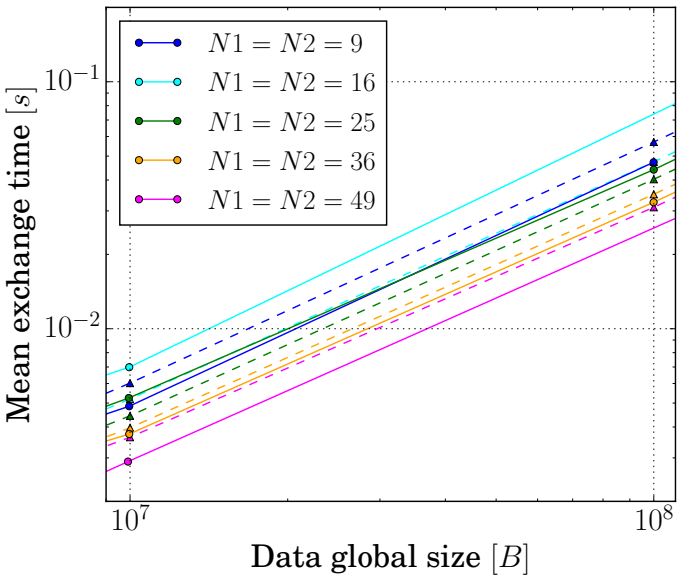

Figure 4.20: Evolution of the exchange time as a function of the total amount of data on the grid, for various numbers of cores. In solid lines, are the results from the toy and in dashed lines the results obtained with the model. Zoom on the range $[10^7 ; 10^8]$ for some values of $N_1 = N_2$.

The model proposed here allows to decompose the components of the communication time. Besides, it provides an improvable but still interesting evaluation of the communication times between the toy codes and is able to reproduce most phenomena highlighted by the toy. However, those results are machine dependent. The achievement of the same battery of tests on another supercomputer would be necessary to improve this model and assess its validity on different architectures. However, all the features evidenced here are determined by the machine characteristics and the coupled application and can not be changed or improved. The ultimate purpose is not the production of a universal model but instead the understanding of the underlying processes involved in coupling exchanges to identify some good practices and more importantly paths of improvements of the current coupling methods. Such goals are addressed in the following.

4.4.3 Case $N_1 \neq N_2$

In a real coupled application, the exchange interface between two codes is rarely partitioned in the same way and/or distributed over the same number of computing cores. To investigate this point, the toy is run for cases where the number of allocated cores is different for each executable ($N_1 \neq N_2$). These tests are performed for every possible N_1 and N_2 value combinations. The global tendencies remain the same for all cases. Therefore, for brevity, Figs. 4.21 and 4.22 present only the results for the cases where $N_1 = 16$ or $N_1 = 25$ respectively and $N_2 = 1; 4; 9; 16; 25; 36; 49$. Exchange times are plotted as a function of the total amount of data on the grid. The legend also

indicates the number of communication stages, f, associated to the different combinations of N_1 and N_2. Exchange times evolve within the same range as those presented for the case $N_1 = N_2$ (Fig. 4.12) and increase globally in the same way with the total amount of data. However, it is worth noting that for every tested case, given a fixed number of cores N_1, every values of N_2 different from N_1 leads to communication times superior or similar to the $N_1 = N_2$ case.

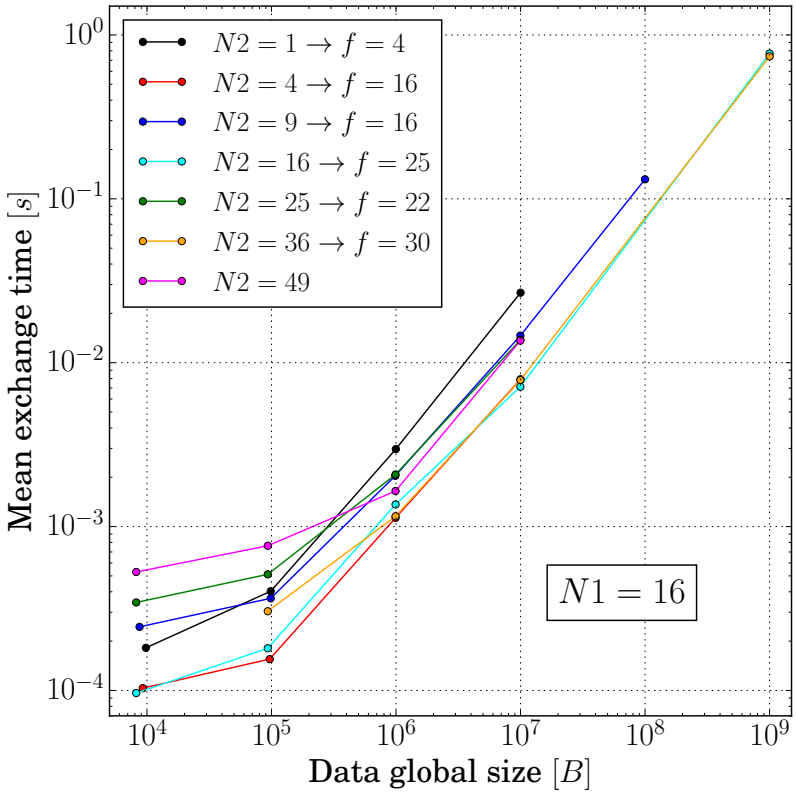

Figure 4.21: Evolution of the exchange time as a function of the total amount of data on the grid, for $N_1 = 16$ and different values of N_2. The legend also indicates the number of communication stages f corresponding to the N_1 and N_2 combinations.

The extension of the previously proposed model to the general case where $N_1 \neq N_2$ raises two kind of issues. First, some parameters such as the total amount of data on the grid or the number of cores are different for each executable, hence these variables are duplicated. It is then necessary to adapt the model, either by including both variables or by taking into account an average value. Moreover, the number of communication stages (indicated in the legend in Figs. 4.21 and 4.22) does not seem to be sufficient (or even adapted) to accurately mimic the impact of the number of cores on communication times. Indeed, considering for instance, two cases with the

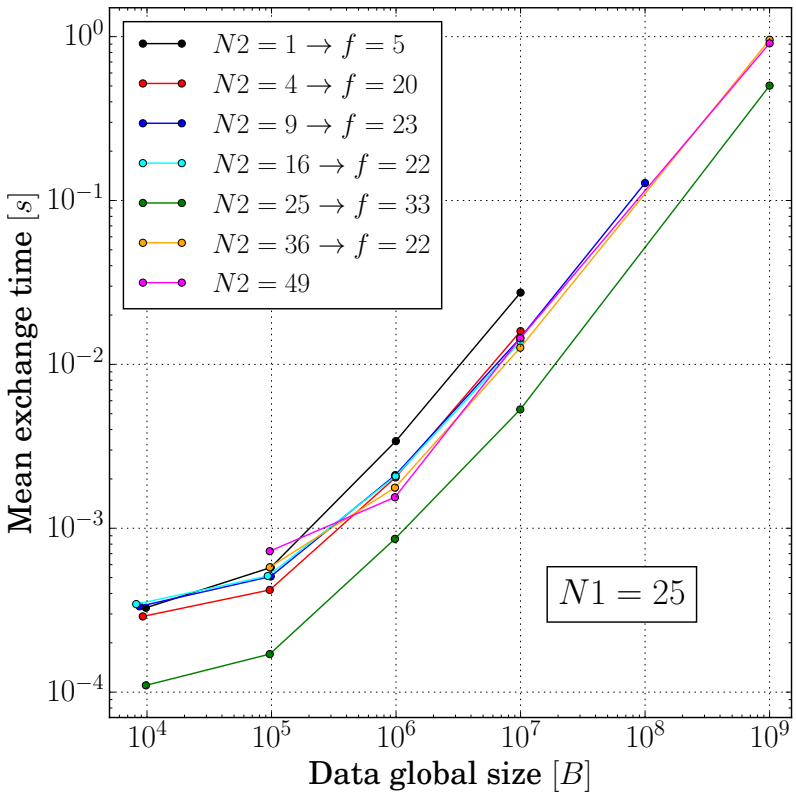

Figure 4.22: Evolution of the exchange time as a function of the total amount of data on the grid, for $N_1 = 25$ and different values of N_2. The legend also indicates the number of communication stages f corresponding to the N_1 and N_2 combinations.

same maximal distance between cores in the network (i.e using the same bandwidth evolution as input for the model), the case $N_1 = 16$ and $N_2 = 25$ (green curve in Fig. 4.21) has a lower number of communication stages ($f = 25$) than the $N_2 = 36$ case (yellow, $f = 30$), but presents longer communication times whatever the amount of data on the grid. The results presented in Fig. 4.22 are even more convincing: the larger value of f is obtained for $N_2 = 25$ whereas this case depicts exchange times smaller than all other cases. As a result, if the same concepts are used to adapt the model from the $N_1 = N_2$ cases to the $N_1 \neq N_2$ cases, the model will not sort correctly the curves, hence leading to wrong results.

Although not easy to model, the current results highlight some very interesting features. Indeed, for $N_1 = 16$, the three most favorable cases in terms of low exchange times are found for $N_2 = 4$, $N_2 = 16 (= N_1)$ and $N_2 = 36$. These cases correspond to partitionings of the two executable grids that are either identical or quite coincident (hence minimizing the number of communications

required between the two codes). To further investigate this point, Fig. 4.23 shows the evolution of the communication time as a function of the total amount of data for three different cases. For each of them, the relative positions of the partitioning are indicated on the top of the figure. Identical and quite coincident partitionings show similar communication times, whereas totally non-coincident partitionings induce systematically longer exchange times whatever the amount of data on the grid. Therefore, to accurately predict exchange times, a performance model should include a criteria linked to the partitioning concordance at the coupled interface. More importantly, an intelligent partitioning of both domains with respect to each other could lead to lower exchange times and hence better performance of the coupled simulations. To conclude, according to these observations, future work should focus on the development of co-partitioning techniques able to decrease greatly the communications time between solvers. The development of such co-partitioning algorithms is currently under study within the HiePACS team of the INRIA laboratory (Predari & Esnard, 2014).

4.4.4 Towards realistic thermally coupled problems

Previous analyses confirmed that to optimize the computing core distribution among different entities of a real coupled application, it would be theoretically necessary to consider simultaneously internal computational times and exchange times. Still, methodology described in Section 4.3 is directly applicable to real coupled problems but things are more complicated. Indeed, in the present application, an implicit formulation is applied to solve the heat equation in the solid. As a consequence, the variation of the number of sub-iterations required to converge the matrix inversion leads to variable time per iteration. This variability has been investigated on the CHT simulation of an industrial burner discussed in Part III. If the solid is converged for given boundary conditions, the time per iteration converges to a fixed range. Still, when the fluid and solid solvers are coupled, solid boundaries are constantly updated by the fluid and time per iteration does not rapidly stabilize. Therefore, a mean value of the solid solver time per iteration is used as an input to solve the load balancing problems of internal computational times. Valuable future developments could include a dynamic approach for core distribution to compensate this issue.

Focusing now on the communication time and to avoid CPU resource waste, one should carefully look at the exchange times obtained with the load balancing determined from the internal computational time. Indeed, an additional difficulty for the core distribution optimization, comes from the two components (internal and communication times) being potentially in competition. This point is highlighted on the previously discussed fluid/solid (AVBP/AVTP) coupled case of the Turbomeca burner (Duchaine *et al.*, 2015). For this simulation, the computation of one fluid iteration requires to perform more operations than one solid iteration. The fluid performs 20 iterations between two coupling events whereas the solid is advanced in time for one iteration. As a result, the fluid solver is largely more CPU consuming than the solid solver. Considering

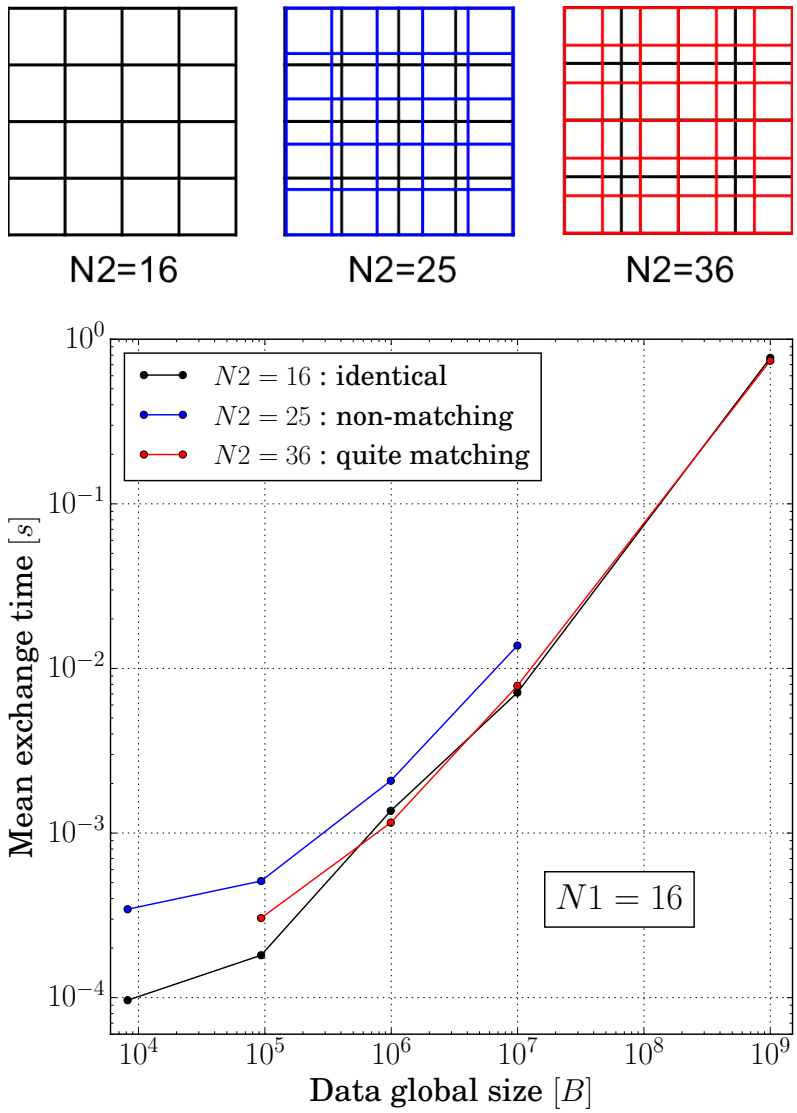

Figure 4.23: Evolution of the exchange time as a function of the total amount of data on the grid, for cases where the partitioning of the two executables is either identical, or quite coincident, or totally non-coincident.

each solver internal computational time, the load balancing requires to allocate many cores to the fluid computation and much less to the solid one. In order to evaluate the impact of that kind of distribution on the communication times, Fig. 4.24 shows the exchange time as a function of the ratio between the number of cores allocated to the fluid and those allocated to the solid (in abscissa) as well as the total number of cores involved in the exchange (which increases with the bubbles size). The total number of exchanging cores (indicated with the bubbles size) does not have a leading role in the variation of the communication times. Instead Fig. 4.24 highlights two

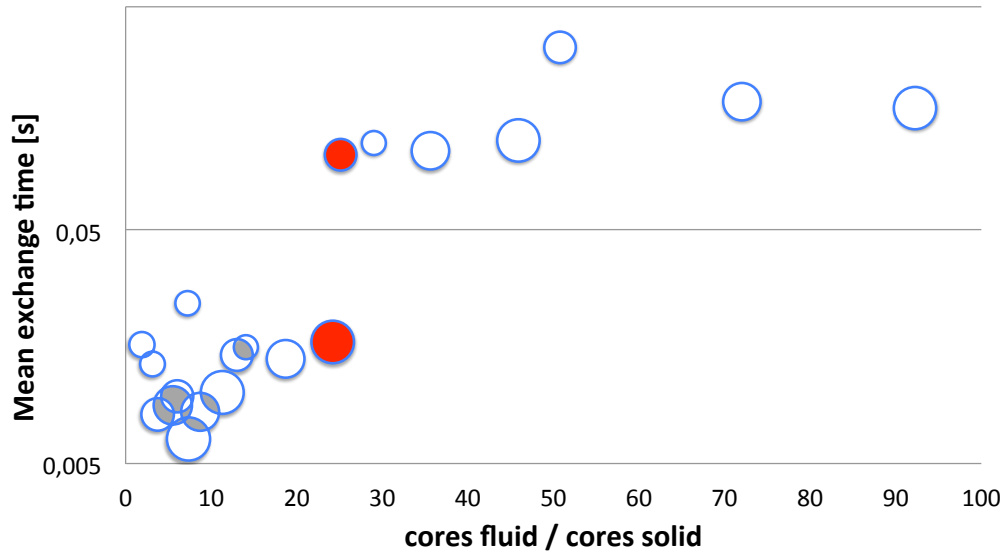

Figure 4.24: Evolution of the exchange time as a function of the ratio between the number of cores allocated to the fluid and the number of cores allocated to the solid (abscissa) and the total number of cores involved in the exchange (increasing with the bubbles size). Data extracted from (Duchaine *et al.*, 2015)

kinds of behaviors as a function of the ratio between the number of cores allocated to the fluid and the solid:

- ▷ short exchange times ($< 0,005s$) for ratios ranging from 1 to 24,
- ▷ longer exchange times ($> 0,005s$) when the ratio is beyond 25.

Interestingly, two points (colored in red in Fig. 4.24) exhibit very close core ratios, 24 and 25 with very different communications times around 0.017 and 0.105. Neither switching the rate from 24 to 25, nor the corresponding total number of cores can explain by themselves the differences in the communication time between the two cases. Other underlying parameters are involved. This difference could, for instance, come from the relative code partitioning previously highlighted on the toy which further emphasizes the need for coupling-aware partitioning techniques.

From all the previous results, it is clear that both the internal computational time and the communications should be taken into account when distributing cores between the solvers involved in a coupled application. However, improvements are still required to deal with external communications in a clever way. In practice, for all the applications discussed in the present manuscript, a first guess of the optimal core distribution is determined through the load balancing equations (Eq. (4.11)). Adjustments are then performed thanks to specific timers installed within the coupled

applications. Note that these times record at the same time waiting and external communication times and do not provide any information on their respective impact.

4.5 Conclusion

The restitution time and CPU cost of a coupled simulation are determined both by the internal computational time of each code and by the communication time between solvers. Knowing the computational time required to perform one iteration for each code (or a mean value when this quantity evolves in time), it is easy to distribute the load between the computing cores available for the simulation. The optimal distribution is given by the equations presented in the first section of this chapter and can be applied as such for the implementation of realistic coupled applications. Including the effect of the data exchange time is much more complex. This is why this component has been studied on a simplified toy model. Many parameters can impact the toy communication times, such as the number of cores, the communication mode (synchronous or asynchronous), the global size of the exchanged fields or the amount of data per core. A first model has been proposed, taking into account these parameters as well as machine diagnoses, for the simplified case where the number of cores is identical for each code ($N_1 = N_2$). Its extension to the case where $N_1 \neq N_2$ is not trivial. Indeed, new variables and new parameters are involved. The results obtained with the toy for this case and on additional coupled simulations of an industrial burner, allowed to identify parameters that strongly influence the communication times such as the partitioning coincidence and the disparity of the computing core distribution between codes. An evolution of the current coupling techniques through dynamic core distribution or co-partitioning techniques is to be considered. The latter is currently under study within the HiePACS team of the INRIA laboratory.

Conclusion

In this first part, the various issues which needs to be addressed to perform highly performant multi-physics coupled simulations of a burner thermal state have been successively discussed. The different nature of the three physics at play, namely combustion, solid conduction and radiation have been recalled as well as the various resolution approaches retained for the present study. A high-fidelity resolution of the reactive flow is obtained through the use a DNS/LES approach. Such a technique induces however important computational costs which require to be handled correctly in a multi-physics context to ensure a high performance of the coupled application. Besides, for the real industrial burner computations proposed in Part III, the LES resolution of the viscous wall region is computationally unaffordable and a model will be introduced. The heat equation is solved in its unsteady form and a DOM formalism is used to solve the radiative heat transfer. To perform such radiation computations at an affordable computational cost, the spectral dependency of radiant species is taken into account via a global spectral model.

To provide a solution to the coupled thermal problem, the numerical treatment of the various interactions between all these sub-systems have then been detailed. For this purpose, the global thermal problem have been decomposed into three smaller multi-physics problems including two sub-systems and their interaction. The numerical resolution of the CHT, RFTI and RSTI have thus been considered separately. To solve the CHT problem, solvers are desynchronized in time, allowing to obtain mean quantities representative of the thermal permanent regime at a reduced CPU cost. Note that such a temporal desynchronization between the fluid and the solid domains is equivalent to a decrease of the solid quantity ρC. Interface variables between the flow and the solid conduction solvers are set with Dirichlet-Neumann boundary conditions, ensuring both stability and high convergence rate for the coupled methodology retained (high coupling exchange frequency). For the RFTI and RSTI simulations, the treatment of physical time is intrinsically different. Indeed, radiation adapts instantaneously to the flow and wall conditions and the update of the radiative fields is thus set in accordance with the fluid and solid fields evolution. In RFTI simulations, interface variables from the fluid are imposed in the radiative solver through the dependency of radiative properties on fluid properties while the radiative source term is directly imposed in the fluid energy equation. Finally, the interface variables of RSTI simulations are set just like for the CHT computations with Dirichlet-Neumann boundary conditions.

The last issue investigated in this part concerns the CPU cost mismatch between the various solvers involved in coupled simulations. To ensure high performance of the coupled application, the consideration of both the internal computational time of each code and the external communication time between solvers is required. While an optimal distribution of the computing resources between the codes can easily be approximated through simple equations when considering only the internal computational time, inclusion the external communications is not straightforward. This last point has thus been studied separately on a toy model and realistic coupled simulations of an industrial combustion chamber. The results, allowed to identify parameters of importance for the communication times and evidenced in particular the negative effect on performance of a too large imbalance between the number of cores attributed to different solvers as well as the great potential of co-partitioning techniques for performance gains.

The specific framework and methods discussed in this part are then employed to analyze the thermal state and the physical interactions between the different sub-systems in two different burner devices in the two following parts of this manuscript.

Part II

Thermal state detailed analysis of a bluff-body stabilized laminar premixed flame

Introduction

The first multi-physics problem considered in the present manuscript is the thermal state of a physically practical burner device. The configuration consists of a laminar premixed flame stabilized thanks to a squared body in a channel flow (Kedia & Ghoniem, 2014*a*,*b*, 2015). Such an academic configuration although more representative of some canonical laboratory burners than industrial aeronautical combustors allows deeper understanding and identification of the phenomena involved and their interactions. In particular, the choice of studying at first a laminar regime arises from three specific constraints:

- ▷ First, the absence of turbulence in the channel flow allows to resolve the problem thanks to 2D computations that are physically relevant which reduce the CPU cost of the simulations. As a result, the influence of various physical and numerical parameters can be investigated on a large range of values without CPU availability restrictions.

- ▷ Second, DNS are clearly affordable without any need of flow modelisation. When considering non-canonical turbulent flows, DNS are hardly achieved and models are required which raise issues on the effect of turbulent combustion modeling and near-wall treatment. Such modelisation issues clearly make the result interpretations more complex and care is required. The low Reynolds number of the present simulation allows to decouple the additional complexities of turbulent flow resolution. Simplifications are limited to the chemistry modelisation through a reduced kinetic scheme (detailed hereafter in Chapter 5).

- ▷ Third, since the flow is naturally stationary in such a configuration, the variables exchanged at the fluid-solid interface when performing coupled simulations do not contain any frequency. Therefore, no potential bias inferred by the time desynchronization process highlighted in Section 3.1.1 can be introduced in the present simulations.

Because of their large field of application and use for academic studies or model development, bluff-body flames are widely documented in the literature. In particular and as detailed just below, chemical and aerodynamical aspects have been extensively investigated. Such a large already existing body of knowledge on bluff-body based combustion devices allows to build the present result understanding while exploiting previous findings from various authors and to focus on thermal

related issues. Bluff-body flames rely on a simple principle: introduction of an non-streamlined object in a reactive flow to create just downstream of the body a recirculation zone of burnt gases. These recirculating hot gases that constantly heat up the fresh mixture to the ignition point help maintaining the flame nearby the obstacle. For this specific reason, this object is often called a flame holder. When it comes to stabilization matters, most early studies (1940s – 1950s) seek to determine flame holder stability limits; meaning the range of fluid and/or flame holder parameters for which the flame does not blow-off (Williams & Shiman, 1953; Kundu *et al.*, 1977, 1980; Kiel *et al.*, 2007; Fan *et al.*, 2013). It was shown that two parameters are of primary importance: the fresh mixture equivalence ratio and the incoming flow velocity. Various studies concluded that the incoming velocity ensuring a stable flame is maximum close to stoichiometry, while the limits of stability in terms of maximum and minimum equivalence ratio are wider as the incoming velocity decreases. Aside from these two major parameters, the influence of the blocking ratio, pressure, fresh mixture temperature, fuel type as well as various fluid and geometric parameters were extensively studied to assess their impact on flame stability. Some of the studies conducted in the middle of the last century are listed by Williams & Shiman (1953). Beside experimental results, some attempts to produce a generalized theory of flame stabilization behind bluff-bodies can be found, for instance in Longwell *et al.* (1953) or Kundu *et al.* (1977, 1980). These theoretical analyses rely on the understanding of the central role of the recirculation zone on flame stability. Once the flame exists, it is maintained if heat exchange from the recirculation zone to the fresh reactants is in equilibrium with the heat gained by the recirculation zone from the flame (Kundu *et al.*, 1980). Therefore, flame stability is strongly dependent on the recirculation strength and to some extent on heat transfers.

While early studies focus mostly on aerodynamic and chemical aspects, recent publications can be found solving the Conjugate Heat Transfer (CHT) between the reactive flow and flame holder solid material (Fan *et al.*, 2013; Kedia & Ghoniem, 2014*a*,*b*). In these studies, the solid thermal properties are shown to have a significant effect on the flow features (Fan *et al.*, 2013; Kedia & Ghoniem, 2014*a*) and dynamic response to periodic excitation (Kedia & Ghoniem, 2014*b*). However, since both fluid and solid domains are taken into account simultaneously, one can not isolate the specific influence of the flame holder wall temperature on flame stabilization. This important dependency is one of the target investigations carried out and reported in the present part. To do so, several DNS are performed for which only the fluid domain is numerically solved as a first step to isolate the effect of the wall temperature distribution on flame anchoring. The present study details the variations in the stabilization pattern when varying the bluff-body wall temperature. Note that, stabilization is not investigated in terms of stability limits but in terms of flow pattern and flame anchoring location for constant fluid parameters and a given flame holder geometry.

In parallel, it is of note that several fundamental issues are not directly addressed in the context of the CHT numerical simulations in the literature. Typically, issues related to the choice of the initial condition either for the fluid or the solid domains are known to directly impact convergence

time of such CHT computations and in extreme cases the final solution. In such a context, identifying potential fluid only solutions at thermal equilibrium with the solid for prescribed solid wall temperatures are potentially of great interest to a CHT numerical problem. Likewise understanding the impact of the solid temperatures on a flame is also of interest to understand CHT temporal evolution towards fully balanced thermal fields. All such issues are targeted by the following work which is then used as a step stone for more detailed analyses of CHT bluff-body flame simulations. The coupled simulations are exploited both from a physical point of view as well as with detailed investigations of the potential impact of the multi-physics numerical approaches retained on the solutions. To do so the impact of varying some coupling numerical parameters is explored and the coupling strategy proposed by Errera & Chemin (2013) is tested within the current framework.

The studied case as well as the fluid numerical resolution are detailed in Chapter 5. In addition, the flow mechanisms are discussed on the basis of a baseline case. In Chapter 6, the burner thermal state is investigated: the effects of the flame holder wall temperature on the fluid-only solutions are detailed and CHT computations acknowledging the previous findings are discussed. Finally, the potential influence of the methodology on the results of the coupled computation is assessed.

Chapter 5

DNS of a bluff-body stabilized laminar premixed flame

Contents

The academic bluff-body configuration chosen for the present study is first investigated through the detailed analysis of a fluid-only baseline case. Such a simulation allows to understand the mechanisms responsible for flame stabilization in regard to existing conclusions from the literature. These observations will thus provide a reference for further evaluation of the variation in the flow mechanisms in the next chapter.

The configuration investigated as well as the fluid solver setup are described in Section 5.1. The accuracy of the DNS is then assessed by investigating the mesh resolution in the flame front and at the walls. Finally, in Section 5.2 a detailed description of the flow patterns is proposed for a baseline case.

5.1 Numerical approach

5.1.1 Studied configuration

The test configuration consists of a squared cylinder placed in a laminar channel flow. The two-dimensional computational domain is schematized in Fig. 5.1. The channel is $L = 6.25 \times 10^{-2}\ m$ long and $H = 2.5 \times 10^{-2}\ m$ wide while the bluff-body side is $d = 5 \times 10^{-3}\ m$. The corresponding blocking ratio imposed to the flow by the obstacle equals $d/H = 0.2$ (Fig. 5.1). The positive x coordinate is directed streamwise from left to right (main stream direction) while the y coordinate

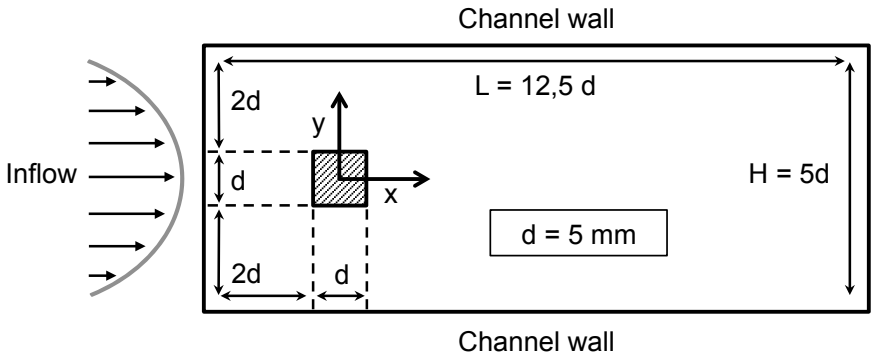

Figure 5.1: Schematic view of the computational domain.

is transverse to the flow. The origin of the axis is located at the flame holder center. The flow Reynolds number, based on the inflow quantities and the flame holder dimension, is $R_e = 500$. For combustion to proceed, a perfectly premixed mixture of methane and air is injected at the inflow at an equivalence ratio of $\phi = 0.7$. This bluff-body stabilized flame configuration is derived from the study of Kedia & Ghoniem (2014*a*,*b*, 2015). In their work, authors solved the Conjugate Heat Transfer (CHT) between the reactive fluid and the bluff-body solid materials by simultaneously solving the equations corresponding to each domain.

Boundary conditions

At the inflow boundary condition, a fully-developed laminar parabolic profile is prescribed with a bulk velocity equal to $U_0 = 1.6\ m.s^{-1}$. Fresh gases enter the channel at a temperature $T_0 = 300\ K$. The outflow condition is set at atmospheric pressure $P = 1\ atm$. Both inlet and outlet are set with characteristic boundary conditions (Poinsot & Lele, 1992). Finally, walls are prescribed with no slip conditions and are either adiabatic for the channel walls or isothermal at the same temperature all over the surface for the bluff-body walls. For the baseline computation, this latter temperature equals $T_w = 700\ K$. A characteristic formulation (Poinsot & Lele, 1992) is once again used to prescribe the flame holder wall quantities.

5.1.2 Computational method

For all the simulations discussed in the following, the LW scheme is used to solve the convective terms (Section 2.1.2). For comparisons, additional simulations performed with two different Taylor-Galerkin schemes (TTGC and TTG4A, Section 2.1.2) providing a higher order of accuracy in space and time gave similar results than the LW scheme. Full triangular cell based meshes of different resolutions are used for the present calculations. The corresponding CFL limited time steps range from $\Delta t = 2.7 \times 10^{-8} s$ for the coarsest mesh to $\Delta t = 8.8 \times 10^{-9} s$ for the finest one (Tab. 5.1). To account for combustion, a two-step six species reduced kinetic scheme called 2S_CH4_BFER (Franzelli *et al.*, 2012) is chosen. This scheme was especially designed to reproduce

the laminar flame speed and the adiabatic flame temperature of methane/air laminar premixed flames in a large range of reactant temperature, equivalence ratio and pressure.

The baseline computation (isothermal bluff-body walls at $T_w = 700\ K$) is initialized with a non-reacting homogeneous mixture flow with null velocity. After a transient phase, this non-reacting flow reaches a limit cycle in which vortices are periodically shed from the bluff-body, forming a Von Karman street. The Strouhal number of this shedding flow equals:

$$St = \frac{fd}{U_0} = 0.25 \tag{5.1}$$

where f is the vortex-shedding frequency. A similar value of the Strouhal number $St = 0.23$ was obtained by Kedia & Ghoniem (2014*a*), by computing the same cold flow without modifying the flame holder wall temperature compared to the fresh reactant temperature (i.e. $T_w = T_0 = 300\ K$). The reactive simulation is then obtained by local ignition of the cold flow: a sphere of burnt gases is deposited near the flame holder back face and spreads to find its stabilization position. Therefore, the simulation again goes through a transient phase and eventually stabilizes to a steady laminar flow. Note that, unless explicitly mentioned, all the results presented in this part come from converged steady solutions. Therefore, for clarity reasons the mention is not reported neither in the text nor in the figure captions.

Considering the operating conditions the adiabatic flame temperature equals $T_{adia} = 1844\ K$. Besides, the computation of a fully premixed laminar 1D flame (Goodwin, 2002) at these specific conditions allows to determine the laminar flame speed $S_L = 1.76 \times 10^{-1}\ m.s^{-1}$ as well as the flame thickness (deduced from the temperature profile)[1]:

$$\delta_L = \frac{T_{adia} - T_0}{max\left(\left|\frac{\partial T}{\partial x}\right|\right)} = 5 \times 10^{-4}\ m. \tag{5.2}$$

Based on this reference flame scale length the meshes are refined accordingly to accurately resolve the flame. The cell size within the flame region is set to $\Delta x = 96\ \mu m$ which is in agreement with the resolution used by Kedia & Ghoniem (2014*a*,*b*, 2015) ($\Delta x = 98\ \mu m$). This ensures approximately 5 points in the flame front for all meshes used in this study.

Since the present investigations rely on DNS, accurate resolution of the physical fields at the walls is mandatory. To assess the proper resolution of the fields, three levels of mesh refinement are tested (without changing the grid resolution in the flame region) on the baseline computation.

[1]Note that, different definitions of the flame thickness which do not require flame computations exist in the literature. Among them are the so-called diffusive thickness derived from the asymptotic analysis of Zeldovich, Frank-Kamenetski and von Karman (ZFK) (Peters, 1991) and for which the flame thickness is computed from fresh gases properties only. Such an evaluation is however found to be generally too approximate and more complex correlations have been developed such as the definition proposed by Blint (Blint, 1986).

Mesh	Number of cells	Wall mesh size Δx $[m]$	Time step Δt $[s]$	CPU cost $[h]$
M1	229354	5×10^{-5}	2.7×10^{-8}	137
M2	233384	4×10^{-5}	1.8×10^{-8}	207
M3	245950	2×10^{-5}	8.8×10^{-9}	467

Table 5.1: Meshes characteristics. The CPU cost is given for arbitrarily 10 *ms physical computation.*

Mesh characteristics are detailed in Tab. 5.1 in which the total number of cells, the mesh size at the walls, the corresponding CFL limited time step as well as an indicative total CPU cost of an arbitrarily chosen physical computation duration of 10 ms are given. Since the reactive flow fields are symmetric with respect to the domain centerline, the results are only presented on the top half of the domain in the following discussions.

First, mesh convergence is assessed through the non-dimensional distance to the wall of the first cell y^+ (Eq. (2.4)). The values along the bluff-body skin are shown in Fig. 5.2 for the three different meshes. The curvilinear abscissa s is oriented as indicated in Fig. 5.2 (top). The same convention is used throughout this part. The bottom plot of Fig. 5.2 shows values of y^+ below one on the whole bluff-body skin for the three meshes. These small values of y^+ indicate that the aerodynamic process is well resolved at the wall. To assess the potential dependency of the solution to the wall mesh size both in terms of aerodynamic and thermal aspects, the spatial evolution of the wall friction τ (Eq. (2.3)) and wall heat flux Q_w along the bluff-body skin are plotted in Fig. 5.3. Note that $Q_w = -\lambda \frac{\partial T}{\partial n}\big|_w$, where n is the inward flow domain wall normal unit vector and λ the fluid thermal conductivity (Eq. (A.14)). Similar values are obtained with the different meshes for both wall quantities except at the flame holder corners (that correspond to geometric singularities). Therefore, leaving aside the corners, mesh independence of the aerothermal fields is achieved with mesh M1. Note also that the flame stabilization remains unchanged for the three meshes. For these reasons, mesh M1 is retained for the next set of computations.

5.2 Flow characteristics description: baseline case

An analysis of the flame stabilization mechanism for the baseline case is proposed in this section. The flow pattern is shown in Fig. 5.4 which depicts the temperature field along with heat release contours at $HR = 10^8\ J.m^{-3}.s^{-1}$ and $HR = 10^9\ J.m^{-3}.s^{-1}$ (white) to visualize the flame, complemented by a zero axial velocity contour (red). A flame with two distinct fronts stabilizes symmetrically in the vicinity of the bluff body back corners. Additionally, a large recirculation zone encompasses the back and lateral faces of the bluff-body. The zero velocity contour slightly bends near the flame holder corners, where the flame foot stabilizes.

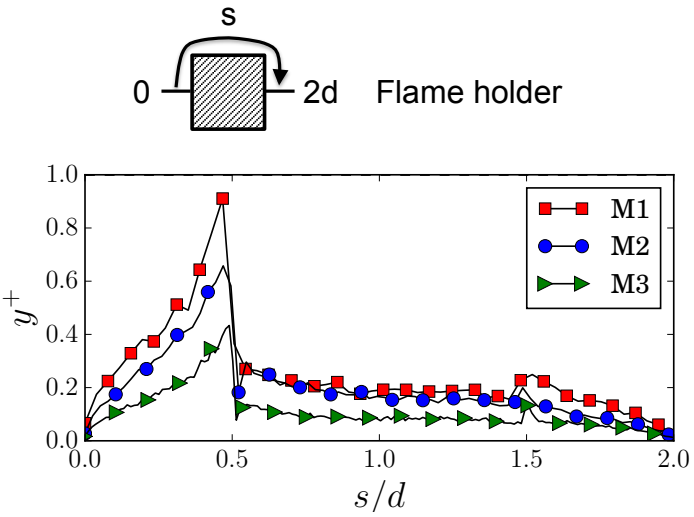

Figure 5.2: Scheme of the flame holder and the abscissa along its skin (top). Evolution of the non-dimensional distance to the wall of the first cell y^+ along the skin of the bluff-body top half for the three meshes M1, M2 and M3 (bottom).

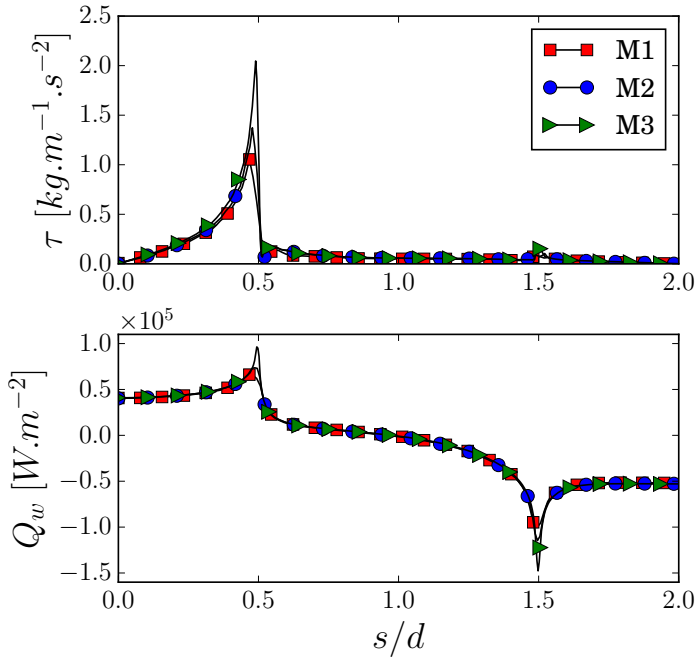

Figure 5.3: Evolution of wall friction τ (top) and wall heat flux Q_w (bottom) along the skin of the bluff-body top half for the three meshes M1, M2 and M3.

To illustrate the flame stabilization pattern, Figs. 5.5 and 5.6 show a zoomed view of the domain

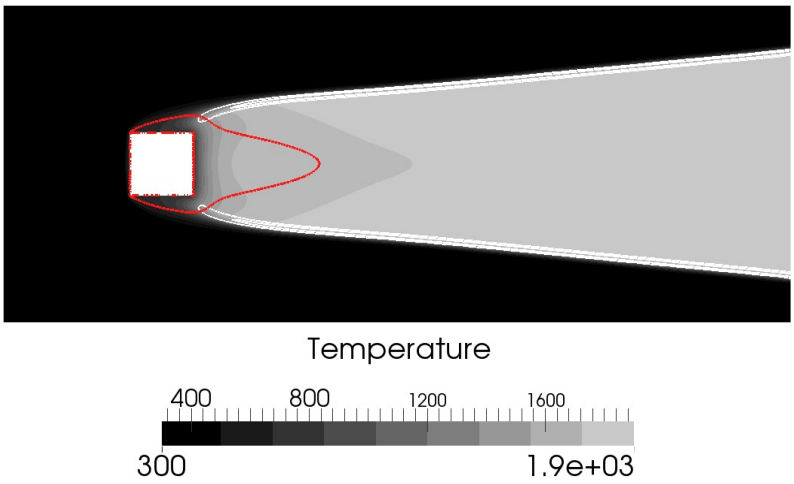

Figure 5.4: Temperature field with zero axial velocity contours (red) and heat release contours at $HR = 10^8\ J.m^{-3}.s^{-1}$ *(outer flame contour) and* $HR = 10^9\ J.m^{-3}.s^{-1}$ *(inner most flame contour) in white for the baseline case (*$T_w = 700\ K$*).*

focused on the flame foot location. Figure 5.5 shows the temperature field along with heat release contours at $HR = 10^8\ J.m^{-3}.s^{-1}$ and $HR = 10^9\ J.m^{-3}.s^{-1}$ (white) as well as flow streamlines in the recirculation zone (red). Focusing first on the streamlines indicates a recirculation zone with two kernels rotating clockwise: the recirculation zone is thus composed of two parts connected to each other, one located downstream of the flame holder ((B) on Fig. 5.5) and a second one near the lateral face (A). The flame foot stabilizes in-between the two kernels, in a region where the velocity is particularly low and hence favorable to flame development.

Then, looking at the temperature contours near the bluff-body centerline in zone (B) shows a gradual cooling of the burnt gases by convection and diffusion from the cold back face of the bluff-body as the gases get closer to the wall. In the region downstream of the flame holder back face, the isotherms are not parallel to the wall. The aerodynamic field is responsible for the isotherm distortions (indicated with arrows in Fig. 5.5): the isotherms cluster close to the flame holder centerline (C) whereas they are moved downstream and form a peak near the exterior of the recirculation zone (D). This distortion is however, significant away from the flame holder. Very close to the wall, the isotherms remain parallel to it. Near the bluff-body lateral face, in zone (A), gases are warmed both by the hot gases convected from the back and by diffusion from the hot lateral walls. Ignition temperature is thus reached thanks to the conjunction of these two warming processes. However, for the flame to ignite, not only is temperature important but also is mixture composition.

Figure 5.6 presents the CH_4 mass fraction field with the same heat release contours and streamlines of Fig. 5.5. The back part of the recirculation zone (B) is entirely filled with burnt gases. The

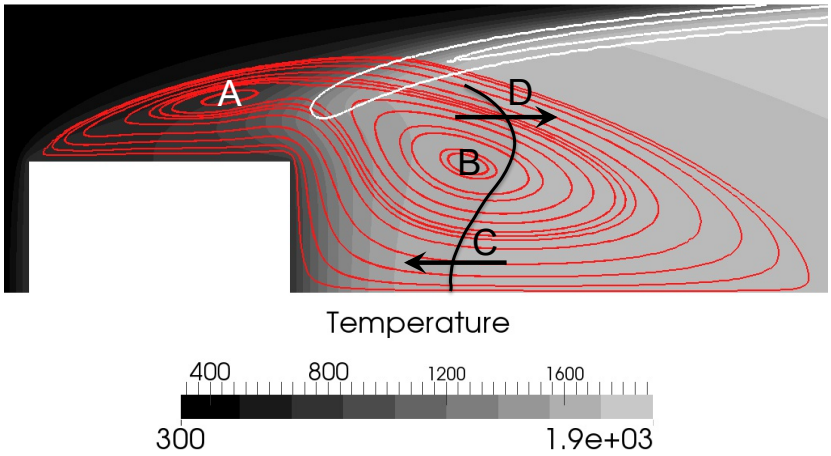

Figure 5.5: Temperature field with heat release contours at $HR = 10^8\ J.m^{-3}.s^{-1}$ (outer flame contour) and $HR = 10^9\ J.m^{-3}.s^{-1}$ (inner most flame contour) in white and streamlines in the recirculation zone (red) in the vicinity of the flame holder on the top half of the domain for the baseline case ($T_w = 700\ K$).

upstream flow motion in the recirculation zone brings burnt gases from the back to the most upstream point of the recirculation zone (arrow with solid line on Fig. 5.6). However, burnt gas upstream convection is offset by streamwise and lateral diffusion of fresh gases into the lateral part (A) of the recirculation zone (arrow with dashed line). With respect to composition, the recirculation zone has a negative effect on the flame development: it lowers the fresh gas quantity available at the flame foot location by dilution with the burnt gas composition convected from the most downstream part (B) of the recirculation zone.

To conclude, the recirculation zone has various effects: it brings hot temperature burnt gases upstream, warming up and diluting the fresh gases and it provides a favorable aerodynamic region with very low velocity. The recirculation zone actions added to the heating/cooling effect of the flame holder wall result in flame stabilization. Naturally, acting on one of these processes could affect greatly the other parameters and hence the flame stabilization pattern.

The aerodynamic field around the bluff-body as well as the temperature distribution induced by the flame stabilization pattern result in a specific wall friction and heat flux distribution along the bluff-body surface. The effect of the near wall aerodynamic field is evidenced through a fictive wall velocity: the friction velocity u_τ (Eq. (2.3)). The evolution of this quantity along the bluff-body skin is plotted in Fig. 5.7 (top). Two flow stagnation points are evidenced where u_τ reaches near zero values at normalized abscissa equal to $s/d = 0$ and $s/d = 2$. First, as the inflow reaches the squared obstacle front face, its velocity decreases from inlet values towards zero at the stagnation point ($s/d = 0$). The flow is deviated from the centerline towards the bluff-body corners and accelerates. Therefore, the friction velocity increases from the centerline stagnation

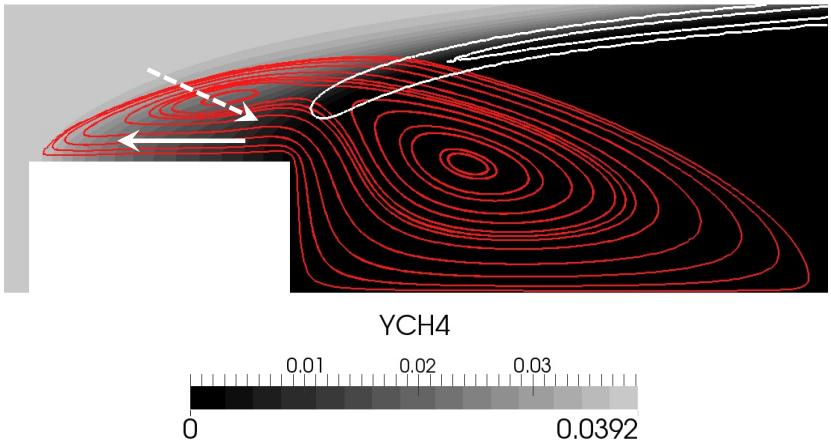

Figure 5.6: CH_4 mass fraction field with heat release contours at $HR = 10^8\ J.m^{-3}.s^{-1}$ (outer flame contour) and $HR = 10^9\ J.m^{-3}.s^{-1}$ (inner most flame contour) in white and streamlines in the recirculation zone (red) in the vicinity of the flame holder on the top half of the domain for the baseline case ($T_w = 700\ K$).

point ($s/d = 0$) to the first bluff-body sharp corner ($s/d = 0.5$). u_τ reaches its maximum value slightly ahead of the corner and drops suddenly to approximately 0.4 $m.s^{-1}$ at the lateral face forward part. Along this face ($s/d \in [0.5; 1.5]$), the surrounding recirculation zone leads to a rather constant value of the friction velocity far from the corners. Finally, due to the recirculation zone in the flame holder wake, the aerodynamic field pattern surrounding the back face is similar to that near the front face: the flow accelerates from the centerline second flow stagnation point ($s/d = 2$) to the back corners ($s/d = 1.5$) and so does the friction velocity. However, the flow in the recirculation zone being greatly slower than the incoming velocity, it yields a lower friction velocity along the bluff-body back face than on the front face.

The heat flux at the flame holder walls Q_w is greatly correlated with the friction velocity. Figure 5.7 (bottom) shows the wall heat flux distribution along the skin of the bluff-body. Note that by convention here, positive fluxes correspond to heating of the fluid. On the flame holder front face, the temperature difference between the fresh gases and the wall does not evolve significantly. Therefore, the heat flux level is mainly driven by the local value of the friction velocity which correlates with a convective process. On this face, Q_w increases from the centerline ($s/d = 0$) to the corner ($s/d = 0.5$). The heat flux distribution on the lateral face, on the other hand, is controlled by the local temperature difference between the wall and the fresh gas, which was observed to evolve significantly with the axial coordinate in Fig. 5.5. As the abscissa increases, the surrounding gas temperature increases gradually from values below the wall temperature that induce a positive flux from the wall to the fluid to temperatures greatly hotter than the wall leading to a negative flux. At the bluff-body back corner ($s/d = 1.5$), the negative heat flux peaks because of the slight increase of friction velocity at that location and more importantly because of

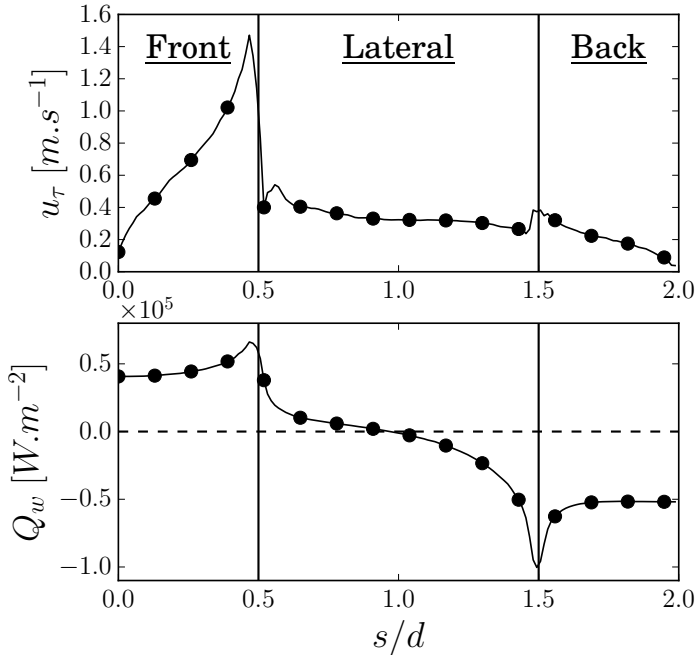

Figure 5.7: Evolution of the friction velocity (top) and the wall heat flux (bottom) along the skin of the bluff-body top half for the baseline case.

the isotherms getting closer to the wall, increasing the local temperature gradient at this specific location. Finally, along the bluff-body back face, the relatively low friction velocity associated with the very high and spatially uniform temperature difference between the burnt gases and the wall lead to important negative fluxes and a rather flat profile far from the corners.

5.3 Conclusion

An analysis of the flow fields obtained for a baseline computation (isothermal bluff-body walls at $T_w = 700\ K$) allowed to gain insight in the flame stabilization mechanism. A flame with two distinct fronts was observed to stabilize symmetrically in the vicinity of the bluff body back corners. This was enabled by a large recirculation zone composed of two parts connected to each other and encompassing the back and lateral faces of the bluff-body. The recirculation zone was observed to have various effects: it brought hot temperature burnt gases upstream, both warming up and diluting the fresh gases and it provided a favorable aerodynamic region with very low velocity. The heating of fresh gases allowed by the recirculation zone combined with that of the flame holder walls resulted in flame stabilization by allowing the fresh gases to reach ignition temperature. The resulting aerodynamic and temperature fields were observed to induce specific wall friction and heat flux distributions along the bluff-body surface.

All these observations highlighted the strong relations between the aerodynamic and thermal fields and the flame stabilization pattern. Therefore, a local modification of one of the parameters is expected to drastically affect the equilibrium and thereby lead to a totally different flame stabilization pattern with very different wall heat fluxes. In particular, the impact of a variation of the flame holder wall temperature is the first focus of the following chapter.

Chapter 6

Variations of anchoring pattern as a function of the thermal state

Contents

The thermal equilibrium response of the present bluff-body configuration is investigated in this chapter. First, fluid-only simulations are analyzed to gain insight into the thermal interactions between the aerodynamic and thermal fields as well as the flame stabilization pattern. Acknowledging previous fluid-only findings, several coupled CHT simulations are then performed to further examine the coupling effects between the fluid and the solid domain. In particular, the potential impact of the initial conditions on the coupled simulation solutions is assessed. Finally, the reproducibility of the results through a specific chained methodology is evaluated.

Fluid-only computations with varying flame holder wall temperatures are first discussed in Section 6.1 to evaluate the influence of such a variation on the flow fields and stabilization pattern. To investigate further the physical relevance of the conclusions drawn from the results obtained with the fluid-only approach, several CHT simulations are considered in Section 6.2. Section 6.3

is then dedicated to the detailed analysis of the convergence history of the CHT computations as well as on the underlying physical phenomena. Finally, computations performed with the chaining methodology proposed by Errera & Chemin (2013) are discussed in Section 6.4.

6.1 Fluid-only approach: influence of the flame holder wall temperature

As a first step, simulations account for the fluid domain only, hence allowing to assess the effect of the bluff-body wall temperature on the fluid solution leaving aside the potential effect of conduction in the solid. To investigate the influence of the bluff-body temperature on the flame stabilization pattern and flow fields, 15 simulations are performed for flame holder wall temperatures ranging from $T_w = 600\ K$ to $T_w = 2000\ K$ with a $100\ K$ difference between each simulation. Note that for wall temperatures from $T_w = 500\ K$ and below self-sustained oscillatory unsteady solution is observed. These cases are off-topic for the present analyses and are not investigated, the discussion being restrained to steady solutions. All simulations are initialized with the $T_w = 700\ K$ reactive reference case described in Section 5. They all go through a transient phase before a steady state is eventually reached for the cases of interest i.e. $T_w \in [600; 2000]\ K$.

6.1.1 Flame stabilization and flow field variations

The bluff-body temperature effect on the flow fields is first investigated qualitatively. Figure 6.1 presents for each case, the temperature field along with heat release contours at $HR = 10^8\ J.m^{-3}.s^{-1}$ and $HR = 10^9\ J.m^{-3}.s^{-1}$ (white) to indicate the flame location as well as flow streamlines in red within the recirculation zone. The heat release contours highlight an upstream displacement of the flame foot as the wall temperature increases:

- $T_w = 600\ K \rightarrow$ the flame is located downstream of the flame holder,
- $T_w = 1000\ K \rightarrow$ the flame anchors near the lateral face of the flame holder and the flame foot starts to bend towards the wall,
- $T_w = 1200\ K \rightarrow$ the two flame feet (symmetric field) eventually meet along the flame holder front face,
- $T_w = 1900\ K \rightarrow$ the wall temperature is above the adiabatic flame temperature ($T_{adia} = 1845\ K$), the flame is totally stabilized upstream of the flame holder front face.

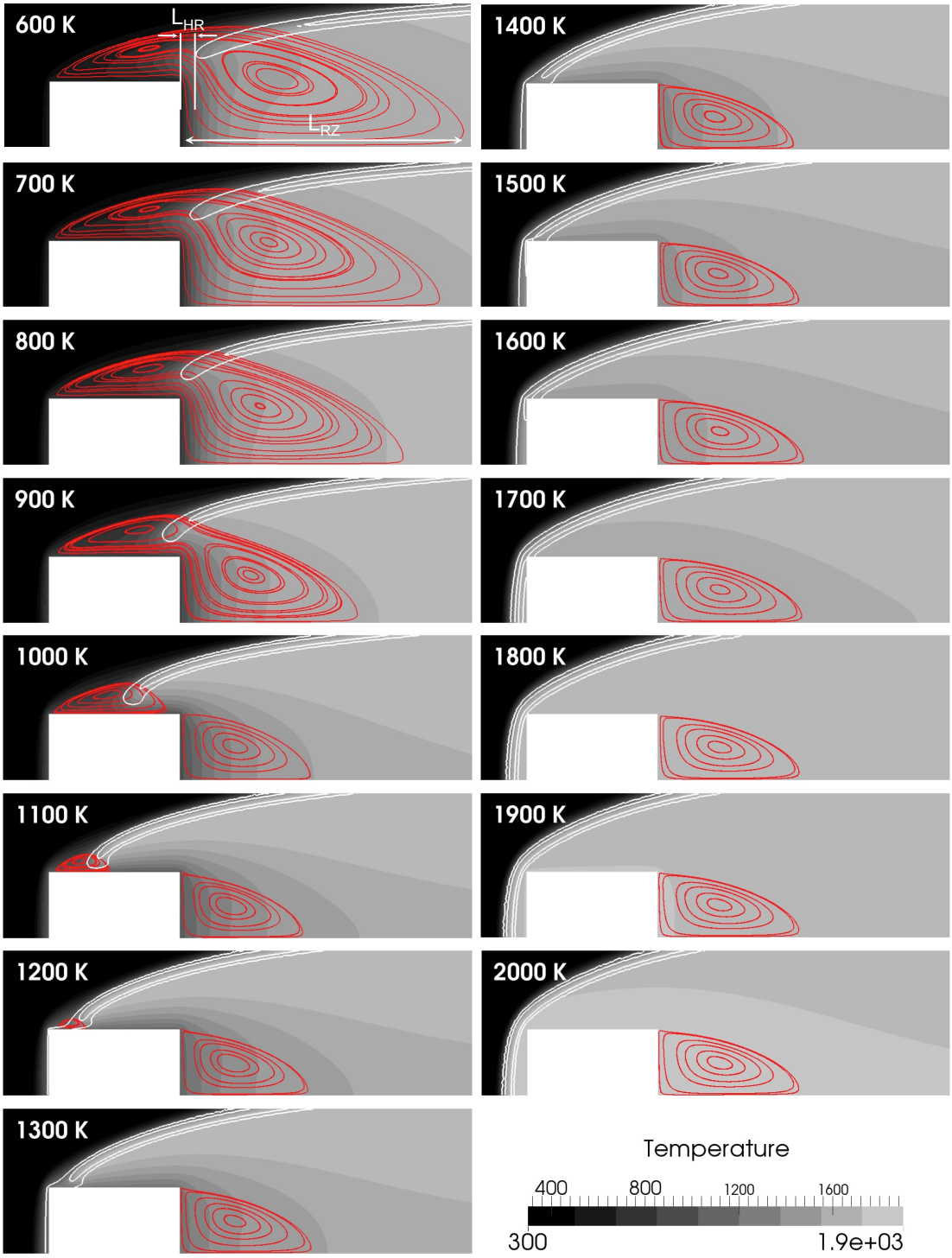

Figure 6.1: Temperature field with heat release contours at $HR = 10^8\ J.m^{-3}.s^{-1}$ (outer flame contour) and $HR = 10^9\ J.m^{-3}.s^{-1}$ (inner most flame contour) in white and flow streamlines within the recirculation zone (red) in the vicinity of the flame holder on the top half of the domain.

The flame foot location modification with wall temperature is evaluated in Fig. 6.2 which gives the normalized most upstream axial coordinate L_{HR} of the $HR = 10^8\ J.m^{-3}.s^{-1}$ contour for each bluff-body wall thermal condition. Vertical dashed lines indicate the bluff-body front and back face location. L_{HR} evolves monotonously as a function of bluff-body wall temperature. The contour coordinate moves ahead of the bluff-body back face for wall temperatures equal to $T_w = 800\ K$ and ahead of the front face for $T_w = 1200\ K$. For simulations with a bluff-body wall temperature within this interval, the flame foot location greatly shifts between two consecutive simulations. Additionally, from $T_w = 600\ K$ to $T_w = 1100\ K$, the heat release contours at $HR = 10^8\ J.m^{-3}.s^{-1}$ and $HR = 10^9\ J.m^{-3}.s^{-1}$ get closer to each other as the wall temperature is increased (Fig. 6.1), indicating an enhancement of the chemistry near the flame foot and hence an increased flame foot strength.

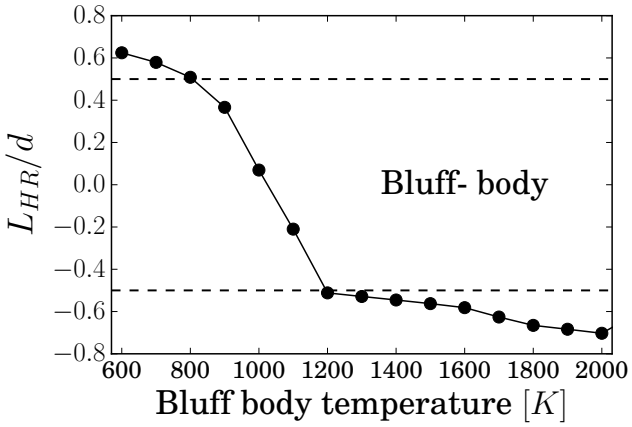

Figure 6.2: Normalized axial coordinate of the upstream extreme of the $HR = 10^8\ J.m^{-3}.s^{-1}$ contour.

As the flame moves upstream with the increasing wall temperature, the whole recirculation shape and length are modified. Figure 6.3 indicates the length L_{RZ} of the back part of the recirculation zone (referred to as zone B in Fig. 5.5). Modifications of this part of the recirculation zone with increasing bluff body wall temperature are clearly highlighted. First, its axial length decreases rapidly and quasi linearly from approximately 2.2 times the flame holder side length (d) at $T_w = 600\ K$ to 1 at $T_w = 1000\ K$. At the latter wall temperature value, the global recirculation zone splits into two distinct zones, the lateral part (referred to as zone (A) in Fig. 5.5) and the downstream part (B) of the recirculation are no longer connected (Fig. 6.1). Figure 6.1 indicates that above $T_w = 1000\ K$, the size of the lateral recirculation zone (A) reduces with increased wall temperature and eventually vanishes for $T_w = 1300\ K$. At the same time, the length of the downstream recirculation (B) keeps a rather constant value. From $T_w = 1100\ K$ to $T_w = 1600\ K$ it eventually increases gradually to stop evolving above $T_w = 1600\ K$.

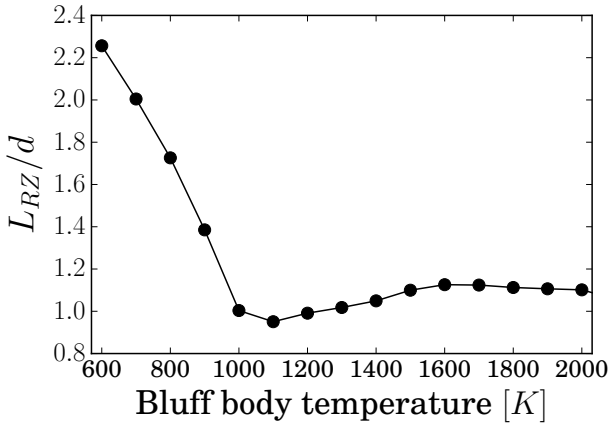

Figure 6.3: Normalized distance between the flame holder back face and the end of the recirculation zone behind the bluff body (corresponding to the maximal x coordinate of zero axial velocity).

Flow solutions clearly evolve non-linearly from the downstream stabilized two front flame at $T_w = 600\ K$ to a unique flame front stabilized ahead of the bluff-body at $T_w = 2000\ K$. Observations of the flow fields allow to identify three main categories and stabilization mechanisms as a function of bluff-body wall temperature:

- ▷ $T_w \in [600; 900]\ K \rightarrow$ lifted flame: the global recirculation zone has a central role on the flame stabilization as reported in the literature. This pattern corresponds to the reference case described in Section 5. The shape of the recirculation although potentially complex, allows hot gas upstream convection and hence maintains high temperatures at the flame foot location. However, as the wall temperature increases, the recirculation strength effectively decreases and preheating is achieved by heat transfer from the walls. Within the present wall temperature range, the flame foot stabilizes between the lateral (A) and downstream (B) parts of the recirculation. The isotherms near the flame holder back face, initially distorted by the recirculation zone align with the flame holder back face as the recirculation zone weakens with increased wall temperature. This type of flame is usually referred to in the literature as a lifted flame.

- ▷ $T_w \in [1000; 1800]\ K \rightarrow$ anchored flame: at $T_w = 1000\ K$ the isotherm shapes change and the recirculation zone splits into two distinct parts, hence greatly reducing the heat provided to the fresh reactants by the recirculating flow. Heating of the fresh gases is however achieved by the walls. Both contributions remain important until $T_w = 1200\ K$. Above this wall temperature, the flame foot is no longer surrounded by a recirculation zone. The walls alone maintain the flame. As the wall temperature is further increased, the flame stabilizes more and more ahead of the flame holder front face and detaches from the lateral face. These flames are for now on referred to as anchored flames.

- ▷ $T_w \in [1900; 2000]\ K \rightarrow$ bowed flame: on this interval of flame holder wall temperature, the

adiabatic flame temperature is well surpassed. The bluff-body wall has no longer potentially local cooling effects on the surrounding gases. It even heats up already burnt gases. The flame in this case detaches from the flame holder walls and moves upstream away from the walls as their temperature is increased to a point where combustion can sustain through a pseudo auto-ignition process. These flames will be called bowed flames with respect to their shape and as a reference to bowed shocks.

6.1.2 Impact on the bluff body wall fluxes

The evolution of the flame stabilization pattern with wall temperature induces considerable modifications of the wall flux distribution along the bluff-body surface. These are presented in Fig. 6.4 on four separated plots corresponding to the main categories described in Section 6.1.1. Plots present the wall heat flux distribution, a) for the lifted flames, b) and c) for the anchored flames and d) for what was called the bowed flames. Fluxes follow the same convention given in Section 5: they are positive when oriented towards the fluid. Focusing first on lifted flames shows no clear modification of the wall heat flux distribution when varying the wall temperature: whatever the flame holder wall temperature is, the flux evolution follows what was evidenced on the baseline case of Section 5. Although the overall pattern is unaltered, flux amplitudes evolve as the wall temperature increases:

- ▷ along the front face, fluxes are positive, their amplitude increases because of the increased temperature difference between the fresh reactants at $T_0 = 300\ K$ and the wall,
- ▷ along the back face, the opposite phenomenon can be observed: negative flux amplitude decreases with an increased wall temperature because the surrounding burnt gases are less efficiently cooled by the hotter wall temperature,
- ▷ along the lateral face, cases with a flame holder wall temperature between $T_w = 600\ K$ and $T_w = 800\ K$ gradually join as the abscissa increases to eventually meet just ahead of the back corner, where $s/d = 1.45$. The case with $T_w = 900\ K$ differs from the other lifted flame cases. At this temperature, the flame starts interacting with the bluff-body walls and induces a slight modification of the flux distribution: the $T_w = 900\ K$ curve separates from the colder cases for abscissa $s/d \in [1.2; 1.5]$ and the negative peak amplitude at the back corner increases.

The interaction between the flame and the wall greatly amplifies as the wall temperature is further increased, thus allowing the flame to switch from a lifted mechanism to an anchored one. On Fig. 6.4b, the curve shape on the lateral face $s/d \in [0.5; 1.5]$ evolves with the bluff-body wall temperature and bends more and more. At $T_w = 1100\ K$, a clear negative peak appears at the flame foot location $s/d = 0.9$. At this point, flame-wall interactions become important. These interactions are widely studied in the literature and early work on the topic can be found for

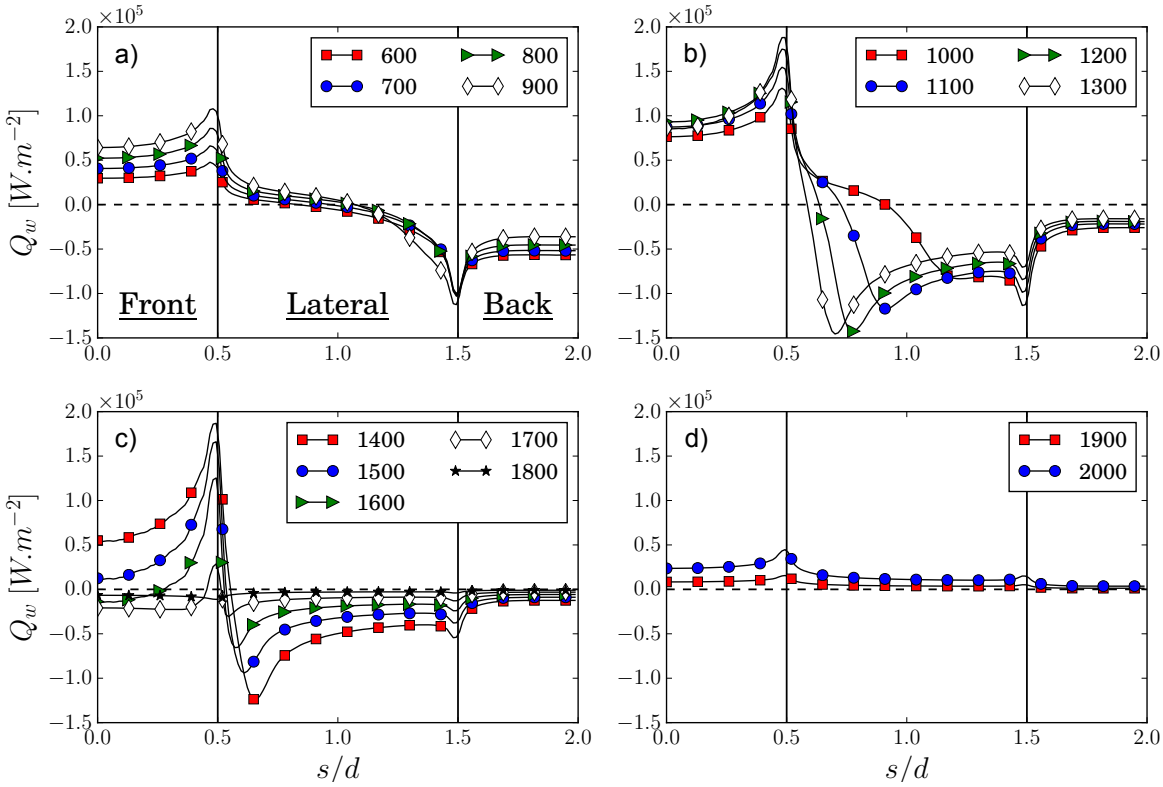

Figure 6.4: Wall heat fluxes distribution along the skin of the bluff-body top half, a) for the lifted flames ($T_w \in [600; 900]\ K$), b) and c) for the anchored flames ($T_w \in [1000; 1800]\ K$) and d) for the bowed flames ($T_w \in [1900; 2000]\ K$). Fluxes are oriented towards the fluid.

instance in von Kármán & Millan (1953); Williams (1985); Lu *et al.* (1990). In such cases, the flame propagates towards a cold wall which extracts more and more energy from the flame as it gets closer to it. As a result, the flame weakens and the fuel consumption speed decreases until the flame eventually quenches at a distance away from the wall. In the present study, the wall has two antagonistic effects: first it removes energy from the flame in the classic flame-wall interaction manner but at the same time it preheats the fresh reactants, hence providing energy for the flame to be maintained. The flame foot distance to the wall results therefore from an equilibrium between heat removed and supplied by the wall. For simulations with a bluff-body wall temperature going from $T_w = 1000\ K$ to $T_w = 1300\ K$, preheating is more and more enhanced as the wall temperature increases, the flame thus gets closer to the flame holder lateral face leading to an increase of the wall heat flux negative peak. For wall temperatures above $T_w = 1300\ K$, Fig. 6.4c, a negative peak is still visible near the flame location. However, its amplitude decreases with increased wall temperatures as the flame transfers from the vicinity of the flame holder lateral face to the front face $s/d \in [0; 0.5]$. This modification of the flame stabilization location is also responsible for the decrease of the wall heat flux on the bluff-body front face. At $T_w = 1700\ K$, a strong flame stabilizes ahead of the flame holder (Fig. 6.1): the flux profile along the front face

becomes flat far from the corners. Further increasing the wall temperature ($T_w = 1800\ K$) makes the flame moving away from the walls. The bluff-body is almost entirely plunged in burnt gases and the wall heat flux remains nearly constant along the whole surface. Similar observations can be made for bowed flames, (Fig. 6.4d). However, in these cases, fluxes are now positive.

To investigate the influence of the flame holder wall temperature from a more global point of view, heat flux distributions are integrated separately on the front, the back and both lateral faces of the bluff-body separately as well as on the whole surface. Results are presented in Fig. 6.5. On the flame holder back face, integrated fluxes evolve monotonously with wall temperature, following the evolution of the temperature difference between the burnt gases and the wall (detailed in Fig. 6.4). The integrated fluxes on the lateral and front faces evolve in a more complex manner. On the front face, the heat flux first increases as the wall temperature goes from $T_w = 600\ K$ to $T_w = 1200\ K$. Beyond this temperature, the reaction zone developing along the bluff-body front face induces a reduction of the heat transferred from the wall to the fresh reactants. Finally, from $T_w = 1700\ K$ and above, the heat flux distribution is found to keep a rather constant value along the bluff-body skin in Fig. 6.4. Therefore, the integrated flux sign and amplitude are linked to the temperature difference between the wall and the burnt gases both on the front and the lateral faces. Leaving aside these hot cases, the evolution of integrated fluxes on the lateral faces highlight three distinct behaviors as a function of the wall temperature. On the interval $T_w = [600-800]\ K$, the temperature difference between walls and the surrounding fluid decreases: negative fluxes are less and less important. Then from $T_w = 900\ K$ to $T_w = 1200\ K$, the flame interacts with the wall and gets closer to the lateral face as the wall temperature increases, creating hot areas in the vicinity of the wall and hence increasing the temperature gradients and eventually the negative flux. Above $T_w = 1200\ K$, the flame stabilizes upstream and takes off from the flame holder lateral face, fluxes decrease again.

The heat flux is now integrated on the whole flame holder surface in Fig. 6.5 bottom. This gives the total power supplied or removed by the wall to the fluid. First, note that a proportionality factor of 150 to 3200 (not shown) depending on the case, exists between the total heat released by the flame front and the wall heat flux. Therefore, the power transmitted or taken out of the fluid at the bluff-body walls remains negligible for the entire domain size. It is the local effect on the flow field that creates strong modifications of the global behavior in the domain. Focusing now on the wall temperature influence on the integrated heat flux, shows surprisingly that leaving aside cases where the wall temperature is beyond the adiabatic flame temperature, the more energetic case is found for $T_w = 900\ K$. Meaning that the total power supplied by the wall to the fluid is maximum for this case. More importantly, the integrated flux curve evolves non-monotonously as a function of flame holder wall temperature. As a result, a given value of the integrated flux corresponds to various wall flux distributions and hence potentially highly different flow patterns. In particular the curve crosses null integrated flux axis three times corresponding to bluff-body temperatures slightly below $T_w = 800\ K$ and above $T_w = 1000\ K$ as well as a value close to

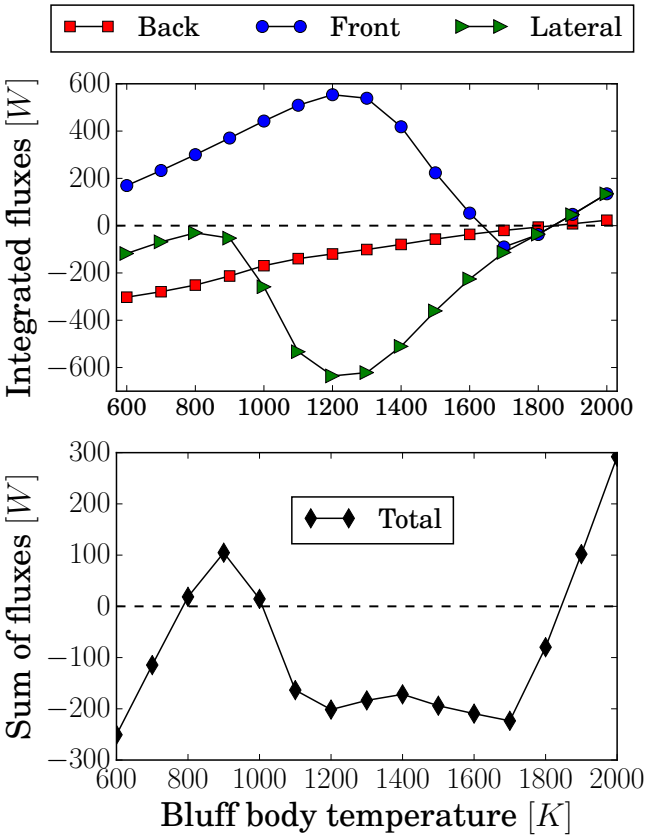

Figure 6.5: Integrated fluxes along the walls of the bluff-body for the different thermal conditions.

$T_w = 1850\ K$. These points are three theoretical equilibrium states and suggest that computation of a more realistic case solving conduction inside the flame holder solid part could lead to different converged results depending on the thermal initial state. This last conclusion is assessed through the computation of the joint problem both in the fluid and the solid domain in the next section.

6.2 Conjugate Heat Transfer: physical equilibrium states

To analyze the physical relevance of the three equilibrium states outlined by the fixed temperature computations, CHT simulations are performed with various initial conditions. The latter are inherited from the previously detailed fluid-only fixed temperature computations. Indeed, each of the fluid converged solutions obtained for $T_w \in [600; 2000]\ K$ are used to initialize the fluid domain of the different CHT computations. For all these coupled simulations, the solid initial field is homogeneous and at the corresponding fluid wall temperature. The various simulations discussed here are therefore identified through this initial condition: $T_{init} = T_w \in [600; 2000]\ K$. For brevity reasons only 7 of the 15 simulations performed are presented in this section. These correspond to the

initial conditions $T_{init} = T_w$(at the initialization) = 700, 900, 1000, 1100, 1400, 1700, 2000 K.

6.2.1 CHT results with a ceramic bluff-body

A first set of simulations is performed for solid properties corresponding to those of a ceramic bluff-body simulated by Kedia & Ghoniem (2014*a*). The density, the specific heat capacity, and the thermal conductivity are respectively $\rho_s = 673\ kg.m^{-3}$, $c_s = 840\ J.kg^{-1}.K^{-1}$, and $\lambda_A^s = 1.5\ W.m^{-1}K^{-1}$. Note that these quantities do not evolve with local solid temperature and the corresponding theoretical problem is thus linear (Eq. (2.15)). The convergence criterion of the matrix free conjugate gradient of the solid solver is fixed at $crit_{cv} = 10^{-6}$ and the Fourier number equals $F = 5$, leading to a solid time step $\Delta t_s = 4.71 \times 10^{-3}\ s$.

Interface physical fields are set with the couple of Dirichlet-Neumann conditions detailed in Section 3.1.1. Note that, only the stationary solution is pursued here, thus allowing the use of a desynchronization technique (Section 3.1.1) to enhance the simulations convergence rate. Coupling exchanges are performed each $nit_f = 10$ fluid iterations and $nit_A^s = 1$ solid iteration. The fluid and solid solvers are therefore physically desynchronized by a factor of the order of:

$$\frac{t_{cpl}^s}{t_{cpl}^f} = O(10^4). \tag{6.1}$$

Additional simulation have been performed for different desynchronization factor and evidenced the exact same results but naturally different associated CPU costs to reach a converged state. With the setup retained, the physical desynchronization of the solvers slightly evolves during the numerical transient phase. Indeed in the present wall resolved case, the smallest mesh cells are located near the bluff-body wall. Therefore, from the CFL and speed of sound expressions (Eqs. (2.11) and 2.12), the time step decreases slightly when very hot temperatures are seen in the vicinity of the walls and thus evolves with the adaptation of the flow and flame stabilization pattern.

Convergence history of the CHT simulations for the various initial conditions is reported in Fig. 6.6. To ease the visualization, only half of the total physical time computed is shown. Besides, to allow the investigation of the whole coupled system convergence, the temporal evolution of fluid quantities is reported in the solid time scale. Detailed analyses of Fig. 6.6 highlights two different converged end states of the joint problem and originating from the various initial conditions of the CHT simulations. For $T_{init} = \ \in [700,\ 900\ K]$, the coupled fluid-solid system converges towards a 'cold' case for which the flame stabilized in the flame holder wake. For this case, the solid and fluid spatially averaged temperatures are respectively $T_{ave}^s = 878\ K$ and $T_{ave}^f = 969\ K$. For $T_{init} = \ \in [1000,\ 2000\ K]$, fresh gases preheating achieved both by the flame and the solid walls allow the flame to move upstream. At convergence, the solid domain temperature is homogeneous

and equal to the adiabatic flame temperature $T^s = T_{adia} = 1844\ K$ while the fluid spatially averaged temperature is above 100 K hotter than in the 'cold' case and equals $T^f_{ave} = 1083\ K$. This bifurcation between two possible thermal solutions of the problem is highlighted with different background colors (white or grey) in Fig. 6.6. Accordingly, two different scales are used to evaluate the various quantities evolution. Note that this choice of presentation is kept unchanged within this part of the manuscript to ease interpretation and reading of results.

Within each category ($T_{init} = \quad \in [700,\ 900\ K]$ and $T_{init} = \quad \in [1000,\ 2000\ K]$), the converged thermal states obtained from any initial condition are strictly equivalent. These two states are presented in Fig. 6.7. Both fluid and solid thermal fields are shown along with heat release contours at $HR = 10^8\ J.m^{-3}.s^{-1}$ and $HR = 10^9\ J.m^{-3}.s^{-1}$ as well as flow streamlines within the recirculation zone. The spatially averaged solid temperature is indicated in white at the top left of the plot to allow an easier identification of the various cases. The 'cold' and 'hot' converged states fall respectively into the lifted and bowed regimes evidenced by the fixed temperature computations (Section 6.1). As could be expected, the stabilization pattern of the $T^s_{ave} = 878\ K$ case in terms of flame foot location, recirculation zone shape and length as well as fluid temperature field lies between the patterns observed for the fluid-only isothermal cases $T_w = 800\ K$ and $T_w = 900\ K$. The same conclusion can be drawn for the $T^s = 1844\ K$ case whose fields are in between those of the $T_w = 1800\ K$ and $T_w = 1900\ K$ fluid-only solutions. Note that in Kedia & Ghoniem (2014*a*) the CHT simulations were initialized from non-reactive states and hence only a solution similar to the $T^s_{ave} = 878\ K$ case was obtained.

The low conductivity of the ceramic material leads to large thermal heterogeneities in the solid domain for the lifted converged case as observed in Figs. 6.6 and 6.7. In addition, the low conductivity is also responsible for the significant difference between the actual spatially averaged solid temperature and the theoretical equilibrium state predicted by the fixed temperature case in Fig. 6.5 (theoretical equilibrium obtained for a temperature slightly below $T_w = 800\ K$). Indeed, the isothermal condition imposed at the wall in the fluid-only simulations corresponds, in terms of physics, to a hypothesis of infinite conductivity and uniform solid temperature. The ceramic conductivity is particularly low and hence far from this hypothesis. The 'hot' case on the contrary is equivalent to what was predicted by Fig. 6.5. The solid is entirely plunged into burnt gases and hence at the adiabatic flame temperature irrespective of the conductivity.

Finally, an interesting result lies in the fact that only two cases from the three theoretical equilibrium states identified earlier seem actually achievable with CHT computations. Even the case with an initial wall temperature at $T_{init} = 1000\ K$ initially very close to the third theoretical equilibrium state does not converge towards this pseudo solution but instead converges to a bowed flame. To further investigate the physical relevance of the third equilibrium state, additional simulations are performed for increased solid conductivities, and thus for cases closer to the infinite

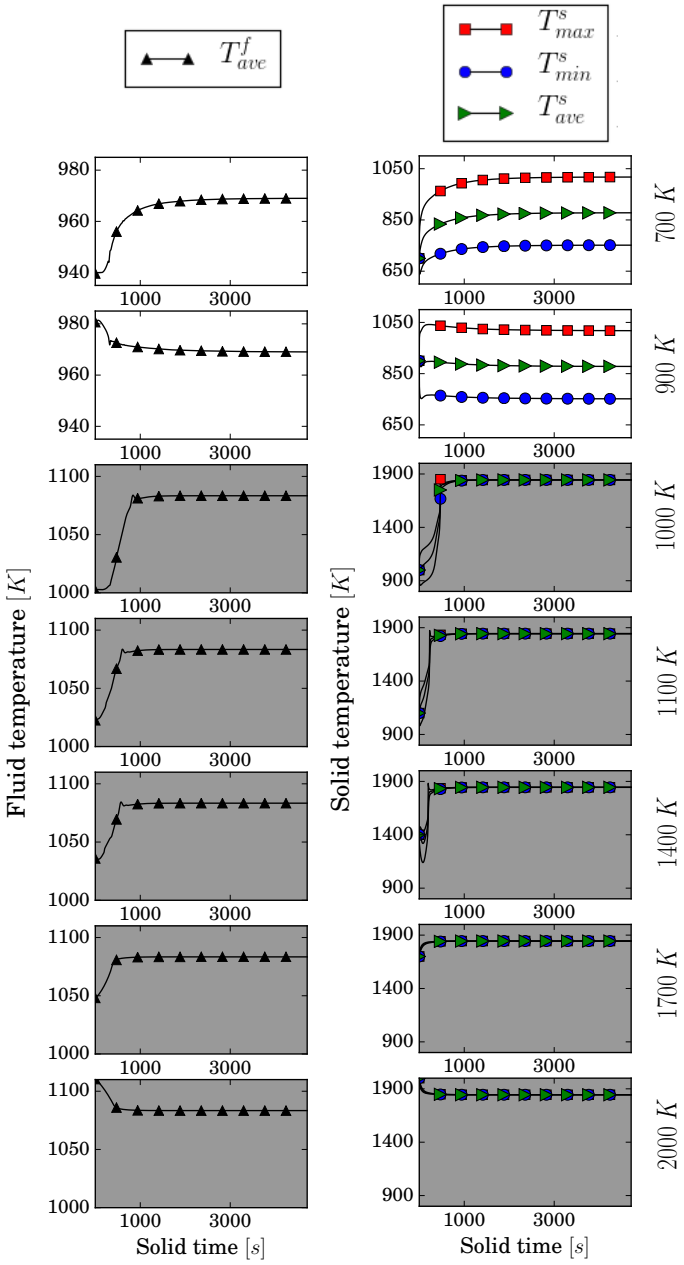

Figure 6.6: Convergence of the CHT simulations for the various initial conditions $T_{init} = 700, 900, 1000, 1100, 1400, 1700, 2000\ K$ *(indicated on the right of each plot). Fluid spatially averaged temperature (left), solid minimal, maximal and spatially averaged temperatures (right). The two different ordinate scales are highlighted with white or grey plot backgrounds.*

conductivity hypothesis.

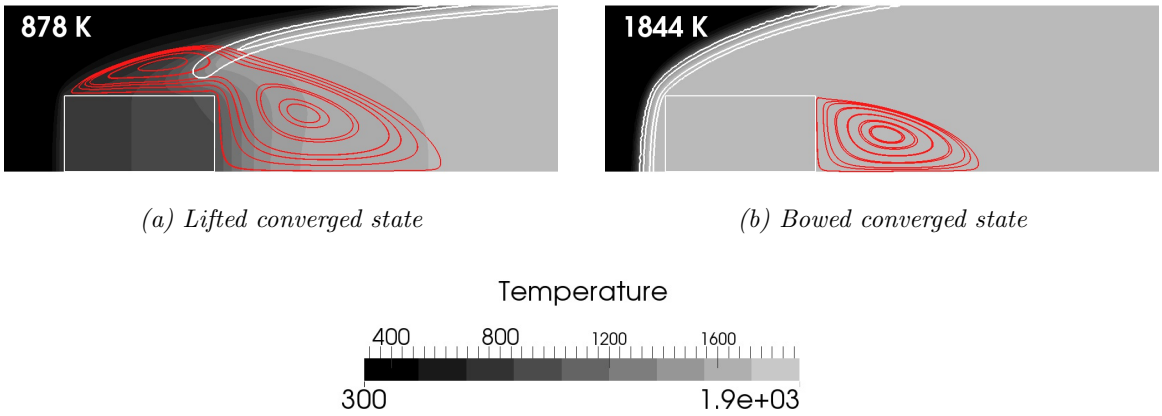

(a) Lifted converged state *(b) Bowed converged state*

Figure 6.7: Temperature field of the two CHT converged states in both fluid and solid domains with heat release contours at $HR = 10^8\ J.m^{-3}.s^{-1}$ (outer flame contour) and $HR = 10^9\ J.m^{-3}.s^{-1}$ (inner most flame contour) in white and flow streamlines within the recirculation zone (red) in the vicinity of the flame holder on the top half of the domain. The solid domain is indicated with the white square.

6.2.2 Impact of solid conductivity on the equilibrium states

Two additional sets of CHT simulations are performed: the various initial conditions remain the same than for the previous computations while the solid conductivity is multiplied by 10 and 100. The previous and new sets of results are denoted cases A, B and C and correspond hence to solid conductivities respectively equal to: $\lambda^s_A = 1.5\ W.m^{-1}K^{-1}$, $\lambda^s_B = 15\ W.m^{-1}K^{-1}$ and $\lambda^s_C = 150\ W.m^{-1}K^{-1}$. The other solid properties are kept unchanged. As a consequence, since the Fourier number (Eq. (2.20)) is not modified, the time steps in the solid conduction solver are respectively divided by 10 and 100. To maintain unchanged the physical desynchronization between the solvers for all the cases, the number of solid iterations between two coupling events initially equal to $nit^s_A = 1$ for case A is modified in accordance for the two new conductivities: $nit^s_B = 10$ and $nit^s_C = 100$.

Convergence of the solid minimal, maximal and spatially averaged temperatures are shown in Fig. 6.8 for all simulations. Similarly to the previous observation these 21 computations converge towards only two stable states: the lifted and bowed regimes. Interestingly, depending on the conductivity, the bifurcation between these two states is either between $T_{init} = 900\ K$ and $T_{init} = 1000\ K$ for case A or $T_{init} = 1000\ K$ and $T_{init} = 1100\ K$ for cases B and C. Note that for the present investigations, the CHT computation initial conditions are separated by wall temperature steps equal to $100\ K$ minimum. However, it is most likely that performing simulations with smaller steps (each $10\ K$ for instance) would lead to potentially different bifurcation points for both conductivities λ^s_B and λ^s_C.

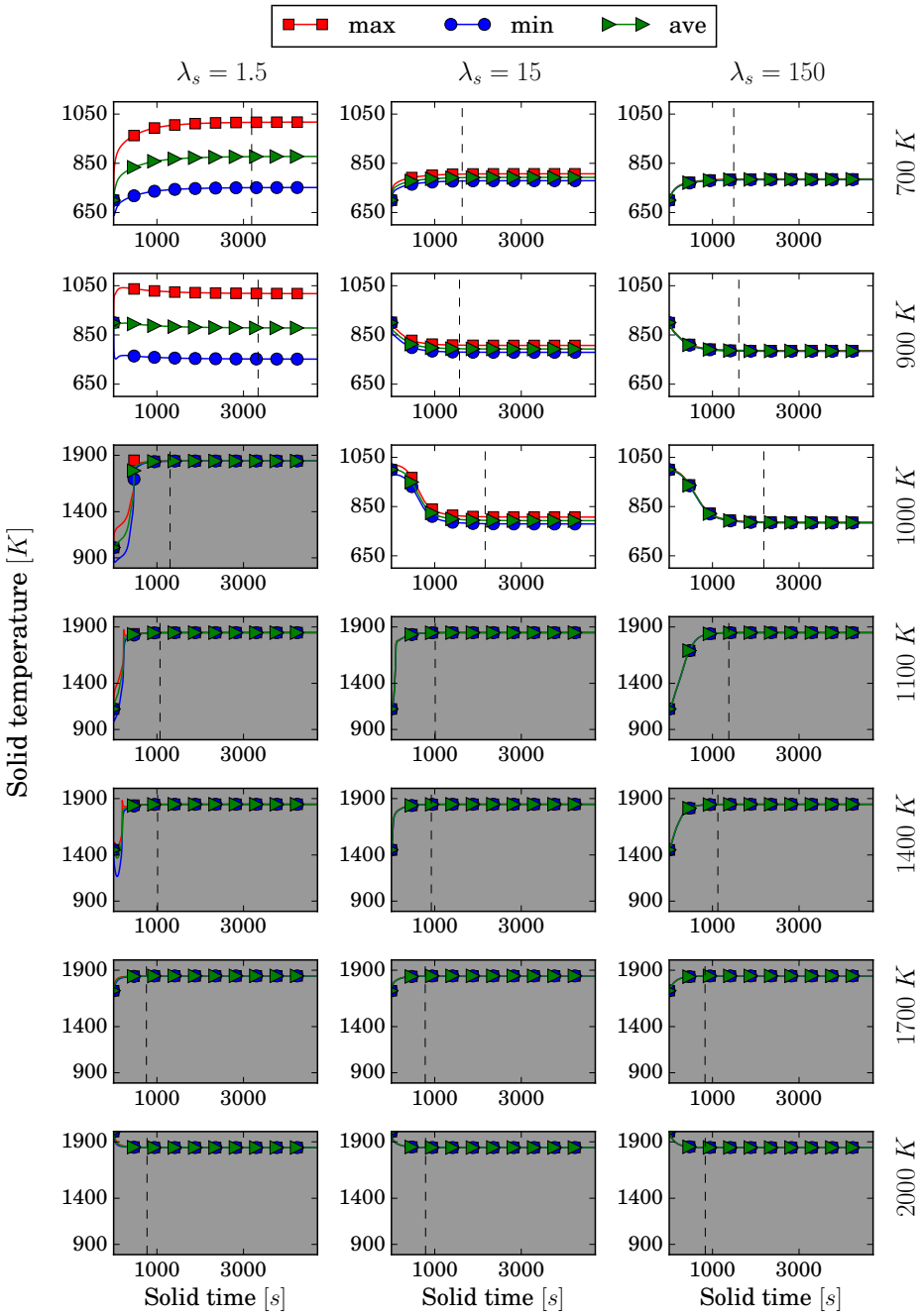

Figure 6.8: Convergence of the solid minimal, maximal and spatially averaged temperatures for three different values of the solid thermal conductivity λ_s. Initial conditions T_{init} = 700, 900, 1000, 1100, 1400, 1700, 2000 K are indicated on the right of each plot and the two different ordinate scales are highlighted with white or grey plot background.

Besides, while all the converged bowed regime solutions are strictly equivalent whatever the initial conditions or the solid conductivity, the lifted converged regimes are impacted by the conductivity of the material. Indeed, changes in conductivity result in different thermal equilibriums of the coupled fluid-solid system. Therefore, the lifted flame thermal fields obtained for the three conductivities differ which is evidenced by the different spatially averaged temperature of the solid. The higher the conductivity, the most homogeneous the solid temperature is and the lower is the spatially averaged solid temperature. This latter observation is explained in the following with a simple analytic model (page 131). As the conductivity increases and gets closer to the infinity hypothesis, the spatially averaged solid temperature gets closer to the value at which the integrated heat flux of the isothermal computations crosses zero (Fig. 6.5). More importantly, it appears that even for very high conductivity, the anchored regime is not a physical stable regime.

The four stable solutions obtained from the CHT simulations are now explored in details. Figure 6.9 presents the three lifted converged states corresponding to cases A, B and C along with the bowed converged regime identical for all three solid conductivities. Just like in Fig. 6.7, the different cases are identified by the spatially averaged solid temperature T^s_{ave} indicated in the top left of each figure. Likewise in Fig. 6.7, the CHT results fluid fields compare well with fluid-only solutions at wall temperatures close to the solid spatially averaged temperature of the coupled solutions. In particular, the colder solid temperature solutions issued by cases B and C compared to case A lead to a localization of the flame foot slightly farther downstream than for case A. Furthermore, although the solid conductivity is multiplied by the same factor 10 between cases A and B and cases B and C, significant modifications of the solid and fluid fields are observed when comparing Figs. 6.9a and 6.9b while Figs. 6.9b and 6.9c remain very similar. Such important variations between cases A and B and reduced changes between cases B and C are also evidenced through the solid spatially averaged temperature. Indeed, this quantity differs by 85 K between cases A and B while only 8 K differentiates cases B and C.

Lifted solid thermal fields are presented with more details in Fig. 6.10. Just like for the fluid domain, solid fields are perfectly symmetric with respect to the x axis. Therefore, the temperature field is shown on the top half of the solid domain while the heat flux magnitude along with heat flux vectors are presented on the bottom half of the solid domain. The heat flux magnitude scale remains unchanged for all the three cases while the temperature scale is adapted to match the minimal and maximal temperature reached in the solid for each case.

The patterns exhibited for different solid conductivities are very similar. In all the cases, the isothermal contours are quite perpendicular to the x axis near the centerline and slightly distorted at corners. This last feature results from an enhanced exchange rate at these locations due to a large friction velocity at the flame holder front corner as well as a clustering of isotherms close to the wall at the back corner (Fig. 5.7). The heat flux fields are in accordance with such conclu-

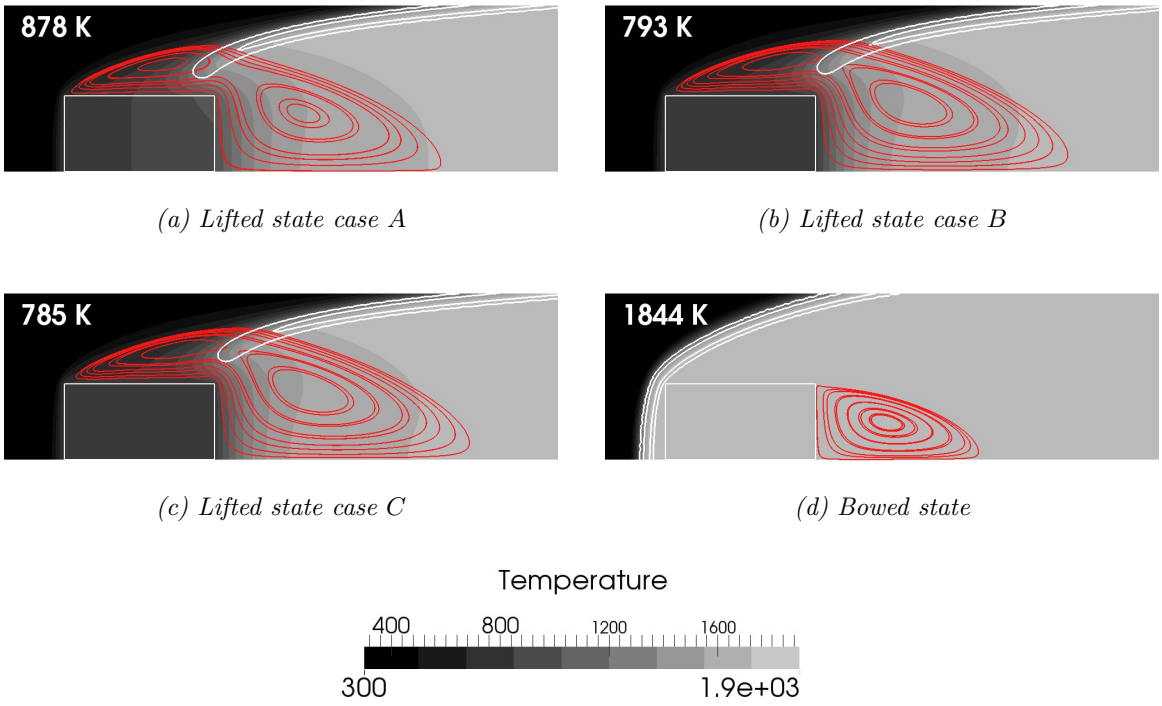

(a) Lifted state case A

(b) Lifted state case B

(c) Lifted state case C

(d) Bowed state

Figure 6.9: Temperature field of the four CHT converged states in both fluid and solid domains with heat release contours at $HR = 10^8\ J.m^{-3}.s^{-1}$ (outer flame contour) and $HR = 10^9\ J.m^{-3}.s^{-1}$ (inner most flame contour) in white and flow streamlines within the recirculation zone (red) in the vicinity of the flame holder on the top half of the domain. The solid domain is indicated with the white square.

sions. Heat flux magnitude is indeed maximal at the corners while low values are reached near the centerline. Note also that fluxes are mainly oriented from the back to the front faces of the solid with a tangential penetration of heat that is enforced mainly by the back face corner. Finally, for case A, the flame foot is located upstream the back corner and slightly closer to the wall than for cases B and C (Fig. 6.9). This results in little differences in fluxes fields along the lateral face or close to the flame holder back corner (Fig. 6.10).

This is further emphasized by the flux repartition along the bluff-body surface displayed in Fig. 6.11. To allow comparison with fluid-only solutions, the flux distribution is also reported for the isothermal cases with $T_w \in [800; 900]\ K$. Note that for clarity, flux repartition obtained for the bowed converged solution is not shown. In this specific case, the walls and the surrounding fluid are at the same temperature and fluxes equal zero all along the flame holder surface. Fluxes obtained with CHT simulations for the lifted regimes are very similar to those predicted by the fluid-only simulations. All the three cases exhibit fluxes close to the $T_w = 800\ K$ curve along the bluff-body front and first half of the lateral faces, which is coherent with the solid temperature

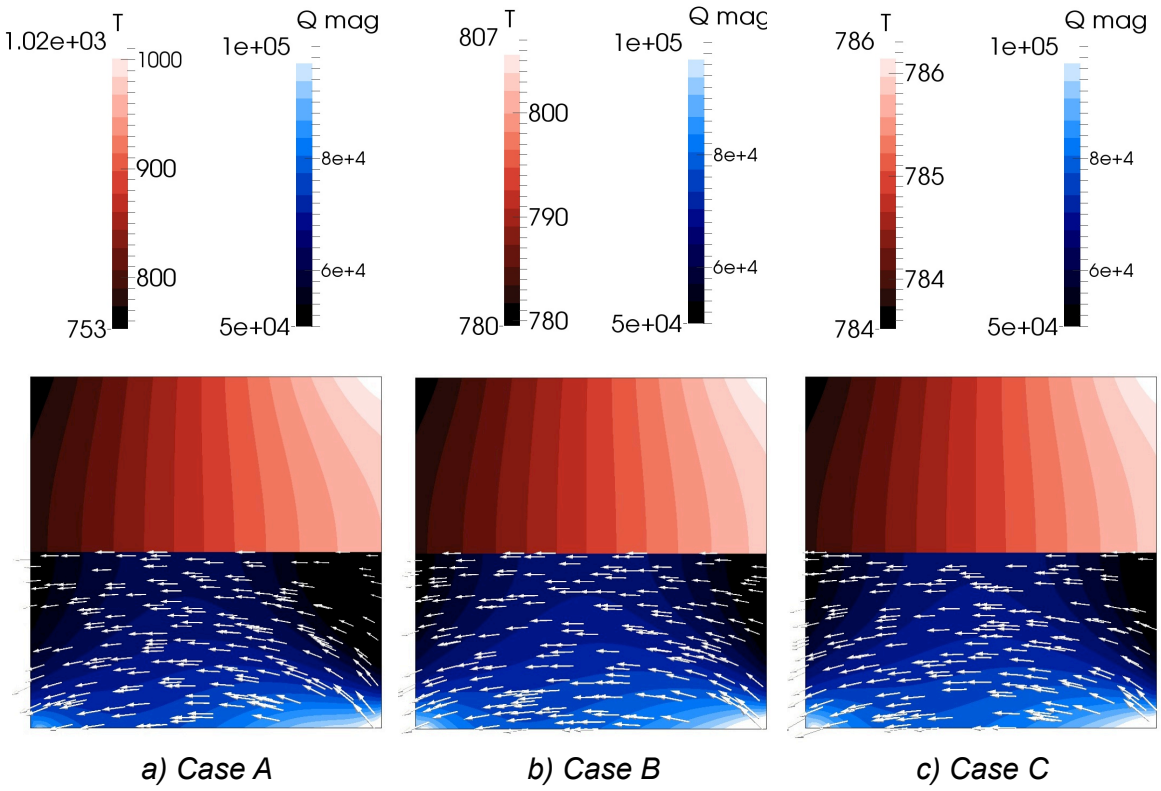

Figure 6.10: Solid thermal fields of the lifted CHT converged states. Temperature on the top of the domain (red levels) and heat flux magnitude along with heat flux vectors on the bottom of the domain (blue levels).

in these regions (Fig. 6.9). At the lateral face mid-length, the solution obtained with the lowest conductivity (case A) separates from the other curves and gets closer to the behavior obtained for the fluid-only solution with a wall temperature $T_w = 900\ K$. To conclude, wall fluxes obtained with CHT and fluid-only solutions are very similar and bifurcations of the CHT curve for case A from one isothermal curve to another are only issued by the changes in local temperature along the faces associated with the low conductivity of the solid material.

The decrease of the spatially averaged steady solid temperature with increased conductivity previously observed for lifted cases in Figs. 6.9 and 6.10 is now explained with a simple analytic model. Note that, to ease the use of this model and understand the bluff-body configuration evolution, the same quantity denominations as for the full 2D problem are used in the model. The quasi one-dimensional distribution of the solid thermal fields evidenced in Fig. 6.10 allow to simplify the problem and consider the simple one-dimensional model proposed in Fig. 6.12. The domain of interest is now reduced to a solid of thickness d in the axial direction and infinite in the other

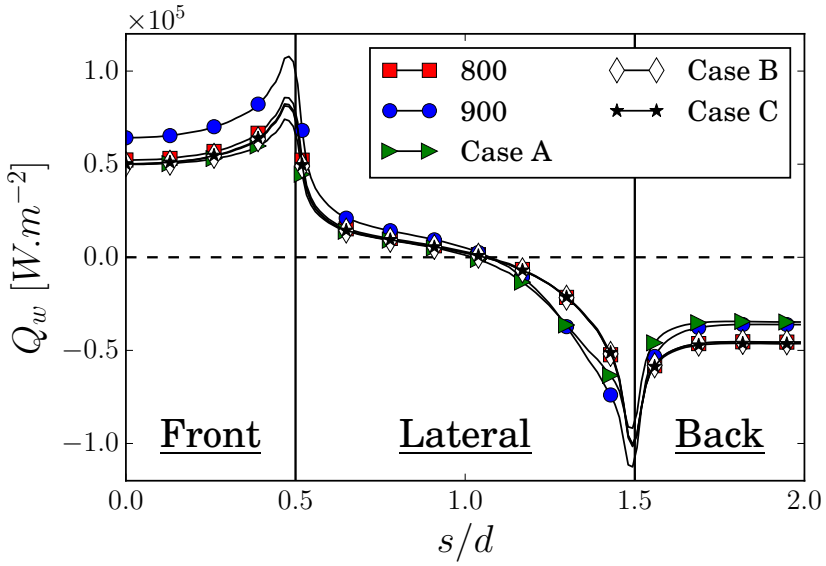

Figure 6.11: Wall heat fluxes distribution along the skin of the bluff-body top half, for the lifted fluid-only flames $T_w \in [800; 900]$ K) and CHT lifted solutions. Fluxes are oriented towards the fluid.

direction. The material conductivity is λ_s and the solid is submitted to convective fluxes on both left and right surfaces respectively denoted ϕ_1 and ϕ_2. These thermal conditions may hence be expressed as:

$$\phi_1 = h_1(T_w^1 - T_0) \quad and \quad \phi_2 = h_2(T_w^2 - T_{adiab}), \tag{6.2}$$

where h_1 and h_2 are the convective heat transfer coefficients respectively for the left and right surfaces and T_w^1 and T_w^2 stand for the wall temperatures on both sides (Fig. 6.12).

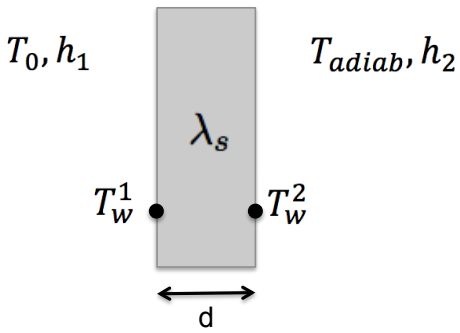

Figure 6.12: Schematic description of the 1D solid model.

Since only the steady state is considered here, fluxes are equal. As a result, one can get the

expression of the wall temperatures at steady state[1]:

$$\begin{cases} T_w^1 = \dfrac{\lambda_s\,(h_1\;T_0\;+\;h_2\;T_{adiab})\;+\;h_1\;h_2\;d\;T_0}{\lambda_s\,(h_1+h_2)\;+\;h_1\;h_2\;d} & (6.3) \\ T_w^2 = \dfrac{\lambda_s\;T_w^1\;+\;h_2\;d\;T_{adiab}}{\lambda_s\;+\;h_2\;d} & (6.4) \end{cases}$$

From these equations, two limit cases appear:

- ▷ If $\lambda_s \longrightarrow 0$

$$T_w^1 = T_0 \quad and \quad T_w^2 = T_{adiab} \tag{6.5}$$

  Temperature is strongly heterogeneous within the solid which behaves as adiabatic.

- ▷ If $\lambda_s \longrightarrow +\infty$

$$T_w^1 = T_w^2 = \frac{h_1\;T_0\;+\;h_2\;T_{adiab}}{h_1\;+\;h_2} \tag{6.6}$$

  Temperature is homogeneous in the solid and governed by the respective value of convective coefficients on each side of the solid (i.e. for the bluff-body case by the respective upstream and downstream aerodynamic fields).

The spatially averaged temperature in the solid T_{ave} can then be deduced for these two extreme cases and reads:

$$\underset{\lambda_s \longrightarrow 0}{T_{ave}} = \frac{T_w^1 + T_w^2}{2} = \frac{T_0 + T_{adiab}}{2} \tag{6.7}$$

and

$$\underset{\lambda_s \longrightarrow +\infty}{T_{ave}} = \frac{T_w^1 + T_w^2}{2} = T_w^1 = \frac{h_1\;T_0\;+\;h_2\;T_{adiab}}{h_1\;+\;h_2} \tag{6.8}$$

As a result, the larger the conductivity, the higher is the impact of the ratio h_1/h_2 on T_{ave}. Besides, whether the solid spatially averaged temperature increases or decreases with increased conductivity depends on the value of the convective heat transfer coefficients ratio compared to one (i.e. whether h_1 is superior or inferior to h_2).

These equations are now used to compute a theoretical solid spatially averaged temperature for the three converged lifted regimes obtained on the bluff-body configuration. The convective heat transfer coefficients on the flame holder front and back face are deduced from Eq. (6.2), where T_w^1 and T_w^2 are obtained by a spatial average of the temperature over the corresponding face. Results are given in Tab. 6.1 where T_{ave}^{th} is the computed theoretical solid spatially averaged temperature, T_{ave}^{simu} the corresponding temperature obtained in the simulations and $\Delta T_{rel} = (T_{ave}^{th} - T_{ave}^{simu})/T_{ave}^{simu}$ the relative difference between these two temperatures. Tab. 6.1 indicates a very reduced variability

[1] Note that it is clear from these expressions that these can also be expressed as a function of the Biot number (Eq. (3.3))

of the ratio h_1/h_2 between the three cases which lies around 2.5. As a result, since T_0 is naturally inferior to T_{adiab}, the solid spatially averaged temperature decreases when the solid conductivity increases. Such a tendency is accurately predicted both by the theoretical calculation and the simulation. However, T_{ave}^{th} slightly underestimates the solid spatially averaged temperature obtained in the simulations of around 5% for cases B and C and 12% for case A. For the latter case, the flame foot is closer to the flame holder walls (Fig. 6.9), inducing more interactions with the flame on the lateral surface. As a consequence, the one-dimensional hypothesis is less valid for this case (Fig. 6.10) and hence can induce larger behavior differences with the model. Nevertheless, the model evidences clearly the physical phenomena responsible for the decrease of the spatially averaged solid temperature and provides a fairly good first approximation of this temperature.

Case	h_1 $[Wm^{-2}K^{-1}]$	h_2 $[Wm^{-2}K^{-1}]$	h_1/h_2 $[-]$	T_{ave}^{th} $[K]$	T_{ave}^{simu} $[K]$	ΔT_{rel} $[-]$
A	120	48	2.5	775	878	11.7%
B	122	50	2.4	755	793	4.8%
C	122	50	2.4	750	785	4.5%

Table 6.1: Quantities deduced from the three converged lifted regimes.

The lifted converged cases have now been investigated into details. Still a specific investigation of the physical phenomena at the origin of the bifurcations between lifted and bowed converged states is required. For this purpose, the numerical establishment of the various states is investigated in the next section.

6.3 Analysis of the convergence history of the coupled simulations

The convergence history of all the CHT simulations for the three cases A, B and C is investigated to gain insight into the mechanisms responsible for the different converged state selection. As a reminder, due to the desynchronization process, the transient phase does not correspond to the real time response of the system which is actually accelerated. However the physical mechanisms described here are not expected to be altered by this specific coupling strategy, the time scale of the fluid being several orders of magnitude lower than the solid one (stationary laminar flow).

As observed in Fig. 6.8 and among all the cases investigated here, the initial solution $T_{init} = 1000\ K$ is the only one which can lead both to the lifted and bowed flame converged regimes depending on the solid conductivity. Therefore, the study naturally focuses first on this bifurcation. For this purpose, the whole convergence history of the two cases for which $T_{init} = 1000\ K$ and the solid conductivity equals either λ_A^s or λ_B^s are discussed.

6.3.1 Investigation of the numerical establishment of the different converged states obtained for $T_{init} = 1000\ K$

For the initial state $T_{init} = 1000\ K$, case A converges to the bowed regime observed in Fig. 6.9d while the lifted regime presented in Fig. 6.9b is obtained for case B. As a reminder, all the numerical and physical parameters but the conductivity are similar in both cases. In particular, the temporal acceleration of the solid domain is the same (this is equivalent to the same decrease of the quantity ρC) in the two cases. The bifurcation between the two distinct solutions is easily illustrated when summing the wall flux contributions over the whole flame holder surface. This quantity evolution in time is presented for both cases in Fig. 6.13. Results are shown as a function of the solid time for the beginning of the coupled simulations. The energy balance evolution clearly illustrates the bifurcation between the two cases: during the quasi totality of the transient phase, heat is transferred from the fluid to the solid in case A and in the opposite direction in case B. However, and although these fluxes are symptomatic of the two separate evolutions, they do not provide any indication on the different physical phenomena responsible for the bifurcation. The two considered cases are thus further investigated through instantaneous 2D fields.

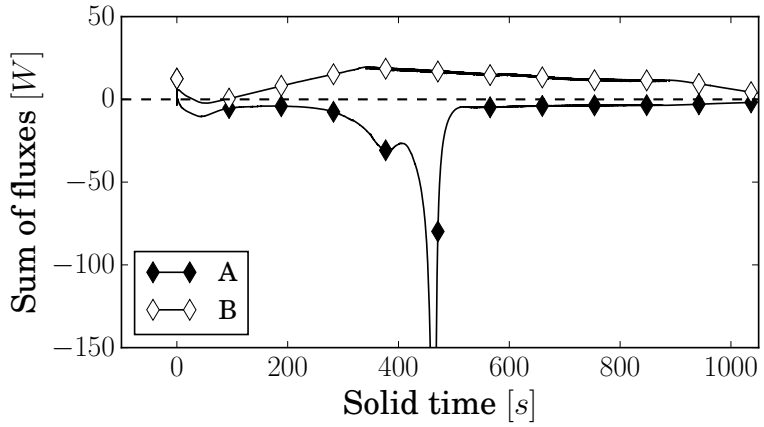

Figure 6.13: Evolution of the heat flux integrated over the entire flame holder surface for $T_{init} = 1000\ K$ with $\lambda_A^s = 1.5\ W.m^{-1}K^{-1}$ and $\lambda_B^s = 15\ W.m^{-1}K^{-1}$. Results are presented in the solid reference time only for the first half of the simulation.

Figure 6.14, presents the thermal fields in both fluid and solid domains at various instants during the transient phase. In the solid domain, the temperature field is shown on the top of the domain (red levels) while the bottom half presents the heat flux magnitude along with the heat flux vectors. The fluid domain is colored by temperature and additional HR and zero velocity contours are shown respectively in black and white. Note that the same color scales are used in both cases for all quantities. From top to bottom, fields are shown in the solid time scale at $t_s = 9.42, 236$ and $471\ s$.

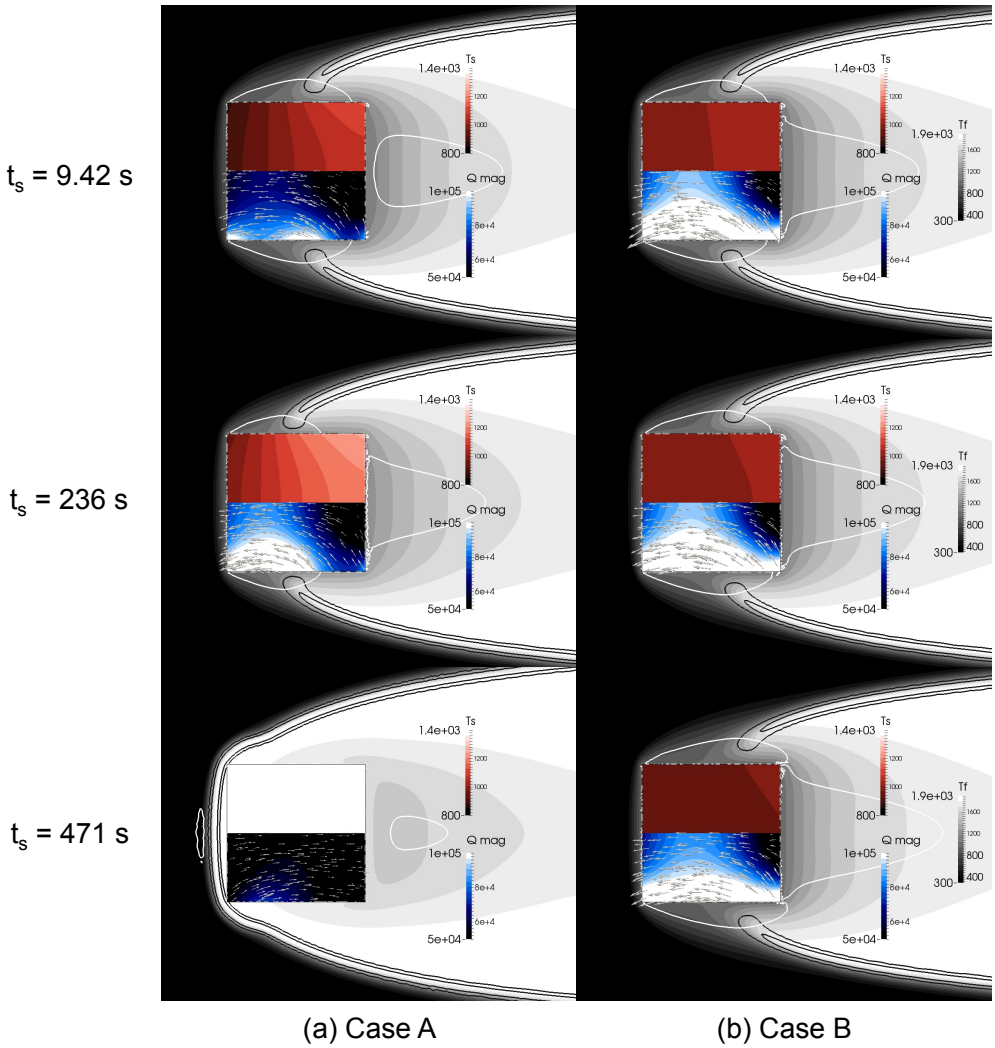

Figure 6.14: Instantaneous temperature fields of two cases for which $T_{init} = 1000\ K$ and the solid conductivity equals either λ_A^s or λ_B^s in both fluid and solid domains with heat release contours at $HR = 10^8\ J.m^{-3}.s^{-1}$ (outer flame contour) and $HR = 10^9\ J.m^{-3}.s^{-1}$ (inner most flame contour) in black and zero velocity contour in white. The solid domain is indicated with the white square. For both computations, results are given from top to bottom at $nit_{cpl} = 2000, 50000$ and 100000 corresponding respectively in the solid time scale to $t_s = 9.42, 236$ and $471\ s$.

▷ At $t_s = 9.42\ s$, the fields obtained from the two cases A and B indicate a very similar location of the flame and differences between fluid fields are only exhibited through modifications of the back part of the recirculation zone. As expected, the solid temperature field is clearly more heterogeneous for case A than for case B. Besides, the latter evidences more important heat fluxes within the solid domain and at the bluff-body front face (corresponding to an enhanced evacuation of heat towards fresh gases surrounding that face).

- ▷ For $t_s = 236\ s$, an opposite response is observed on the fluid and solid counterparts of the two cases. With a low solid conductivity (case A), the solid temperature is increased compared to the previous instant. The flame has moved upstream and heat fluxes in the solid are stronger (because of the flame foot location closer to the wall). According to the flame displacement, fluid temperature contours in the vicinity of the flame holder back face get hotter. In case B, opposite effects are observed: the solid domain is cooler than at $t_s = 9.42\ s$ and the flame foot positions slightly downstream.
- ▷ Finally, for $t_s = 471\ s$, the previously observed tendencies are even more amplified. The flame has reached the bluff-body front face in case A and the two flame branches have joined upstream of the body. As a result, heat fluxes in the solid reverse and orient from the front to the back face. Heat is supplied from upstream to downstream until the solid and the fluid in the solid wake reach the adiabatic flame temperature. At the same time, case B flame keeps moving downstream.

The observations of the heat flux are then considered from a more quantitative point of view: the distributions along the flame holder walls are integrated separately on the front, back and lateral faces. Just like for Fig. 6.13, results are shown as a function of the solid time (only for the beginning of the coupled simulations) in Fig. 6.15. To ease understanding, the temporal location of the solutions presented Fig. 6.14 are indicated with vertical grey lines.

At initialization, all the fluxes of case A peak, indicating a discontinuity and an imbalance between the fluid and the solid domain initial conditions. Such a feature although exhibited in case B is observed to yield a reduced amplitude compared to case A: the initially homogeneous temperature solid field is more coherent with the fluid field in case B than with case A (as expected). Then, the evolution of the fluxes integrated over the various faces are in accordance with previous observations. During the first instants of the simulations (first vertical grey line), lateral fluxes are similar for both cases. Heat fluxes on the front face are somewhat more significant for case B than for case A, indicating an enhanced evacuation of heat towards the fluid for the former case. This, however is offset by fluxes at the back face that depicts a superior magnitude in case B, corresponding to more heat brought to the solid domain through that face.

After these first instants, all the flux components (front, lateral and back face) evolutions are seen to clearly differ comparing case A and case B. The lateral flux magnitude of case A increases with time as the flame gets closer to this wall. This increasing heat transfer from the fluid to the solid at the lateral face leads to a symmetrical increase of the heat provided from the solid to the surrounding gases at the front face, ensuring an enhanced fresh gases preheating. Lateral and front flux magnitudes in case A eventually reach an extreme before to suddenly decrease in magnitude as the flame foot approaches the front face. At that point, a negative peak appears in the heat flux of the front face, closely followed by a positive peak on the back face: heat is no more

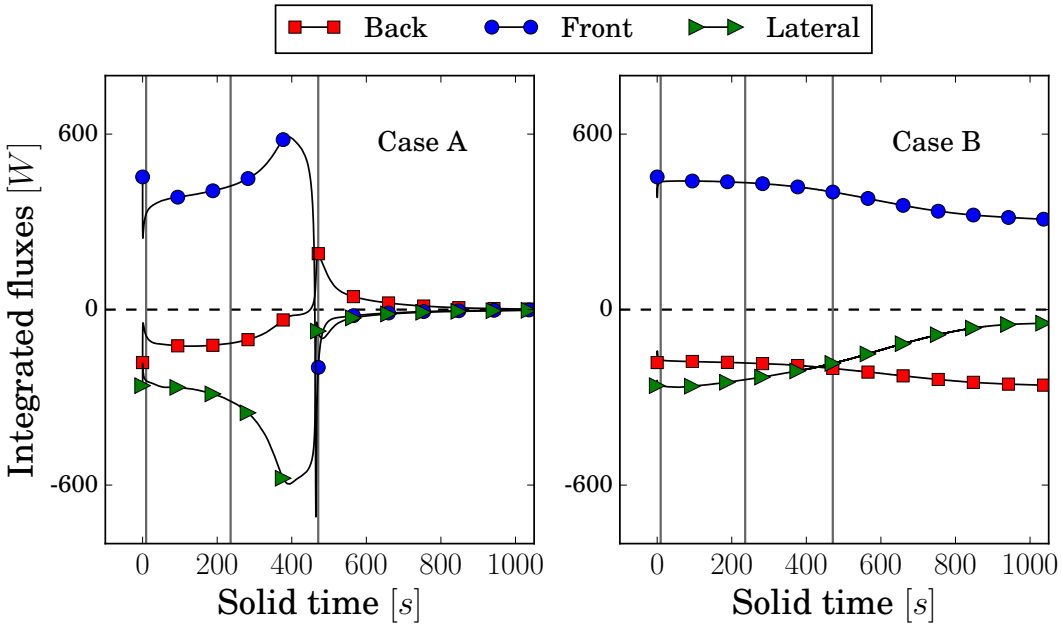

Figure 6.15: Evolution of the integrated heat fluxes on the front, the back and both lateral faces of the flame holder for $T_{init} = 1000\ K$ with $\lambda_A^s = 1.5\ W.m^{-1}K^{-1}$ and $\lambda_B^s = 15\ W.m^{-1}K^{-1}$. Results are presented in the solid reference time. Vertical grey lines indicate the temporal locations of the solutions presented in Fig. 6.14.

supplied from downstream to upstream by the solid body but rather takes an opposite stream which settles when the flame has passed ahead of the flame holder (third vertical grey line). Finally, considering the high conductivity case B, all heat fluxes on every sides depict a monotonous evolution: as the flame moves downstream, the solid is less and less heated through the lateral faces. The resulting temperature decrease in the solid leads to an increase of the temperature difference between the body and the burnt gases, enhancing heat fluxes at the back face. At the same time, the temperature difference between the solid and the fresh gases decreases, leading to smaller heat exchanges at the front face.

From the observations of Figs. 6.14 and 6.15, the natural processes of solid warming or cooling illustrated in Fig. 6.16 and underlying the evolution of cases A and B are evidenced. However, the key role of conductivity in selecting one of these two loops or the phenomena responsible for the beginning of a different loop is not clear. Besides, the aerodynamic fields play also a key role in flame stabilization and heat exchanges as evidenced for example in Chapter 5 with the central action of the recirculation zone or in the determination of the spatially averaged solid temperature in the previous section (Fig. 6.2). The impact of aerodynamics on the bifurcation between the lifted and the bowed regimes remains however hardly identifiable.

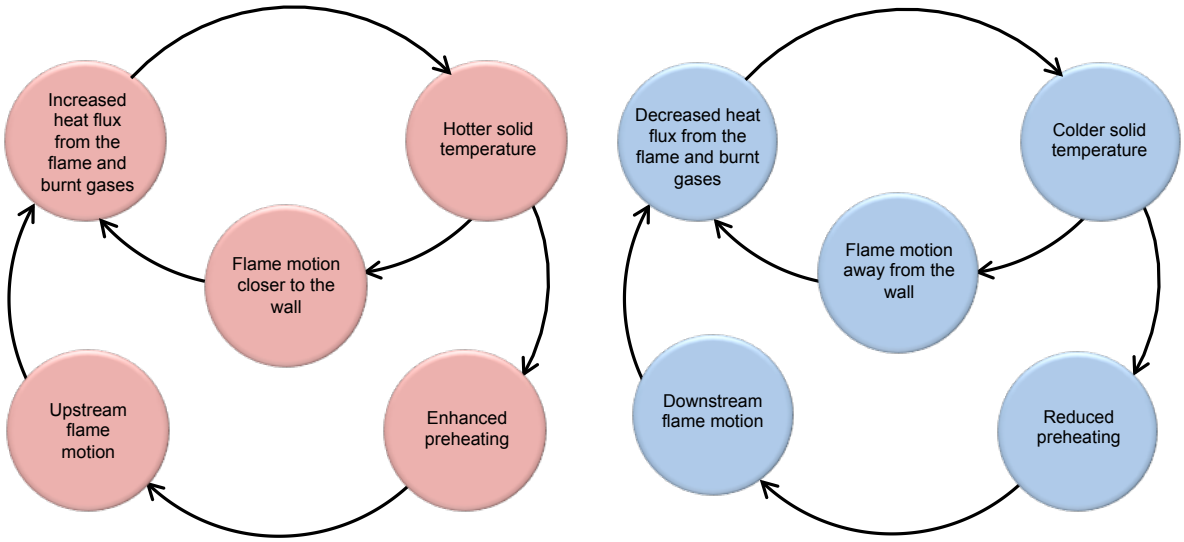

(a) Heating loop *(b) Cooling loop*

Figure 6.16: Natural loop processes of solid warming and cooling.

To conclude, in case A, the local conditions at the flame foot location provide sufficiently robust heat local conditions for the flame to maintain and in turn heat the solid. This heating leads to an upstream propagation of the flame enlarging the hot gas region on the lateral faces until a stabilization in a bowed regime. On the other hand, in case B, because of the high conductivity, the solid body does not manage to heat up: neither the flame nor the hot burnt gases on the back face are sufficient to warm up the solid body against the convection mechanism of fresh gases. The flame then moves downstream until a stable lifted flame appears. The only difference between these two simulations being the solid conductivity, this quantity is clearly responsible for the bifurcation. However, the tight coupling existing between the various phenomena responsible for flame stabilization makes complicated a clear identification of the specific key phenomena triggered by the different conductivity and at the origin of the bifurcation.

For all initial temperatures different from $T_{init} = 1000\ K$, the solid conductivity is shown to have no effect on the selection between the lifted and bowed regimes (Fig. 6.8). Further generalization of the present observations to cases with a different initial temperature emphasize that for initial temperatures above $T_{init} = 1000\ K$, the solid domain is initially at a sufficient temperature to allow the upstream flame displacement whatever the solid conductivity while the opposite conclusion can be drawn for cases with an initial temperature below $T_{init} = 1000\ K$.

6.3.2 Global convergence of all the CHT simulations

The evolution of all the CHT coupled simulations is now investigated. As a reminder, three sets of simulations have been performed with varying solid conductivities corresponding to cases A, B and C. Each set includes 7 simulations for which the initial conditions are $T_{init} = T_w$(at the initialization) = 700, 900, 1000, 1100, 1400, 1700, 2000 K. These are initialized in the fluid domain from the fluid-only converged solutions at the corresponding wall temperature and in the solid domain with a homogeneous temperature equal to the fluid wall temperature. To investigate the overall convergence path of the coupled simulations, the evolution of integrated wall heat fluxes on the front, back and lateral faces as a function of the solid spatially averaged temperature is shown for all tested cases in Fig. 6.17. The two different ordinate scales corresponding to the lifted and bowed regimes are highlighted with white or grey plot backgrounds. Besides, for each simulation, an arrow indicates the simulation direction of evolution from the initial state to convergence.

The evolution of integrated wall heat fluxes on the front, back and lateral faces as a function of the solid spatially averaged temperature evidences three different progressions of the CHT simulations highlighted with three boxes in Fig. 6.17:

- ▷ Blue solid line boxes (——): The solid convergence is monotonous for all computations converging towards lifted flame solutions as well as for the bowed flame results if the flame is initially located upstream of the flame holder (T_{init} = 1700 and 2000 K). In these two cases, only slight flame motions are encountered during the transient phase and aside from clear heat flux peaks at the initialization of some simulations (due to the discontinuity and imbalance between the fluid and solid domains), all the physical fields evolve in a smooth way.

Leaving aside these monotonous cases, two different types of wall heat flux evolutions are observed for, on one hand λ^s_A or λ^s_B and on the other hand λ^s_C:

- ▷ Red dash-dotted line box (– · –): For low conductivities, cases depict a transient evolution consistent with the temporal evolution observed in Fig. 6.15 for T_{init} = 1000 K with λ^s_A. For the cases within this category, a peak negative flux is observed at the front immediately followed by a smaller peak at the back face. These correspond to the flame getting over the bluff-body front face when the solid spatially averaged temperature reaches a value between T_{ave} = 1600 K and T_{ave} = 1700 K which correlates with the observations made on fluid-only solutions (Fig. 6.1).
- ▷ Red dashed line box (– – –): For the high conductivity value of cases (C), no significant peak is observed in the front, back and lateral integrated fluxes. For all these cases, the solid domain is thermally quasi-homogeneous all along the transient phase and no reversal of the heat flux from downstream-to-upstream to upstream-to-downstream appears when the flame gets over the flame holder front face.

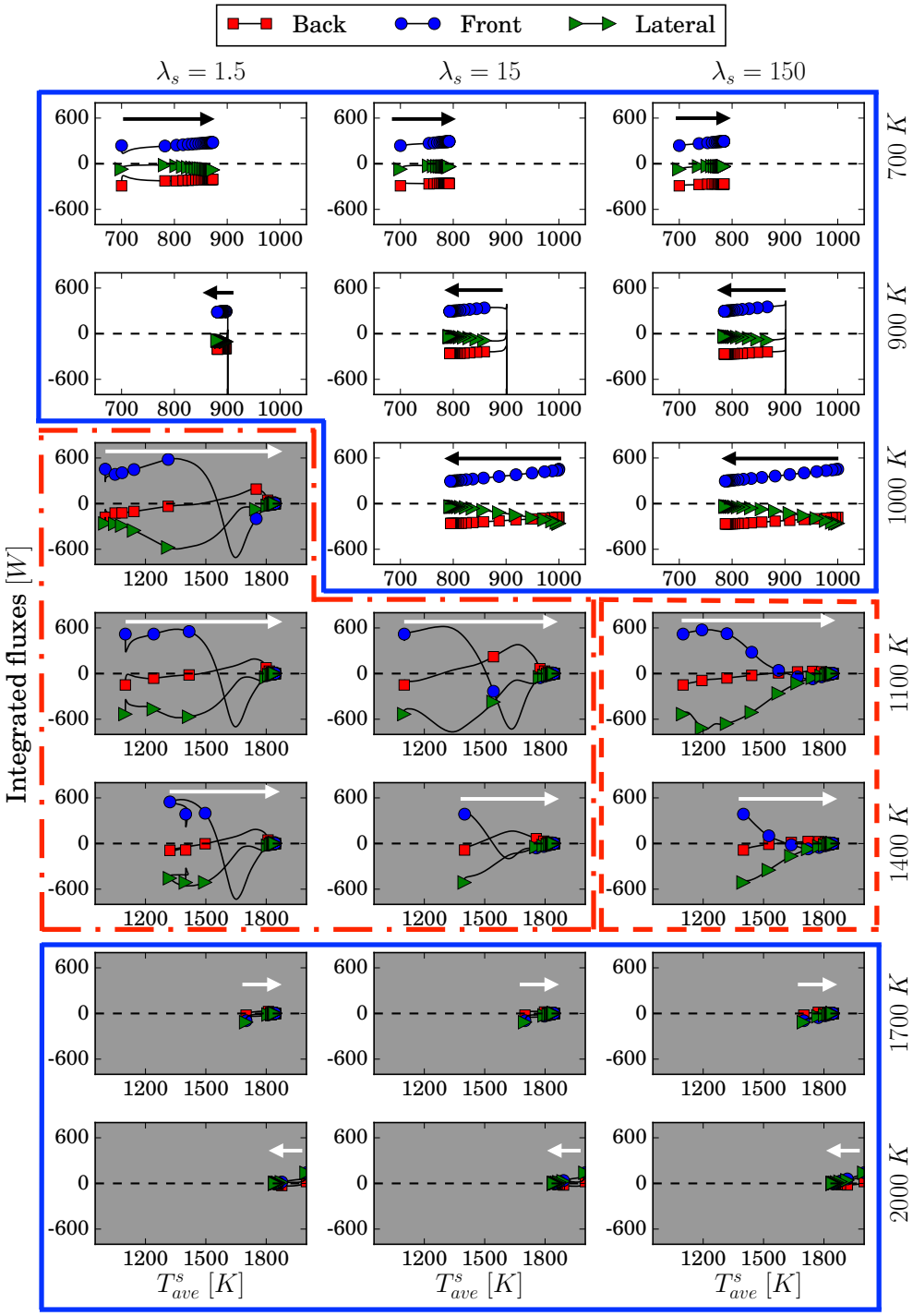

Figure 6.17: Evolution of the integrated heat fluxes on the front, the back and both lateral faces of the flame holder for all CHT simulations. Results are presented in the solid reference time.

Note that the evolution of the wall heat flux over the entire bluff-body surface (not shown) leads to the same conclusion with two evolution types.

These different processes but also the "distance" between the initial conditions and the converged solutions may affect the convergence time of the coupled simulations. This specific point is now investigated through an evaluation of the convergence time associated to each computation. This time corresponds to the physical time which needs to be computed to reach convergence of the joint fluid-solid system and is determined through two convergence criteria, one for each domain. The statistical data used for convergence determination are collected in both domains at each coupling iteration (hence at the same physical sampling rate whatever the solid conductivity). The solid convergence time is determined so that:

- ▷ The spatially averaged temperature as well as the minimal and maximal temperatures in the domain equal the corresponding final temperatures within more or less 1 K. Note that these final temperatures are determined a posteriori at the end of each computation.
- ▷ The spatially averaged temperature as well as the minimal and maximal temperatures in the domain variation between the current coupling iteration and an averaging window encompassing the previous 1000 coupling iterations is below 1 K.

Likewise, convergence of the fluid domain is assumed when similar conditions are satisfied for the spatially averaged temperature (the minimal and maximal temperatures in the domain being fixed respectively by the inlet and adiabatic flame temperatures and hence not subject to variations). The convergence criteria proposed here provide orders of magnitude of the coupled simulation convergence times and allow the comparison of the different cases. Note however that the choice of a tolerance (here equal to 1 K) for both criteria is arbitrary.

Both solid and fluid convergence times are reported in the solid time scale in Fig. 6.18 where the fluid spatially averaged temperature convergence history is presented. The solid convergence time is indicated with a vertical dashed line while the solid line stands for the fluid convergence time. In all the cases presented here, the fluid domain converges either faster or at the same rate as the solid domain (Fig. 6.18). Therefore, with the criteria chosen here, the solid domain is the limiting domain for the coupled computation convergence and is thus retained for comparison between the various cases.

Figure 6.19 presents the solid convergence times as a function of the initial conditions of the coupled simulations for all the three solid conductivities of cases A, B and C. All bowed cases lead to faster convergence than the lifted cases. Considering first coupled simulations converging towards the bowed flame, convergence times decrease as T_{init} increases up to $T_{init} = 1700\ K$ whatever the solid conductivity. For $T_{init} = 1700$ or $2000\ K$, the flame is initially stabilized upstream of the flame

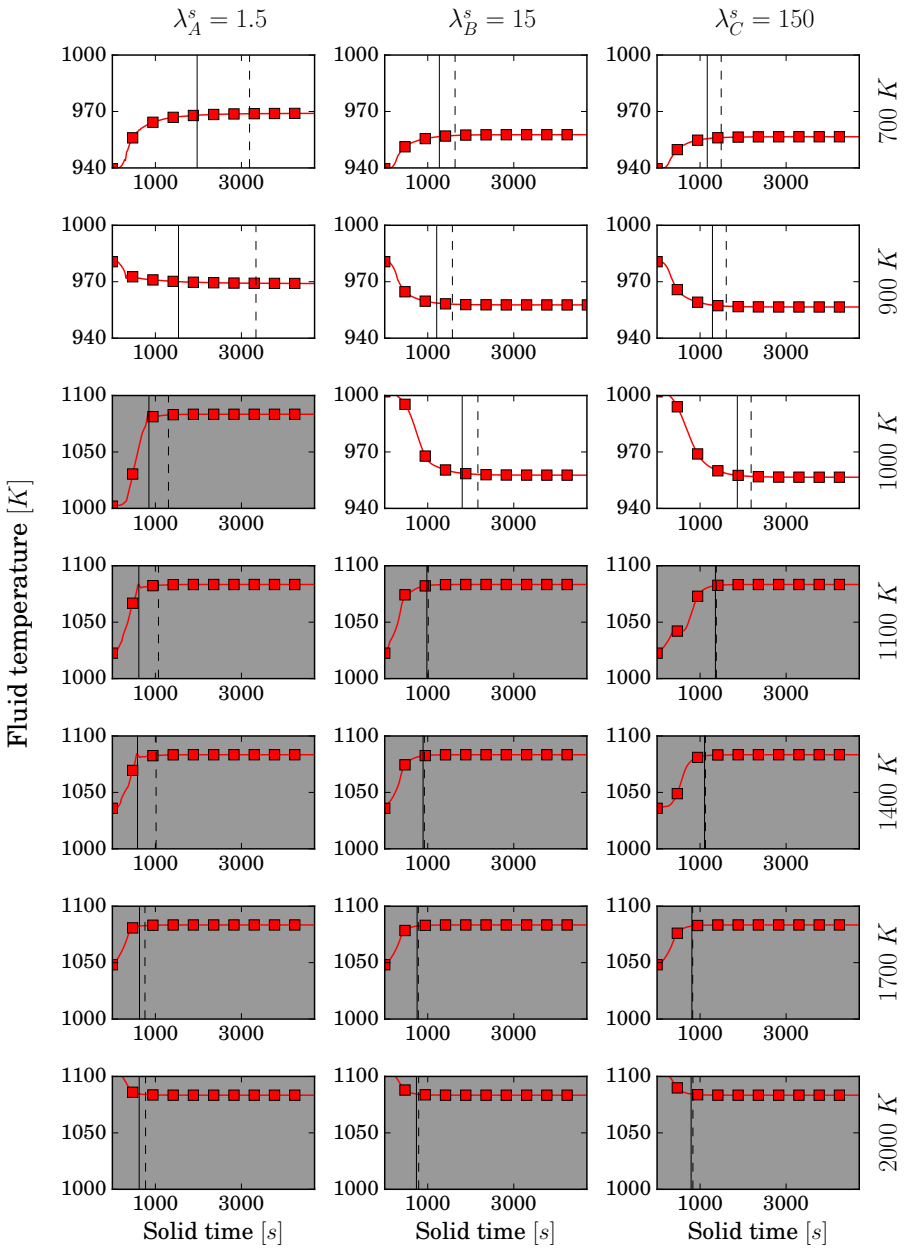

Figure 6.18: Convergence of the fluid spatially averaged temperature for three different values of the solid thermal conductivity λ_s in the solid time scale. Initial conditions T_{init} = 700, 900, 1000, 1100, 1400, 1700, 2000 K are indicated on the right of each plot and the two different ordinate scales are highlighted with white or grey plot background. The solid convergence time is indicated with a vertical dashed line while the solid line stands for the fluid convergence time.

holder (Fig. 6.1) and convergence times are no longer altered by the initial state. The lifted cases exhibit larger convergence times especially for the lowest conductivity (case A). In this last case, diffusivity is low which leads to an increase of the the solid response time compared to cases B and C which in turn limits the convergence of the whole fluid-solid system. Besides, the gap between fluid and solid convergence times is particularly large in this specific case (Fig. 6.18). In cases B and C, similar convergence times are obtained for $T_{init} = 700$ or $900\ K$, these initial conditions yield significantly shorter times of convergence than for $T_{init} = 1000\ K$. From the convergence times obtained for both bowed and lifted cases, it is clear that the "closer" the initial state is from the converged state the faster is the convergence of the coupled simulation. Therefore, aside from the previously highlighted bifurcation between two different converged solutions depending on the initial state, a good initial guess of the coupled converged solution allows clear saving of CPU effort.

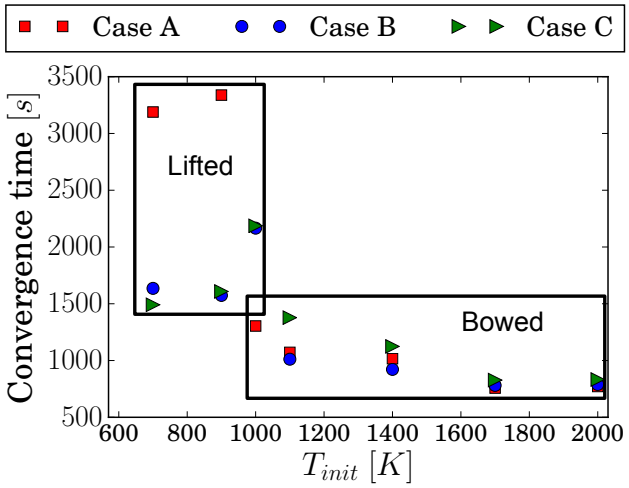

Figure 6.19: Solid convergence time of all the CHT simulations.

In the next section, the two specific cases for which $T_{init} = 1000\ K$ and the solid conductivity equals either λ_A^s or λ_B^s are again computed with a different coupling methodology derived from that proposed in Errera & Chemin (2013). Such simulations allow first to assess the reproducibility of the present results as well as to compare the previously discussed convergence times with those obtained with this different approach.

6.4 Comparison with the results obtained with a chaining methodology derived from Errera & Chemin (2013)

To assess the potential impact of the presently chosen coupling strategy on the CHT simulation converged solutions, additional computations are performed with a different approach derived

from the chaining methodology proposed in Errera & Chemin (2013) and previously discussed in Section 3.1.2. For this purpose, the two simulations investigated in Section 6.3.1 and for which $T_{init} = 1000\ K$ and the solid conductivity equals either λ_A^s or λ_B^s are selected.

Just like the main approach employed in this manuscript, the methodology proposed in Errera & Chemin (2013) targets steady state applications. However, the latter was developed in a chaining (rather than coupling) context involving a steady solid solver and a pseudo-steady fluid solver in which time-marching is used to converge flow quantities. Therefore the initial methodology is slightly adapted for the unsteady solvers employed here. As a reminder, a chained computation consists in running each solver successively for a fixed number of iterations or until convergence, update of the interface fields appears only at the beginning of each simulation. For the present computations, while the fluid solver is advanced in time so the associated fluid Fourier number (Eq. (2.20)) is of the order of $F = 20$ (i.e. $nit_f = 10000$), the solid domain is systematically brought to convergence. Note that while for previous CHT computations, the solvers desynchronization is equivalent to a reduction of the quantity ρC in the solid domain (Section 3.1.1), the systematic convergence of the solid domain in Errera & Chemin (2013)'s chained methodology corresponds to the limit case where $\rho C \longrightarrow 0$. This observation can be mathematically formalized thanks to Eqs. (3.6) when $t \longrightarrow \infty$.

Besides, since the solid domain is brought to convergence, the unsteady solid conduction solver is here employed to solve a stationary problem in the solid. Therefore and as mentioned in Section 2.2 the system is under-determined if only Neumann conditions are applied at its boundaries. As a result, to avoid any drift of the solid domain, the Neumann condition applied at the boundary conditions of the solid computations is replaced by a Fourier condition, leading to the interface equations of Eq. (3.20). The value of the CRP γ_f ensuring both stability and the theoretical highest convergence rate is then determined through the relation given in Errera & Chemin (2013) and recalled in Eq. (3.23). Note that the optimal value of γ_f is computed from local fluid quantities. Other parameters of the two simulations are kept unchanged and correspond to previously discussed CHT simulations.

For the purpose of the present comparison and to ease a better distinction of the coupled CHT simulations and the newly performed chained simulations, these are respectively referred to as *desynchronized CHT* and *chained* in the present section. Comparison between *desynchronized CHT* and *Chained* results is presented in Fig. 6.20 where the convergence history of fluid and solid temperatures as well as fluxes are shown for cases A and B. Note that contrary to previous results and since the solid domain is brought to convergence at each simulation loop, both fluid and solid results are presented in the fluid time scale. In addition, and since the fluid solver is several orders of magnitude more CPU consuming than the solid solver, the comparison between convergence rates of both methodologies performed in the following is thus representative of the

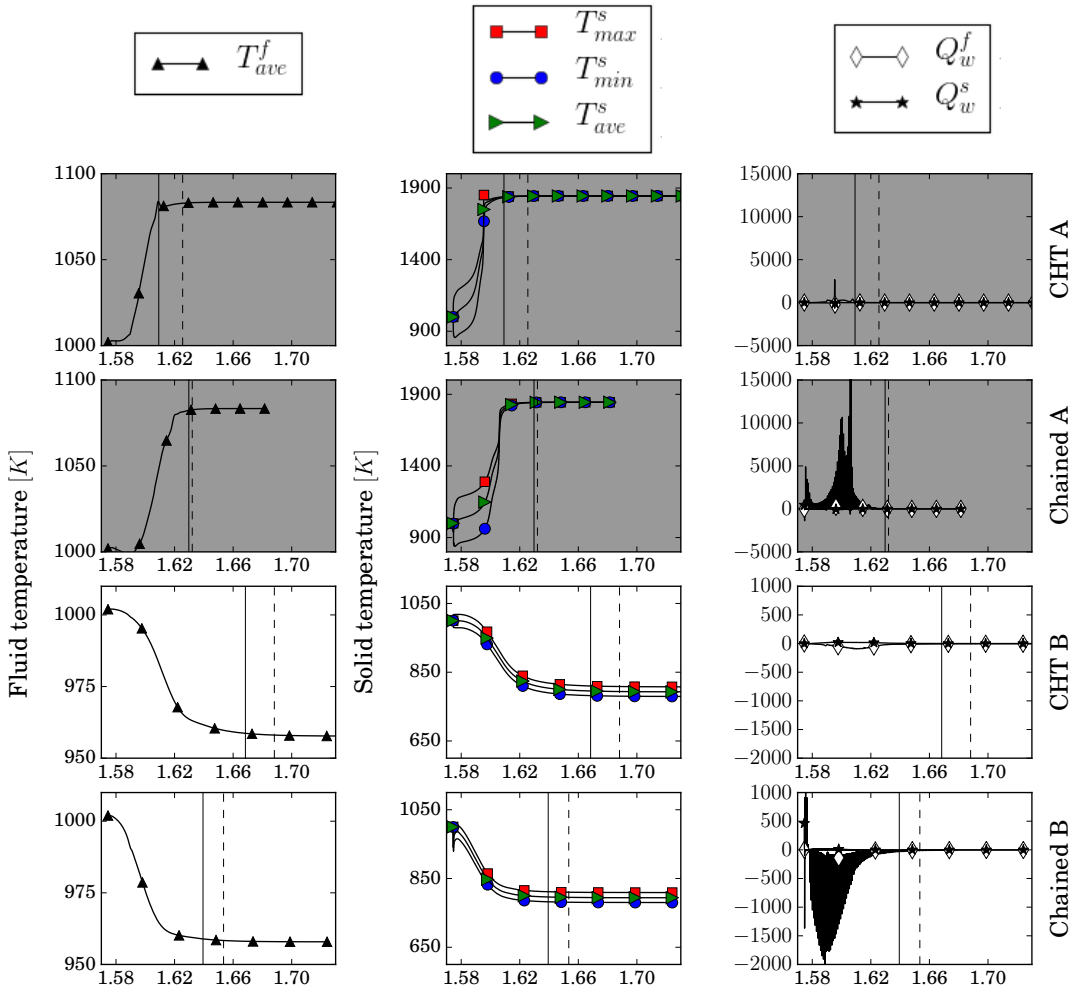

Figure 6.20: Convergence of the desynchronized CHT and Chained simulations for the initial conditions $T_{init} = 1000\ K$ and solid conductivity equal either to λ^s_A or to λ^s_B. Fluid spatially averaged temperature (left), solid minimal, maximal and spatially averaged temperatures (center), and solid and fluid fluxes integrated over the whole flame holder walls (right). The two different ordinate scales are highlighted with white or grey plot backgrounds.

CPU cost of the coupled simulation. Figure 6.20 indicates that the exact same converged solutions of the coupled problems are reached with both methodologies. Note that a comparison of the 2D fields (not shown) confirmed this conclusion. For the two cases A and B, the global convergence history of the *desynchronized CHT* and the *Chained* simulations are relatively similar. However, slight differences can be observed in the convergence rate. To further quantify such differences and just like in Fig. 6.18, the solid convergence time is indicated with vertical dashed lines. While convergence times towards the bowed flame of case A are very similar with both methodologies, this quantity is larger in the *desynchronized CHT* computation compared to the *Chained* simulation of

case B. However, this last observation does not allow to fully conclude on the respective CPU cost of both methods since a change of numerical parameters such as the fluid Fourier number of the *Chained* computation or the desynchronization factor between solvers of the *desynchronized CHT* computation modifies the convergence rate of both methods (not shown). Note that additional *Chained* computations performed for $nit_f = 50000$ (i.e. a Fourier number 5 times superior than previous cases) confirmed this conclusion and led to comparable convergence times in case B but almost doubled the convergence time of case A. Finally, note that in the present reactive context, where the flame motions are altered by the solid temperature, comparison and interpretation of the convergence rates becomes even more complex.

6.5 Conclusion

The strong coupling between flame stabilization and the thermal state of the whole system was investigated in this chapter. First, several fluid-only simulations with different bluff-body wall temperatures allowed to study the influence of such variations on the flame stabilization pattern and flow fields. These computations evidenced an upstream displacement of the flame foot as the wall temperature was increased and led to the identification of three main stabilization regimes. Indeed, as the flow pattern evolved with an increasing wall temperature, the flow switched from a lifted flame in which the recirculation zone provided the heat necessary to maintain the flame, to an anchored flame where fresh gas preheating was assured almost entirely by the walls or, for very hot temperatures, a bowed flame (stabilized ahead of the bluff-body) where combustion sustained through a pseudo auto-ignition process. Heat flux distributions along the bluff-body walls were observed to be dictated by the flame stabilization process, illustrating the different mechanisms. An integration of these fluxes on the whole flame holder surface highlighted a non-monotonous behavior as a function of flame holder wall temperature. In particular, three theoretical equilibrium states (for which the curve crossed null integrated flux axis) were evidenced for this configuration, suggesting that computation of more realistic cases including thermal conduction in the bluff-body solid could lead to different converged results depending on the initial thermal state.

The physical relevance of these three equilibrium states was then assessed by performing CHT simulations with various initial conditions inherited from the fluid-only fixed temperature computations. Since only the stationary solution was pursued, a desynchronization technique was employed to enhance the simulations convergence rate. Three different sets of simulations were performed with similar initial conditions and solid conductivity respectively equal to one (case A), ten (case B) and a hundred (case C) times the conductivity of a ceramic bluff-body. For each case, two different converged end states of the joint problem originating from the various initial conditions of the CHT simulations were exhibited. For initial conditions with low wall temperatures, the joint problem converged towards a lifted flame while a bowed flame was obtained for high initial temperatures. It appeared that even for very high conductivity (hence cases close to

the infinite conductivity hypothesis underlying an isothermal fluid-only case), the anchored regime was not a physical stable regime. Interestingly, depending on the conductivity, the bifurcation between the two equilibrium states was observed either between $T_{init} = 900\ K$ and $T_{init} = 1000\ K$ for case A or $T_{init} = 1000\ K$ and $T_{init} = 1100\ K$ for cases B and C. In addition, while all the converged bowed regimes solutions were strictly equivalent whatever the initial condition or the solid conductivity, the lifted converged regimes exhibited different converged solutions as a function of the solid conductivity. In particular, the solid spatially averaged temperature was observed to decrease with increased conductivity. This phenomenon resulted mainly from the aerodynamic field and was further explained through an analytic 1D model.

From the three sets of simulations, its was observed that the initial solution $T_{init} = 1000\ K$ was the only one leading either to the lifted or bowed converged regimes depending on the solid conductivity. These two different solutions resulted from the processes of solid warming in one case and cooling in the other case induced by the interactions between the solid, the flame and the thermal fields. With low solid conductivity, the local conditions at the flame foot location provided enough heat for the flame to maintain and in turn heat the solid. This heating led to an upstream propagation of the flame enlarging the hot gas region on the lateral faces until a stabilization in a bowed regime. On the other hand, when the solid conductivity was increased, the solid body did not manage to heat up: neither the flame nor the hot burnt gases on the back face were sufficient to warm the solid body to a point where it counteracts the convection mechanism of fresh gases. The flame then moved downstream until a stable lifted flame arises. However, the key role of conductivity in the discrimination between the two processes is still an open topic as well as the potential impact of the aerodynamic field which could play also a determining role in the bifurcation. Further generalization of the present observations to cases with a different initial temperature emphasized that for initial temperatures above $T_{init} = 1000\ K$, the solid domain was initially at a sufficient temperature to allow the upstream flame displacement whatever the conductivity while the opposite conclusion could be drawn for cases with an initial temperature below $T_{init} = 1000\ K$. These different processes as well as the "distance" between the initial conditions and the converged solutions were shown to affect the convergence time of the coupled simulations. In particular, all bowed cases led to faster convergence than the lifted cases and for both cases, the "closer" the initial state was from the converged state the fastest the convergence of the coupled simulation. Therefore, aside from the previously highlighted bifurcation between two different converged solutions depending on the initial state, a good initial guess of the coupled converged solution was shown to allow significant saving of CPU time.

Finally, the reproducibility of the present results was assessed through the realization of two specific CHT computations with a different approach derived from the chaining methodology proposed in Errera & Chemin (2013). These new computations exhibited the exact same converged solutions of the coupled problems further highlighting the accuracy and robustness of the coupling strategy employed in this manuscript.

Conclusion

To validate the added value of a CHT approach in the context of reactive flows and evaluate the coupled aerothermal solution proposed, a simplified academic case was first studied. In this chapter, a detailed investigation of the thermal behavior of a laminar premixed flame stabilized thanks to a square cylinder in a channel flow (Kedia & Ghoniem, 2014*a*,*b*, 2015) was proposed. For this purpose, various standalone fluid DNS as well as coupled CHT simulations have been performed, allowing a deep understanding and identification of the various phenomena involved and their interactions.

A baseline fluid-only computation was first performed to detail the mechanisms responsible for flame stabilization in regard to existing conclusions from the literature and provide a reference for further evaluation of several parameter induced variations in the flow mechanisms. This baseline simulation exhibited a steady flow field with a symmetric flame stabilization in two distinct fronts in the vicinity of the bluff body back corners. This was enabled by a large recirculation zone observed to have various effects: it brought hot temperature burnt gases upstream, both warming up and diluting the fresh gases while providing a favorable aerodynamic region with very low velocity. The heating of fresh gases allowed by the recirculation zone combined with that of the flame holder walls resulted in flame stabilization by allowing the fresh gases to reach ignition temperature. Conclusions drawn from the baseline simulation highlighted a strong relation between the aerodynamic and thermal fields as well as the flame stabilization pattern, suggesting hence a potential impact of the flame holder wall temperature on the found equilibrium.

To isolate the effect of the wall temperature distribution on flame anchoring and flow fields, several DNS with varying bluff-body wall temperature were then performed for which only the fluid domain was numerically solved. These computations evidenced an upstream displacement of the flame foot as the wall temperature was increased and led to the identification of three main stabilization mechanisms. Indeed, as the flow pattern evolved with an increasing wall temperature, the flow switched from a lifted flame in which the recirculation zone provided the heat necessary to maintain the flame, to an anchored flame where fresh gas preheating was assured almost entirely by the walls or, for very hot temperatures, a bowed flame (stabilized ahead of the bluff-body) where combustion sustained through a pseudo auto-ignition process. Heat flux distribution along the bluff-body walls was observed to be dictated by the flame stabilization process illustrating the

different mechanisms while integration of these fluxes on the whole flame holder surface evidenced that three theoretical equilibrium states may exist for the joint fluid-solid system.

The physical relevance of these equilibrium states was then assessed by performing CHT simulations with various initial conditions inherited from the fluid-only fixed temperature computations. Three different sets of simulations were performed for all these initial conditions with varying solid conductivities. All the simulations were observed to converge to only two of the three equilibrium states: the lifted regime for low initial temperatures and the bowed regime for large initial temperatures. Interestingly, depending on the conductivity, the bifurcation between the two equilibrium states was observed for different initial conditions. In addition, while all the converged bowed regime solutions were strictly equivalent whatever the initial condition or the solid conductivity, the lifted converged regimes exhibited different converged solutions function of the solid conductivity.

From the three sets of simulations, its was observed that the initial solution $T_{init} = 1000\ K$ was the only one leading either to the lifted or bowed converged regimes depending on the solid conductivity. These two different solutions resulted from the natural processes of solid warming in one case and cooling in the other case induced by the interactions between the solid, the flame and the thermal fields. For all other cases, an initial temperature above $T_{init} = 1000\ K$ ensured a solid domain at a sufficient temperature to allow the upstream flame displacement while an initial temperature below $T_{init} = 1000\ K$ induced the opposite effect.

These different processes as well as the "distance" between the initial conditions and the converged solutions were shown to affect the convergence time of the coupled simulations. In particular, all bowed cases led to faster convergence than the lifted cases and for both cases, the "closer" the initial state was from the converged state the fastest the convergence of the coupled simulation. Therefore, aside from the previously highlighted bifurcation between two different converged solutions depending on the initial state, a good initial guess of the coupled converged solution was shown to allow saving of CPU time. Finally, the reproducibility of the present results was demonstrated with a different approach derived from the chaining methodology proposed in Errera & Chemin (2013).

Some of the results presented in this part have been published in the following conference articles:

Berger, S., Duchaine, F. & Gicquel, L.Y.M. 2016 Influence des conditions aux limites thermiques sur la stabilisation d'une flamme laminaire prémélangée. *Congrés Français de Thermique*.

Berger, S., Richard, S., Duchaine, F. & Gicquel, L.Y.M. 2016 Variations of anchoring pattern of a bluff-body stabilised laminar premixed flame as a function of the wall temperature. *ASME Turbo Expo 2016: Turbine Technical Conference and Exposition, Seoul, South Korea*.

Part III

Aerothermal prediction of an aeronautical combustion chamber

For confidentiality reasons this part of the manuscript has been removed.

General conclusion and perspectives

The work presented in this manuscript follows current efforts deployed to support the development of the new generation of aeronautical burners and more specifically to provide efficient numerical tools able to accurately predict combustion chamber wall temperatures. In this context, a multi-physics study of the various thermal processes at play in a combustion chamber was proposed. More specifically, three specific aspects not fully addressed in the literature have been treated:

- ▷ To fully benefit from the performance capabilities of the partitioned coupling approach and avoid CPU resource waste, the CPU cost mismatch between the various sub-systems included in a simulation has to be carefully handled. In this context, while an intuitive distribution of the computing resources based on load distribution is often discussed in the literature (especially in the CPU consuming LES context), the cost overhead induced by external communications between solvers is rarely addressed. Such a topic was hence investigated to identify potential paths of improvement.

- ▷ Reactive flow simulations are commonly performed with either adiabatic of approximately fixed thermal boundary conditions which do not allow an accurate representation of the interactions between the wall thermal fields and the flow fields. In a reactive context, this two-way coupling between the fluid and the solid can particularly be enhanced through local flame/wall interaction processes. In this context, the added value of a CHT approach has been investigated for a simplified academic case, allowing an evaluation of the coupled aerothermal solution proposed.

- ▷ Finally, most existing multi-physics studies of industrial burners consider the coupling of combustion and either solid conduction or radiation. From the author knowledge, a full simultaneous consideration of combustion, radiation and solid conduction in such devices has never been performed in the context of LES, raising the need to evaluate the respective impact of the three physics on the other sub-components.

All these three topics have been covered and discussed in this manuscript, allowing to bring specific conclusions.

When seeking to distribute computing resources between the different solvers encompassed in a coupled simulation, one needs to consider two specific components of the total CPU cost: the internal computational time of each code and the communication time between solvers. The optimal core distribution considering only the load balancing can be approximated by straightforward equations whose inputs are obtained from simple performance tests. Including the effect of the data exchange time is much more complex. A detailed investigation carried out both on a toy model and on additional coupled simulations of an industrial burner, allowed to identify key parameters having an influence on the communication times. In particular, the negative effect on performance of a too large imbalance between the number of cores attributed to different solvers was evidenced as well as the potential improvement which could be obtained with co-partitioning techniques.

Multi-physic thermal coupling was then investigated from a physical point of view on two different burner configurations. The thermal behavior of a laminar premixed flame stabilized on a square bluff-body was first analyzed through various fluid-only DNS and CHT simulations. A strong relation between the aerodynamic and thermal fields as well as the flame stabilization pattern was observed, suggesting a potential large impact of the wall thermal fields for this configuration. This impact was first isolated by performing several DNS with varying bluff-body wall temperature. The results revealed an upstream displacement of the flame foot as the wall temperature was increased, leading to the identification of three different regimes: lifted, anchored and bowed flames. For low bluff-body wall temperatures, flame stabilization was ensured mainly by the recirculation zone. As the wall temperature was increased and the flame moved upstream, stabilization was ensured more and more by the walls, decreasing the influence of the recirculation zone. An investigation of the resulting heat fluxes for the different flame holder wall temperatures evidenced three theoretical equilibrium states of the joint fluid-solid system. The physical relevance of these equilibrium states was then evaluated through CHT simulations with various initial conditions inherited from the fluid-only fixed temperature computations. All the simulations were observed to converge to only two of the three equilibrium states: the lifted regime for low initial temperatures and the bowed regime for large initial temperatures. This bifurcation between two different equilibrium states was observed to depend on the solid conductivity and resulted from the natural processes of solid warming or cooling induced by the interactions between the solid, the flame and the flow thermal fields. Besides, these different processes as well as the "distance" between the initial conditions and the converged solutions were shown to affect the convergence time of the coupled simulations emphasizing to need for a good initial guess to save CPU time. Finally, the reproducibility of the present results was demonstrated with a different approach derived from the chaining methodology proposed in Errera & Chemin (2013).

In the last part, the steady thermal state of an industrial burner was investigated while assessing the interaction between the various physical sub-components. For the operating conditions considered, a moderate impact of the wall temperature on the flow fields was observed. Although

locally significant in regions where the flame approached the walls, its impact at a global scale was relatively reduced. Comparatively the effect of radiative heat transfer on the flow fields was observed to be clearly smaller in accordance with the total radiative heat loss representing less than 1% of the total power delivered by the chemical reaction. However, radiation was observed to be decisive for wall temperature predictions since global levels of wall radiative heat fluxes were shown to be comparable to wall convective fluxes. This last observation was further confirmed by the 3CR coupled simulation including all the three phenomena at the same time. A comparison between experimental thermocolor tests and both CHT and 3CR solid temperatures showed encouraging results, global levels being correctly predicted except in the dome region. As expected, significant improvements of the results were observed when including radiative heat fluxes in the coupled simulation.

The results obtained on the different topics addressed in this manuscript evidenced various possible work perspectives. First, The potential added value of dynamic load distribution and copartitioning techniques to further improve coupled simulation performance has clearly been highlighted. As already mentioned, the latter is currently under study within the HiePACS team of the INRIA laboratory. In addition, the CHT simulations of the bluff-body flame configuration was a first step for the model free study of coupled thermal effects. This work raised in the end more questions than it actually answered, highlighting the need for further investigations. Among them,

- ▷ A detailed analysis of physical transitory phases (solvers synchronized in physical time) and on the role played by the aerodynamics on the bifurcation between the two converged regimes would most probably allow a better understanding of the various interactions between the processes responsible for the system evolution.
- ▷ An inclusion of radiative heat transfer would be very valuable in particular due to the potential impact of this physic on the wall temperature which will affect the flame stabilization process.
- ▷ Similar investigations with a more detailed chemical model as well as for different fuels would provide additional insight into the physical phenomena at play.
- ▷ A comparison with experimental results would provide a physical validation of present and future conclusions.

Finally, the coupled simulations performed on the industrial burner provided valuable insight on the impact of the various interactions between the sub-systems. Besides, the methodology implemented has already been transferred to Turbomeca during this PhD. However, similar simulations of different burner configurations and operating conditions are required to enlarge the validity of the observations. In addition, only non-luminous radiation was considered in the simulations, leaving aside the contribution of soot particles. The latter can be expected to largely impact the

results and should be included in the simulations for an increase of results accuracy. Finally, an improvement of the multiperforated wall model is mandatory for a better predictivity of the results in such complex systems. Note that further work on this last point has already been impulsed in Lahbib (2015) and is still ongoing at CERFACS.

Bibliography

Alexandrov, A., Ionescu, M.F., Schauser, K.E. & Scheiman, C. 1995 LogGP: incorporating long messages into the logP model–one step closer towards a realistic model for parallel computation. *Proceedings of the seventh annual ACM symposium on Parallel algorithms and architectures* pp. 95–105. (Not cited.)

Alonso, J., Hahn, S., Ham, F., Herrmann, M., Laccarino, G., Kalitzin, G., LeGresley, P., Mattsson, K., Medic, G., Moin, P., Pitsch, H., Schluter, J., Svard, M., Van der Weide, E., You, D. & Wu, X. 2006 Chimps: A high-performance scalable module for multi-physics simulations. *42nd AIAA/ASME/SAE/ASEE Joint Propulsion Conference & Exhibit* (AIAA-Paper 2006-5274). (Not cited.)

Amaya, J. 2010 Unsteady coupled convection, conduction and radiation simulations on parallel architectures for combustion applications. PhD thesis, Institut National Polytechnique de Toulouse. (Not cited.)

Amdahl, G.M. 1967 Validity of the single processor approach to achieving large scale computing capabilities. *Proceedings of the April 18-20, 1967, Spring Joint Computer Conference* pp. 483–485. (Not cited.)

Andreini, A., Bonini, A., Da Soghe, R., Facchini, B., Ciani, A. & Innocenti, L. 2012 Conjugate heat transfer calculations on a GT rotor blade for industrial applications part II: Improvement of external flow modeling. , vol. 4, pp. 681–692. (Not cited.)

Bar-Noy, A. & Kipnis, S. 1994 Designing broadcasting algorithms in the postal model for message-passing systems. *Mathematical Systems Theory* **27** (5), 431–452. (Not cited.)

Barlow, R.S. & Frank, J.H. 1998 Effects of turbulence on species mass fractions in methane/air jet flames. *Symposium (International) on Combustion* **27** (1), 1087–1095. (Not cited.)

Bédat, B. & Giovannini, A. 2012 *Transfert de Chaleur*. Editions Cépaduès. (Not cited.)

Blint, R.J. 1986 The relationship of the laminar flame width to flame speed. *Combustion Science and Technology* **49**, 79–92. (Not cited.)

Bockhorn, H., Habisreuther, P. & Hettel, M. 2009 Numerical Modelling of Technical Combustion. *Notes on Numerical Fluid Mechanics and Multidisciplinary Design* 100, pp. 325–340. Springer Berlin Heidelberg. (Not cited.)

Boltzmann 1872 Weitere studien über das wärmegleichgewicht unter gasmolekülen (plusieurs études sur l'équilibre thermique des molécules dans un gaz). *Sitzungsberichte der Akademie der Wissenschaften, Wien* **II** (66), 275–370. (Not cited.)

Butler, T.D. & O'Rourke, P.J. 1977 A numerical method for two-dimensional unsteady reacting flows. *Proceedings of the Combustion Institute* **16** (1), 1503 – 1515. (Not cited.)

Carlson, B.G. 1971 Tables of equal weight quadrature eqn over the unit sphere. *Tech. Rep.*. Los alamos Scientific Lab., N. Mex. (Not cited.)

Cebeci, T. & Cousteix, J. 2005 *Modeling and computation of boundary-layer flows*. Springer. (Not cited.)

Chandrasekhar, S. 1960 *Radiative Transfer*. Dover, Mineola, NY. (Not cited.)

Charlette, F., Veynante, D. & Meneveau, C. 2002 A power-law wrinkling model for LES of premixed turbulent combustion: Part I - non-dynamic formulation and initial tests. *Combustion and Flame* **131**, 159–180. (Not cited.)

Chemin, S. 2007 Etude des interactions thermiques fluide-structure par un couplage de codes de calcul. PhD thesis, Université de Reims Champagne Ardenne. (Not cited.)

Chen, J.H. 2011 Petascale direct numerical simulation of turbulent combustion—fundamental insights towards predictive models. *Proceedings of the Combustion Institute* **33** (1), 99–123. (Not cited.)

Chen, J.H., Hawkes, E.R., Sankaran, R., Mason, S.D. & Im, H.G. 2006 Direct numerical simulation of ignition front propagation in a constant volume with temperature inhomogeneities: I. Fundamental analysis and diagnostics. *Combustion and Flame* **145** (1–2), 128–144. (Not cited.)

Chin, J.H., Panczak, T.D. & Fried, L. 1992 Spacecraft thermal modelling. *International Journal for Numerical Methods in Engineering* **35** (4), 641–653. (Not cited.)

Coelho, J. 2009 Approximate solutions of the filtered radiative transfer equation in large eddy simulations of turbulent reactive flows. *Combustion and Flame* **156** (5), 1099–1110. (Not cited.)

Coelho, P.J. 2004 Detailed numerical simulation of radiative transfer in a nonluminous turbulent jet diffusion flame. *Combustion and Flame* **136** (4), 481–492. (Not cited.)

Coelho, P.J. 2007 Numerical simulation of the interaction between turbulence and radiation in reactive flows. *Progress in Energy and Combustion Science* **33** (4), 311–383. (Not cited.)

Coelho, P.J. 2014 Advances in the discrete ordinates and finite volume methods for the solution of radiative heat transfer problems in participating media. *Journal of Quantitative Spectroscopy and Radiative Transfer* **145**, 121–146. (Not cited.)

Coelho, P.J., Perez, P. & El Hafi, M. 2003*a* Benchmark Numerical Solutions for Radiative Heat Transfer in Two-Dimensional Axisymmetric Enclosures with Nongray Sooting Media. *Numerical Heat Transfer, Part B: Fundamentals* **43** (5), 425–444. (Not cited.)

Coelho, P.J., Teerling, O.J. & Roekaerts, D. 2003*b* Spectral radiative effects and turbulence/radiation interaction in a non-luminous turbulent jet diffusion flame. *Combustion and Flame* **133** (1–2), 75–91. (Not cited.)

Colin, O., Ducros, F., Veynante, D. & Poinsot, T. 2000 A thickened flame model for large eddy simulations of turbulent premixed combustion. *Physics of Fluids* **12** (7), 1843–1863. (Not cited.)

Colin, O. & Rudgyard, M. 2000 Development of high-order taylor-galerkin schemes for unsteady calculations. *Journal of Computational Physics* **162** (2), 338–371. (Not cited.)

Culler, D., Karp, R., Patterson, D., Sahay, A., Schauser, K.E., Santos, E., Subramonian, R. & Von Eicken, T. 1993 LogP: Towards a realistic model of parallel computation. *Fourth ACM SIGPLAN Symposium on Principles and Practice of Parallel Programming* **28**. (Not cited.)

Darici, S., Bilir, Ş. & Ateş, A. 2015 Transient conjugated heat transfer for simultaneously developing laminar flow in thick walled pipes and minipipes. *International Journal of Heat and Mass Transfer* **84**, 1040–1048. (Not cited.)

Deardorff, J.W. 1970 A numerical study of three-dimensional turbulent channel flow at large Reynolds numbers. *Journal of Fluid Mechanics* **41** (02), 453–480. (Not cited.)

Deshmukh, K.V., Haworth, D.C. & Modest, M.F. 2007 Direct numerical simulation of turbulence–radiation interactions in homogeneous nonpremixed combustion systems. *Proceedings of the Combustion Institute* **31** (1), 1641–1648. (Not cited.)

Divo, E. & Kassab, A.J. 2007 An Efficient Localized Radial Basis Function Meshless Method for Fluid Flow and Conjugate Heat Transfer. *Journal of Heat Transfer* **129** (2), 124–136. (Not cited.)

Domke, J. & Wang, D. 2012 Runtime tracing of the community earth system model: Feasibility study and benefits. *Procedia Computer Science* **9**, 1950–1958. (Not cited.)

Donde, P., Raman, V., Mueller, M.E. & Pitsch, H. 2012 Les/pdf based modeling of soot–turbulence interactions in turbulent flames. *Proceedings of the Combustion Institute* . (Not cited.)

Donea, J. & Huerta, A. 2003 *Finite Element Methods for Flow Problems*. John Wiley & Sons Inc, New York. (Not cited.)

Donéa, J., Roig, B. & Huerta, A. 2000 High-order accurate time-stepping schemes for convection-diffusion problems. *Computer Methods in Applied Mechanics and Engineering* **182**, 249–275. (Not cited.)

Dorfman, A. & Renner, Z. 2009 Conjugate problems in convective heat transfer: Review. *Mathematical Problems in Engineering* **2009**. (Not cited.)

Duchaine, F., Corpron, A., Pons, L., Moureau, V., Nicoud, F. & Poinsot, T. 2009*a* Development and assessment of a coupled strategy for conjugate heat transfer with large eddy simulation: application to a cooled turbine blade. *International Journal of Heat and Fluid Flow* **30** (6), 1129–1141. (Not cited.)

Duchaine, F., Jauré, S., Poitou, D., Quémerais, E., Staffelbach, G., Morel, T. & Gicquel, L. 2015 Analysis of high performance conjugate heat transfer with the OpenPALM coupler. *Computational Science & Discovery* **8** (1), 015003. (Not cited.)

Duchaine, F., Maheu, N., Moureau, V., Balarac, G. & Moreau, S. 2013 Large-eddy simulation and conjugate heat transfer around a low-mach turbine blade. *Journal of Turbomachinery* **136** (5), 051015–051015. (Not cited.)

Duchaine, F., Mendez, S., Nicoud, F., Corpron, A., Moureau, V. & Poinsot, T. 2008 Coupling heat transfer solvers and large eddy simulations for combustion applications. *Proceedings of the CTR Summer Program* pp. 113–126. (Not cited.)

Duchaine, F., Morel, T. & Gicquel, L.Y.M. 2009*b* Computational-fluid-dynamics-based kriging optimization tool for aeronautical combustion chambers. *AIAA Journal* **47** (3), 631 – 645. (Not cited.)

Dunn, W.L. & Shultis, J.K. 2011 *Exploring Monte Carlo Methods*. Elsevier. (Not cited.)

Eiberger, F., Habisreuther, P., Zarzalis, N. & Turrini, F. 2015 Evaluation of the Turbulence Radiation Interaction and the Validity of the Optically Thin Fluid Approximation in a High Turbulent Premixed Methane Flame. *ASME Turbo Expo 2015: Turbine Technical Conference and Exposition, Montréal, Quebec, Canada* . (Not cited.)

Ern, A. & Giovangigli, V. 1994 *Multicomponent Transport Algorithms*. Heidelberg: Springer Verlag. (Not cited.)

Errera, M.-P. & Baqué, B. 2013 A quasi-dynamic procedure for coupled thermal simulations. *International Journal for Numerical Methods in Fluids* **72**, 1183–1206. (Not cited.)

Errera, M.-P. & Chemin, S. 2013 Optimal solutions of numerical interface conditions in fluid–structure thermal analysis. *Journal of Computational Physics* **245**, 431–455. (Not cited.)

Errera, M.-P. & Duchaine, F. 2016 Comparative study of coupling coefficients in Dirichlet–Robin procedure for fluid–structure aerothermal simulations. *Journal of Computational Physics* **312**, 218–234. (Not cited.)

Euler, L. 1757 Principes generaux du mouvement des fluides. *Mémoires de l'académie des sciences de Berlin* **11**, 274–315. (Not cited.)

Facchini, B., Magi, A. & Del Greco, A.S. 2004 Conjugate heat transfer simulation of a radially cooled gas turbine vane. *ASME Turbo Expo 2004: Power for Land, Sea, and Air* pp. 951–961. (Not cited.)

Faeth, G.M., Gore, J.P. & Jeng, S.M. 1987 Spectral and total radiation properties of turbulent carbon monoxide/air diffusion flames. *AIAA Journal* **25** (2), 339–345. (Not cited.)

Fan, A., Wan, J., Maruta, K., Yao, H. & Liu, W. 2013 Interactions between heat transfer, flow field and flame stabilization in a micro-combustor with a bluff body. *International Journal of Heat and Mass Transfer* **66**, 72–79. (Not cited.)

Fischer, S.J., Hardouin-Duparc, B. & Grosshandler, W.L. 1987 The structure and radiation of an ethanol pool fire. *Combustion and Flame* **70** (3), 291–306. (Not cited.)

Fiveland, W.A. 1987 Discrete Ordinate Methods for Radiative Heat Transfer in Isotropically and Anisotropically Scattering Media. *Journal of Heat Transfer* **109** (3), 809–812. (Not cited.)

Fourier, J.B.J. 1822 *Théorie Analytique de la Chaleur*. F. Didot, Paris. (Not cited.)

Fransen, R. 2013 Simulation aux grandes echelles pour la modélisation aérothermique des aubages de turbines refroidies. PhD thesis, Université de Toulouse - MeGeP - Dynamique des Fluides. (Not cited.)

Franzelli, B., Riber, E., Gicquel, L.Y.M. & Poinsot, T. 2012 Large Eddy Simulation of combustion instabilities in a lean partially premixed swirled flame. *Combustion and Flame* **159** (2), 621–637. (Not cited.)

Frayssé, V., Giraud, L., Gratton, S. & Langou, J. 2005 A set of gmres routines for real and complex arithmetics on high performance computers. *ACM Transactions on Mathematical Software (TOMS)* **31** (2), 228—238. (Not cited.)

Gauntner, D.J. & Sucec, J. 1978 Method for calculating convective heat-transfer coefficients over turbine vane surfaces. *NASA STI/Recon Technical Report N* **78**. (Not cited.)

Gerardin, J., Seiler, N., Ruyer, P., Trovalet, L. & Boulet, P. 2012 P1 approximation, MDA and IDA for the simulation of radiative transfer in a 3d geometry for an absorbing scattering medium. *Journal of Quantitative Spectroscopy and Radiative Transfer* **113** (2), 140–149. (Not cited.)

Germano, M., Piomelli, U., Moin, P. & Cabot, W. 1991 A dynamic subgrid-scale eddy viscosity model. *Physics of Fluids* **3** (7), 1760–1765. (Not cited.)

Gicquel, L.Y.M., Staffelbach, G. & Poinsot, T. 2012 Large eddy simulations of gaseous flames in gas turbine combustion chambers. *Progress in Energy and Combustion Science* **38** (6), 782–817. (Not cited.)

Giles, M.B. 1997 Stability analysis of numerical interface conditions in fluid-structure thermal analysis. *International Journal for Numerical Methods in Fluids* **25** (4), 421–436. (Not cited.)

Gimenez, G., Errera, M., Baillis, D., Smith, Y. & Pardo, F. 2016 A coupling numerical methodology for weakly transient conjugate heat transfer problems. *International Journal of Heat and Mass Transfer* **97**, 975–989. (Not cited.)

Giovangigli, V. 1999 *Multicomponent Flow Modeling*. Boston: Birkhauser. (Not cited.)

Godunov, S.K. & Ryabenki, V.S. 1964 Theory of difference schemes-an introduction. *Amsterdam: North Holland, 1964* **1**. (Not cited.)

Gomez, A. & Rosner, D.E. 1993 Thermophoretic effects on particles in counterflow laminar diffusion flames. *Combustion Science and Technology* **89**, 335–362. (Not cited.)

Goodwin, D.G. 2002 *Cantera C++ Users Guide. http://sourceforge.net/projects/cantera*. (Not cited.)

Gourdain, N., Gicquel, L.Y.M., Montagnac, M., Vermorel, O., Gazaix, M., Staffelbach, G., García, M., Boussuge, J.F. & Poinsot, T. 2009 High performance parallel computing of flows in complex geometries - part 1: methods. *Computational Science and Discovery* **2** (November). (Not cited.)

Grosshandler, W.L. & Joulain, P. 1986 The effect of large-scale fluctuations on flame radiation. *Progress in Astronautics and Aeronautics* **105**, 123–152. (Not cited.)

Gupta, A., Haworth, D.C. & Modest, M.F. 2013 Turbulence-radiation interactions in large-eddy simulations of luminous and nonluminous nonpremixed flames. *Proceedings of the Combustion Institute* **34** (1), 1281–1288. (Not cited.)

Gad-el Hak, M. 1995 Questions in fluid mechanics: Stokes' hypothesis for a newtonian, isotropic fluid. *Journal of Fluids Engineering* **117** (1), 3–5. (Not cited.)

Hallez, Y., Jouhaud, J.C. & Poinsot, T. 2011 On the relative impact of subgrid-scale modelling and conjugate heat transfer in les of hot jets in cross-flow over cold plates. *International Journal for Numerical Methods in Fluids* **67** (10), 1321–1340. (Not cited.)

Han, Z.X., Dennis, B.H. & Dulikravich, G.S. 2001 Simultaneous prediction of external flowfield and temperature in internally cooled 3d turbine blade material. *International Journal of Turbo and Jet Engines* **18** (1), 47–58. (Not cited.)

He, L. 2013 Fourier spectral modelling for multi-scale aero-thermal analysis. *International Journal of Computational Fluid Dynamics* **27** (2), 118–129. (Not cited.)

He, L. & Oldfield, M.L.G. 2011 Unsteady conjugate heat transfer modeling. *Journal of turbomachinery* **133** (3). (Not cited.)

Heidmann, J.D., Kassab, A.J., Divo, E.A., Rodriguez, F. & Steinthorsson, E. 2003 Conjugate heat transfer effects on a realistic film-cooled turbine vane. Atlanta, Georgia, USA. (Not cited.)

Heil, M., Hazel, A.L. & Boyle, J. 2008 Solvers for large-displacement fluid–structure interaction problems: segregated versus monolithic approaches. *Computational Mechanics* **43** (1), 91–101. (Not cited.)

Hirschfelder, J.O., Curtiss, C.F. & Bird, R.B. 1969 *Molecular theory of gases and liquids*. New York: John Wiley & Sons. (Not cited.)

Hirsh, C. 1988 *Numerical computation of internal and external flows. Vol. 1: Fundamentals of numerical discretization*. Wiley. (Not cited.)

Jauré, S. 2012 Methodology for conjugate heat transfer simulations relying on large eddy simulations in massively parallel environments. PhD thesis, Institut National Polytechnique de Toulouse. (Not cited.)

Jauré, S., Duchaine, F. & Gicquel, L.Y.M. 2011 Comparisons of coupling strategies for massively parallel conjugate heat transfer with large eddy simulation. *IV International Conference on Computational Methods for Coupled Problems in Science and Engineering, Kos Island, Greece* . (Not cited.)

Jauré, S., Duchaine, F., Staffelbach, G. & Gicquel, L.Y.M 2013 Massively parallel conjugate heat transfer methods relying on large eddy simulation applied to an aeronautical combustor. *Computational Science & Discovery* **6** (1), 015008. (Not cited.)

Jeans, J.H. 1917 The equations of radiative transfer of energy. *Monthly Notices Royal Astronomical Society,* **78**, 28–36. (Not cited.)

Jeng, S.M., Lai, M.C. & Faeth, G.M. 1984 Nonluminous Radiation in Turbulent Buoyant Axisymmetric Flames. *Combustion Science and Technology* **40** (1-4), 41–53. (Not cited.)

Jones, W.P. & Paul, M.C. 2005 Combination of DOM with LES in a gas turbine combustor. *International journal of engineering science* **43** (5), 379–397. (Not cited.)

Joseph, D. 2004 Modélisation des transferts radiatifs en combustion par méthode aux ordonnées discrètes sur des maillages non structurés tridimensionnels. PhD thesis, Institut National Polytechnique de Toulouse. (Not cited.)

Joseph, D., El Hafi, M., Fournier, R. & Cuenot, B. 2005 Comparison of three spatial differencing schemes in discrete ordinates method using three-dimensional unstructured meshes. *International Journal of Thermal Sciences* **44** (9), 851–864. (Not cited.)

Joseph, D., Perez, P., El Hafi, M. & Cuenot, B. 2009 Discrete Ordinates and Monte Carlo Methods for Radiative Transfer Simulation Applied to Computational Fluid Dynamics Combustion Modeling. *Journal of Heat Transfer* **131** (5), 052701–052701. (Not cited.)

Joshi, O. & Leyland, P. 2012 Implementation of Surface Radiation and Fluid-Structure Thermal Coupling in Atmospheric Reentry, Implementation of Surface Radiation and Fluid-Structure Thermal Coupling in Atmospheric Reentry. *International Journal of Aerospace Engineering, International Journal of Aerospace Engineering* **2012**. (Not cited.)

Ju, Y., Masuya, G. & Ronney, P.D. 1998 Effects of radiative emission and absorption on the propagation and extinction of premixed gas flames. *Symposium (International) on Combustion* **27** (2), 2619–2626. (Not cited.)

Kader, B.A. 1981 Temperature and concentration profiles in fully turbulent boundary layers. *International Journal of Heat and Mass Transfer* **24** (9), 1541–1544. (Not cited.)

von Kármán, T. & Millan, G. 1953 Thermal theory of laminar flame front near cold wall. pp. 173–177. Munich: The Combustion Institute, Pittsburgh. (Not cited.)

Kayakol, N., Selçuk, N., Campbell, I. & Gülder, Ö.L. 2000 Performance of discrete ordinates method in a gas turbine combustor simulator. *Experimental Thermal and Fluid Science* **21** (1–3), 134–141. (Not cited.)

Kedia, K.S. & Ghoniem, A.F. 2014*a* The anchoring mechanism of a bluff-body stabilized laminar premixed flame. *Combustion and Flame* **161** (9), 2327–2339. (Not cited.)

Kedia, K.S. & Ghoniem, A.F. 2014*b* The response of a harmonically forced premixed flame stabilized on a heat-conducting bluff-body. *Proceedings of the Combustion Institute* **35** (1), 1065–1072. (Not cited.)

Kedia, K.S. & Ghoniem, A.F. 2015 The blow-off mechanism of a bluff-body stabilized laminar premixed flame. *Combustion and Flame* **162** (4), 1304–1315. (Not cited.)

Kedia, K.S., Safta, C., Ray, J., Najm, H.N. & Ghoniem, A.F. 2014 A second-order coupled immersed boundary-SAMR construction for chemically reacting flow over a heat-conducting cartesian grid-conforming solid. *Journal of Computational Physics* **272**, 408–428. (Not cited.)

Kennedy, I.M. 1997 Models of soot formation and oxidation. *Progress in Energy and Combustion Science* **23** (2), 95–132. (Not cited.)

Kiel, B., Garwick, K., Gord, J., Miller, J., Lynch, A., Hill, R. & Phillips, S. 2007 A Detailed Investigation of Bluff Body Stabilized Flames. *45th AIAA Aerospace Sciences Meeting and Exhibit* (AIAA 2007-168). (Not cited.)

Kirchhoff, G. 1860 I. On the relation between the radiating and absorbing powers of different bodies for light and heat. *Philosophical Magazine Series 4* **20** (130), 1–21. (Not cited.)

Koch, R. & Becker, R. 2004 Evaluation of quadrature schemes for the discrete ordinates method. *Journal of Quantitative Spectroscopy and Radiative Transfer* **84** (4), 423–435. (Not cited.)

Kolmogorov, A.N., Petrovski, I.G. & Piskunov, N.S. 1937 *Bjul Moskosvkovo Gos Univ* **1** (7), 1–72. (Not cited.)

Koren, C. 2016 Modeling conjugate heat transfer phenomena for multi-physics simulations of combustion applications. PhD thesis, Université Paris-Saclay. (Not cited.)

Krebs, W., Koch, R., Bauer, H.J., Kneer, R. & Witting, S. 1994 Effect of turbulence on radiative heat transfer inside a model combustor. *Proceeding of Eurotherm seminar no. 37-heat transfer in radiating and combusting systems 2, Saluggia, Italy* pp. 349–362. (Not cited.)

Krishnamoorthy, G., Rawat, R. & Smith, P.J. 2005 Parallel computations of radiative heat transfer using the discrete ordinates method. *Numerical Heat Transfer, Part B: Fundamentals* **47** (1), 19–38. (Not cited.)

Kundu, K.M., Banerjee, D. & Bhadhuri, D. 1977 Theoretical Analysis on Flame Stabilization by a Bluff-Body. *Combustion Science and Technology* **17** (3-4), 153–162. (Not cited.)

Kundu, K.M., Banerjee, D. & Bhaduri, D. 1980 On Flame Stabilization by Bluff-Bodies. *Journal of Engineering for Power* **102** (1), 209–214. (Not cited.)

Kundu, P., Cohen, I. & Dowling, D. 2011 *Fluid Mechanics (5th Edition ed.)*. Academic Press. (Not cited.)

Kuo, C.H. & Ronney, P.D. 2007 Numerical modeling of non-adiabatic heat-recirculating combustors. *Proceedings of the Combustion Institute* **31** (2), 3277–3284. (Not cited.)

Lahbib, D. 2015 Modeling of aerodynamic and thermal effects in multi-perforations using LES. PhD thesis, Université de Montpellier. (Not cited.)

Lamarque, N. 2007 Schémas numériques et conditions limites pour la simulation aux grandes échelles de la combustion diphasique dans les foyers d'hélicoptère. Phd thesis, INP Toulouse. (Not cited.)

Lax, P.D. & Wendroff, B. 1960 Systems of conservation laws. *Communications on Pure and Applied Mathematics* **13**, 217–237. (Not cited.)

Leacanu, M. 2005 Couplage multi-physique combustion turbulente - rayonnement - cinétique chimique. PhD thesis, Ecole centrale Paris. (Not cited.)

Lefebvre, A.H. 2010 *Gas turbine combustion: alternative fuels and emissions; 3rd ed.*. Hoboken, NJ: CRC Press. (Not cited.)

Li, Y. & Kong, S.-C. 2011 Coupling conjugate heat transfer with in-cylinder combustion modeling for engine simulation. *International Journal of Heat and Mass Transfer* **54** (11–12), 2467–2478. (Not cited.)

Lilly, D.K. 1966 *On the application of the eddy viscosity concept in the inertial sub-range of turbulence*. National Center for Atmospheric Research. (Not cited.)

Lindström, Jens & Nordström, Jan 2010 A stable and high-order accurate conjugate heat transfer problem. *Journal of Computational Physics* **229** (14), 5440–5456. (Not cited.)

Liu, J., Shang, H.M., Chen, Y.S. & Wang, T.S. 2000 Development of an unstructured radiation model applicable for two dimensional planar, axisymmetric and 3-dimensional geometries. *Journal of Quantitative Spectroscopy and Radiative Transfer* **66**, 17–33. (Not cited.)

Liu, M.F., Yang, G.J., Smallwood, G.J. & Zhang, H. 2004 Evaluation of the snb based full spectrum ck method for thermal radiation calculations in CO2/H2O mixtures. *Proceedings of ICHMT* . (Not cited.)

Lommel, E. 1889 Die photometrie der diffusen zurückwerfung. *Annalen der Physik* **272** (2), 473–502. (Not cited.)

Longwell, J.P., Frost, E.E. & Weiss, M.A. 1953 Flame Stability in Bluff Body Recirculation Zones. *Industrial & Engineering Chemistry* **45** (8), 1629–1633. (Not cited.)

Lu, J.H., Ezekoye, O., Greif, R. & Sawyer, F. 1990 Unsteady heat transfer during side wall quenching of a laminar flame. *23rd Symposium (International) on Combustion* pp. 441–446. (Not cited.)

Luo, J. & Razinsky, E.H. 2007 Conjugate heat transfer analysis of a cooled turbine vane using the V2F turbulence model. *Journal of turbomachinery* **129** (4), 773–781. (Not cited.)

Mahesh, K., Constantinescu, G., Apte, S., Iaccarino, G. & Moin, P. 2001 Large-eddy simulation of gas turbine combustors. In *Annual Research Briefs* , pp. 3–17. Center for Turbulence Research, NASA Ames/Stanford Univ. (Not cited.)

Maheu, N., Moureau, V., Domingo, P., Duchaine, F. & Balarac, G. 2012 Large-eddy simulations of flow and heat transfer around a low-mach number turbine blade. *Proceedings of the CTR Summer Program* p. 137. (Not cited.)

Mazumder, S. & Modest, M.F. 1999 Turbulence-radiation interactions in nonreactive flow of combustion gases. *Transactions-American Society of Mechanical Engineers Journal of Heat Transfer* **121**, 726–728. (Not cited.)

Mercier, E., Tessé, L. & Savary, N. 2006 3D full predictive thermal chain for gas turbine combustor metal temperature. *Proceedings of the 25th International Congress of the Aeronautical Sciences (ICAS 2006), Hamburg, Germany* . (Not cited.)

Mishra, S.C., Roy, H.K. & Misra, N. 2006 Discrete ordinate method with a new and a simple quadrature scheme. *Journal of Quantitative Spectroscopy and Radiative Transfer* **101** (2), 249–262. (Not cited.)

Modest, M.F. 2003 *Radiative heat transfer (2nd ed.)*. New York: Academic Press. (Not cited.)

Modest, M.F. & Haworth, D.C. 2016 *Radiative Heat Transfer in Turbulent Combustion Systems*. Springer International Publishing. (Not cited.)

Modest, M.F. & Yang, J. 2008 Elliptic PDE formulation and boundary conditions of the spherical harmonics method of arbitrary order for general three-dimensional geometries. *Journal of Quantitative Spectroscopy and Radiative Transfer* **109** (9), 1641–1666. (Not cited.)

Morel, T. & Keribar, R. 1985 A Model for Predicting Spatially and Time Resolved Convective Heat Transfer in Bowl-in-Piston Combustion Chambers. *SAE Technical Paper 850204* . (Not cited.)

Narasimhan, T.N. 1999 Fourier's heat conduction equation: History, influence, and connections. *Proceedings of the Indian Academy of Sciences - Earth and Planetary Sciences* **108** (3), 117–148. (Not cited.)

Navier, C.L.M.H. 1822 Mémoire sur les lois du mouvement des fluides. *Mémoire de l'académie des sciences de l'institut de France* **6**, 389–440. (Not cited.)

Nordström, J. & Berg, J. 2013 Conjugate heat transfer for the unsteady compressible navier–stokes equations using a multi-block coupling. *Computers & Fluids* **72**, 20–29. (Not cited.)

Patankar, S.V. 1980 *Numerical Heat Transfer and Fluid Flow*. New York: McGraw Hill. (Not cited.)

Perelman, T.L. 1961 On conjugated problems of heat transfer. *International Journal of Heat and Mass Transfer* **3** (4), 293–303. (Not cited.)

Peters, N. 1991 Length scales in laminar and turbulent flames. *Tech. Rep.*. AIAA. (Not cited.)

Peters, N. & Rogg, B., ed. 1993 *Reduced Kinetic Mechanisms for Applications in Combustion Systems*, *Lecture Notes in Physics Monographs*, vol. 15. Berlin, Heidelberg: Springer Berlin Heidelberg. (Not cited.)

Piacentini, A., Morel, T., Thévenin, A. & Duchaine, F. 2011 O-palm: An open source dynamic parallel coupler. *Proceedings of the IV International Conference on Computational Methods for Coupled Problems in Science and Engineering–Coupled Problems* . (Not cited.)

Piomelli, U. 2008 Wall-layer models for large-eddy simulations. *Progress in Aerospace Sciences* **44** (6), 437–446. (Not cited.)

Pitsch, H. 2006 Large eddy simulation of turbulent combustion. *Annual Review of Fluid Mechanics* **38**, 453–482. (Not cited.)

Planck, M. 1901 Distribution of energy in the spectrum. *Annalen der Physik* **4** (3), 553–563. (Not cited.)

Poinsot, T. 1996 Direct simulation and modelling of flame-wall interaction. *Sixth SIAM International Conf. on Numerical Combustion* . (Not cited.)

Poinsot, T. & Lele, S. 1992 Boundary conditions for direct simulations of compressible viscous flows. *Journal of Computational Physics* **101** (1), 104–129. (Not cited.)

Poinsot, T. & Veynante, D. 2005 *Theoretical and numerical combustion*. RT Edwards, Inc. (Not cited.)

Poitou, D. 2009 Modélisation du rayonnement dans la simulation aux grandes échelles de la combustion turbulente. PhD thesis, Institut National Polytechnique de Toulouse. (Not cited.)

Poitou, D., Amaya, J., Bushan Singh, C., Joseph, D., El Hafi, M. & Cuenot, B. 2009 Validity limits for the global model fs-snbck for combustion applications. *Proceedings of Eurotherm83–Computational Thermal Radiation in Participating Media III* . (Not cited.)

Poitou, D., Amaya, J. & Duchaine, F. 2012*a* Parallel Computation for Radiative Heat Transfer Using the DOM in Combustion Applications: Direction, Frequency, Subdomain Decompositions, and Hybrid Methods. *Numerical Heat Transfer, Part B: Fundamentals* **62** (1), 28–49. (Not cited.)

Poitou, D., Amaya, J., El Hafi, M. & Cuenot, B. 2012*b* Analysis of the interaction between turbulent combustion and thermal radiation using unsteady coupled les/dom simulations. *Combustion and Flame* **159** (4), 1605–1618. (Not cited.)

Poitou, D., El Hafi, M. & Cuenot, B. 2007 Diagnosis of turbulence radiation in turbulent flames and implications for modeling in Large Eddy Simulation. *Turkish Journal of Engineering and Environmental Sciences* **31**, 371–381. (Not cited.)

Poitou, D., El Hafi, M. & Cuenot, B. 2011 Analysis of radiation modeling for turbulent combustion : development of a methodology to couple turbulent combustion and radiative heat transfer in LES. *Journal of Heat Transfer* **133** (6), 062701 – 10 pages. (Not cited.)

Pope, S.B. 2000 *Turbulent flows*. Cambridge University Press. (Not cited.)

Predari, M. & Esnard, A. 2014 Coupling-aware graph partitioning algorithms: Preliminary study. *HiPC-21th International Conference on High Performance Computing* . (Not cited.)

Quartapelle, L. & Selmin, V. 1993 High-order Taylor-Galerkin methods for non-linear multi-dimensional problems. *In: Finite Elements Fluids, Pineridge Press* pp. 1374–1384. (Not cited.)

Radenac, E. 2006 Développement et validation d'une méthode numérique pour le couplage fluide / structure en aérothermique instationnaire. PhD thesis, Ecole Nationale Supérieure de l'Aéronautique et de l'Espace. (Not cited.)

Radenac, E., Gressier, J., Laroche, E., Donjat, D. & Millan, P. 2008 Couplage aérothermique et simulation de refroidissement par jet. *Congrès Francais de Thermique, SFT 2008, Toulouse, France* . (Not cited.)

Radenac, E., Gressier, J., Millan, P. & Giovannini, A. 2005 Une méthode conservative de couplage instationnaire de codes en aérothermique. *Congrès Français de Thermique, SFT 2005, Reims, France* . (Not cited.)

Refahi, S. 2013 Développement d'un code de transfert radiatif et de son couplage avec un code LES. PhD thesis, Ecole Centrale Paris. (Not cited.)

Refloch, A., Courbet, B., Murrone, A., Villedieu, P., Laurent, C., Gilbank, P., Troyes, J., Tessé, L., Chaineray, G., Dargaud, J.B., Quémerais, E. & Vuillot, F. 2011 Cfd platforms and coupling - cedre software. *Onera Aerospacelab Journal* . (Not cited.)

Reynolds, O. 1883 An experimental investigation of the circumstances which determine the motion of water shall be direct or sinuous, and the law of resistance in parallel channels. *Philosophical Transactions of the Royal Society London A* **174**, 935–982. (Not cited.)

Reynolds, O. 1894 On the dynamical theory of incompressible viscous flows and the determination of the criterion. *Philosophical Transactions of the Royal Society London A* **186**, 123–161. (Not cited.)

Richardson, L.F. 1922 *Weather Prediction by Numerical Process*, cambridge edn. Cambridge University Press. (Not cited.)

Rochoux, M.C., Ricci, S., Lucor, D., Cuenot, B. & Trouvé, A. 2014 Towards predictive data-driven simulations of wildfire spread – part I: Reduced-cost ensemble kalman filter based on a polynomial chaos surrogate model for parameter estimation. *Natural Hazards and Earth System Science* **14** (11), 2951–2973. (Not cited.)

Roe, B., Jaiman, R., Haselbacher, A. & Geubelle, P.H. 2008 Combined interface boundary condition method for coupled thermal simulations. *International journal for numerical methods in fluids* **57** (3), 329–354. (Not cited.)

Roger, M., Coelho, P.J. & Da Silva, C.B. 2010 The influence of the non-resolved scales of thermal radiation in large eddy simulation of turbulent flows: A fundamental study. *International Journal of Heat and Mass Transfer* **53** (13–14), 2897 – 2907. (Not cited.)

Roger, M., Da Silva, C.B. & Coelho, P.J. 2009 Analysis of the turbulence–radiation interactions for large eddy simulations of turbulent flows. *International Journal of Heat and Mass Transfer* **52** (9–10), 2243–2254. (Not cited.)

Rosner, D.E., Israel, R.S. & Mantia, B.L. 2000 "heavy" species ludwig-soret transport effects in air-breathing combustion. *Combustion and Flame* **123,**, 547–560. (Not cited.)

Rothman, L.S., Gordon, I.E., Barber, R.J., Dothe, H., Gamache, R.R., Goldman, A., Perevalov, V.I., Tashkun, S.A. & Tennyson, J. 2010 HITEMP, the high-temperature molecular spectroscopic database. *Journal of Quantitative Spectroscopy and Radiative Transfer* **111** (15), 2139–2150. (Not cited.)

Sakami, M. & Charette, A. 1998 A new differencing scheme for the discrete ordinates method in complex geometries,. *Revue générale de thermique* **37**, 440–449. (Not cited.)

Gonçalves dos Santos, R., Ducruix, S., Gicquel, O. & Veynate, D. 2015 A study of three-dimensional LES of turbulent combustion with radiative heat transfer. *Journal of the Brazilian Society of Mechanical Sciences and Engineering* **38** (1), 33–48. (Not cited.)

Schlichting, H. 1955 *Boundary layer theory*. New York: McGraw-Hill. (Not cited.)

Schmitt, P. 2005 Simulation aux grandes échelles de la combustion étagée dans les turbines à gaz et son interaction stabilité-polluants-thermique. Phd thesis, INP Toulouse. (Not cited.)

Siegel, R. & Howell, J. 2002 *Thermal radiation heat transfer*. New York: Taylor and Francis. (Not cited.)

Smagorinsky, J. 1963 General circulation experiments with the primitive equations: 1. the basic experiment. *Monthly Weather Review* **91**, 99–164. (Not cited.)

Song, T.H. & Viskanta, R. 1987 Interaction of radiation with turbulence - Application to a combustion system. *Journal of Thermophysics and Heat Transfer* **1** (1), 56–62. (Not cited.)

Soucasse, L., Rivière, Ph. & Soufiani, A. 2014 Subgrid-scale model for radiative transfer in turbulent participating media. *Journal of Computational Physics* **257, Part A** (0), 442 – 459. (Not cited.)

Soufiani, A., Mignon, P. & Taine, J. 1990 Radiation effects on turbulent heat transfer in channel flows of infrared active gases. In *Radiation heat transfer: Fundamentals and applications*. American Society of Mechanical Engineers. (Not cited.)

Stamnes, K. & Stamnes, J.J. 2015 *Radiative Transfer in Coupled Environmental Systems: An Introduction to Forward and Inverse Modeling*. John Wiley & Sons. (Not cited.)

Stokes, G.G. 1845 On the theories of the internal friction of fluids in motion, and of the equilibrium and motion of elastic solids. *Transactions of the Cambridge philosophical society* **8**, 287–305. (Not cited.)

Ströhle, J., Schnell, U. & Hein, K.R.G. 2001 A mean flux discrete ordinates interpolation scheme for general coordinates,. *3rd International Conference on Heat Transfer, Antalya* . (Not cited.)

Stull, D.R. & Prophet, H. 1971 JANAF thermochemical tables, 2nd Edition. *Tech. Rep.* NSRDS-NBS 37. US National Bureau of Standards. (Not cited.)

Sundberg, J. 2006 *Heat Transfer Correlations for Gas Turbine Cooling*. Linköpings universitet. (Not cited.)

Sundén, B. 1980 Conjugated heat transfer from circular cylinders in low reynolds number flow. *International Journal of Heat and Mass Transfer* **23** (10), 1359–1367. (Not cited.)

Sutter, H. 2005 The free lunch is over: A fundamental turn toward concurrency in software. *Dr. Dobb's journal* **30** (3), 202–210. (Not cited.)

Taine, J. & Petit, J.-P. 1995 *Cours et données de base. Transferts thermiques. Mécanique des fluides anisotherme*. Ed. DUNOD. (Not cited.)

Thurgood, C.P., Pollard, A. & Becker, H.A. 1995 The TN Quadrature Set for the Discrete Ordinates Method. *Journal of Heat Transfer* **117** (4), 1068–1070. (Not cited.)

Townsend, A.A. 1958 The effects of radiative transfer on turbulent flow of a stratified fluid. *Journal of Fluid Mechanics* **4** (04), 361–375. (Not cited.)

Truelove, J.S. 1987 Discrete-Ordinate Solutions of the Radiation Transport Equation. *Journal of Heat Transfer* **109** (4), 1048–1051. (Not cited.)

Tucker, P.G. & Lardeau, S. 2009 Applied large eddy simulation. *Philosophical Transactions of the Royal Society of London A: Mathematical, Physical and Engineering Sciences* **367** (1899), 2809–2818. (Not cited.)

Van Dyke, M. 1982 *An Album of Fluid Motion*. The Parabolic Press, Stanford, CA. (Not cited.)

Veynante, D. & Moureau, V. 2015 Analysis of dynamic models for large eddy simulations of turbulent premixed combustion. *Combustion and Flame* **162** (12), 4622–4642. (Not cited.)

von Kármán, T. 1930 Mechanische Ahnlichkeit und Turbulenz. *Nach. Ges. Wiss. Gøttingen, Math. Phys. Klasse* pp. 58–68. (Not cited.)

Wang, A. & Modest, M.F. 2007 An adaptive emission model for Monte Carlo simulations in highly inhomogeneous media represented by stochastic particle fields. *Journal of Quantitative Spectroscopy and Radiative Transfer* **104** (2), 288–296. (Not cited.)

Wang, A., Modest, M.F., Haworth, D.C. & Wang, L. 2008 Monte Carlo simulation of radiative heat transfer and turbulence interactions in methane/air jet flames. *Journal of Quantitative Spectroscopy and Radiative Transfer* **109** (2), 269–279. (Not cited.)

Wang, G., Boileau, M. & Veynante, D. 2011 Implementation of a dynamic thickened flame model for large eddy simulations of turbulent premixed combustion. *Combustion and Flame* **158** (11), 2199 – 2213. (Not cited.)

Wang, H. 2011 Formation of nascent soot and other condensed-phase materials in flames. *Proceedings of the Combustion Institute* **33** (1), 41–67. (Not cited.)

Wang, Y. 2005 Direct numerical simulation of non-premixed combustion with soot and thermal radiation. PhD thesis, University of Maryland. (Not cited.)

Williams, F.A. 1985 *Combustion Theory*. Menlo Park, CA: Benjamin Cummings. (Not cited.)

Williams, G.C. & Shiman, C.W. 1953 Some properties of rod-stabilized flames C homogeneous gas mixtures. *Symposium (International) on Combustion* **4** (1), 733–742. (Not cited.)

Wlassow, F., Duchaine, F., Leroy, G. & Gourdain, N. 2010 3D simulation of coupled fluid flow and solid heat conduction for the calculation of blade wall temperature in a turbine stage. *ASME Turbo Expo 2010: Power for Land, Sea and Air, Glasgow, UK* (GT2010-22513). (Not cited.)

Woo, D.H. & Lee, H.-H.S. 2008 Extending amdahl's law for energy-efficient computing in the many-core era. *Computer* **41** (12), 24–31. (Not cited.)

Worley, P.H., Craig, A.P., Dennis, J.M, Mirin, A.A., Taylor, M.A. & Vertenstein, M. 2011 Performance of the community earth system model. *International Conference for High Performance Computing, Networking, Storage and Analysis, Seatle, WA* pp. 1–11. (Not cited.)

Woschni, G. 1967 A Universally Applicable Equation for the Instantaneous Heat Transfer Coefficient in the Internal Combustion Engine. *SAE Technical Paper 670931* . (Not cited.)

Wu, Y., Haworth, D.C., Modest, M.F. & Cuenot, B. 2004 Direct numerical simulation of turbulence/radiation interaction in premixed combustion systems. *Proceedings of the Combustion Institute* **30**, 639 – 646. (Not cited.)

York, W.D. & Leylek, J.H. 2003 Three-dimensional conjugate heat transfer simulation of an internally-cooled gas turbine vane. *ASME Turbo Expo 2003, collocated with the 2003 International Joint Power Generation Conference* pp. 351–360. (Not cited.)

Zhang, J. 2011 Radiation monte carlo approach dedicated to the coupling with LES reactive simulation. PhD thesis, Ecole Centrale Paris. (Not cited.)

Zheng, Y., Sivathanu, Y.R. & Gore, J.P. 2002 Measurements and stochastic time and space series simulations of spectral radiation in a turbulent non-premixed flame. *Proceedings of the Combustion Institute* **29** (2), 1957–1963. (Not cited.)

Zhu, X.L. & Gore, J.P. 2005 Radiation effects on combustion and pollutant emissions of high-pressure opposed flow methane/air diffusion flames. *Combustion and Flame* **141** (1–2), 118–130. (Not cited.)

Appendices

Chapter A

Large Eddy Simulation of reactive flows: equations and models

Contents

In this chapter, the compressible Navier-Stokes equations of multi-species reactive flows are first recalled in section A.1. The second section (A.2.1) details the filtered LES equations as well as the Sub-Grid Scale (SGS) and turbulent combustion models used for the present study.

A.1 Compressible Navier-Stokes equations of multi-species reactive flows

The balance equations governing compressible multi-species reactive flows in the absence of external forces are detailed in the present section. Indexes follow the Einstein summation convention except the index k which refers to the k^{th} species.

A.1.1 Momentum conservation

$$\frac{\partial \rho\, u_i}{\partial t} + \frac{\partial}{\partial x_j}(\rho\, u_i\, u_j) = -\frac{\partial}{\partial x_j}(P\,\delta_{ij} - \tau_{ij}) \quad \text{for } i = 1,3 \tag{A.1}$$

with

- ▷ ρ the mixture density,
- ▷ u_i the i$^{\text{th}}$ velocity component,
- ▷ P the pressure deduced from the perfect gas equation
- ▷ δ_{ij} the Kronecker symbol,
- ▷ τ_{ij} the viscous stress tensor.

The viscous stress tensor τ_{ij}

In a Newtonian fluid, the viscous stress tensor τ_{ij} is linearly dependent on the rate-of-strain tensor S_{ij}. Under Stokes' assumptions (Gad-el Hak, 1995) and with null bulk viscosity the relation reads:

$$\tau_{ij} = 2\mu \left(S_{ij} - \frac{1}{3}\delta_{ij} S_{ll} \right) \tag{A.2}$$

where the rate-of-strain tensor is given by:

$$S_{ij} = \frac{1}{2} \left(\frac{\partial u_j}{\partial x_i} + \frac{\partial u_i}{\partial x_j} \right). \tag{A.3}$$

The dynamic viscosity μ is supposed to depend only on the local temperature T. For the computations described in this manuscript, this dependency is approximated with a standard power law:

$$\mu = \mu_{ref} \left(\frac{T}{T_{ref}} \right)^b \tag{A.4}$$

where the constant b depends on the mixture.

A.1.2 Mass and species conservation

Introducing a multi-species formulation, the mass conservation equation splits into N species mass fraction conservation equations. Each of the N species transported satisfies the following mass fraction conservation equation:

$$\frac{\partial \rho Y_k}{\partial t} + \frac{\partial}{\partial x_j} [\rho Y_k \left(u_j + V_{j,k} \right)] = \dot{\omega_k} \quad \text{for } k = 1, N \tag{A.5}$$

with

- ▷ Y_k the mass fraction of species k,

- ▷ $V_{j,k}$ the j^{th} component of the diffusion velocity of species k,
- ▷ $\dot{\omega}_k$ the reaction source term of species k.

Given that formulation, total mass conservation imposes:

$$\sum_{k=1}^{N} Y_k V_{j,k} = 0 \tag{A.6}$$

The species diffusion velocity $V_{j,k}$

Species diffusion results from local differential of species concentration (Fickian diffusion), pressure and temperature (Soret effect) (Hirschfelder *et al.*, 1969). In combustion applications, the two latter are often neglected (Hirschfelder *et al.*, 1969; Ern & Giovangigli, 1994; Giovangigli, 1999). Note however that if sooting flames are considered the Soret effect might have a significant effect (Gomez & Rosner, 1993; Rosner *et al.*, 2000).

Considering that species diffusion is only dependent on species concentration gradients and using the first order approximation proposed by Hirschfelder *et al.* (1969) yields the relation:

$$Y_k V_{j,k} = -D_k \frac{W_k}{W} \frac{\partial X_k}{\partial x_j} \tag{A.7}$$

where D_k, W_k and X_k are respectively the diffusion coefficient, the molar mass and the molar fraction of species k and W is the mixture molar mass.

In AVBP, the diffusion coefficients are computed under the assumption of constant species Schmidt numbers Sc_k (ratio between viscous and mass diffusivity) hence:

$$D_k = \frac{\mu}{\rho Sc_k} \tag{A.8}$$

The Hirschfelder-Curtis approximation does not ensure mass conservation. Therefore, a correction velocity is added (Poinsot & Veynante, 2005):

$$V_{j,c} = \sum_{k=1}^{N} D_k \frac{W_k}{W} \frac{\partial X_k}{\partial x_j} \tag{A.9}$$

Including the correction term, the species diffusion velocity becomes:

$$Y_k V_{j,k} = -D_k \frac{W_k}{W} \frac{\partial X_k}{\partial x_j} + V_{j,c} \tag{A.10}$$

The chemical species source term $\dot{\omega}_k$

In AVBP, reduced kinetic schemes are developed to account for the chemical reaction. Reaction rates are computed thanks to classic Arrhenius laws. For a scheme including M reactions m, the source term $\dot{\omega}_k$ of species k is given by

$$\dot{\omega_k} = W_k \sum_{m=1}^{M} (\nu''_{km} - \nu'_{km})\, Q_m \tag{A.11}$$

where ν'_{km} and ν''_{km} are respectively the reactants and the products stoichiometric coefficients and Q_m is the reaction rate of reaction m.

A.1.3 Energy conservation

$$\frac{\partial \rho\, E}{\partial t} + \frac{\partial}{\partial x_j}(\rho\, E\, u_j) = -\frac{\partial}{\partial x_j}[u_i\,(P\,\delta_{ij} - \tau_{ij}) + q_j] + \dot{\omega_T} + \dot{Q} \tag{A.12}$$

with

- E the total energy defined as the sum of internal e and kinetic energy: $E = e + \frac{1}{2}u_j^2$,
- q_j the heat flux,
- $\dot{\omega}_T$ the heat released by combustion,
- $\dot{Q}$ the heat source term (reduced to the radiative source term in the present work).

The heat flux vector q_j

The heat flux vector includes the conductive flux and the energy transport due to species diffusion. The Dufour effect (heat flux induced by species concentration gradients) is neglected. The heat flux is therefore given by:

$$q_j = -\lambda \frac{\partial T}{\partial x_j} + \rho \sum_{k=1}^{N} Y_k V_{j,k} h_{s,k} \tag{A.13}$$

where λ is the thermal conductivity of the mixture and $h_{s,k}$ the sensible enthalpy of species k which is read from a database (Stull & Prophet, 1971).

Assuming a constant Prandtl number Pr (ratio between viscous and thermal diffusivity), the mixture conductivity is computed with:

$$\lambda = \frac{\mu C_p}{Pr} \tag{A.14}$$

with C_p the heat capacity of the mixture $C_p = \sum_{k=1}^{N} Y_k C_{p,k}$.

Note that for each species, mass and heat diffusivities are linked via the Lewis number Le_k:

$$Le_k = \frac{Sc_k}{Pr} \tag{A.15}$$

The heat released by combustion $\dot{\omega}_T$

Knowing the species source terms (Eq. A.11), the energy source term equals:

$$\dot{\omega_T} = -\sum_{k=1}^{N} \dot{\omega_k} \Delta h^0_{f,k} \tag{A.16}$$

where $\Delta h^0_{f,k}$ is the formation enthalpy of species k and is read from a database (Stull & Prophet, 1971).

A.2 Large Eddy Simulation

The LES Navier-Stokes equations are obtained by spatial filtering of the original balance equations. Hence, introducing a filter F_Δ of size Δ to a quantity Q yields:

$$\bar{Q} = \int Q(x') F_\Delta(x - x') dx' \tag{A.17}$$

For variable density flows, a mass-weighted Favre filtering is introduced to prevent the appearance of complex additional terms in the equations:

$$\bar{\rho}\tilde{Q} = \int \rho Q(x') F_\Delta(x - x') dx' \tag{A.18}$$

The filtered LES equations thus reads:

$$\frac{\partial \overline{\rho}\, \widetilde{u_i}}{\partial t} + \frac{\partial}{\partial x_j}(\overline{\rho}\, \widetilde{u_i}\, \widetilde{u_j}) = -\frac{\partial}{\partial x_j}[\overline{P}\, \delta_{ij} - \overline{\tau_{ij}} - \overline{\rho}(\widetilde{u_j u_i} - \widetilde{u_j}\widetilde{u_i})] \quad \text{for } j = 1, 3 \tag{A.19}$$

$$\frac{\partial \overline{\rho}\, \widetilde{Y_k}}{\partial t} + \frac{\partial}{\partial x_j}(\overline{\rho}\, \widetilde{Y_k}\, \widetilde{u_j}) = -\frac{\partial}{\partial x_j}[\overline{\rho V_{j,k} Y_k} + \overline{\rho}(\widetilde{u_j Y_k} - \widetilde{u_j}\widetilde{Y_k})] + \overline{\dot{\omega_k}} \quad \text{for } k = 1, N \tag{A.20}$$

$$\frac{\partial \overline{\rho}\, \widetilde{E}}{\partial t} + \frac{\partial}{\partial x_j}(\overline{\rho}\, \widetilde{E}\, \widetilde{u_j}) = -\frac{\partial}{\partial x_j}[\overline{u_i\,(P\,\delta_{ij} - \tau_{ij})} + \overline{q_j} + \overline{\rho}(\widetilde{u_j E} - \widetilde{u_j}\widetilde{E})] + \overline{\dot{\omega_T}} \tag{A.21}$$

Some of the unclosed terms arising from the filtered equations are expressed as a function of resolved quantities through simple approximations or gradient assumptions (see Poinsot & Vey-

nante (2005) for details). Nevertheless, the unresolved Reynolds stresses $\overline{\rho}(\widetilde{u_j u_i} - \widetilde{u_j}\widetilde{u_i})$, species flux $\overline{\rho}(\widetilde{u_j Y_k} - \widetilde{u_j}\widetilde{Y_k})$ and energy flux $\overline{\rho}(\widetilde{u_j E} - \widetilde{u_j}\widetilde{E})$ as well as chemical source terms are intrinsically affected by sub-grid turbulent processes and justify the need for dedicated Sub-Grid Scale (SGS) models. Specific models used in AVBP are briefly recalled below.

A.2.1 Sub-grid closures and models

Unresolved Reynolds stresses

The unresolved Reynolds stresses tensor seeks to describe the energy transfer between resolved large scales and modeled small scales. Most models are produced under the basic assumption that SGS are purely dissipative (referring to the energy cascade described previously). Therefore, a turbulent viscosity ν_t is introduced. The sub-grid stress tensor reads:

$$-\overline{\rho}(\widetilde{u_i u_j} - \widetilde{u_i}\widetilde{u_j}) = 2\overline{\rho}\nu_t(\widetilde{S_{ij}} - \frac{1}{3}\widetilde{S_{ll}}\delta_{ij}) \tag{A.22}$$

SGS models then differs in the formulation of the turbulent viscosity. For the present study, the algebraic Smagorinsky model is used (Smagorinsky, 1963) (it was shown on Turbomeca burners that its dynamic formulation (Germano *et al.*, 1991) increased the CPU cost with no significant improvement of the results). The turbulent viscosity is thus evaluated with:

$$\nu_t = \left(C_S\overline{\Delta}\right)^2\sqrt{2\widetilde{S_{ij}}\widetilde{S_{ij}}} \tag{A.23}$$

where the constant C_s depends on the flow and is fixed at 0.18 for common industrial applications.

The SGS species and heat flux

To model the unresolved species and energy fluxes, turbulent versions of the mixture conductivity λ_t and the species diffusion coefficient D_k^t are introduced:

$$\overline{\rho}\left(\widetilde{u_i Y_k} - \widetilde{u_i}\widetilde{Y_k}\right) = -\overline{\rho}\left(D_k^t\frac{W_k}{W}\frac{\partial\widetilde{X_k}}{\partial x_i} - \widetilde{Y_k}\widetilde{V_{k,i}}^{c,t}\right) \tag{A.24}$$

and

$$\overline{\rho}\left(\widetilde{u_i E} - \widetilde{u_i}\widetilde{E}\right) = -\overline{\lambda_t}\frac{\partial\widetilde{T}}{\partial x_i} + \sum_k \overline{\rho}(\widetilde{u_j Y_k} - \widetilde{u_j}\widetilde{Y_k})\widetilde{h_{s,k}} \tag{A.25}$$

where

$$\widetilde{V_{k,i}}^{c,t} \approx \sum_k D_k^t\frac{W_k}{W}\frac{\partial\widetilde{X_k}}{\partial x_i} \tag{A.26}$$

$$D_k^t = \frac{\mu_t}{\overline{\rho} Sc_k^t} \tag{A.27}$$

$$\lambda_t = \frac{\nu_t \overline{c_p}}{Pr_t} \tag{A.28}$$

The turbulent Schmidt $Sc_k^t = Sc_t$ (equal for all species) and Prandtl Pr_t numbers are assumed constant and are both set equal to 0.65 for the present LES applications.

A.2.2 Turbulent combustion: the thickened flame model

Significant interactions exist between the chemical reaction and turbulent mixing. In LES, these interactions need to be accounted for both at the resolved and at the sub-grid scale. In general, the premixed laminar flame thickness is below the mesh cell size. To overcome this issue, the approach used in AVBP and first proposed by Butler & O'Rourke (1977) consists in artificially thickening the flame front by a factor F (Fig. A.1) to obtain a sufficient resolution. To preserve

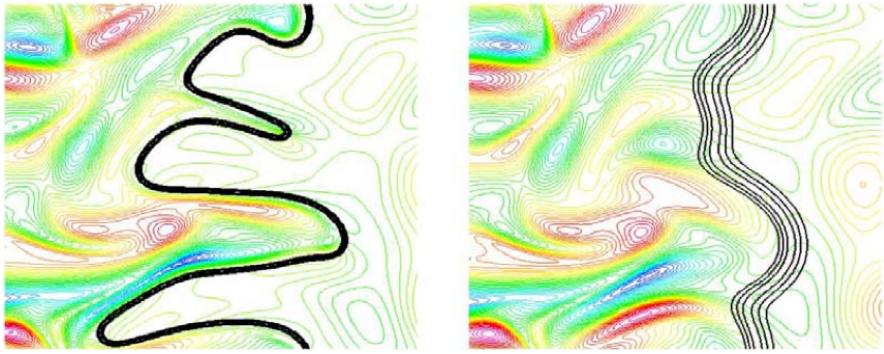

Figure A.1: Reference flame (left) and flame thickened by a factor $F = 5$ (right). Reaction rate contours are represented in black along with the velocity field from blue to red. From Poinsot & Veynante (2005).

original global flame properties while obtaining a thickened flame, species and heat diffusivities are multiplied by the thickening factor F while the reaction rate is divided by F. However, as observed in Fig. A.1 the thickening process reduces the actual flame wrinkling. To compensate this effect and model combustion/turbulence interactions (Colin *et al.*, 2000), an additional efficiency function (Charlette *et al.*, 2002) is applied to the reaction term. Note that the development of more accurate dynamic efficiency functions is still a topic under study (Wang *et al.*, 2011; Veynante & Moureau, 2015).